

**Civilian Radioactive Waste Management System  
Management & Operating Contractor**

**Total System Performance Assessment-  
Viability Assessment (TSPA-VA) Analyses  
Technical Basis Document**

**Chapter 6  
Waste Form Degradation, Radionuclide Mobilization, and  
Transport Through the Engineered Barrier System**

**B00000000-01717-4301-00006 REV 01**

**November 13, 1998**

Prepared for:

U.S. Department of Energy  
Yucca Mountain Site Characterization Office  
P.O. Box 30307  
North Las Vegas, Nevada 89036-0307

Prepared by:

TRW Environmental Safety Systems Inc.  
1261 Town Center Drive  
Las Vegas, Nevada 89134

Under Contract Number  
DE-AC08-91RW00134

#### **DISCLAIMER**

This report was prepared as an account of work sponsored by an agency of the United States Government. Neither the United States nor any agency thereof, nor any of their employees, makes any warranty, expressed or implied, or assumes any legal liability or responsibility for the accuracy, completeness, or usefulness of any information, apparatus, product, or process disclosed, or represents that its use would not infringe privately owned rights. Reference herein to any specific commercial product, process, or service by trade name, trademark, manufacturer, or otherwise, does not necessarily constitute or imply its endorsement, recommendation, or favoring by the United States Government or any agency thereof. The views and opinions of authors expressed herein do not necessarily state or reflect those of the United States Government or any agency thereof.

**Civilian Radioactive Waste Management System  
Management & Operating Contractor**

**Total System Performance Assessment-  
Viability Assessment (TSPA-VA) Analyses  
Technical Basis Document**

**Chapter 6  
Waste Form Degradation, Radionuclide Mobilization, and  
Transport Through the Engineered Barrier System**

**B00000000-01717-4301-00006 REV 01**

**November 13, 1998**

Prepared by:

\_\_\_\_\_  
William G. Halsey  
Performance Assessment Operations

\_\_\_\_\_  
Date

Checked by:

\_\_\_\_\_  
Peter K. Mast  
Performance Assessment Operations

\_\_\_\_\_  
Date

Approved by:

\_\_\_\_\_  
Robert W. Andrews  
Performance Assessment Operations

\_\_\_\_\_  
Date



## CHANGE HISTORY

<u>Rev/Change Number</u>	<u>Effective Date</u>	<u>Description and Reason for Change</u>
00	8/14/98	Initial issue.
01	11/13/98	In response to LVMO-98-D-141: correct production errors and omissions; incorporate Department of Energy comments; improve traceability of data and information sources.

INTENTIONALLY LEFT BLANK

## ACKNOWLEDGMENTS

The development of the TSPA-VA Technical Basis Document Chapter on Waste Form Degradation, Radionuclide Mobilization, and Transport through the Engineered Barrier System has benefited from the support of people from many different organizations across the Yucca Mountain Project. A number of Performance Assessment personnel and principal investigators from the scientific program made contributions to the technical content of this document. These contributors are:

Bill Bourcier (M&O/LLNL), Yeuting Chen (M&O/DE&S), Jim Duguid (M&O/DE&S), Kevin McCoy, Jerry McNeish (M&O/DE&S), Bill O'Connell (M&O/LLNL), Dave Sassani (M&O/DE&S), Eric Siegmann (M&O/DE&S), Anthony Smith (M&O/DE&S), Steve Steward (M&O/LLNL), Christine Stockman (M&O/SNL), Ray Stout (M&O/LLNL), Vinod Vallikat (M&O/DE&S), Ananda Wijesinghe (M&O/LLNL).

INTENTIONALLY LEFT BLANK

## CONTENTS

	Page
6. WASTE FORM DEGRADATION, RADIONUCLIDE MOBILIZATION, AND TRANSPORT THROUGH THE ENGINEERED BARRIER SYSTEM.....	6-1
6.1 INTRODUCTION.....	6-1
6.1.1 Waste Form Processes Important to Performance .....	6-2
6.1.1.1 Waste Form Degradation and Radionuclide Mobilization.....	6-2
6.1.1.2 Engineered Barrier System Transport Processes .....	6-2
6.1.1.3 Summary of Models for Waste Form Degradation, Radionuclide Mobilization, and Engineered Barrier System Transport .....	6-3
6.1.2 Previous Treatment in YMP Performance Assessment Modeling Efforts.....	6-4
6.1.2.1 Previous Commercial Spent Nuclear Fuel Models .....	6-4
6.1.2.2 Previous Defense High-Level Waste Glass Models .....	6-5
6.1.2.3 Previous Engineered Barrier System Transport Models .....	6-5
6.1.3 Prioritization of Waste Form Model Issues.....	6-6
6.1.3.1 Development of Issues .....	6-6
6.1.3.2 Prioritization of Issues.....	6-7
6.1.3.3 Workshop Analysis Plans.....	6-8
6.1.3.4 Goals for Model Development.....	6-9
6.1.4 External Input to Model Development.....	6-10
6.1.5 Approach and Implementation of Abstraction for Process Models .....	6-11
6.1.6 Use of Natural Analogues .....	6-13
6.1.7 Data and Model Status and Tracking .....	6-14
6.2 WASTE FORM TYPES .....	6-14
6.2.1 Waste Forms.....	6-14
6.2.1.1 Commercial Spent Reactor Fuel .....	6-14
6.2.1.2 Defense High-Level Waste .....	6-15
6.2.1.3 DOE-Owned Spent Reactor Fuel, Navy Fuel and Pu Disposition Wastes.....	6-15
6.2.2 Radionuclide Inventories.....	6-16
6.3 WASTE FORM DEGRADATION.....	6-16
6.3.1 Commercial Spent Nuclear Fuel .....	6-19
6.3.1.1 Cladding.....	6-19
6.3.1.2 Spent Fuel Air Oxidation Models .....	6-54
6.3.1.3 Aqueous Dissolution of Spent Fuel.....	6-59
6.3.2 DOE-Owned Spent Nuclear Fuel, Navy Fuel, and Pu Disposition Wastes ....	6-67
6.3.2.1 DOE-Owned Spent Fuel.....	6-67
6.3.2.2 Navy Fuel .....	6-72

## CONTENTS (Continued)

	Page
6.3.2.3 Pu Disposition Wastes.....	6-72
6.3.3 Defense High-Level Waste Glass .....	6-72
6.3.3.1 Canister.....	6-72
6.3.3.2 Defense High-Level Waste Glass Alteration Conceptual Model.....	6-72
6.3.3.3 Defense High-Level Waste Glass Model Abstraction .....	6-75
6.4 RADIONUCLIDE MOBILIZATION.....	6-80
6.4.1 Radionuclide Solubility.....	6-81
6.4.1.1 Goal.....	6-81
6.4.1.2 Conceptual Model: Solubility-Limited Aqueous Radionuclide Concentrations.....	6-81
6.4.1.3 Input Data and Assumptions .....	6-82
6.4.1.4 Results of Conceptual Model – Np Solubility Re-evaluation .....	6-87
6.4.1.5 Abstraction and Implementation into RIP.....	6-90
6.4.1.6 Representation/Validity.....	6-90
6.4.2 Colloid Mobilization .....	6-96
6.4.2.1 Goal .....	6-97
6.4.2.2 Conceptual Model .....	6-97
6.4.2.3 Implementation in RIP .....	6-100
6.4.2.4 Colloid Results .....	6-104
6.4.3 Secondary Phase Formation/Radionuclide Retention.....	6-105
6.4.3.1 Secondary Phase Formation/Radionuclide Retention: Interpretive Models for Unsaturated Drip Flow Tests .....	6-106
6.4.3.2 Secondary Phase Formation/Radionuclide Retention: Detailed Numerical Modeling .....	6-118
6.5 ENGINEERED BARRIER SYSTEM TRANSPORT .....	6-130
6.5.1 Overview of the Conceptual Model .....	6-131
6.5.2 Implementation of Conceptual Model into RIP .....	6-133
6.5.2.1 RIP Code .....	6-133
6.5.2.2 The Base Case Model.....	6-136
6.5.3 Behavior of RIP Expected Value Base Case Model .....	6-139
6.6 SENSITIVITY .....	6-141
6.6.1 Sensitivity Calculations–Base Case Waste Forms.....	6-141
6.6.1.1 Cladding Credit .....	6-141
6.6.1.2 Dissolution Models .....	6-142
6.6.1.3 Solubilities and Secondary Phases .....	6-142
6.6.1.4 Water Contact.....	6-143
6.6.2 Sensitivity Calculations: DOE-Spent Nuclear Fuel, Navy Fuel and Pu Disposition Wastes.....	6-147
6.6.2.1 Dose From Defense Spent Nuclear Fuel.....	6-148
6.6.2.2 Pu Disposition Wastes.....	6-151

## CONTENTS (Continued)

	Page
6.7 SUMMARY AND RECOMMENDATIONS.....	6-152
6.7.1 Implications for Performance.....	6-153
6.7.2 Guidance for License Application.....	6-153
6.8 REFERENCES.....	6-156
APPENDIX A .....	A-1
APPENDIX B .....	B-1
APPENDIX C .....	C-1
APPENDIX D .....	D-1

INTENTIONALLY LEFT BLANK

## FIGURES

		<b>Page</b>
6-1	Waste Form Degradation, Radionuclide Mobilization and Transport Through the Engineered Barrier System.....	F6-1
6-2	EBS Model Architecture .....	F6-2
6-3	Schematic of Waste Form/Waste Package/Engineering Barrier System.....	F6-3
6-4	CSNF Degradation/Radionuclide Mobilization Process Flow.....	F6-4
6-5	TSPA-VA Cladding Abstraction.....	F6-5
6-6	Cladding Oxide Thickness vs. Burnup.....	F6-6
6-7	Total Hydrogen Content for Cladding vs. Burnup.....	F6-7
6-8	Cladding Radial Hydrogen Profiles .....	F6-8
6-9	Fractional Fission Gas Release for PWR Fuel as a Function of Burnup .....	F6-8
6-10	Center Pin Temperature vs. Time .....	F6-9
6-11	Base-Case Waste Package Failure .....	F6-9
6-12	WAPDEG Corrosion Rate Used for Cladding Corrosion.....	F6-10
6-13	Fraction of Fuel Exposed from Zircaloy Clad Corrosion .....	F6-10
6-14	Comparison of Creep Correlations from Peehs and Fleisch, 1986 and Matsuo, 1987 at Constant Temperature .....	F6-11
6-15	Fracture Toughness vs. Hydrogen Content of Zircaloy-4 .....	F6-12
6-16	$K_{IH}$ as a Function of Hydrogen in Solution.....	F6-13
6-17	Temperature and Stress at Which Hydrogen Reorientation was Observed for Cold Worked Zirc-2, 4 .....	F6-14
6-18	A Comparison of the Empirical Equation, Equations 6-10 and 6-11, and the Exact Treatment for the Force-Displacement Relationship Using Standard Elastic-Plastic Beam Theory .....	F6-14
6-19	A Sketch of the Simplified Conceptual Model of the Mechanical Damage Process.....	F6-15

## FIGURES (Continued)

		Page
6-20	Schematized Geometry of a Block and its Impact .....	F6-16
6-21	Two Types of Punches are Considered .....	F6-17
6-22	Clad Unzipping vs. Waste Package Failure Time .....	F6-18
6-23	Time-to-Cladding-Splitting (in Hours) from Einziger and Strain (1986), with a More General Proposed Fit Added (the Longer, Lesser-Slope Line) .....	F6-19
6-24	Log/Log Comparison of the CSNF Dissolution Rate Input Data (Experimentally Measured) with the Calculated Dissolution Rate Predicted by the Fitted Function, Using All the Spent Fuel and UO <sub>2</sub> Data .....	F6-20
6-25	Error Bars for Two Typical Data Series Through the Span of Data Covered by the Fitting Data and Extending Beyond the Fitting Data; Errors in the Coefficients, i.e., Fitting Errors, Only .....	F6-21
6-26	Error Bars for Two Typical Data Series Through the Span of Data Covered by the Fitting Data and Extending Beyond the Fitting Data; Same Data Series as in Fig. 6-25; Fitting Errors and Residual Error are Included .....	F6-22
6-27	Different Logarithmic Interpolations from End Points Based on the Low- End and the 30 MW-Days/kgu Points of Equation 6-27 .....	F6-23
6-28	Comparison of Dissolution Rates for HLW, Metallic Spent Fuel, Oxide Spent Fuel, Carbide Spent Fuel, and Ceramic Spent Fuel .....	F6-24
6-29	Glass Dissolution Mechanism .....	F6-25
6-30	Normalized Elemental Release from SRL-165 Glass Reacted in 0.003M NaHCO <sub>3</sub> at 150°C, SA/V 0.01cm <sup>-1</sup> .....	F6-26
6-31	Log <sub>10</sub> (Dissolution Rate, g/m <sup>2</sup> /day) Versus Solution pH .....	F6-27
6-32	Area Increase of Thermally Shocked Simulated Nuclear Waste Glass .....	F6-27
6-33	Range of Revised Solubility-Limited Np Concentration Distribution (Shading) for TSPA-VA (After Figure 3-1 CRWMS M&O 1998) .....	F6-28
6-34	Colloidal Mobilization of Plutonium and Transport Through the EBS .....	F6-29
6-35	Experimental Test Configuration .....	F6-30
6-36	Equilibrium Film Mass Concentrations Fitted to ATM-103 Spent Fuel Vapor Test and Low-Drip Test Data Using Advective Transport Limited Approximate Model .....	F6-31

## FIGURES (Continued)

		Page
6-37	Equilibrium Film Mass Concentrations Fitted to ATM-106 Spent Fuel Vapor Test and Low-Drip Test Data Using Advective Transport Limited Approximate Model .....	F6-32
6-38	Comparison of Long-Term Equilibrium Film Mass Concentrations Fitted to Spent Fuel Vapor Test and Low-Drip Test Data Against TSPA 1995 Recommended Solubility Limits.....	F6-33
6-39	Schematic of AREST-CT Simulation Configurations for 1-D Reactive Transport Analysis of the Evolution of CSNF Under Low Water Flow Conditions .....	F6-34
6-40	Profiles of Dissolution Rate .....	F6-35
6-41	Volume Profiles of Secondary Minerals Precipitated when Spent Fuel Dissolves .....	F6-36
6-42	Paragenetic Sequence of Secondary Minerals Observed in the Simulation Results .....	F6-38
6-43	pH and U(Total) Concentration Changes for Case A .....	F6-38
6-44	Simulated Schoepite Profiles for Case-1 at Different Time.....	F6-39
6-45	Simulated Uranophane Profiles for Case-1 .....	F6-39
6-46	Simulated Concentrations of U .....	F6-40
6-47	Simulated Concentrations of Np for Case-1 .....	F6-40
6-48	Calculated Np Concentrations at the Bottom of WP for the 8 Simulations.....	F6-41
6-49	Potential Water Flow in EBS .....	F6-42
6-50	Schematic Representation of the Implementation of the EBS Model Showing the Reaction Cells used in RIP.....	F6-43
6-51	Fraction of Seep Entering Package Through Patches, Expected Value Case .....	F6-44
6-52	EBS Release of <sup>237</sup> Np from four Four Environments .....	F6-45
6-53	Release from Waste Form, Expected Value Case, Commercial Spent Fuel, Region 6, Environment 2, 20,000 Years .....	F6-46
6-54	Comparison of Tc Releases from the WF Using Different Diffusive Pathway Definitions.....	F6-47

**FIGURES (Continued)**

		<b>Page</b>
6-55	Release from Waste Form and from the Engineered Barrier System, Expected Value Case, Commercial Spent Fuel, Region 6, Environment 2, 400,000 Years.....	F6-48
6-56	Sensitivity of Dose Rate to Variation in Cladding Performance .....	F6-49
6-57	Sensitivity of Dose Rate Between TSPA-VA and TSPA-95 CSNF Dissolution Models .....	F6-50
6-58	Sensitivity of EBS Release Rate Between TSPA-VA and TSPA-95 CSNF Dissolution Models .....	F6-51
6-59	Impact of EBS Release Rate from the Revised HLW Dissolution Model.....	F6-52
6-60	Effect on Dose Rate from Experimentally Observed Mobilization Rates (10 <sup>5</sup> Years).....	F6-53
6-61	Effect on Dose Rate from Experimentally Observed Mobilization Rates (10 <sup>6</sup> Years).....	F6-54
6-62	Effect on Dose Rate from Calculated Np Concentration Controlled by Secondary Evolution .....	F6-55
6-63	Advective Release of Np from the First 6 WF Cells in the More Finely Discretized Run.....	F6-56
6-64	Comparison of Np Advective Release from the WF Cells, Two Different Discretizations.....	F6-57
6-65	Comparison of the Advective Np Release from the WF Cells, to the invert, Three Different Discretizations .....	F6-58
6-66	<sup>99</sup> Tc Release Rate from EBS, CSNF, Region 6, Environment 2, Eight Cases.....	F6-59
6-67	Tc and Np Cumulative EBS Release from CSNF, Region 6, Environment 2, Eight Cases .....	F6-60
6-68	Np WF Release from CSNF, Region 6, Environment 2, Eight Water Contact Cases F6-61	
6-69	400,000 Year Np EBS Release Rate for Eight Water Contact Cases .....	F6-62
6-70	Expected-Value Total Dose History at 20 Kilometers over 100,000 Years from all of Categories 1 Through 7 DOE SNF .....	F6-63

**FIGURES (Continued)**

		<b>Page</b>
6-71	Expected-Value Total Dose History at 20 Kilometers over 100,000 Years from all of Categories 8 Through 13, 15, and 16 DOE SNF.....	F6-64
6-72	Expected-Value Dose History at 20 Kilometers over 100,000 Years from 2,496 MTHM of DOE SNF and from 2,496 MTHM of Commercial Spent Fuel .....	F6-65
6-73	Expected-Value Dose History at 20 Kilometers over 100,000 Years from 2,333 MTHM of DOE SNF, from 2,333 MTHM of the Surrogate DOE SNF used in the Base Case, and from 2,333 MTHM of Commercial Spent Fuel.....	F6-66
6-74	Expected-Value Total Dose History at 20 Kilometers over 100,000 Years from the Base Case Repository, 2,333 MTHM of DOE SNF, and 9,334 Canisters of HLW.....	F6-67
6-75	Expected-Value Total Dose History at 20 Kilometers over 100,000 Years from 63,000 MTHM of Commercial Spent Fuel, 2,333 MTHM of DOE SNF, and 2,496 MTHM of DOE SNF .....	F6-68
6-76	Expected-Value Total Dose History at 20 Kilometers over 100,000 Years from 400 Canisters of HLW, 9,334 Canisters of HLW, and 18,994 Canisters of HLW .....	F6-69
6-77	Expected-Value Dose History at 20 Kilometers over 100,000 Years from 75 Packages of Mixed Oxide Spent Fuel and 159 Packages of Can-in-Canister Ceramic (33 Metric Tons of MOX and 17 Metric Tons of Ceramic).....	F6-70
6-78	Expected-Value Dose History at 20 Kilometers over 100,000 Years from 436 Packages of Can-in-Canister Ceramic Compared to 436 Packages of HLW.....	F6-71
6-79	Expected-Value Dose History at 20 Kilometers over 100,000 Years from 75 Packages of MOX Spent Fuel Compared to 75 Packages of Commercial Spent Fuel.....	F6-72

INTENTIONALLY LEFT BLANK

## TABLES

		<b>Page</b>
6-1	Summary of Waste Form Degradation Models, Radionuclide Mobilization Models, and EBS Transport Models for the TSPA-VA Calculations.....	T6-1
6-2	List of Waste Form Issues as Agreed Upon by Participants at Waste Form Degradation and Radionuclide Mobilization Abstraction/Testing Workshop.....	T6-3
6-3	Final Ranked Scores of Sub-Issues from Waste Form Degradation and Radionuclide Mobilization Abstraction/Testing Workshop .....	T6-4
6-4	Base-Case Waste Inventory Packaging.....	T6-5
6-5	DOE SNF in Each Category for the Total and Base Case Inventories .....	T6-5
6-6	Radionuclide Inventory in Curies per Waste Package (Average).....	T6-6
6-7	Composition of Cladding.....	T6-7
6-8	Design Characteristics of the Assembly (Westinghouse W1717WL, Base Case Fuel Assembly).....	T6-7
6-9	Cladding Oxide Thickness, Wall Thickness, and Fission Gas Release and Hydrogen Content vs. Burnup.....	T6-8
6-10	Concentration of Hydrogen in PPM as a Function of Burn-up and Depth into Cladding Surface .....	T6-8
6-11	Saturation Limits for Hydrogen in Zirconium as a Function of Temperature .....	T6-9
6-12	Causes of Fuel Failures in PWRs.....	T6-10
6-13	Pin Crack Size Probability Distribution.....	T6-11
6-14	Fission Gas Pressure, and Stress vs. Burn-up (27°C Temperature) .....	T6-12
6-15	General Corrosion of Zircaloy as a Function of WP Failure Time.....	T6-12
6-16	Comparison of Zr702 and C-276 Corrosion Rates.....	T6-13
6-17	Experimental Measurements of Zircaloy Creep.....	T6-13
6-18	Temperature Dependency of the Matsuo Creep Correlation .....	T6-14
6-19	Measured Strain Limits for Zircaloy with Hydrides .....	T6-14

## TABLES (Continued)

		Page
6-20	Pressure Effect from Helium Production .....	T6-15
6-21	Stress and Stress Intensity Factors vs. Burn-up at 350° C .....	T6-15
6-22	Threshold to Stress Intensity Factors for Two Burn-ups .....	T6-16
6-23	Puls' Zircaloy-2 Strain Tests on Zirconium with Reoriented Hydrides .....	T6-16
6-24	Amount of Fuel Damage as a Function of the Focusing Parameter for Fuel Struck by Blocks with a Circular Punch .....	T6-17
6-25	Amount of Fuel Damage as a Function of the Focusing Parameter for Fuel Struck by Blocks with a Linear Punch (Composite of Eight Punch Orientations).....	T6-17
6-26	Total Measured Release Fraction from Wilson Series 1 Tests .....	T6-18
6-27	Fractional Distribution of Gap Inventory Species Used in TSPA-1995 .....	T6-18
6-28	Regression Analysis .....	T6-19
6-29	Physical Characteristics of DOE SNF.....	T6-21
6-30	Log <sub>10</sub> Glass Dissolution Rate in g/m <sup>2</sup> /day .....	T6-22
6-31	Amorphous Silica Solubilities (Log <sub>10</sub> [molality]).....	T6-22
6-32	Distributions of Solubility-Limited Aqueous Radionuclide Concentrations for Base Case.....	T6-23
6-33	Table 3-1 from CRWMS M&O (1998a)—Summary of Np concentrations determined from spent fuel alteration/dissolution rate studies compared to the range of values provided by project-expert elicitation, which are based on the data of Nitsche et al. (1993, 1994). .....	T6-25
6-34	Preliminary results of calculated solubility limits for Np, Pu, and U .....	T6-26
6-35	Summary of UO <sub>2</sub> Alteration Phases .....	T6-27
6-36	Spent Fuel Transformation Mineral Phases in Vapor and Drip Tests.....	T6-27

**TABLES (Continued)**

		<b>Page</b>
6-37	Equilibrium Film Mass Concentrations Fitted to ATM-103 Spent Fuel Vapor Test and Low-Drip Test Data Using the Advective Transport Limited Model .....	T6-28
6-38	Equilibrium Film Mass Concentrations Fitted to ATM-106 Spent Fuel Vapor Test and Low-Drip Test Data Using the Advective Transport Limited Model .....	T6-29
6-39	Comparison of Long-Term Equilibrium Film Mass Concentrations Fitted to Spent Fuel Vapor Test and Low-Drip Test Data Against TSPA (1995) Recommended Solubility Limits.....	T6-29
6-40	Temperature, Incoming Water Composition, and Gas Fugacities .....	T6-30
6-41	Equilibrium Reactions Considered in the Step-1 Simulations .....	T6-31
6-42	Solid Reactions.....	T6-33
6-43	Rate Constants of Solid Dissolution .....	T6-33
6-44	Equilibrium Reactions Considered in the Simulations .....	T6-34
6-45	Inventory and U:Np Ratio .....	T6-36
6-46	Eight Cases of Simulation from the Possible Combinations of Scenarios, Hypotheses, and Conditions .....	T6-36
6-47	Base Case Parameters for EBS Transport Model.....	T6-37

INTENTIONALLY LEFT BLANK

## ACRONYMS

ATM	approved testing material
BWR	boiling water reactor
CDF	cumulative distribution function
CRTP	controlled release time period
CRWMS M&O	Civilian Radioactive Waste Management System Management and Operating Contractor
CSNF	commercial spent nuclear fuel
DHC	delayed hydride cracking
DHLW	defense high-level waste
DKM	dual permeability model
DOE	U.S. Department of Energy
DSNF	DOE-owned spent nuclear fuel
DWPF	Defense Waste Processing Facility
EBS	Engineered Barrier System
ECM	equivalent continuum model
EPRI	Electric Power Research Institute
FEHM	Finite Element Heat and Mass
HLW	high-level waste
IAEA	International Atomic Energy Agency
INEEL	Idaho National Engineering and Environmental Laboratory
LA	license application
LLNL	Lawrence Livermore National Laboratory
LTA	long-term average
LWR	light water reactor
INPO	Institute for Nuclear Plant Operation

## ACRONYMS (Continued)

MOX	mixed oxide fuel
MTHM	metric tons of heavy metal
MWd/kgU	megawatt day/kg of uranium
MWd/MTU	megawatt day/metric tons of uranium
NDR	never drip
NEA	Nuclear Energy Agency
NFGE	Near-Field Geochemical Environment
NMR	nuclear magnetic spectroscopy
NRC	U.S. Nuclear Regulatory Commission
O/M	oxygen/metal ratio
PA	performance assessment
PCI	pellet-clad interaction
PGE	platinum group elements
PRA	probabilistic risk assessment
PWR	pressurized water reactor
QA	quality assurance
QARD	Quality Assurance Requirement Document
RIP	Repository Integration Program
RH	relative humidity
SCC	stress corrosion cracking
SCCTP	substantially complete containment time period
SNF	spent nuclear fuel
SolWoG	Solubility Working Group

## ACRONYMS (Continued)

SZ	saturated zone
T	temperature
TAN	Test Area-North
TBD	to be determined
TBV	to be verified
TSPA-VA	Total System Performance Assessment–Viability Assessment
TST	transition state theory
UZ	unsaturated zone
WAPDEG	Waste Package Degradation Model
WF	Waste Form
WFCR	Waste Form Characteristics Report
WP	waste package
YMP	Yucca Mountain Project

INTENTIONALLY LEFT BLANK

## 6. WASTE FORM DEGRADATION, RADIONUCLIDE MOBILIZATION, AND TRANSPORT THROUGH THE ENGINEERED BARRIER SYSTEM

### 6.1 INTRODUCTION

The purpose of the repository is to dispose of radioactive wastes in a manner to protect people from potential harm from radionuclides contained in those wastes. While retained in intact solid waste forms, these radionuclides are an irradiation hazard only near the waste package (WP). To become a health risk, the waste form must be degraded and the radionuclides must become mobilized. This section addresses the performance modeling of the waste forms for which the repository has been designed, primarily commercial spent nuclear fuel (CSNF) and vitrified defense high-level wastes (DHLW), with some discussion of other Department of Energy (DOE)-owned spent nuclear fuel (DSNF). Processes important to performance include the long-term degradation of the waste forms in the Yucca Mountain environment and the mobilization of radionuclides for potential release and transport to the accessible environment.

This chapter will discuss the processes of waste form degradation and radionuclide mobilization, important issues in modeling those processes. It will present the approach taken to develop the process models and to abstract those models for use in Total System Performance Assessment-Viability Assessment (TSPA-VA) analysis. It will also present sensitivity analyses run with variations on the base-case models. Key features and processes within the Engineered Barrier System (EBS) are shown schematically in Figure 6-1. This chapter is divided into several major sections:

- Section 6.1—Introduction and model development process
- Section 6.2—Waste form types and radionuclide inventories
- Section 6.3—Waste form degradation processes and models
- Section 6.4—Radionuclide mobilization: solubilities, colloids, and secondary phases
- Section 6.5—Transport of radionuclides through the EBS
- Section 6.6—Sensitivity analyses
- Section 6.7—Summary and recommendations

After the initial failure of the waste package, the waste is potentially exposed to air, water vapor, and flowing water. This does not, however, imply that all of the radionuclides are available for transport out of the EBS. The waste forms themselves are robust containers of the radionuclides, and releases from the WP require degradation of these waste forms and mobilization of the radionuclides in a transportable form. These processes of waste form degradation and radionuclide mobilization result in a source term of mobile species available for transport through the EBS and into the unsaturated zone (UZ) of the host rock.

All of the waste form models have basic features in common. No radionuclides are mobilized until after the WP has failed, and the waste matrix is exposed to the drift environment. Other than a few limited species that have the potential for gaseous mobilization, radionuclides require aqueous mobilization to escape from the waste form and transport out of the EBS. This TSPA-VA analysis does not consider gaseous mobilization. Aqueous mobilization can be either dissolved in solution or suspended as a microparticulate or colloid. Waste form degradation

models include representations of the rate at which waste form matrix alters, either dissolving or forming secondary phases, also called the forward reaction rate. This determines the rate that radionuclides are made available for potential mobilization and forms an upper bound mobilization and release rate. However, aqueous solubility limits and retention in secondary phases are expected to limit many radionuclides to lower mobilization rates. These fundamental processes provide the framework for the models discussed in this section: surface area exposure, matrix reaction rate, secondary phase formation, solubility, colloid formation, and dissolved and colloidal transport through the EBS. The models used include detailed process models as well as the probabilistic total system performance code Repository Integration Program (RIP) (Version 5.19.01, CSCI 30055 V.5.19.01) (Golder Associates 1998). Many of the detailed process modeling results have been implemented into the RIP code for analysis of the total system performance of the repository, either in the base-case analysis or into sensitivity analyses. The EBS model architecture for TSPA-VA is shown in Figure 6-2.

### **6.1.1 Waste Form Processes Important to Performance**

The waste forms in the repository will initially be contained in and protected by the WPs. Upon failure of the packages, spent fuel assemblies and DHLW canisters will be exposed to the drift environment including air, water vapor, and potentially dripping water. Radionuclides are not available for transport until three things have occurred: failure of the fuel cladding or DHLW canister, degradation of the solid form of the waste ( $UO_2$  or glass), and the mobilization of radionuclides into aqueous solution, aqueous particulate suspension colloids, or gaseous form. These mobile radionuclides would then potentially be transported through the degraded WP and through the EBS to the UZ transport pathways.

#### **6.1.1.1 Waste Form Degradation and Radionuclide Mobilization**

The processes of waste form degradation and radionuclide mobilization depend heavily on design features and drift environment processes. The thermal history and package lifetime determine the temperature of the waste forms when they are exposed to degrading processes. The gas phase composition and aqueous chemistry of incoming water, along with the waste temperature, will control the rates of waste form degradation and the nature of mobilized products available for transport. The goal for the waste form degradation and radionuclide mobilization modeling effort is to begin with the best current understanding of these processes and the most important interdependencies, and abstract them into a form simple enough to fit within the TSPA-VA framework without excessive demand on computation time.

#### **6.1.1.2 Engineered Barrier System Transport Processes**

The EBS described here comprises all repository components within the drift (Figure 6-3). The overall waste form degradation, radionuclide mobilization, and transport of radionuclides within the EBS is dependent on numerous processes as shown on the process flow chart (Figure 6-4). The transport is influenced by the WP degradation, the waste form degradation (including cladding degradation), the thermal-hydrologic environment, the chemical environment, and the design of the EBS. The radionuclides released from the EBS are then transported to the natural system for ultimate transport through the UZ and on to the saturated zone (SZ).

The dissolution rates of the waste forms (spent nuclear fuel [SNF] and vitrified DHLW) to be used in TSPA-VA were derived from experimental data using the flow-through technique (Bates et al. 1995a; Gray et al. 1992; Steward and Gray 1994; Knauss et al. 1990). Radionuclide concentrations mobilized from the waste form are then constrained by the solubility limit of each radionuclide. The solubility limit model is a hybrid of solubility limit distributions determined by expert elicitation (Wilson et al. 1994, p. 9-1 through 9-11), and observed equilibrium concentrations reported by Finn (DTN LL980813151021.052). The incorporation of the observed equilibrium concentrations into the solubility model, provides an initial attempt to incorporate the effect of secondary precipitation phases into the evaluation of release from the waste form. In some cases, the elicited solubility constraints were described as a function of temperature (Am, Cm, Np, Pu), and pH (Am, Np, Pu). The elicited solubility constraints for Np were reevaluated in 1997 (CRWMS M&O 1998a). Along the transport pathways in the EBS, the radionuclide concentrations are checked against the solubility limit.

**Input**—The key input to the EBS transport model is the quantity and nature of radionuclides mobilized from the waste form. Also important are the flux and chemistry of the water moving through the system. Other transport parameters including retardation and permeability of the EBS materials (e.g., waste package, corrosion products, inert materials) also are significant inputs to the system.

**Output**—The output from the EBS transport model is a release of radionuclides from the EBS into the geosphere, including both aqueous and gaseous release.

#### **6.1.1.3 Summary of Models for Waste Form Degradation, Radionuclide Mobilization, and Engineered Barrier System Transport**

The major elements of the waste form degradation processes are composed of numerous submodels that must be represented in the performance assessment for the TSPA-VA. For example, these submodels include corrosion and mechanical failure of cladding, dissolution of all waste forms in the repository, solubility for radionuclides, and retardation parameters within the EBS. Table 6-1 identifies all the submodels considered for the waste degradation processes, identifies the section of this chapter that describes the submodel and its abstraction, and provides a brief description of the implementation of each abstraction within the RIP code. In effect, Table 6-1 is a “roadmap” to the numerous models discussed in this chapter and a “bridge” to the implementation of the resulting abstractions within the RIP input deck for the TSPA-VA.

It is worthwhile to note the following points about the submodels and abstractions:

- Waste Package Degradation Model (WAPDEG Version 3.07, CSCI 30048 V.3.07) simulates the generalized and localized corrosion of the Zircaloy cladding for commercial spent nuclear fuel. WAPDEG (Version 3.09, CSCI 30048 V.3.09, Rev. 2) defines the presence of patches and pits for EBS flow and transport.
- Other submodels are represented as external callable routines for RIP, as table look-ups defined through RIP input parameters, or through the source term definition for spent fuel.

- Several submodels have been excluded from the base case but are included in the sensitivity studies. For example, cladding unzipping, dissolution of Navy fuel, and the impact of decay chains with 39 radionuclides rather than the 9 radionuclides selected for the base case are identified in the table.

### 6.1.2 Previous Treatment in YMP Performance Assessment Modeling Efforts

Performance assessment of the potential Yucca Mountain repository site has been an ongoing iterative process. Before discussing development of waste form models for the current TSPA-VA, it is useful to consider the representation used for these processes in previous analyses, primarily the last complete TSPA performed in 1995 (CRWMS M&O 1995). This prior model is the starting point for the current developments discussed later. Only commercial SNF and DHLW glass were modeled in previous analyses. DOE SNF was not included in TSPA-95, but has been evaluated in CRWMS M&O (1997a). Also, degradation/dissolution models were presented for the current categorization of the DOE SNF waste forms in CRWMS M&O (1997a).

In prior analyses, initial bounds on the aqueous concentration of radionuclides in groundwater that reacted with the waste form were derived from the waste form dissolution rate model. Subsequently, another filter was applied that compares the dissolution-based aqueous radionuclide concentration with a solubility-limited value sampled from either a distribution of solubility limits for radionuclide-bearing minerals or a functional form for the solubility limit for each radionuclide considered. If the sampled solubility-limited value is lower for a given radionuclide than its concentration derived from the waste-form dissolution, then the aqueous concentration is set to the solubility-limited value and the difference in mass is calculated to precipitate out of solution. These solubility-limited values place constraints on the aqueous concentration of the particular radionuclide *element* considered, with each isotope of that element present in proportion to its isotopic abundance.

#### 6.1.2.1 Previous Commercial Spent Nuclear Fuel Models

In TSPA-95 (CRWMS M&O 1995), the entire waste form surface area was assumed to be exposed to the near-field environment as soon as the first pit penetrated the waste package. The  $\text{UO}_2$  waste form was then assumed to be covered by a thin water film, and alteration processes were initiated. For SNF, a semi-empirical model for intrinsic alteration rate of the spent fuel matrix was developed from the experimental data reported by Gray et al. (1992) and Steward and Gray (1994). The model was expressed as a function of temperature, total carbonate concentration, and pH of contacting water. The alteration rate strongly depended on temperature and total carbonate concentration, and was less influenced by pH. The surface area used was the geometric area of fuel pellets with a multiplication factor of 18 to account for cracking and grain boundary penetration of corrosion, consistent with the experimental observations of Gray et al. (1992). When the fuel was considered to have oxidized to  $\text{U}_3\text{O}_8$ , this factor was increased to 100 to account for the increase in surface area resulting from the volume increase. This number is an assumed approximation for the effect of oxidation to  $\text{U}_3\text{O}_8$ . Oxidation modeling assumed a constant 0.2 atmosphere of oxygen in the vapor phase. The base-case analysis gave no credit for cladding, although sensitivity cases were run to consider the potential performance contribution

from Zircaloy cladding. No credit was given to the role of secondary phases in retaining radionuclides, and no mobilization by colloid or particulates was considered.

Several limitations evident in the TSPA-95 representation of CSNF became goals for improvement in the current TSPA-VA. These include cladding credit, oxygen partial pressure dependence, burnup dependence, secondary phase formation, postdissolution water chemistry, and colloid formation.

#### 6.1.2.2 Previous Defense High-Level Waste Glass Models

For DHLW glass, the TSPA-95 dissolution rate equation was primarily a function of temperature and pH, but included the effects of dissolved silica in the contacting solution. The entire surface of the glass waste was assumed to be wetted by the available water. No credit was taken for the stainless steel pour canister. Surface area was a calculated geometric surface area with a multiplier (sampled between 10 and 30) to account for glass fracturing. The glass dissolution rate model predicted monotonically increasing dissolution rate with temperature. The radionuclides were assumed to be released as fast as the glass structure breaks down. Radionuclide release from high-level waste (HLW) glass should also be constrained by their solubility limit. The model did not include any solution chemistry other than pH and the dissolved silica concentration.

Goals for improving the DHLW model included temperature effect on the long-term rate, secondary phase formation, potential chemical effects from EBS materials, and colloid generation.

#### 6.1.2.3 Previous Engineered Barrier System Transport Models

Taking into account the approaches and the conceptual models for the release from a failed waste container and the EBS in TSPA-1995, both steady-state and quasi-transient diffusive mass transport models were developed (Lee et al. 1996a). The term *quasi-transient* is used because the model incorporates steady-state diffusive transfer through the perforations of the failed waste container combined with transient diffusive mass transfer through the spherical shell of the invert (other EBS components) surrounding the waste container.

Three EBS release conceptual models were developed for TSPA-1995:

**Drips-On-Waste Form**—Assumed that after one pit penetrated a waste package, the inside of the WP became the same as the drift environment. Advective flux through the WP and onto the waste form was also permitted as soon as a single pit penetrated the waste package. Diffusive releases were dependent on the surface area of the waste package, which was degraded or pitted through, and the water film thickness on the waste form.

**Drips-On-Waste Package**—Assumed only diffusive releases out of the waste package. Advective flow remained on the surface of the WP and did not flow. The corrosion products in the pits were assumed to prevent the advective or dripping water from entering the WP (Lee et al. 1996b).

**No Advective Transport through the Drift**—This model assumed no advective flow into the drift, leading to only diffusive release from the EBS. This model could be operational if the engineered system provided for diversion of all advective flow away from the drift, through such mechanisms as a capillary barrier or a drip shield.

It was assumed in previous TSPAs that the interior conditions of failed (or perforated) WP are immediately the same as the in-drift conditions. Previous TSPAs did not account explicitly for colloidal transport of radionuclides. The EBS release models were implemented in the RIP as external modules in TSPA-1995.

The distributions of solubility limits used in TSPA-1995 were based primarily on an elicitation of chemical/geochemical experts held at Sandia National Laboratories on April 13, 1993 (Wilson et al. 1994, p. 9-1 through 9-11). Judgment of the expert panel was based on both empirical studies and modeling results, but did not include consideration of distributions used in the 1991 TSPA (Barnard et al. 1992). The results of the expert elicitation were reviewed in 1993 by the Solubility Working Group (SolWoG). (SolWoG is composed primarily of project scientists conducting actinide solubility/speciation studies), which recommended only two modifications to the distributions of Np and Pu as discussed below. The assumptions behind the elicitation's development of the distributions are (1) the UZ water composition is between the composition of J-13 well water and that of UE-25p#1, (2) the solubility limits will be determined by the far-field groundwater environment, (3) the environment is oxidizing, and (4) future climate changes may cause groundwater compositional changes. A number of additional sources were used to further constrain the distributions of solubility limits for the radionuclides used in TSPA-1995. The elicited solubility constraints were input to RIP as stochastic distributions.

### **6.1.3 Prioritization of Waste Form Model Issues**

Issues associated with waste form degradation and radionuclide mobilization have been discussed in many papers and reports (Stout and Leider 1997; CRWMS M&O 1995; Andrews et al. 1994; Wilson et al. 1994; Grambow 1998; plus NRC documents, Performance Assessments [PAs], and peer reviews). Only a subset of issues and concerns could be addressed in preparation for TSPA-VA. To assist organization and prioritization of these issues into development actions for TSPA-VA, a workshop was held bringing together testing, modeling, and PA staff from within the project and interested participants and observers from outside the project.

#### **6.1.3.1 Development of Issues**

A workshop to develop plans for waste form degradation and radionuclide mobilization model abstraction and testing for the Yucca Mountain Project (YMP) was conducted in Livermore, California on February 19-21, 1997. This workshop was the fifth of ten workshops conducted for different PA topics to address key parts of the TSPA in support of the Yucca Mountain VA, scheduled for FY-98. The purpose of this workshop was to prioritize the complex set of technical issues within the topics of waste form degradation and radionuclide mobilization and develop plans to abstract the current state of understanding of the most important issues into models usable in TSPA-VA. The goal of the abstraction/testing process was then to develop simplified representations of the important processes for use in this TSPA.

The workshop followed a general format developed for, and evolving during, the series of PA workshops. Several distinct stages were included:

- Presentations of the workshop goals, TSPA, and model abstraction
- Presentation of the topics and preliminary organization of issues
- Presentations and discussion by participants to further develop the comprehensive list of issues and sub-issues
- Prioritization of the issues and sub-issues to focus effort on those issues with the most impact on long-term performance
- Development of preliminary draft analysis plans to address these issues

The entire process and product of this workshop are documented in the *Waste Form Degradation and Radionuclide Mobilization Abstraction/Testing Workshop Results* (CRWMS M&O 1997b).

A preliminary organization of issues was developed using preworkshop input from the participants. While there were suggestions for revision and addition, the participants decided to leave the preliminary organization intact and deal with changes within each session as the details were discussed. During the presentations and discussion, the issues were modified by participant consensus, resulting in a final list of issues for prioritization. Through this process, the key concerns and perspectives of the diverse participants were captured in a consensus list of issues (Table 6-2).

#### **6.1.3.2 Prioritization of Issues**

Prioritization criteria developed prior to the workshop were presented and discussed by the participants. It was decided to use the criteria as prepared following discussion of content and intent. The four general criteria are intended to represent important TSPA questions regarding the issues of the workshop. The bullets under each criterion indicate some of the contributing processes and features.

#### **Performance Assessment Criteria**

- Radionuclide Concentration at Waste Form
  - Aqueous dissolved concentration
  - Colloidal species concentrations
  - Precipitates, secondary phase formation, etc.
- Mass Release Rate of Radionuclides from the EBS
  - Peak mass release rate into UZ
  - Transported through EBS
  - Advective, diffusive, gaseous, etc.

- Time and Spatial Variability in Mass Release Rate
  - Due to variation in inventory, waste forms, flux, chemistry, temperature, package failure
- Form of Radionuclides Entering UZ for Transport
  - Chemical form of dissolved species
  - Colloidal species

These criteria were used in the ranking process. Workshop participants ranked for each issue against each of the criteria. The prioritization process is not presented here in detail, but resulted in a quantitative score for each issue within a session. Participants also established a priority cutoff, generally agreeing that the entire list of issues was too ambitious, and the best use of resources would be to focus on the highest priority issues. The final quantitative scores and action cut-off line for each set of issues is in Table 6-3. Details of the process are discussed in the workshop report (CRWMS M&O 1997b).

### 6.1.3.3 Workshop Analysis Plans

Workshop participants were divided into working groups. Priority issues were divided into topical areas and assigned to the groups. The groups then prepared abstraction/testing plans intended to guide the activities leading to TSPA-VA model inputs. Plans that address the higher priority issues were prepared. Lower priority issues will be addressed in model development. Therefore, the list of issues addressed includes many of those with lower scores. The issues addressed by the final abstraction/testing plans are itemized below. Each issue is listed once, although some may be addressed in part within more than one plan.

#### 1. CLADDING AND CANISTER CREDIT

- 1.2.1 Cladding degradation model
- 1.2.2 SNF Oxidation model
- 2B1 Cladding and Canister Credit

#### 2. SPENT NUCLEAR FUEL DISSOLUTION

- 1.2.3 SNF Dissolution model
- 1.4 Representation of data uncertainty/variability
- 1.5 Exposed SNF surface area
- 2B2 Evolution of NFE
- 2B3 Dissolution

#### 3. SNF POST DISSOLUTION WATER CHEMISTRY AND PRECIPITATED PHASES

- 1.2.4 Time dependent evolution of solution and alteration layer
- 1.3 Representation of evolution of the near-field environment

#### 4. DHLW GLASS DEGRADATION AND RELEASE

- 2.4 Vapor hydration
- 2.5 Dissolution rate
- 2.6 Time dependent evolution of solution and alteration layer
- 2.7 Evolution of NFE
- 2.8 Representation of data uncertainty/variability
- 2.9 Exposed glass waste surface area

#### 5. SOLUBILITY LIMITS

- 3.3 Chemical processes - mobilization temp dependence
- 3.4 Chemical processes - mobilization - solid dependence
- 3.5 Chemical processes - mobilization - fluid dependence

#### 6. EBS TRANSPORT AND RELEASE

- 3.1 Physical processes - water contact mode
- 3.2 Physical processes - transport paths
- 3.6 Mobilization - Colloids
- 3.7 EBS transport aqueous through WP (includes corrosion products)
- 3.8 EBS transport aqueous - through other EBS (invert)
- 3.9 EBS transport - colloid - through WP (includes corrosion products)
- 3.10 EBS transport - colloid - through other EBS (invert)

##### 6.1.3.4 Goals for Model Development

The goals for waste form model development, and abstraction and testing plans, which were developed in the Waste Form Degradation and Radionuclide Mobilization Workshop, included:

##### **Cladding and Canister Credit**

*Objective*—Develop a time-dependent distribution for cladding and/or canister perforation and fuel exposure.

##### **Spent Fuel Dissolution**

*Objective*—Develop quantitative inputs of time-dependent input water chemistry and spent fuel surface area. These inputs will be used by a dissolution model providing output water chemistry to the post-dissolution water chemistry and precipitated phase formation abstraction.

##### **Post-dissolution Water Chemistry and Precipitated Phase Formation**

*Objective*—Take dissolution model output, including water chemistry, to determine rate of precipitated phase formation (secondary phases). The output includes: dissolved and transportable species (colloids) that provide radionuclide release rate from waste form, and altered water chemistry for further waste form interactions.

## **Defense High-Level Waste Glass Degradation and Radionuclide Release**

*Objective*—Model alteration of DHLW glass waste and release of radionuclides as a function of temperature, water chemistry, water contact mode, and the extent of vapor hydration prior to liquid water contact.

## **Solubility Limits on Dissolved Radionuclides**

*Objective*—Derive constraints on dissolved radionuclide concentrations based on long-term interactions with the geologic environment.

## **Engineered Barrier System Transport**

*Objective*—Develop updated model radionuclide release from the EBS as a function of seepage, WP failure, waste form degradation, and material properties.

### **6.1.4 External Input to Model Development**

Several external groups helped develop and review waste form models for TSPA-VA.

The TSPA for the VA will be peer reviewed. The objective of the TSPA-VA peer review is to provide a formal, independent evaluation and critique of the TSPA-VA for the Civilian Radioactive Waste Management System Management and Operating Contractor (CRWMS M&O). The TSPA-VA Peer Review Panel is to consider not only the analytical approach, but also its traceability and transparency. The review of the analytical approach is to include an evaluation of

- Physical events and processes considered in the analyses
- Use of appropriate and relevant data
- Assumptions made
- Abstraction of process models into the total systems model
- Application of accepted analytical methods
- Treatment of uncertainties

The review criteria include:

- Validity of the basic assumptions
- Alternative assumptions
- Appropriateness and limitations of methods and implementing documents
- Accuracy of the calculations
- Validity of the conclusions
- Uncertainty in the results

The TSPA-VA peer review began in February 1997 and is expected to end by March 1999. The peer review has been divided into four phases: Phase 1: TSPA Orientation; Phase 2: Modeling, Scenarios, and Abstractions; Phase 3: Draft TSPA Review; and Phase 4: Final TSPA Peer Review. Interim reports are to be completed following the first three phases, and a final report

concludes Phase 4. The interim reports will allow TSPA analysts to assure significant issues are not overlooked in the TSPA-VA. The initial interim report was completed in June 1997 (Whipple et al. 1997). The final peer review report will provide comments, concerns, conclusions, and recommendations that support the development and conduct of the License Application TSPA.

The TSPA Peer Review Panel has observed the model development and abstraction process and has reviewed the initial models for the TSPA-VA base case. Panel member comments are being considered during the evolution of the base case and for sensitivity analyses.

An Expert Elicitation panel will independently make suggestions for alternative conceptual representations of waste form processes and recommend parameter ranges for either TSPA-VA base-case models or alternative models. Recommendations from this panel have guided development of the sensitivity studies.

### **6.1.5 Approach and Implementation of Abstraction for Process Models**

Because of uncertainty, variability, and complexity of the overall repository system and subsystems, some simplification of the process-level models used in the TSPA analyses are generally necessary. One reason for this simplification is to allow a range of alternative hypotheses to be investigated in a reasonable amount of computational time using probabilistic methods analogous to those used in nuclear reactor safety analyses, commonly referred to as probabilistic risk assessments (PRAs). The abstract PRA approach is useful because of the inherent uncertainties in predicting the behavior of any geologic or man-made system many thousands of years into the future. In particular, there is always a degree of uncertainty and variability in both natural geologic and engineered systems, which, when carried forward to predictions of future behavior, requires a probabilistic method. The hundreds of model realizations necessary to adequately characterize the probability distribution of future system behavior would require hundreds of computer simulations of the various process-level models. Because the simulations of the detailed process-level models are restricted by finite computer resources, some simplifications (here called abstractions) are generally necessary.

For the TSPA, the word *abstraction* connotes development of a simplified/idealized process model (with appropriately defined inputs) that reproduces/bounds the results of the underlying detailed process model. The inputs for the abstracted model can be either a subset of those required for the detailed process model or intermediate results from the detailed process model that have been analyzed to develop response functions, which can then be used as inputs to the abstracted model.<sup>1</sup> In either case, it is necessary to demonstrate that predictions of both the detailed process model and the abstracted model are reasonably similar. A general discussion of various levels of abstraction follows.

---

<sup>1</sup> These response functions (developed from the process model output) may themselves be the abstracted model.

Abstraction is defined as a process of capturing or simplifying complex and multifaceted processes that occur over many spatial and temporal scales in a manner that permits the important aspects of the processes to be included in total-system performance calculations. Abstraction is an essential element of performance assessment because of computer and personnel resource limitations. In particular, probabilistic TSPA predictions require numerous computer simulations to create performance-measure distributions that adequately cover the range of possible outcomes. However, these numerous simulations would not be feasible with existing resources if conducted with detailed process-level models, thus the need for simplification.

The major types of model abstractions to be used in TSPA-VA include (1) domain-based abstractions, (2) process-based abstractions, (3) dimensionality abstractions, and (4) response-surface abstractions. Each type of abstraction is briefly discussed below.

**Domain-Based Abstractions**—Because of gravity, fluid generally flows in one direction in the potential repository, which allows for a more or less natural division of the spatial domain into a series of regions, each dominated by one or more physical-chemical processes. At Yucca Mountain, the obvious decoupling in space is the waste form, the waste package, the emplacement drift and engineered materials surrounding the waste package, the UZ between the drift and the water table, the SZ, and the biosphere. Both energy and mass are transported downstream (i.e., with gravity) from domain to domain, but since the main goal of TSPA is to track and predict radionuclide mass transport from the waste-form domain to the biosphere domain, the main rationale of this spatial abstraction is based on the transport of mass from one domain to the next. Thus, there is a separate radionuclide transport model for each spatial domain, each run sequentially in the TSPA-VA code, with output-mass versus time from an upstream spatial domain serving as the input-mass versus time for the spatial domain immediately downstream.

**Process-Based Abstractions**—In addition to the decoupling in space of the transport models, there is another logical decoupling by physical-chemical process, for example, the decoupling of thermal-hydrologic and flow processes from transport processes. This is based on the assumption that the energy and entropy of the decoupled processes flow primarily in one direction. In particular, it is assumed that the thermal-hydrology (or just hydrology, after the thermal pulse decays) establishes and controls the liquid flux field for the transport-based models, but that transport-induced processes, such as mineral precipitation, only weakly feed back to thermal-hydrology or hydrology. If further assumption is made of steady-state flow (i.e., the parameters from the flow equations that appear in the transport equations are constant with time), then the thermal-hydrology and hydrology models can be solved first, followed by the transport models. It should be noted that abstractions such as these may change as coupled process data and models become available.

**Dimensionality Abstractions**—In general, the process models are constructed to be fully three-dimensional. Including this level of detail is believed necessary to capture all of the details of the flow and transport in geologic media. However, including this detail in TSPA predictions is not always necessary in that the dimensionality of the model may not significantly affect the predicted response from a performance perspective. Therefore, a range of dimensionality abstractions may be conducted, including:

- 1-D vertical models of drift-scale thermal-hydrology representing the 'center' and 'edge' responses of the repository, abstracted from 2-D x-z or 3-D models
- 2-D vertical cross-section flow and transport models at representative locations in the UZ (e.g., E-W or N-S transects through the center of the repository), abstracted from the overall 3-D site-scale flow and transport models
- 1-D horizontal models of SZ transport representing multiple noninteracting streamtubes, abstracted from 3-D ambient flow/transport models
- 2-D vertical models of liquid dripping onto the waste packages, abstracted from 3-D thermal-hydrology models

**Response-Surface Abstractions**—Response surfaces (multidimensional tables of the key output parameter as a function of key input parameters) are the next level of abstraction. This level requires even less computational time within the probabilistic TSPA-VA model, but could require a great amount of computational time and resources before running the overall TSPA model if it is determined that the response surfaces must be created with the highest dimensionality, most-detailed, process-level model. For instance, it may be true that proposed simple models (reduced dimensionality, simplified representation of processes, etc.) are inadequate. Perhaps they have so few measurable parameters or the dimensionality and discretization have been reduced so much that they cannot adequately predict system response over the supposed uncertainty range. Or perhaps they do not allow enough coupling to other domain- and process-based abstracted models. In this case, the only possible abstraction or simplification alternative may be to develop response surfaces based on the complex model. In this case, the complex model is run relatively few times to develop a curve fit of the nonlinear system response as a function of time, space, and the key model input parameters. Then the system response for other values of the input parameters is interpolated from the response function. (Ideally, extrapolation would never be attempted.) Consider the thermal-hydrology process model as an example. Temperature (T) and relative humidity (RH), which are the primary outputs (dependent variables) of the thermal-hydrology models, could be determined as a function of uncertainties in material properties, conceptual model, and local fluid flux ( $q$ ) by running several process-level calculations over the uncertainty ranges of these independent variables. The results could then be tabulated as a multidimensional table of T as a function of material properties, conceptual model (e.g., equivalent continuum model [ECM] vs. dual permeability model [DKM]), and liquid flux and similarly for RH.

#### 6.1.6 Use of Natural Analogues

Natural analogues can serve several useful purposes on the repository project. They can provide some insight regarding the microstructural changes to a system over time, can provide some insight into the prediction of long-term performance, and can provide some guidance to the current testing and modeling programs.

The paragenetic sequence of the glass phases over time has been studied and compared to those observed in laboratory tests of vapor and liquid exposure to radioactive glasses and simulated glasses (D. Wronkiewicz et al. 1996; J.J. Mazer 1994; Ewing and Jercinovic 1987). The phase

sequence has been found to be very similar. The sequence of changes to natural uranium ore bodies has been studied by many experimenters (B.W. Leslie et al. 1993; Finch and Ewing 1992). The results have been compared to those observed in laboratory tests of uranium oxide and spent nuclear fuel. Here again, the phase sequence has been found to be similar. These comparisons provide confidence that the degradation of these waste forms over time is well represented by the models, and that the long-term prediction of alteration rates is reasonably realistic.

### **6.1.7 Data and Model Status and Tracking**

Beginning with this analysis and document, an attempt is being made to bring the performance assessment under the control of the quality assurance (QA) program. This effort includes tracking data sources, conceptual models, assumptions, numerical codes, and parameter values. As part of this effort, data tracking information tables are included as Appendix D of this chapter. Each figure or table in this chapter (including Appendices A, B and C) which presents data is listed with reference to appropriate data source, numerical code, input and output files, QA status, and data tracking reference. While several of the analyses described in this chapter are being prepared as qualified calculations, at the time of this writing all data must be listed as not qualified (NQ) and to be verified (TBV). As this qualification effort is in progress, items with incomplete compliance are being tracked on an exceptions list for future completion.

## **6.2 WASTE FORM TYPES**

The repository program has traditionally focused on a limited set of waste types for performance assessment, including spent commercial reactor fuel and classified defense waste. This analysis has expanded the range of waste forms considered with the inclusion of DOE-owned spent reactor fuel and plutonium disposition wastes.

### **6.2.1 Waste Forms**

Radioactive waste forms that would be placed in a repository at Yucca Mountain are irradiated nuclear reactor fuel elements and solidified waste from reprocessing of irradiated reactor fuel. The radionuclides include fission products from nuclear fission during reactor operation, assorted actinides from neutron capture in uranium and plutonium, and activation products from neutron irradiation of structural materials and trace elements.

The waste forms for the baseline repository design include CSNF, DHLW, and DSNF.

The baseline repository design provides for 70,000 metric tons of heavy metal (MTHM) capacity, with 90 percent of that capacity allocated to CSNF, 6.67 percent allocated to DHLW, and the remaining 3.33 percent allocated to DSNF (CRWMS M&O 1997c). The packaging of the base-case inventory of waste is shown in Table 6-4 and totals 63,000 MTHM CSNF, 2,333 MTHM of DSNF, and 4,667 MTHM (equivalent) of DHLW allocated to 10,306 waste packages.

#### **6.2.1.1 Commercial Spent Reactor Fuel**

CSNF includes both boiling water reactor (BWR) and pressurized water reactor (PWR) fuel inventories. The allocated capacity is accommodated with a total of 7,760 CSNF waste

packages. Details of initial enrichment, burnup in reactor usage and cooling time since removal from the reactor are simplified in this analysis to average values for each fuel type. The averaged values are (CRWMS M&O 1997c):

PWR	40,958 MTHM	39.56 MWd/kgU	30 years out of core
BWR	22,045 MTHM	32.24 MWd/kgU	30 years out of core

### 6.2.1.2 Defense High-Level Waste

The available inventory of processed defense wastes available at all sites significantly exceeds the repository capacity (in metric tons of initial heavy metal equivalent) allocated to DHLW in this analysis. In this current analysis, the DHLW radionuclide inventory represents an average of glass waste from the Savannah River Vitrification Plant, processed waste from Hanford, Idaho National Engineering and Environmental Laboratory (INEEL) and the West Valley facility, reduced in magnitude to meet the allocated capacity. However, the degradation model is based on SRL-202 glass from the Savannah River Vitrification Plant only. Models for the other vitrified waste forms will be considered in future analyses.

### 6.2.1.3 DOE-Owned Spent Reactor Fuel, Navy Fuel and Pu Disposition Wastes

DSNF has over 250 potential waste form types for disposal (Stroupe 1998). For the TSPA-VA base-case analysis, these are grouped into a few representative categories. Table 6-5 provides information on the grouping of DSNF and the inventories for 16 categories. In this analysis, these forms are represented by four models (metal, carbide, ceramic and glass), with suitable variations. DSNF and DHLW are assumed to be co-disposed, that is, much of the DSNF is placed in the center of the 1,663 WPs containing DHLW glass canisters. In addition, 883 WPs contain DSNF only, for a total of 2,546 packages allocated for DHLW and DSNF. The co-disposed DHLW glass and DOE SNF are modeled independently in this analysis, without chemical interactions (interactions will be examined in future studies).

Not all of the DSNF potentially requiring disposal is included in the base-case analysis, because the available inventory exceeds the repository capacity allocated to DSNF. In addition, Category 14 for sodium-bonded fuel is recommended for processing rather than direct disposal due to the reactive nature of the metallic sodium, and is not considered in this analysis. The remaining inventory is represented by a weighted average of radionuclide inventory and is reduced to meet the capacity allocated to DSNF.

Two other DOE-owned materials were considered in separate analyses. These waste forms included spent Navy reactor fuel, and both spent mixed U-Pu oxide (MOX) fuel or immobilized Pu from the disposition of excess weapons fissile material. The MOX spent fuel is similar in composition and manufacture to commercial fuel, is burned in a commercial PWR, and the spent fuel is disposed in a 21-assembly PWR waste package. The MOX fuel contains about 5 percent Pu by weight (Murphy 1997). The MOX fuel is assumed to have Zircaloy cladding. The can-in-canister ceramic is a waste form where Pu ceramic disks are contained in 28 cans that are then

encapsulated in HLW in a HLW canister (Gould 1998). The 28 cans displace about 12 percent of the volume of a standard HLW canister. Four canisters of can-in-canister ceramic are disposed in each HLW package. Appendices A and B to this chapter include more detailed discussion of all DOE-owned materials.

### 6.2.2 Radionuclide Inventories

The radionuclide inventory varies considerably both within and between each of these waste forms. Nearly two hundred radionuclides are in these waste forms. Previous analyses indicate a limited number of radionuclides are expected to be important to repository performance. A radionuclide must meet several criteria to be significant to TSPA. One criterion is a long enough half-life to transport from the repository and create a potential exposure. Radionuclides with half life less than a few decades will decay to insignificant levels before they can escape and cause exposure to humans. Other criteria include sufficient inventory and radiotoxicity to pose a potential threat to the environment or human health and sufficient potential for transport from the repository to the accessible environment. The expected average inventory per WP for CSNF, DHLW, and DSNF waste forms for 39 radionuclides of potential interest is presented in Table 6-6. This list of 39 radionuclides is available for analysis in this current TSPA (Stroupe 1998). While these 39 radionuclides are available for consideration in this TSPA, specific analyses may further reduce the overall number of radionuclides considered in order to capture the key contributors to dose.

For many of the detailed TSPA-VA analyses, a subset of nine of these 39 radionuclides was defined. The logic for selecting seven of these isotopes ( $^{14}\text{C}$ ,  $^{99}\text{Tc}$ ,  $^{129}\text{I}$ ,  $^{79}\text{Se}$ ,  $^{231}\text{Pa}$ ,  $^{234}\text{U}$ , and  $^{237}\text{Np}$ ) was a combination of five attributes. These attributes are high solubility, low sorption affinity, amount of isotope in waste stream, a high dose conversion factor, and sufficiently long half-life to transport significant quantity to accessible environment. The other two isotopes, both plutonium ( $^{239}\text{Pu}$  and  $^{242}\text{Pu}$ ), were included (despite being highly sorbing) because of the possibility of their transport attached to colloids. Further discussion of radionuclide selection and sensitivity analysis using all 39 radionuclides can be found in Appendix C of this chapter.

This analysis did not account for decay chain details during transport of radionuclides from the waste form to the accessible environment. Instead, cases where the daughter products were potentially important were dealt with individually. Where daughter products have a significantly longer half-life than the parent, all the parent was assumed to have decayed to the daughter at the beginning of the analysis. In cases where the daughter half-life is short compared to the parent, the daughter is forced into secular equilibrium with the parent at all times on an activity basis. Further discussion of radionuclide chain decay during transport can be found in Appendix C of this chapter.

The radionuclide inventories for the DOE-owned waste forms are discussed in Appendices A and B to this chapter.

## 6.3 WASTE FORM DEGRADATION

**Introduction**—This section addresses degradation of the waste forms in air and water environments, including cladding of spent fuel and the pour container of glass waste forms. See

Section 6.1.1 for an overview of the relationship to other processes. For use in the TSPA-VA analysis code RIP, the waste form degradation processes are abstracted into dissolution rate equations for reactor fuel and vitrified waste, while cladding credit is abstracted into a limit on exposed fuel surface area.

**Goals for Model Development**—The goals for recent enhancements of waste form models (see Section 6.1.3.4) pertinent to this section included:

### ***Cladding***

*Objective*—Develop a time-dependent of fraction of fuel available for dissolution as input to the RIP code.

### ***Spent Fuel Dissolution***

*Objective*—Develop quantitative inputs of time-dependent input water chemistry and spent fuel surface area. These inputs will be used by a dissolution model providing output water chemistry to the post-dissolution water chemistry and precipitated phase formation abstraction.

### ***Defense High-Level Waste Glass Degradation and Radionuclide Release***

*Objective*—Model alteration of DHLW glass waste and release of radionuclides as a function of temperature, water chemistry, water contact mode, and the extent of vapor hydration prior to liquid water contact.

While not all details within these goals have been implemented in TSPA-VA, significant progress has been made, as will be described in the remainder of this chapter. Continued development of waste form models is anticipated beyond the viability assessment, primarily to replace remaining bounding models with more realistic representations.

## **6.3.1 Commercial Spent Nuclear Fuel**

This section examines cladding failure and unzipping, spent fuel oxidation, and the rate at which radionuclides become accessible to water-based transport processes. (See Figure 6-4 and discussion in Section 6.1, which outlines the processes addressed in each report section.) The rate of exposure of radionuclides includes the cladding gap fraction when cladding is breached or when breached cladding is wetted, and the forward dissolution rate of the spent fuel matrix exposing the contained radionuclides. Section 6.4 addresses the question of how much of this exposed material can actually remain in solution or be joined with colloids.

This discussion applies to both PWR and BWR fuels. These fuels are composed of a uranium dioxide matrix enriched to several percent  $^{235}\text{U}$  and fabricated into pellets by a press and sinter process. The pellets are enclosed in welded Zircaloy cladding to form fuel pins, which are then bundled into fuel assemblies. During irradiation in the reactor to a typical burnup of perhaps 37,000 MWd/MTU, a significant fraction of the  $^{235}\text{U}$  and a small portion of the  $^{238}\text{U}$  are converted to fission products, and some of the  $^{238}\text{U}$  is converted to higher actinides such as  $^{239}\text{Pu}$  and  $^{241}\text{Am}$ . During reactor operation, a small fraction of fission gases and elements volatile at high temperatures, mainly iodine and cesium, migrate outward from the fuel pellets and deposit

in the fuel-cladding gap. In the repository, the eventual failure of the cladding and oxidation and/or aqueous oxidative dissolution of the  $\text{UO}_2$  matrix will make these radionuclides available for potential transport out of the repository.

The larger-scale EBS model assumes that WP and spent fuel are dry if no liquid water is present, and wet if water is present as a liquid film or as seeping water. It assumes that once a WP becomes wet, it remains wet. It assumes that for a wet and breached package, all the spent fuel in breached rods becomes wet. With these assumptions about the local environment of the spent fuel, air oxidation of spent fuel only applies for a breached WP and fuel rod cladding in a dry condition. After wetting, aqueous dissolution proceeds, with the wetted fuel surface being the full fuel surface, including existing cracking and an area contribution from intergranular penetration, plus an added factor if oxidation preceded the wetting.

**Cladding Model**—Credit for Zircaloy cladding has been provided for TSPA-VA in the form of a fractional multiplier on the SNF available for dissolution. This multiplier is calculated from the fraction of fuel pin surface area failed from several potential degradation modes for Zircaloy that are dependent on the thermal history and time of container failure.

The model addresses juvenile failure of Zircaloy-4 cladding. Self-standing analytical models are developed for Zircaloy-4 cladding failure from creep strain, delayed hydride cracking, and mechanical failure from rock drops. General and local corrosion of the Zircaloy cladding is addressed. Finally, cladding unzipping because of fuel oxidizing from  $\text{UO}_2$  to  $\text{U}_3\text{O}_8$  is considered. The stainless steel clad fuel is assumed to be available for dissolution. (No credit is taken for stainless steel cladding.)

Cladding modeling results predict fewer than 2 percent of the pins will perforate in the early stages when temperature is elevated; perforation of this 2 percent or less is principally caused by juvenile failures and creep rupture, which would occur whether or not the WP is breached. The model predicts 5 percent of the pins will fail because of rock drops after the WP offers little or no protection. Unzipping due to air oxidation is rare due to the small fraction of combined WP and cladding breaches during the early elevated-temperature period, and is absent in the base-case conditions. The abstraction of the cladding analysis generates the fraction of  $\text{UO}_2$  fuel available for dissolution for the RIP code.

**Oxidation Model**—Once the WP and cladding have failed, the fuel is exposed to the drift environment. If this exposure occurs early enough for the fuel temperature to be significantly elevated because of radioactive decay heat, then the  $\text{UO}_2$  can oxidize to higher oxidation states. The importance of this process depends on the large increase in active surface area upon transition to  $\text{U}_3\text{O}_8$ , due to the significant increase in specific volume. An oxidation model has been developed from  $\text{UO}_2$  experimental data.

In this TSPA-VA analysis, the oxidation model is not a significant contributor to the results, and is only important for the limited case of early container cladding failure. This is due to the long life of the WP and the expected aqueous conditions on the waste surface exposed to the drift environment (expected because of the deliquescent properties of the fuel). In general, by the time a WP fails in this analysis, the fuel temperature has dropped low enough that  $\text{U}_3\text{O}_8$  conversion is not expected and aqueous dissolution is expected.

**Cladding Gap Fraction of Radionuclides**—Spent fuel exposed to aqueous flow shows an initial rapid release of a small fraction of the radionuclide inventory. This inventory is attributed to a portion of certain radionuclides residing in a form readily mobilized on the cladding surfaces, on the UO<sub>2</sub> surface, in the gap between the fuel and cladding or in grain boundaries near the UO<sub>2</sub> surface. This inventory is considered immediately available for mobilization on exposure.

In this TSPA-VA analysis, the rapid release fraction is not a significant factor because it is assumed that aqueous dissolution of the fuel begins with exposure and because of the relatively long time steps in most of the analyses. The fractional dissolution in the time step of initial exposure generally exceeds the rapid release fractions.

**SNF Intrinsic Dissolution**—A more detailed model of SNF intrinsic dissolution rate, also known as the forward reaction rate, has been fitted to high-flow-rate data on SNF and UO<sub>2</sub>. This fit provides dependence on temperature, pH, CO<sub>3</sub>, burnup, and oxygen potential—more environmental parameters than in the TSPA-95 model, as requested by the workshop results. This rate equation is used as the upper bound on the availability of radionuclides for potential mobilization.

To the extent that one or more of these parameters are held constant in the TSPA-VA base case or sensitivity analyses, this equation is effectively the same as a simpler form with fewer terms.

### 6.3.1.1 Cladding

An initial model has been developed to represent the fuel matrix protected by Zircaloy cladding. For long-lived waste packages, fuel pin temperatures will have dropped to near ambient at the time the cladding is exposed to the drift environment. With these reduced temperatures, the stress level from internal gas pressure in the fuel pin will be small. Additionally, the oxidation rate of Zircaloy is very low at reduced temperatures. This section discusses potential degradation modes for the cladding at long times in the repository, and develops a cladding performance credit in terms of limitation of the surface area of fuel matrix exposed to the drift environment.

#### 6.3.1.1.1 Cladding Summary

Most commercial nuclear fuel is encased in Zircaloy cladding. Models were developed to describe cladding degradation from creep, corrosion, and mechanical failure (rock falls). No cladding credit was taken for the stainless steel-clad fuel (1.15 percent of inventory) or fuel with defective cladding from reactor operation (0.1 percent). Figure 6-3 shows the various cladding degradation mechanisms, Figure 6-4 shows the incorporation of cladding credit into the fuel dissolution process, and Figure 6-5, Cladding Abstraction, summarizes the three specific abstractions for the fraction of the fuel in a WP available for fuel dissolution as a function of time. The abstraction to the RIP code separately calculates the fuel available from local corrosion, mechanical failures, and juvenile failures (stainless steel and reactor failed fuel). Both the maximum and minimum values are shown. For the multiple realization base case, the RIP code samples between the maximum and minimum values using a log uniform distribution. Before about 10,000 years, only the stainless steel and defective fuel are available for dissolution when the WP is penetrated. At about 100,000 years, both mechanical failures and corrosion start

to expose more fuel for dissolution. At one million years, about 50 percent of the fuel is available for dissolution. Both creep and delayed hydride cracking were modeled, but neither contributes significantly to the amount of fuel available for dissolution. The overall effect of the cladding degradation model is to reduce the amount of fuel at any give time that is available for dissolution.

#### **6.3.1.1.2 Cladding in Commercial Light Water Reactor Operation**

Commercial reactor fuel design has been evolving. Eight of the earlier reactors used stainless steel cladding but no operating reactor currently uses this type of cladding. A total of 723 metric tons of uranium is contained in this type of fuel, 1.15 percent of the estimated 63,000 metric tons of commercial fuel to be placed in the repository. No cladding credit is taken for stainless steel and it is assumed that this fraction of the fuel is exposed for dissolution when the WP fails. The model currently spreads the stainless steel cladding over all WPs in the repository. This model is appropriate if you have large numbers of WPs failing and sufficient mixing. With current WP corrosion models, unsaturated flow models, and saturation flow models, which all produce less mixing, this assumption will be reevaluated during license application (LA).

Zirconium first became available in industrial quantities in 1946 when a commercially viable process to refine it was developed. The metal was first used in the chemical industry for corrosion control applications such as boiling HCl. Because of its high cost (\$15-\$20/lb for commercial grade tubing), its use tends to be limited.

Zirconium was introduced as a fuel cladding material in the early 1950s. There are two types of light water reactors (LWRs): BWRs and PWRs. In a BWR, the coolant is permitted to boil in the reactor core and the steam is piped to a steam turbine to make electricity. In a PWR, the reactor coolant is pressurized so that it does not boil and is piped to a steam generator where a second coolant is permitted to boil, generating steam to be piped to the steam turbine. Both types of reactors are fueled by zirconium alloy rods containing pellets of UO<sub>2</sub> ceramic material.

The behavior of these materials in reactor operation has been extensively researched. Such work is reported in the American Society for Testing and Materials "Zirconium in the Nuclear Industry" held every 2.5 years, the American Nuclear Society's topical meetings "International Topical Meeting on Light Water Reactor Fuel Performance," or other technical publications.

#### **6.3.1.1.2.1 Types of Cladding**

Alloys of zirconium were introduced as cladding early in the LWR development because this material has excellent corrosion properties and low thermal neutron capture cross section. Nuclear grade zirconium differs from commercial grades in that the hafnium, which naturally occurs with zirconium and has a large neutron cross section, is removed. Using materials with low neutron absorption cross sections reduces fuel cost because more neutrons are available for neutron fissioning and energy production.

Two different alloys of zirconium are currently used: Zircaloy-2 and Zircaloy-4. These alloys were produced to reduce the general corrosion rate in water. Zircaloy-2 tends to be used in BWRs and Zircaloy-4 is used in PWRs. The primary difference is the nickel content (see

Table 6-7). As reactor fuel cycles are extended, advanced alloys are being developed. New alloys such as M-4, M-5, and ZIRLO have been developed for reduced corrosion and hydrogen pickup (see Section 6.3.1.1.2.2). McCoy (CRWMS M&O 1998b) describes the various fuel element designs that have been used in the United States. The fuel element design integrates the cladding thickness with other features such as cladding material, pin linear power, gas plenum volume, expected burnup, and pin center temperatures so that desired pressures and stresses are maintained.

For this cladding degradation analysis, the Westinghouse W1717WL (17 x 17 Lopar) assembly was selected. This is the most commonly used element, constituting 21 percent of the discharged PWR assemblies (CRWMS M&O 1998b, Table 4.1.1-1). The W1717WL is the largest fraction of the more general W1717 type design that constitutes 34 percent of the discharged PWR fuel. The W1717 design is the thinnest clad fuel (570 microns) (CRWMS M&O 1998b, Table 4.1.2-1). McCoy (CRWMS M&O 1998b) summarizes all the fuel assembly designs. Table 6-8 gives typical characteristics of a Westinghouse W1717WL design. Because it operates under higher stress, is thinner, and is not enclosed in a flow channel, PWR fuel was selected for cladding degradation analysis. The PWR type is the more limiting type. This assumption will be reviewed for LA.

#### 6.3.1.1.2.2 Surface Corrosion

As the fuel is irradiated in the reactor, the outer surface oxidizes, thinning the cladding and producing hydrogen, some of which is absorbed into the cladding. Figure 6-6, taken from Garde (1991) (plotted curve in the figure is Garde's fit), shows the maximum oxide thickness as a function of rod average burnup. This was fitted by a quadratic equation:

$$\text{Ox } (\mu\text{m}) = 49 - 2.775 \text{ Bu} + 0.05625 \text{ Bu}^2 \quad (6-1)$$

where

Ox = oxide thickness in  $\mu\text{m}$

Bu = burnup, in MWd/kgU

This equation should not be applied for burnups below 25 MWd/kgU because it diverges from the data. Table 6-9 gives both the oxide thickness and cladding thickness for various burnups. Metal loss is approximately 57 percent of the theoretical oxide thickness because of the reduced density and voids in the  $\text{ZrO}_2$ . This is the inverse of the Pilling-Bedworth factor of 1.75 given by Van Swam et al. 1997, p. 426. The reported value is slightly higher than earlier values of 1.56.

#### 6.3.1.1.2.3 Hydride Formation

As the cladding oxidizes, hydrogen is absorbed and forms hydrides in the cladding. The hydride content affects the potential for delayed hydride cracking and cladding embrittlement. Mardon et al. (1997) shows the increase in hydrogen content as a function of burnup. Figure 6-7 presents his figure, which was fitted with a quadratic equation:

$$H_{\text{ppm}} = 4.75 \text{ Bu} + 0.0875 \text{ Bu}^2 \quad (6-2)$$

where

$H_{\text{ppm}}$  = the radial averaged hydrogen content in weight, ppm

Bu = burnup, in MWd/kgU

This equation, for Zircaloy-4, was fitted to 20, 40, and 60 MWd/kgU and, by happenstance, the constant term dropped out and the equation predicts zero hydrogen content at zero burnup. Table 6-9 gives the average hydrogen content for various burnups using the above correlation.

The hydrogen content is highest at the outer surface and decreases toward the center. Figure 6-8 gives the normalized distribution measured by Schrire and Pearce (1994). Assuming this shape is preserved, the curve for the peak oxide location was used to predict the concentration of hydrogen across the cladding as a function of burnup and distance from the cladding outer surface (Table 6-10). The curve used is for the peak oxide thickness that has the peak hydrogen pickup. Other locations have less hydrogen and a flatter profile. This table shows that the outermost surface of the cladding contains hydrides in excess of 1,000 ppm and becomes fairly brittle, but most of the cladding maintains its structural strength (see Figure 6-15 for plot of fracture toughness). This table should be compared with the saturation limit for hydrogen on zirconium. The correlation is recommended by Pescatore et al. (1989), in his equation 6, and is given in Table 6-11. This table gives the saturation limit as a function of temperature. For most burnups and radial positions in the cladding, the amount of hydrogen exceeds the saturation limit as the cladding cools from the maximum temperature of 350°C to 45°C as the repository cools (120 ppm). Hydrides are expected to be in the cladding at 350°C, and as the repository cools, up to 120 ppm of hydrogen will become available for hydride formation as the cladding cools. The hydrogen could migrate to cooler areas, help for reoriented hydrides, or participate in delayed hydride cracking. The failure modes will be discussed later.

This analysis is for today's most commonly used cladding material in PWRs, Zircaloy-4. Zircaloy-2 and Zircaloy-4 are very similar. Both Figures 6-6 and 6-7 show that as higher burnups are approached, the oxidation and hydrogen content of the cladding increase geometrically. Today's advanced fuels are being discharged with burnups of 45 - 50 MWd/kgU with a few test assemblies being discharged as high as 60 MWd/kgU (DOE 1996). As higher burnup fuels are developed, designers will be forced to use special alloys such as M4 or M5 shown in Figure 6-7. These types of alloys will reduce the amount of oxidation. Charquet et al. (1994) shows that the amount of hydrides in the fuel depends on the amount of oxidation of the cladding, and advanced cladding alloys will produce hydride quantities proportional to the reduced oxidation rates. Although current plant technical specifications permit reactor operations with failed fuel, operators make a concerted effort to identify and remove fuel at the next refueling outage. Future fuels will need to be as reliable as current ones. This will require advanced alloys with reduced oxidation rates.

#### 6.3.1.1.2.4 Crack Size Distribution

Delayed hydride cracking (DHC) starts with an existing crack. The shape and depth of the crack determine hydride stress intensity factor at the crack tip. For this analysis, a sharp-tipped crack shape is assumed (the limiting case). Sanders et al. (1992, p. III-56) present a method of developing a crack size distribution and recommends a maximum initial crack size for fuel not failing during irradiation to be 28 percent of original cladding thickness based on two different analysis (Sanders et al. 1992, p. I-52). Cladding with larger initial cracks will fail as the cracks propagate through the cladding. This analysis uses both Sanders method and maximum crack size. It is assumed that the crack size distribution is exponentially shaped. Sanders et al. (1992, p. I-52) report that surveys of manufacturing defects verify an exponential shape distribution:

$$P(w) = A e^{-Bw} \quad (6-3)$$

where

$$\begin{aligned} P(w) &= \text{probability of having a crack of depth } w \\ w &= \text{crack depth, } \mu\text{m} \end{aligned}$$

This equation is integrated for crack depth from  $w$  to  $\infty$ , giving the probability of having a crack of size  $w$  or larger:

$$F(w) = e^{-Bw} \quad (6-4)$$

where

$$\begin{aligned} F(w) &= \text{probability of having a crack of depth } w \text{ or larger} \\ w &= \text{crack depth, } \mu\text{m} \end{aligned}$$

The variable  $B$  can be evaluated by reviewing fuel performance and calculating the probability of pin failure from cracks. Yang (1997) reviewed PWR fuel performance and reported 485 fuel assembly failures in 16,153 assemblies over the last 5 years that data are available (the table has been reproduced as Table 6-12). Yang reports the causes of the failures and reports that 240 failures were caused by external events (handling, debris, and grid fretting). It is assumed that the remaining failures (245) were all caused by initial cladding cracks in a pin that were at least 28 percent through wall (160  $\mu\text{m}$  for the W1717WL). This assumption is very conservative because some of these failures were not caused by cracks. Considering the mixture of the different types of PWR assemblies, the average assembly has 221 pins in it. It is also assumed that each failed assembly has 2.2 failed pins in it (EPRI 1997, p. 4-1). The probability of having a crack equal to or greater than 160  $\mu\text{m}$  is:

$$F(160 \mu\text{m}) = 2.2 \cdot 245 / (221 \cdot 16153) = 1.51\text{E-4} = e^{-B \cdot 160} \quad (6-5)$$

This equation is used to evaluate  $B$  ( $B = 0.055 \mu\text{m}^{-1}$ ). Table 6-13 gives the probability of having cracks larger than various sizes. The median (50 percent) crack is about 12  $\mu\text{m}$  (2.1 percent of clad thickness) deep or deeper. A maximum crack size for fuel not failing during

irradiation is calculated to be 28 percent of cladding thickness or larger (Sanders et al. 1992, p. I-52) (160 μm) and has a probability of 1.51E-4/pin.

### 6.3.1.1.2.5 Fission Gas Release, Pressurization, and Hoop Stress

The cladding stress depends on the temperature and quantity of fission gas in the plenum. Stress drives both delayed hydride cracking and creep failure. The quantity of fission gas in the plenum depends on the burnup and fission gas release fraction. Garde (1986) (Table 4 and Table 7) reported that the amount of fission gas produced per MWd/kgU as 0.274 cc (STP)/cc fuel/MWd/kgU burnup. He also measured the effective gas volume as being 150 percent of the plenum volume. Table 6-9 gives the amount of fission gas (cc, STP) produced in a W1717WL pin as a function of burnup. Most of this gas is held in the fuel pellet. Figure 6-9 gives the release fraction reported by Manzel and Coquerelle (1997). These release fractions are for advanced fuels and are higher than those reported by Manaktala (1993, Figure 3-5). Manaktala shows fission gas release of about 1 percent for 30 MWd/kgU, one fourth of that reported by Manzel. It is conservative to use the higher releases for these calculations. Manzel's data was fitted by a quadratic (note that this is different from the equation plotted in Figure 6-9):

$$\text{FGR} = 4.5 - 6.25\text{E-}3 * \text{Bu} + 1.5938\text{E-}3 * \text{Bu}^2 \quad (6-6)$$

where

FGR = fission gas release (%)

Bu = burnup in MWd/kgU

Table 6-9 gives the fission gas release fractions as a function of burnup using the above equation. The gas release fractions are higher than those measured in Approved Testing Material (ATM) fuels ATM-103, ATM-104, ATM-105 and 20 percent lower than that measured for ATM-106, as releases for typical pressurized pins in PWRs are less than 1.5 percent for burnups up to 45 MWd/kgU (see Figure 3-5 in Manaktala 1993). The release fractions reported by Manzel and Coquerelle 1997, and modeled here with the above equation, are higher than those reported by Manaktala. It is conservative, when calculating stress, to use the higher release fractions. The plenum pressure includes an initial He fill pressure of 2.8 MPa. The thin wall approximation for hoop stress was used. The equation used is:

$$\text{St} = \text{P} * \text{ID} / [(2 * (\text{Th-Ox-w})] \quad (6-7)$$

where

St = cladding stress, MPa

P = fission gas pressure, MPa

Th = initial cladding thickness, cm

Ox = oxide layer thickness, cm

- w = crack depth, cm  
ID = cladding inside diameter, cm

No credit was taken for any structural support or compression stress from the oxide layer. The thin wall approximation underestimates the stress at the inside of the cladding by 7 percent, when compared with the thick wall approximation, an error that is small compared with the other uncertainties in this analysis. The difference between oxide thickness and actual metal loss would also reduce the calculated stresses. Stress concentration at a crack tip is discussed in Section 6.3.1.1.6. Table 6-14 gives the pressure and hoop stress at room temperature for both the median and maximum crack depth. The calculated stresses for the median crack agree with the stresses reported for W1717 by Pescatore and Cowgill (1994, Figure 2.2).

Pescatore et al. (1989, Table 9), give both average and maximum hoop stresses for both PWR and BWR fuels. For 320°C, his average values vary from 24 to 62 MPa and his maximum values are up to 134 MPa. He also notes that peak rods represent less than 1 percent of the total rods. He shows that BWR stresses are half that in PWRs, partially explaining why PWR fuel is used as the limiting type fuel for repository design.

#### 6.3.1.1.2.6 Pin Failures During Reactor Operation

The commercial Zircaloy-clad fuel has improved with time. Early cores (up to 1985) had a pin failure rate from 0.02 percent to 0.07 percent (EPRI 1997, p. 4.1–4.4). The assembly failure rates during that period were from 10 percent to 20 percent but few pins (average of 2.2) were failed in a failed assembly. After 1985, the pin failure rate decreased to 0.006 percent—0.05 percent with the assembly failure rates decreasing to 0.5 percent—3 percent. The overall pin failure rate for both time periods is 0.01 percent—0.05 percent. Manaktala (1993 p. 3-4) shows fuel reliability as a function of calendar year for both PWR and BWR fuel from 1969 through 1976. He shows early PWR cores had failure rates over 1 percent but the rates dropped below 0.1 percent by 1973. The BWR failure rates fell below 0.1 percent after 1975. Yang (1997), (see Table 6-12), summarized the frequency and type of assembly failures from 1989 through 1995. Yang's failure data are for assemblies, and can be converted to pin failure rates using 2.2 failed pins per assembly (EPRI 1997, p. 4-1), and an average of 221 pins per assembly. The INEEL dry storage program (McKinnon and Doherty 1997) observed for nonconsolidation, 2 pins leaked/16,700 rods (failure probability = 1.2E-4) from all causes including reactor operation and shipping. These data are relevant because a detailed survey of the fuel was performed after receiving it at INEEL. After consolidation at INEEL, the failure probability was 12 pins/9,800, or 1.22E-3, an increase by 1 order of magnitude, and very close to the value of 0.1 percent used in this analysis for all commercial fuel.

Occasionally a specific core will have a higher failure rate. These data are included in the EPRI fuel failure rate, and affect the averages slightly. After a steam generator replacement in 1981, one reactor operator reported (McDonald and Kaiser 1985) 0.26 percent of the pins (32 percent of the assemblies) damaged by fretting from foreign particles, debris from the steam generated replacement. More recently, a Midwestern utility reported 0.4 percent of the pins failed, possibly from grid support fretting (Siegmann, E.R. 1998). These two cases of severe core damage show that relatively small fractions of the pins are actually damaged. For this analysis, it is

conservatively assumed that 0.1 percent of all the pins are damaged to some degree based on the EPRI 1997 overall pin failure rate of 0.01 percent – 0.05 percent. The French (Ravier et al. 1997, Figure 4) report annual pin failure rates from 5.5E-4 to 0.0 from 1986 through 1996. Their reactors are PWRs based on the Westinghouse design, and have similar fuel designs as the American reactors. The Japanese (Sasaki and Kuwabara 1997, p. 13-14) report failure rates of 0.01 percent for BWRs and 0.002 percent for PWRs. Their BWR design is based on the GE design, and their fuel designs are similar to the Americans. Both rates are similar to the current United States observed rates.

The PWR industry has been plagued with steam generator problems that require steam generator maintenance at most refuelings. This has put great pressure on the operators to keep the primary system as clean as possible. The BWR design runs primary coolant steam through the steam turbine so they also are under pressure to keep the primary coolant as clean as possible. Some refueling contracts require fuel manufactures to replace any failed fuel from an incomplete fuel cycle at the refueling. The Institute for Nuclear Plant Operation (INPO) collects and reports reactor performance in terms on fuel cycle, with or without failed fuel. These occurrences have led to sophisticated detection techniques (Sunderland et al. 1994) to detect failed fuel and identify in which fuel cycle it is located. Sayles et al. (1994) describe identifying single failed pins in operating reactors and using the ratio of  $^{134}\text{Cs}$  to  $^{137}\text{Cs}$  to identify in which fuel cycle the failed pin was located. In most cases, failed fuel pins are removed from the assemblies and replaced before the assembly is reinserted.

Pin damage characteristics in reactor operation (EPRI 1997, p. 4-2, 4-3) is:

Pinhole and through wall hairline cracks	80 to 90 percent
Intermediate condition	10 to 20 percent
Severe damage	0.04 to 0.9 percent

In terms of exposing  $\text{UO}_2$  fuel pellets to the environments after the WP fails, most of the fuel that has failed during reactor operation will still have some protection from the cladding. In future analysis, the radionuclide release from perforated cladding might be included in the modeling.

For the analysis used in TSPA-VA, no credit was taken for the 0.1 percent cladding in fuel damaged during reactor operation. This is based on the EPRI 1997 review of operating experience that concludes that overall pin failure rate for both time periods is 0.01 percent – 0.05 percent.

#### **6.3.1.1.2.7 Spent Fuel Pool Storage**

After discharge from the reactor, the fuel assemblies are stored in open spent fuel storage pools. An International Atomic Energy Agency (IAEA) survey (IAEA 1988, Table XXVI) reported no evidence of fuel degradation in spent fuel pools and no evidence of degradation of fuel damaged during reactor operation. The oldest fuel in the survey was Shippingport PWR fuel that has been in wet storage since 1959. Other fuel reported to have no further degradation has been in wet storage since 1962, 1966, 1968, and the 1970s.

Under the DOE Spent Fuel and Fuel Pool Component Inventory Program, the effect of storing both intact and fuel with failed cladding has been studied. An international survey of water storage (Johnson et al. 1980, p. iii) reports no cases of fuel cladding degradation on pool stored fuels.

Johnson (1977, p. 20), reports: "Operators at several reactors have discharged, stored, and/or shipped relatively large numbers of Zircaloy-clad fuel that developed defects during reactor exposures (e.g., Ginna, Oyster Creek, Nine Mile Point, and Dresden Units I and II). Several hundred Zircaloy-clad assemblies that developed one or more defects in a reactor are stored in the GE-Morris pool without needing special containment. Detailed analysis of the radioactivity in the pool water indicates that the defects are not releasing significant quantities of radioactivity."

The importance of the spent fuel pool storage experience is that fuel failures or degradation is not expected during pool storage, and the fuel failure rates observed from reactor operation are appropriate for the cladding degradation analysis.

#### **6.3.1.1.2.8 Dry Storage**

The DOE has sponsored a Spent Nuclear Fuel Integrity During Dry Storage-Performance Tests Program at the INEEL since 1984 (McKinnon and Doherty 1997). Approximately 26,500 pins have been studied in various commercial dry storage casks. This program also demonstrates what can be expected to happen to fuel in repository WPs early when temperatures are elevated. The cover gas has been monitored and no pin failures have been observed during dry storage. During fuel consolidation, about 10 pins developed small leaks. Consolidation permits 2 subassemblies to be stored in the location of one (408 rods, 2\*204 for Westinghouse 15\*15). Some pins leaked but the release was over 2 months, a very slow gas release. In leakers, only 0.5 percent of  $^{85}\text{Kr}$  is released. After shipment to the INEEL, the observed pin failure was similar to that after reactor operation. For nonconsolidation, 2 pins leaked/16,700 rods, probability =  $1.2\text{E-}4$ , below the 0.1 percent failure rate used in this analysis.

Some utilities performed fuel consolidation before the introduction of dry storage facilities. After consolidation at INEEL (McKinnon and Doherty 1997), 12 pins/9,800 = probability =  $1.22\text{E-}3$ , increased by 1 order of magnitude from their nonconsolidated failure rate. This is slightly larger than the 0.1 percent failure rate used in this analysis.

Dry storage tests were performed at the Nevada Test Site (Johnson et al. 1987) with 17 spent fuel assemblies, each in an individual test. These tests contained 3,468 pins, and cladding temperatures varied from 168 to 380°C. One of the fuel rods failed during these tests. This assembly was exposed to air at 275°C and had nine thermal cycles. The estimated hole size was 1 micron. No further degradation was observed after the initial failure. No visible damage was observed in the other tests.

Accelerated high temperature tests were performed on 15 rods with cladding (Einzigler et al. 1982). Postirradiation studies on failure mechanisms of well-characterized pressurized water reactor rods were conducted for up to a year at 482°C, 510°C, and 571°C in limited air and inert gas atmospheres. No cladding breaches occurred. Rods had crept away from the pellets and

showed a smoother profile. Strains from 1.7 percent to 7 percent were measured. One pin had a local creep as high as 12 percent. The extended lifetime is due to significant creep strain of the Zircaloy cladding, which decreases the internal rod pressure. The cladding creep also contributes to radial cracks, through the external oxide and internal fuel-cladding chemical interaction layers (layer of a few microns where some zirconium/ $\text{UO}_2$  interaction occurs), which propagated into and arrested in an oxygen stabilized alpha-Zircaloy layer. Since cracks extended only for a few microns and were arrested, their significance was small. There were no signs of either additional cladding hydriding, stress corrosion cracking (SCC), or fuel pellet degradation. Additional information is in Section 6.3.1.1.5.

In a second series of tests (Einzigler and Kohli 1984), creep rupture studies on five well-characterized Zircaloy-clad PWR spent fuel rods, which were pressurized to a hoop stress of ~ 145 MPa, were conducted for up to 2101 h at 323°C. The conditions were chosen for limited annealing of in-reactor irradiation hardening. With the stresses in the range of 150 MPa, creep of 0.004 to 0.16 was observed. Additional information about this test is in Section 6.3.1.1.5. No cladding breaches occurred, although significant hydride agglomeration and reorientation took place in one rod that cooled under stress. Einzigler and Kohli state that these high-temperature tests based on creep rupture as the limiting mechanism indicate that storage at temperatures between 400 and 440°C may be feasible for annealed rods.

Schneider and Mitchell (1992, p. 2.7), summarize the foreign dry storage programs. At that time, seven countries had some fuel in dry storage. They conclude that LWR fuel can be stored for up to 100 years at temperatures of 320 to 400°C in an inert atmosphere and, if exposed to air, will last comparable times if the temperature is limited to 135 to 160°C. The Canadians have large quantities of irradiated fuel with Zircaloy cladding exposed to air with favorable results. For 8.3 years, they tested the effects of exposing fuel with defective cladding to moist and dry air with favorable results (no strain or failure propagation).

The importance of the spent fuel dry storage experience (domestic and foreign) is that fuel failure or degradation is not expected during dry storage, and the fuel failure rates observed from reactor operation are appropriate for the cladding degradation analysis. It is also important to note that under repository conditions, most of the cladding creep occurs in the first 50 years, the time when temperatures are higher, closer to dry storage conditions, and dry storage is a good representation of this period.

#### **6.3.1.1.2.9 Fuel Shipment**

During normal shipping of fuel, no failures have been reported in the literature. Sanders et al. (1992), analyzed transportation accidents. The project was funded by DOE to support source-term methodology to replace leak-tightness criteria. Failure probabilities were calculated for regulatory drop (9-m drop) of cask with impact limiters, 0.3-m drop, and normal transport, (i.e., vibration and regulatory fire). The 9-m drop was by far the most severe, with failure probabilities of the order of  $10^{-4}$ , compared to  $10^{-8}$  to  $10^{-12}$  for the other events. This reference generated acceleration versus frequency curves for trucking and rail shipping. It then looks at structural damage from a union of the hazard curves and the structural model and concludes that no additional damage is done in shipping. In "Dynamic Impact Effects on Spent Fuel Assemblies," Witte et al. (1989), performed an analytical evaluation of the potential impacts of

all movements. They conclude (Witte et al. 1989, p. 5) that no yielding of the rods would occur below 63g's. Normal transport would result in stresses much below these values.

Duke shipped 300 fuel assemblies from Oconee to McGuire from 1981 to 1988, (approximately 138 shipments). Although no assemblies were tested at the receiving end to determine cladding condition, any gross assembly degradation would have been observed during unloading and none was reported (Siegmann, E.R. 1998). Carolina Power and Light shipped 141 casks from its Brunswick and Robinson plants with no reported pin failures (Siegmann, E.R. 1998). Thousands of shipments were made to the West Valley and Morris spent fuel facilities with no reported failures (Siegmann, E.R. 1998).

The IF-300 was used to ship lightly burned fuel from Shoreham to Peach Bottom. This fuel was to be reinserted into the Peach Bottom reactors, so it required that there be absolutely no damage to the assemblies. Special tooling was developed to insert spacers between the fuel rods to prevent vibration and possible damage to the spacers. Each assembly was put into a thin stainless shroud before being put into the cask. While these shipments are cited as successful fuel shipments, it is noted that special spacers were used, and would not be present during normal shipping.

IAEA (1988, p. 114) surveyed shipping world wide and reported that "to date, there have been no major incidents during 30 years experience connected with irradiated fuel transport."

The importance of the fuel transportation experience (domestic and foreign) is in demonstrating that fuel failure or degradation is not expected during transportation, and that the fuel failure rates observed from reactor operation are appropriate for the cladding degradation analysis.

### **6.3.1.1.3 Overview of Cladding Degradation Mechanisms at YMP**

Excellent summaries of cladding degradation modes and their models are given by Rothman (1984), Pescatore et al. (1989, 1994) and Cunningham et al. (1987). The cladding degradation modes that were identified were creep rupture, DHC, SCC, general (cladding oxidation) and local corrosion, UO<sub>2</sub> oxidation (cladding unzipping). Mechanical failure has been added to address the time when the WP offers little protection.

Various tests have addressed fuel behavior in repository-type conditions. As mentioned in Section 6.3.1.1.2.8, dry storage tests represent the early stages of repository conditions when the temperature is high. Although the observations only extend over 10s of years, spent fuel pool studies (Section 6.3.1.1.2.7) show that little cladding degradation is expected if the WP fails and fills with water. The presence of perforated or cracked cladding will reduce the release of certain radioisotopes. The Wilson's Series 1 (1985), Series 2 (1987), Series 3 (1990b) tests and tests by others measured releases with damaged cladding (see Section 6.3.1.1.10).

The models for most of the cladding degradation incorporated in this study are based on the processes driven by temperature. Figure 6-10 shows the temperature of the center (hottest pin) in both the average WP and design bases (hottest) WP (CRWMS M&O 1997f). The design bases WP is assumed to contain 21 assemblies, each being the highest (850 W) power permitted to be inserted. The peak temperature of the peak pin in the average WP is below 237°C. The peak

temperature for the design WP is 327°C, below the design limit of 350°C. For the hot pin with a burnup of 40 MWd/kgU, the hoop stress would peak at 58 MPa (average WP) and 68 MPa (design WP).

The WP corrosion analysis is discussed in Section 5. When the WP is perforated, oxygen and water vapor are introduced. This permits cladding oxidation (general corrosion), local corrosion, and UO<sub>2</sub> oxidation. Figure 6-11 gives the fraction of patches penetrated as a function of time. The first WP fails at about 2,500 years and the median (50 percent) WP fails at about 150,000 years. Using these times and reviewing Figure 6-10 shows that the fuel will be quite cool when it is exposed to air and water. A few WPs with defective seals could possibly be placed in the repository. The Canadians give the best estimate probability of 1/5,000 WP (Doubt 1984, p. 30) or 2.0E-4/WP. In the RIP analysis, juvenile WP failure probability is assumed to be log uniformly distributed between 10<sup>-3</sup> to 10<sup>-5</sup>, and the expected value case used 1/7,760, very close to the Canadian value. Juvenile WP failure will be taken into account when considering cladding unzipping.

Creep rupture and DHC are operative until the cladding fails, and the resulting failure is in the form of small cracks or punctures (i.e., the degradation processes stop when the cladding is perforated or cracked, with the release of stresses). Zircaloy dry oxidation and cladding unzipping, which result in a gross cladding rupture, are operative after the WP fails and the inert environment inside the WP is replaced with the near-field environment. The WP protects against the gross failure of cladding and gross exposure of spent fuel inside the cladding. Thus, WP failure must be incorporated into the cladding degradation analysis to estimate the amount of spent fuel exposed to the near-field environment.

#### **6.3.1.1.4 Corrosion**

While Zircaloy is considered extremely corrosion resistant, at very long times, corrosion processes may be important contributors to cladding degradation.

##### **6.3.1.1.4.1 General Corrosion**

General corrosion is synonymous with zirconium oxidation. The outer surface of the cladding becomes coated with a ZrO<sub>2</sub>, which adheres to the surface and slows down further oxidation. The oxidation could be from O<sub>2</sub> consumption (dry oxidation) or H<sub>2</sub>O consumption, wet oxidation. For the fuel in the repository, this does not occur until the WP is penetrated (see Figure 6-11). The effect of surface oxidation is threefold. The oxidation could thin the cladding, permitting cladding failure by creep rupture. Wet oxidation generates hydrogen and some of it is absorbed into the cladding to form hydrides (see Section 6.3.1.1.2.3). This could lead to DHC, or general hydride embrittlement. In the extreme, the oxidation could lead to cladding disintegration and expose the fuel pellets to the environment.

Wet oxidation has been studied for over forty years because of its importance in reactor operation. Rothman (1984, p. 6-13) discusses cladding oxidation in great detail and his Table 6.3.1.3.2-1 compares the predicted cladding loss using six different oxidation correlations and predicts cladding thinning of 4 to 53 microns after 10,000 years at 180°C (a conservative

temperature assumption when considering Figure 6-10). Ahn (1996) also concluded that cladding oxidation under repository conditions would not lead to pin failure.

Recently, Hillner et al. (1998) published a recommended Zircaloy corrosion correlation based on Bettis Atomic Power Laboratory experiments. Bettis developed Zircaloy for Navy reactors in the early 1950s and has an extensive data base on Zircaloy performance. They have continuous autoclave corrosion tests on some samples for 30 years. They have developed oxide thickness as great as 110 microns, greater than those expected during repository corrosion. They show that the corrosion rate is determined by diffusion of oxygen ions through the corrosion film. This corrosion film is generated in layers, with the lower layer staying very consistent. The consistency of the lower 2 microns of oxide film leads to a steady corrosion rate after a transition period. The recommended posttransition rate equation is:

$$\Delta Th = 1.69E+9 * \exp(-111452/T) \quad (6-8)$$

where

$\Delta Th$  = oxide thickness, microns/yr

T = temperature, Kelvin

This correlation rate equation is similar to the equations developed by others, but predicts a slightly higher corrosion rate. It is taken from Equation 7 of Hillner, doubled for a conservative correction for irradiation, and converted to microns per year ( $15 \mu\text{m}/(\text{gm}/\text{dm}^2)$ ) (IAEA 1998, p. 178). The pretransition rate is slower than the posttransition rate. The effect of irradiation conditioning before doing the corrosion is to accelerate the corrosion rate for a few microns. To be conservative, Hillner doubled the corrosion rate for all time. The correlation shows a strong Arrhenius temperature relationship with the corrosion rate becoming very small below  $200^\circ\text{C}$ . This is consistent with the data. Corrosion tests at  $270^\circ\text{C}$  for 8.2 years have produced 5 microns of oxide, while corrosion tests at  $360^\circ\text{C}$  have produced films 62 microns thick (Hillner et al. 1998).

For general corrosion, the WP must be breached. Table 6-15 shows the amount of oxide film from general corrosion as a function of WP failure time. These calculations were carried out from the WP failure time to one million years. Hydrogen pickup was calculated as 17 percent of the hydrogen generated. This is further discussed in Section 6.3.1.1.6.2. The amount of cladding that is consumed is approximately 57 percent of the oxide thickness because of the volume increase with Zircaloy oxidation. This calculation was done for the hot pin in both the average and design WP. In either case, if the WP is not breached for 100 years, little general corrosion is expected. Hillner's Figure 5 compares the corrosion rate in water (the correlation used here) with that of steam. The steam corrosion rate is about 30 percent slower. A steam environment is expected to last for 1,000 to 5,000 years in the near field. Einziger's (1994) equation, (Equation 14) for dry oxidation of zirconium is slightly slower than the wet corrosion rate. The conclusion from this analysis, as shown in Table 6-15, is that general corrosion is not a problem for the average WP but could be a problem for the design WP if the WP fails before 100 years.

Bradley et al. (1981) performed metallurgical examinations of Zircaloy-clad fuel rods from two bundles (0551 and 0074) of Shippingport PWR Core 1 blanket fuel after extended water storage (21 years for 0551, and 16 years for 0074). The metallurgical condition of similar fuel rods was investigated and documented soon after reactor discharge. They found no significant degradation of the Zircaloy cladding even after 21-year water storage times. Prior to reactor exposure, ~0.6  $\mu\text{m}$  of oxide was formed by autoclaving the cladding. The oxide film thickness of the Shippingport fuel rods, during and after reactor operation, was reported to be an average cladding oxide film thickness of 1.8  $\mu\text{m}$  (0551) and 2.4  $\mu\text{m}$  (0074). After extended water storage (Bradley et al. 1981), the average cladding oxide film thickness was found to be 1.7  $\mu\text{m}$  (0551) and 2.3  $\mu\text{m}$  (0074). The slight disagreement in these values is likely due to differences in measurement technique and experimental error. They lead to the conclusion that no significant change in oxide thickness occurred even after 21 years of pool storage. This conclusion is further supported by the observation that Zircaloy tube sheets (that had been cut to remove bundle 0551 fuel rods in 1960) stored in water for over 20 years were unblemished and showed no evidence of any reaction with water.

#### 6.3.1.1.4.2 Localized Corrosion

The Zircaloy cladding on commercial fuel is very thin (W1717WL is 570 microns thick), and there is a large uncertainty about corrosion potential under repository conditions. Corrosion tests are currently being performed for repository type chemicals, but results are not yet available. The probability of pitting, crevice corrosion, or some other form of local corrosion depends on the local water chemistry and needs further study. If the local environment in a crack, pit, or crevice becomes sufficiently reducing, and if a sufficient concentration of oxidizing ions is present and buffer chemicals are not, corrosion will occur. Such corrosion could lead to perforated cladding and permit the release of radionuclides.

Yau and Webster (1987), review the corrosion of zirconium under various chemical environments for commercial applications (corrosion rates and time scales of interest for industrial applications, not for repository time scales). It is resistant to corrosion from HCl, basic solutions (Hansson 1984, reports no corrosion rate increase in cement pore solutions of pHs of 12.0 to 13.8), sea water, brackish water, and polluted water. It is resistant to corrosion from sulfuric acids in concentrations less than 20 percent and corrodes slowly in terms of commercial applications (not repository time scales) in solutions below 65 percent. Zirconium is susceptible to corrosion from fluoride ions ( $> 100$  ppm and pH dependent), hydrofluoric acid, and aqua regia. Yau and Webster report that zirconium is resistant to crevice corrosion. If the zirconium oxide layer is removed, it is susceptible to galvanic corrosion if coupled to a more noble metal (platinum, gold, graphite, titanium, and silver). It has a corrosion rate of 18 microns/yr in 3.5 percent boiling NaCl at a pH of 5 but no observed corrosion at a pH of 6. It is susceptible to pitting from  $\text{FeCl}_3$  ions.  $\text{FeCl}_3$  pitting requires ferric ions, which is the dominant species at pH less than 3. Current analysis of the water chemistry inside the WP predicts pHs greater than 6, not near this threshold but pHs could be lower in a crack or crevice by dissolution of metals into ions (see Section 5.8 for discussion).

Rothman (1984) qualitatively reviews the chemical components of J13 water and the ability of these chemicals to attack zirconium. He concludes that Zircaloy corrosion from these chemicals

is unlikely. Hillner et al. (1998) also qualitatively compare Zircaloy corrosion potential with J13 components and concluded that corrosion is unlikely.

Published results (Yau 1984, p. 140/1 – 140/8) show general, crevice and SCC tests with zirconium in concentrated acids to simulate concentrated geothermal salts. In terms of chemical composition, these tests are probably more severe than expected at YMP, although the time periods are very short. They also looked at crevices and SCC with mixed salts. The solution contained 25% NaCl + 0.5% CH<sub>3</sub>COOH + 0.1% S + saturated H<sub>2</sub>S, with or without saturated CO<sub>2</sub>. Both welded and non-welded samples were exposed in U-bend SCC tests, general and crevice corrosion tests. Tests were conducted both at room temperature and at high temperature/pressure autoclave conditions. The pH was between 2.3 and 3 (measured at room temperature), and the test duration was for 30 or 60 days. The U-bend samples showed no cracking after 60 days. Steel coupled U-bend samples showed no hydrogen pickup, although the steel nuts and bolts were corroded badly. These test solutions became contaminated with iron, but resulted in no degradation of zirconium's corrosion resistance. Crevice tests showed no crevice corrosion. Autoclave tests of general corrosion showed negligible corrosion, with some weight gain of the samples (rate not given in paper). The author also notes that fluoride pitting is not expected in geothermal fluids, because the presence of silica tends to trap the fluoride and form non-corrosive complex ions.

Van Konynenburg et al. (1998) performed some material scoping tests using Zircodyne 702 in 0.01M each of sodium formate (NaCOOH), nitric acid (HNO<sub>3</sub>), NaCl, H<sub>2</sub>O<sub>2</sub>, 0.02M sodium oxalate (Na<sub>2</sub>C<sub>2</sub>O<sub>4</sub>), with a pH of 4 and temperature of 90°C, and test duration of 96 hrs. The test solution was designed to represent highly concentrated forms of acids formed by radiolysis. Possible buffering minerals were not present in the test. They report a corrosion rate of 50 µm/yr for zirconium in their acid solution.

The data presented in the papers by Cragolino and Galvele (1977); and Maguire (1984) show that Zircaloy could pit in KCl and NaCl solution (1M or higher and at room temperature). Cragolino and Galvele experiments studied zirconium and Zircaloy-4 but Maguire only studied zirconium. Data on zirconium may not be directly applicable to Zircaloys. This potential is for the systems exposed to air (without any additional oxidants). Maguire reports that the critical pitting potential values are affected marginally by temperature and pH. He also argues that presence of oxidizing impurities such as Fe<sup>3+</sup> and Cu<sup>2+</sup> would make Zircaloy more susceptible to localized corrosion. A pH of 3 is required for the preferential formation of the Fe<sup>3+</sup> ions (Krauskopf and Bird 1995, Figure 9-2).

Zircaloy is susceptible to pitting with F<sup>-</sup> ions. Uziembo and Smith (1989) measured corrosion rates at various pH and F<sup>-</sup> ion concentrations. At 100 ppm F<sup>-</sup> ions, they found that Zircaloy corroded a negligible amount at pH > 8, 32 µm/yr at pH = 6 and 1 mm/yr at pH = 5. Yau (1984, p. 140/3), states the presence of silica will prevent fluoride pitting.

This experiment shows the importance of pH on the corrosion rate. It also shows the importance of estimating the composition of the water and the degree of concentration for the water that contacts the fuel, since the fluorine content of J13 is about 2.4 ppm. Experiments with 500 ppm Cu<sup>2+</sup> in 3.5 percent boiling NaCl also show a strong pH dependency with a corrosion of 18 µm/yr at pH of 5 and nil at a pH of 6 (Yau and Webster 1987). Chapter 4 of this report discusses

the near field chemistry. The duration of highly alkaline conditions depends on the assumed presence of concrete. If the concrete (liner material) is assumed to not be present, the duration of highly alkaline conditions is less than 5,000 years, with the long-term pH at about 8. With concrete material from the liner present, the expectation is that the pH will be quite basic for the first 10,000. The pH could be significantly lower in a crack or crevice.

Corrosion of Zircaloy was modeled with WAPDEG, which is a stochastic corrosion simulation code described in the TSPA-VA Section 5, Volume 3 (DOE 1998). This model is meant to represent corrosion under the action of some local exposure environment possibly developing in a crack or crevice. The model uses the general corrosion model developed for the Alloy C-22 inner barrier of the WP (see Chapter 5) to simulate the corrosion (general and local) of Zircaloy cladding.

The Alloy C-22 general corrosion rate was scaled by the ratio of the corrosion rate of Zircaloy 702 to Alloy C-276. Zircaloy 702 is similar to the Zircaloys used for fuel cladding (Zircaloy-2 and Zircaloy-4) although it may contain up to a maximum of 4.5 weight percent hafnium and no tin, while fuel cladding contains almost no hafnium and about 1.5 weight percent tin (see Table 6-7). Alloy C-276 is a corrosion resistant material similar to Alloy C-22. It was necessary to use Zircaloy 702 and Alloy C-276 corrosion data as few data sets exist in which Alloy C-22 and Zircaloy-2 or -4 alloys are subjected to identical exposure conditions. Although Zircaloy 702/Alloy C-276 corrosion rate comparisons at modest, repository-type conditions are not available due to the extremely high corrosion resistance of zirconium alloys, experimental results are available for the corrosion of Zircaloy 702 and Alloy C-276, under identical exposure conditions, in hot, concentrated acid solutions. These experimental observations are summarized in Table 6-16 (Yau and Webster 1987). Corrosion rates for Zircaloy 702 tend to be from one to four orders of magnitude (10 to 80,000 times) lower than those of Alloy C-276 under identical acidic exposure conditions.

In the WAPDEG model, the general corrosion rate for a "patch" (see Chapter 5) of Alloy C-22 is determined from three general corrosion rate cumulative distribution functions (CDFs) applicable at different temperatures (25, 50, or 100°C). In modeling Zircaloy cladding, two bounding WAPDEG simulations were performed; one in which the Alloy C-22 general corrosion rate is divided by 10 (upper bound on Zircaloy cladding local corrosion rate) and another in which the Alloy C-22 general corrosion rate is divided by 1,000 (lower bound on Zircaloy cladding local corrosion rate). Figure 6-12 shows the corrosion rate for the Alloy C-22 general corrosion model, the cladding degradation model used here (C-22/Zirc Model) and the Bettis Zircaloy model (Hillner et al. 1998, Equation 7) discussed in Section 6.3.1.1.4.1. The thickness of the Zircaloy cladding was chosen to be 0.0571 cm and the patch area was chosen to be 10 cm<sup>2</sup> or about 110 patches/fuel rod. The results of the cladding WAPDEG simulations are two curves representing the lower and upper bounds of the fraction of cladding patches failed versus time (Figure 6-13, with a "mean" curve also shown for illustration).

For each realization, the RIP code log uniformly samples a Zircaloy cladding degradation history between the upper and lower bounding curves to determine the fuel area exposed (fraction of patches failed) as a function of time for that realization. It is assumed that corrosion degradation of Zircaloy cladding does not begin until the WP is breached (typically 10,000 years or more after emplacement, see Chapter 5). Thus, for each RIP realization, a time history of cladding

degradation is established and applied to the fuel pins in each WP following the initial breach of each package. After one million years from the time of WP breach, the range of fuel area exposed is from 0.3 percent (lower limit) to 40 percent (upper limit).

#### 6.3.1.1.5 Creep Rupture

Creep failure was postulated as the dominant failure mode for fuel in dry storage but has not been observed. DOE sponsored the development of a cladding creep rupture model by Chin and Gilbert (1989). This model was developed for studying temperature limits of cladding for interim storage of spent fuel, and is based on different theoretical failure mechanisms. The dominant failure mechanism is void formation and decohesion at grain boundaries. In earlier cladding failure analyses for the YMP, Santanam et al. (1992) and McCoy (CRWMS M&O 1998b) used the Chin model.

Another cladding creep model was developed by Peehs and coworkers in Germany (Peehs and Fleisch 1986). The German model is an empirical fit for a single set of experiments of strain and assumes that the clad creeps as a function of stress, temperature, and time. The Peehs model was used in Germany for licensing spent fuel storage facilities (Peehs and Fleisch 1986). In the Peehs model, a conservative value for a strain at which cladding failure occurs, 1 percent strain was selected. Tensile strain measurements were also made by Matsuo (1987) and Mayuzumi and Onchi (1990). The tests by Peehs, Matsuo and Mayuzumi were all done with gas pressurization.

Pescatore and Cowgill (1994) compared the Chin and Gilbert (1989) and Peehs models and recommended use of the Peehs model because of a lack of experimental confirmation of Chin's work (void formation at crystal boundaries in strain tests has not been observed). Thus, the Peehs technique is used in this analysis but the creep correlation was changed. Peehs and Fleisch (1986) describe the application of the model but the actual data and description of the creep tests are not published. The model was also criticized as having cladding too strong at higher temperatures. Both Matsuo's and Mayuzumi's creep experiments and derivation of their correlations are better documented. When the three correlations were compared to published data by Einziger and Kohli (1984), each of the others (see Table 6-17), Matsuo's correlation had a variance that was half of Mayuzumi's. Therefore Matsuo's correlation was used. All three grossly over-predicted the strain observed in the Einziger et al. 1982 experiments, which were as high as 571°C. Since the repository cladding temperatures are to be below 350°C, modeling the higher temperatures is not of interest. All three correlations do well in describing the creep experiments at or below 363°C.

Table 6-18 shows the strong temperature dependency of the Matsuo creep correlation. The dominant effect is that material strength is higher at lower temperatures. Figure 6-14 shows the amount of creep that is expected if a pin was held at a constant temperature for 10 years (note log scales for strain). Both Peehs' and Matsuo's correlations show a strong temperature dependency. Peehs' correlation has a higher strain rate at low temperatures but a lower rate at higher temperatures, the region where failure is more probable. When the hot pin in the average WP is exposed to the temperature profile shown in Figure 6-10, the amount of strain expected is 0.001 percent over the entire cooling period of the repository (one million years) using Matsuo's correlation. This strain would not be expected to fail the cladding. For the hot pin in the design

(hot) WP, the amount of strain expected is 0.4 percent using Matsuo's correlation. Again, this strain would not be expected to fail the cladding. This is consistent with dry storage experiments. In the INEEL tests (McKinnon and Doherty 1997), 26,000 pins have been monitored in dry storage canisters without any pin failures. In conclusion, creep failure is not expected to contribute to cladding degradation at the repository and not included in the RIP abstraction. The reason for this is that the temperatures of the cladding in the WP designs are too low to have significant creep. This is true for any of the three creep correlations studied.

**Creep Rupture Failure Limit**—The above analysis of the hot pin in either the average or design (hot) WP predicted small strains. If higher strains were predicted, a strain limit would be needed to predict failure. In the Peehs model (Peehs and Fleisch 1986), a conservative value for a strain at which cladding failure occurs, 1 percent strain, was selected. Sanders et al. (1992, p. III-53) recommends a median value of 6 percent for rupture strain. The mechanical failure analysis, Section 6.3.1.1.7 also used a strain limit of 6 percent. Table 6-19 shows 54 tensile tests or high temperature pin creep tests. The average uniform elongation strain for these tests is 4 percent. A failure criteria of 4 percent is recommended for predicting creep failure but as noted in the previous section, strain failures is not expected for the hot pins in either the design basis of average WP.

**Helium Production**—Both DHC and strain failures are driven by the cladding stress which may be caused by the internal gas (including fission product gases) pressure buildup. The gas pressure will slowly increase over time by the production of helium (He) which is produced in nuclear decay as an alpha particle. Manaktala (1993, Figure 3-4), presents the helium pressure change as a function of time for a pin with 36 MWd/kgU. That pressure change profile (after adjusted for temperature) was used in this analysis. The pressure change curve (in log-log space) was approximated by two linear equations (given at bottom of Table 6-20), one for below 10,000 years and one for above that time. The helium partial pressure is added to the fission gas pressure at each time step and a new stress is calculated (see Table 6-20). Incorporation of the helium gas produced does not affect the cladding failure rates because the clad is sufficiently cool by the time any significant amount of helium is produced. For the hot pin in the design (hot) WP, inclusion of helium pressure changed the predicted creep from 0.440 percent to 0.447 percent, an increase of 1.7 percent. Rothman (1984, p. 21) also considered helium production in a Calvert Cliff PWR pin with a burnup of 36 MWd/kgU. His helium source term would produce a helium partial pressure of 6 MPa at 10,000 years, very close to the 5 MPa using Manaktala 1993.

#### 6.3.1.1.6 Hydride Failures

As discussed in Section 6.3.1.1.2.3, the cladding contains hydrides after reactor operation. It might also pick up more hydrogen from cladding general corrosion (wet oxidation) after the WP is breached. Hydrides might also form from UO<sub>2</sub> oxidation (with WP and cladding perforation). In addition, hydrides may dissolve in warmer areas of the cladding and migrate to cooler areas. Hydrogen can also move from places of low stress to places of high stresses, causing hydride reorientation or DHC. The buildup of hydrides can cause existing cracks to propagate DHC, or hydride embrittlement.

### 6.3.1.1.6.1 Hydride Embrittlement

Hydrogen embrittlement is a generally reduced resistance to fracture. In Zircaloy, hydrogen embrittlement is normally caused by formation of microscopic flakes of zirconium hydride. Since the hydride flakes are quite brittle, a crack can propagate more readily by preferentially following the hydrides. Resistance to fracture (fracture toughness) ( $K_{IC}$ ) is a measure of how much energy is absorbed in crack propagation through the material. Fracture toughness is typically measured in terms of the critical stress intensity factor, that is, the value of the stress intensity factor that will cause growth of a crack. The stress intensity factor is proportional to the far-field stress times the square root of the crack length. Kreyns et al. (1996) show (reproduced as Figure 6-15) that such hydrides could decrease the fracture toughness ( $K_{IC}$ ) from 42 MPa-m<sup>0.5</sup> to 8 MPa-m<sup>0.5</sup> as the hydrogen content increases from zero to 4,000 ppm. In the limit, 100 percent hydride and no metal at all, the fracture toughness is about 1 MPa-m<sup>0.5</sup>. As presented in Table 6-10, the outer surface of the cladding could be fairly brittle (hydrogen content greater than 800 ppm) but much of it has a reasonable strength. Kreyns et al. (1996) showed that the fracture toughness might approach 8 MPa-m<sup>0.5</sup>. To better understand what this degradation means, the  $K_{IC}$  of some other materials are presented. The  $K_{IC}$  for 100 percent pearlitic ductile iron is about 30 MPa-m<sup>0.5</sup> (ASM 1996, p. 675).  $K_{IC}$  is 10 MPa-m<sup>0.5</sup> for overaged (a heat treatment technique) 2xxx (2000 series) aluminum alloys with a yield strength of 450 MPa (ASM 1996, p. 387). Tungsten carbide cermet with 0.1 volume fraction of cobalt has a  $K_{IC}$  of about 9 to 15 MPa-m<sup>0.5</sup> (ASM 1996, p. 390). These materials, also called cemented carbides, are the familiar carbide tips used on cutting tools. Common glasses have a  $K_{IC}$  of about 1. All of the fracture toughness values listed here are fairly low.  $K_{IC} = 80$  MPa-m<sup>0.5</sup> would not be unusual for a steel.

Additional hydrides could be formed from cladding surface general corrosion, which was addressed in Section 6.3.1.1.4.1 and summarized in Table 6-15. The WP was assumed to have failed at various times, permitting water or steam to enter it. Wet oxidation (used for steam if the local temperature is above boiling) occurs, and 17 percent (Lanning et al. 1997, Figure 8.2) of the hydrogen released from the water is absorbed by the cladding. Columns 3 and 5 of Table 6-15 give the hydrogen content increase for the hot pins as a function of WP penetration time. The average WP picks up very little hydrogen. The hot pin in the design (hot) WP again will pick up only small quantities from surface corrosion if the WP remains sealed for the first 100 years. Embrittlement from surface oxidation does not appear to be a problem.

Hydrogen will be generated in the WP as the WP internals corrode. This hydrogen is not directly absorbed, because the H<sub>2</sub> molecules do not migrate through the high-density oxide layer on the metal surface. Yau (1984, p. 140/5) showed that in 60 day corrosion tests with steel and zirconium closely coupled, hydrogen pickup did not occur although the steel nuts and bolts were corroded badly. Hydrogen is introduced into the coolant in PWRs to reduce oxygen ions and reduce corrosion of components and yet it is not absorbed into the cladding.

Hydrides can be formed in the cladding from UO<sub>2</sub> oxidation (Wasywich et al. 1986). The fact that the fuel is reacting means that the cladding has already been perforated. If the embrittlement becomes severe and the cladding is mechanically loaded in excess of its fracture toughness, the cladding could fail, exposing additional fuel to the environment. This type of failure has a small effect on the fuel reaction rate since all of the fuel reacts after the first penetration (Wasywich

et al. 1986). It does affect the amounts and rate of fission product migrating out of the secondary phases of the fuel dissolution. This type of secondary cladding failure has not been modeled.

Hydrides can form in cooler parts of the pin (end sections) because the hydrogen can dissolve into the metal matrix at a warmer area, diffuse toward the cooler area, and condense there. The effect was studied for dry storage (Cunningham et al. 1987, Appendix C) and for a 90-year period was determined not to be a problem. As the repository cools, the driving force for this redistribution (hydrogen solubility, temperature gradient, and diffusion rate) all decrease. The WP internals will act to minimize the temperature distribution across the length of the fuel assembly. McMinn et al. (1998, Figure 14), shows that a minimum of 42°C temperature difference between the hot location and cold location in the cladding is needed to move the hydrogen. At temperatures below 200°C, temperature differences over 75°C are needed to move the hydrogen. These phenomena will need further study but it is unlikely that sufficient hydrogen can be moved because of a lack of large temperature gradients in the WPs.

The loss of fracture toughness depends on how much hydrogen is absorbed during storage. Normal pick-up during reactor operation for 40 MWd/kgU is 400 ppm hydrogen. Stress intensities (to be discussed in the next section) for the median and maximum crack (Section 6.3.1.1.2.4) are 0.14 and 0.72 MPa-m<sup>0.5</sup> respectively (40 MWd/kgU, 50°C) when considering hoop stress from fission gas. Assuming no more than 3,600 ppm is absorbed, this is well below the fracture toughness values predicted by Kreyns et al. (1996) and shown in Figure 6-15, and therefore failure is not expected from internal stress. Cladding failure is still possible from local or temporary loads if they are sufficiently high.

In conclusion, failure of the cladding by hydrogen embrittlement is unlikely and has not been included in the abstraction for the RIP analysis. Hydrogen absorption from surface oxidation and WP corrosion will be negligible. Hydrogen migration should be limited because of the temperature differences required to move the hydrogen. Some embrittlement is possible from UO<sub>2</sub> reactions after the initial cladding has failed.

#### **6.3.1.1.6.2 Delayed Hydride Cracking**

During Delayed Hydride Cracking (DHC), hydrides slowly form at a crack until the crack propagates through the hydride region at the crack tip and stops. This sequence repeats itself and the crack propagates slowly through the metal. DHC failure occurred in some zirconium coolant tubes in a Candu reactor where high temperature gradients caused excess hydride buildup in a specific location. The hydrides preferentially collect at the crack tip because a tensile stress reduced solubility in that region. The critical stress intensity factor ( $K_{IH}$ ) is the minimum stress intensity that will permit any DHC, regardless of velocity (velocity approaches 0). For this analysis, the stress intensities will be calculated and compared to the  $K_{IH}$ . If  $K_I > K_{IH}$ , then the crack will start to propagate and, it is assumed, because of long repository times, failure will occur.

The stress intensity factor,  $K_I$ , is a measure of the increased stress at the tip of a crack. The stress intensity factor is proportional to the far-field stress times the square root of the crack length. For a sharp crack, a limiting case, the stress intensity factor is (Reed-Hill 1973, p. 800):

$$K_I = St * (w * \pi / 2)^{0.5} \quad (6-9)$$

where

$K_I$  = stress intensity factor, MPa-m<sup>0.5</sup>

$St$  = stress, MPa

$w$  = crack size, m

The calculated crack size distribution is discussed in Section 6.3.1.1.2.4 and given in Table 6-13. The median (P = 50 percent) value is 12 μm and the largest size crack (P = 1.51E-4), for non-failed fuel is 160 μm, 28 percent of cladding thickness. Table 6-21 gives the calculated stress intensity factors for both the median and maximum crack size for various burnup values at the maximum design cladding temperature of 350°C. These stress intensities will decrease as the repository cools. The stress intensity factor will be compared to the critical intensity factor. DHC is unlikely at temperatures above 250°C (Mahmood et al. 1998), because of the plasticity of the material.

The threshold stress intensity factor ( $K_{IH}$ ) is the minimum stress intensity where crack propagation is expected. The work of Shi and Puls (1994), predict  $K_{IH}$  in the range of 5 to 7 MPa-m<sup>0.5</sup> for Zr-2.5 percent Nb. Rothman (1984), reports a range for  $K_{IH}$  of 6-10 MPa-m<sup>0.5</sup> for Zircaloy-2. Pescatore et al. (1989) report values of 10 and 14. Huang (1995) gives thirteen measured values for  $K_{IH}$  for Zircaloy-2 and the mean value is 6.7 MPa-m<sup>0.5</sup> (temperature range of 204°C to 260°C). For this work, Huang's mean value of 6.7 MPa-m<sup>0.5</sup> was used. A review of Shi's equation shows that without consideration of hydride reprecipitation,  $K_{IH}$  has a weak temperature dependence (8 percent over the 300°C on interest) and was neglected. Both Shi and Puls (1994) and Sagat et al. (1994) report weak temperature dependency for  $K_{IH}$ .

In the limiting temperatures considered here, the fuel pin is assumed to cool from a maximum cladding temperature of 350°C to 50°C. Table 6-11 shows that this cooling would permit a precipitation of 120 ppm (by weight) of hydrogen. The hydride would tend to preferentially collect at the crack tip because it prefers to precipitate in high tensile stress fields. This would increase the  $K_{IH}$  as the platelets got thicker (see Figure 6-16). Table 6-22 gives the stress intensity factors for both the median and maximum crack. For all cases,  $K_I$  is less than the threshold intensity factor for crack propagation (6.7 MPa-m<sup>0.5</sup>) and crack propagation is not expected. For the median (50 percent) cracks, crack propagation is not expected at any temperature, even if pure hydride ( $K_{IH} \approx 1$  MPa-m<sup>0.5</sup>). The maximum size cracks have  $K_I$ s close to that of pure hydride and would only propagate across a pure hydride platelet. Having pure platelets across the cladding is unlikely, and only a very small fraction would fail by this mechanism. Rothman (1984) also predicted that DHC would not occur in repository conditions. The INEEL dry storage tests (McEachern and Taylor 1997) of 26,000 pins have not seen any pin failures, including those by DHC.

Rothman (1984) reviewed DHC in Zircaloy cladding in a repository. He reports that the threshold stress intensity factor is 50 percent to 100 percent higher than that of Zr-2.5 percent Nb, which is reported as  $6 \text{ MPa}\cdot\text{m}^{0.5}$ . This is consistent with the values reported by Pescatore et al. (1989) but higher than those reported by Huang. Rothman reports that DHC above  $250^\circ\text{C}$  is unlikely because of plastic flow and is only weakly dependent on hydride content up to 400 ppm. Rothman concludes that DHC is unlikely unless the fuel pins have large existing cracks (50 percent of wall thickness) and very high stresses (137 MPa). He also concludes that hydride reorientation is also unlikely because of the lack of large temperature gradients in the repository and the cladding stresses are lower than needed for reorientation. Pescatore et al. (1989, Table 9) give both average and maximum hoop stresses for both PWR and BWR fuels. For  $320^\circ\text{C}$ , Pescatore's average values vary from 24 to 62 MPa and his maximum values are up to 134 MPa. He also notes that rods with maximum stresses represent less than 1 percent of the total rods. He shows that BWR stresses are half that in PWRs, partially explaining why PWR fuel is used as the limiting type fuel for repository design.

In conclusion, failure of the cladding by DHC is unlikely and has not been included in the abstraction for the RIP analysis. Stresses (and stress intensity factors) are too low for crack propagation.

#### 6.3.1.1.6.3 Hydride Reorientation

In commercial reactor cladding during irradiation, hydride precipitation forms in plates circumferentially oriented (the normal to the platelet is in the radial direction) and does not significantly weaken the cladding against hoop stress. In one dry storage test, reorientation to the radial direction was observed in one pin (Einziger and Kohli 1984). This occurred in a fuel rod that had very high stresses (145 MPa at  $323^\circ\text{C}$ ). Reorientation was not observed in fuel rods with lower stresses (13 to 26 MPa). The hydride reoriented so that the normals in the circumferential direction could possibly weaken the cladding. Reorientation was also observed in Candu reactor coolant pipes. Hydride reorientation under repository conditions was investigated as a potential cladding degradation mode.

Figure 6-17 summarizes the data that Pescatore et al. (1989) collected showing reorientation. The points from Marshall show different fractions of reorientation. Hardie's point was reported as minimum stress. The straight line suggests a region in temperature and stress where reorientation occurs. By comparing this region in Figure 6-17 to the temperature and stresses of the pins in the repository (Table 6-21), only pins with highest temperatures ( $350^\circ\text{C}$ ) and maximum crack size (28 percent or greater through wall crack, probability =  $1.5\text{E}-4/\text{pin}$ ) and high burnup (above 55 MWd/kgU) might undergo reorientation. If the general strain and not the local strain associated with a crack was considered, no reorientation would be expected. This implies that only a very small number of pins are expected to undergo reorientation. Rothman (1984) also studied cladding degradation in a repository and concluded that hydride reorientation would not occur.

Pescatore et al. (1989, 1994) states that even with hydride reorientation, stress levels will be insufficient to get DHC and clad failure. For general DHC, he also said that crack propagation would tend to stop when the crack propagates into a hydride platelet. Puls (1988) performed a series of strain tests on Zircaloy-2 with reoriented hydrides. His results are summarized in

Table 6-23. He took samples of Candu coolant tubing and performed strain tests in the circumferential direction. The initial tubing is made in a similar fashion as cladding and develops hydride platelet with their normals in the radial direction. All tests were performed at room temperature. He used samples with both 20 ppm and 90 ppm hydrogen content and used two reorientation techniques to form hydrides of various lengths. One technique cooled the samples from 250°C with the stress near the yield point (designated  $y$  in Table 6-23). Other samples were cooled from 350°C at a stress of 200 MPa. This stress is more than twice that expected for most cladding in the repository (see Table 6-21). Longer hydrides were produced by cooling the samples in a furnace, while shorter ones were produced by bench cooling the samples. Table 6-23 gives the range of hydride lengths. Two types of samples were used, smooth ones and notched ones (designated by  $n$  in the table). The table gives the stress ( $\sigma_y$ ) for which 0.2 percent strain was measured. Also given is the ultimate stress at which necking and imminent failure was observed (or, for the arrested tests, was expected). For some experiments, the tests were stopped when the sample started to neck, but before failure (designated  $a$  for arrested in table). In all of these tests, the reoriented hydrides did not significantly change the stress for 0.2 percent strain or the ultimate stress. Both stresses are much higher than those expected in repository cladding (see Table 6-21). The yield and ultimate strains reported are also higher than the strains failure criteria of 1 percent used in the cladding strain failure analysis developed by Peehs and Fleisch (1986).

In conclusion, failure of the cladding by hydride reorientation is unlikely and has not been included in the abstraction for the RIP analysis. Stresses and temperatures are too low for reorientation to occur and the material will maintain sufficient strength even if reorientation did occur so that failure would not be expected.

#### 6.3.1.1.7 Mechanical Failure

If cladding does not fail by other mechanisms, at very long times mechanical disruption may be the limiting factor for cladding credit.

##### 6.3.1.1.7.1 Introduction

A preliminary model has been developed for the fraction of fuel rods broken and fuel exposed because of mechanical failure of cladding (CRWMS M&O 1998b). The model was implemented in a set of qualified software routines using a mixture of qualified and nonqualified data as indicated in McCoy (CRWMS M&O 1998b). The repository drifts are assumed to collapse at some time a few hundred years after emplacement, so rubble blocks will be piled on the intact containers. At some later time, the containers will degrade to the point that they lose their mechanical integrity. The blocks will then crush the containers and contact the fuel assemblies. The sizes of the rubble blocks are derived from information on rock joint spacing and angles, and the height from which the blocks fall is determined from the design of the WP.

The number of fuel rods that break from the impact of a rubble block is limited by the available energy: breakage stops when the energy of the falling block is consumed. The energy necessary to break a single fuel rod is calculated by using beam theory and an elastic-plastic stress-strain relation. An approximate method is developed for treating the effects of load sharing when one fuel rod contacts another.

Predicting the loading on the fuel rods is difficult because rubble blocks will have irregular bottom faces. As an approximation, the blocks are modeled as having protrusions or "punches" on their bottom faces. Two types of punches are considered; one simulates the vertex of a block, the other simulates an edge. All of the energy of the falling block is concentrated on the rods under the punches. To estimate the exposure of fuel, the length of each broken rod that lies under the punch is assumed to have its cladding entirely removed.

Previous TSPAs have treated cladding by simply assuming a certain level of cladding performance. This model is the first attempt to quantify the effect of mechanical loading on cladding performance.

#### **6.3.1.1.7.2 Details of Cladding Mechanical Failure Process Model**

At long times, the WP containment barriers may degrade to the point that they can no longer mechanically protect the spent fuel inside them. The following sequence of events is considered. The ground support for the emplacement drifts is designed to last only until the repository is closed, so the emplacement drifts will collapse and be filled with rubble blocks. Some of these will lie on the waste containers. When the containers become sufficiently weak, the blocks will crush the container and impact the fuel assemblies inside. The blocks will accumulate kinetic energy as they fall, then dissipate the energy in bending and breaking the fuel rods. Breakage stops when all of the kinetic energy is dissipated.

The fuel cladding and spacer grids of nuclear fuel are typically made of zirconium alloy, so they are extremely resistant to corrosion. Inconel™ 718 (UNS N07718) was common in early PWR spacer grids, and Inconel™ 718 is also extremely corrosion resistant. Because of this corrosion resistance, the fuel assemblies should maintain their geometry even when the disposal containers are breached. The assembly geometry is assumed to be preserved but they are displaced downward so that the rocks are able to fall the distance of 2 times the "D" dimension of the design (distance from top of top assembly to top of WP). Separate misalignment analysis showed that the assemblies could support the weight of the assemblies above them. However, when the disposal containers lose their mechanical integrity, blocks of rock can fall on the assemblies and break them. Since the fuel rods are long and slender, they will act as simple beams with supports at the spacer grids. A span of cladding from one spacer grid to the next is taken to be a simple elastic-plastic beam with clamped ends. The spacer grids will in fact allow some rotation at the ends of the span, but the use of clamped ends simplifies the treatment and conservatively reduces the amount of energy the beam can absorb. The cladding is treated as a thin-walled tube with a radius equal to the arithmetic mean of the inner and outer radii. Although the uranium dioxide fuel will have negligible flexural strength by itself, it will nevertheless contribute to the stiffness of the fuel rod. Since irradiated fuel will be in the form of discrete pellets or fragments, the fuel will resist compression but can be readily extended. As a result, the neutral axis will move toward the compressive surface of the fuel rod. In this treatment, the neutral axis is taken to lie at the surface of the fuel rod. The neutral axis will be on the bottom of the fuel rod near the supports and on the top near the load. This treatment is conservative in that it gives the smallest energy absorption.

Cladding behavior during failure will depend on the stress-strain properties of the cladding. Two types of fuel, with different mechanical properties, were considered. The properties were chosen

to simulate typical and high-burnup fuel assemblies. Fuel rods will mechanically fail only long after emplacement, when temperatures in the repository will be low. Accordingly, room-temperature mechanical properties were used. For typical fuel, the yield strength of the cladding is 780 MPa, the ultimate tensile strength is 925 MPa, and the uniform tensile elongation is 3.5 percent (Lowry et al. 1981). For high-burnup fuel, the uniform tensile elongation is 0.15 percent (Garde 1986). The elongations listed above are taken to include the plastic portion only. For both types of fuel, the elastic modulus of the cladding is 99 GPa. The correlations in Section 6.3.1.1.5 are for a different range of temperature and strain rates than the data given here, so they may give different values. For the calculations, the tensile portion of the stress-strain curve is taken to be composed of two line segments; these connect the origin, the tensile yield stress and strain, and the ultimate tensile stress and uniform tensile elongation (elastic plus plastic), respectively. The stress-strain curve is determined by properties for typical fuel. To simplify the treatment, the curve for high-burnup fuel is conservatively taken to coincide with that for typical fuel, but it is truncated at a smaller strain.

As discussed below, the external load from a rubble block is taken to be a point load at midspan. The loading, the geometry of the cladding, and the stress-strain curve of the cladding have been used with standard elastic-plastic beam theory to calculate the midspan displacement as a function of applied force. This model, however, requires substantial amounts of computation. For efficiency, it is replaced by the following empirical force-displacement (CRWMS M&O 1998b). See Figure 6-18 for a comparison of this empirical equation and the exact treatment:

$$D(F) = F \frac{D_y}{F_y} \quad \text{if } 0 \leq F < F_y \quad (6-10)$$

$$D(F) = F \frac{D_y}{F_y} + \left( D_{ut} - F_{ut} \frac{D_y}{F_y} \right) \left( \frac{F - F_y}{F_{ut} - F_y} \right)^{3.468} \quad \text{if } F_y \leq F < F_{ut} \quad (6-11)$$

In Equations (6-6) and (6-7),  $F$  and  $D$  are the current force and displacement, respectively.  $F_y$  and  $D_y$  are the force and displacement at the onset of yielding, that is, when the maximum fiber stress reaches the yield stress, and  $F_{ut}$  and  $D_{ut}$  are the force and displacement when the maximum fiber strain reaches the uniform elongation for typical fuel. Positive forces and displacements are downward. For a given assembly design,  $F_y$ ,  $D_y$ ,  $F_{ut}$ , and  $D_{ut}$  are constants. They are calculated with the equations

$$F_y = 2.941 \cdot 10^{10} \frac{tR^2}{l} \quad (6-12)$$

$$D_y = 1.636 \cdot 10^{-4} \frac{l^2}{R} \quad (6-13)$$

$$F_{ut} = 4.374 \cdot 10^{10} \frac{tR^2}{l} \quad (6-14)$$

$$D_{ut} = 4.016 \cdot 10^{-4} \frac{l^2}{R} \quad (6-15)$$

where

$t$  = thickness of cladding wall

$R$  = mean cladding radius

$L$  = distance between support

For high-burnup fuel, Equations (6-6) and (6-7) still apply, but the force-displacement curve is truncated at smaller forces and displacements; the force and displacement at failure,  $F_{uh}$  and  $D_{uh}$ , respectively, are

$$F_{uh} = 3.262 \cdot 10^{10} \frac{tR^2}{l} \quad (6-16)$$

$$D_{uh} = 1.829 \cdot 10^{-4} \frac{l^2}{R} \quad (6-17)$$

Equations (6-6) and (6-7) agree with the beam-theory calculation to within 0.22 percent of  $D_{ut}$  for all applicable values of  $F$ .

Data on fuel assembly design were obtained from qualified references. Data of interest include rod diameter, rod pitch, number of rods per side, cladding thickness, rod length, and maximum distance between spacer grids (CRWMS M&O 1998b). Numbers of assemblies discharged were also obtained (DOE 1996). Only pressurized water reactor fuel assemblies were considered, since the fuel cladding of boiling water reactor assemblies will normally be protected by the flow channels. Complete data were available for 20 fuel types. These account for 3,1931 of the 44,598 pressurized water reactor fuel assemblies discharged through 1994 and were taken to be representative of all pressurized water reactor fuel assemblies. No attempt was made to estimate the performance of the remaining assemblies.

Figure 6-19 is a sketch of the simplified conceptual model of the mechanical damage process. The topics of the properties of an assembly of rods, the falling block and its range of properties, its leading surface, absorption of energy and breakage of rods, and exposure of fuel surface are discussed next.

A fuel assembly is not an individual rod but an array of rods. Since the details of loading for individual rods are not known, forces from an impacting block are calculated in a one-dimensional continuum approximation (CRWMS M&O 1998b). In this approximation, the array of rods is replaced by a continuum that has the force-displacement behavior that would result if the rods were smeared over space, and the continuum responds to the impact by being displaced only in the direction of block motion. As a falling block of rock penetrates an assembly, the fuel rods will be compacted from their original density to a substantially higher density. The compacted region will accumulate ahead of the block. At the same time, the deformed but

unbroken fuel rods will exert a retarding force on the block. At first, the force on the block increases as additional rods take up more of the load. At larger penetrations, however, the force becomes constant as rods begin to break and new rods take the place of the broken rods. The one-dimensional continuum model is used to calculate the energy absorbed before rods begin to break and the additional energy per rod to break rods.

In developing the one-dimensional continuum approximation, the block is approximated as a rigid body. Because the rods are light, their mass is neglected. The density of rods in the compacted region is taken to be 90 percent of the density for closely packed rods with a hexagonal pattern. Although not all fuel rod positions are fueled, the number of fuel rod positions is taken to be equal to the square of the number of fuel rods per side.

The standard disposal container for pressurized water reactor fuel will have a capacity of 21 assemblies; these are arranged in three columns of five assemblies and two columns of three assemblies. This arrangement is approximated in the continuum model by a uniform arrangement of assemblies in which each column is 21/5 assemblies tall. Edge effects and end effects are neglected. This is appropriate because blocks that fall near the edge of a WP are expected to strike rubble as well as fuel.

As mentioned before Equation (6-6), two types of fuel were considered: typical and high-burnup. Burnup is significant because cladding tends to become brittle at high burnups. What constitutes high-burnup depends on when the fuel was irradiated because there is a long-term trend toward higher burnups as experience with reactor operations increases. However, the continued demand by utilities for good fuel performance should assure that the strength and ductility of typical fuel assemblies will be maintained even though typical burnups are increasing.

The typical fuel was taken to represent 95 percent of the inventory, and the high-burnup fuel was taken to represent 5 percent of the inventory. The mechanical properties used in this analysis for high-burnup fuel are those for a sample, discharged no later than 1986, with a local burnup of 59.0 MWd/kgU. This is an exceptionally high burnup for fuel that was discharged that early; of the 19,968 PWR fuel assemblies discharged through 1986, only 200 had assembly average burnups greater than 40.0 MWd/kgU (DOE 1996).

The external loading may be described in terms of the types and sizes of blocks that fall onto the assemblies, the exposure of assemblies to falling blocks, and the response of the assemblies upon impact. Each of these is discussed below.

A distribution of block sizes for the repository rock has been developed from information on joint spacings and angles for the geologic member that would contain the repository (CRWMS M&O 1997d). The block size distribution is complex. Block volumes range from 0 to 1.28 m<sup>3</sup>, with a median volume of 0.055 m<sup>3</sup>. The block size distribution has been applied in the following way. Blocks are assumed to fall so that they cover the area of the fuel assemblies exactly once. The shape of the blocks is taken to be a right circular cylinder, and the height and diameter are taken to be equal. The axes of the blocks are taken to be vertical, and the blocks are assumed to fall freely onto the fuel assemblies (see Figure 6-20).

In the standard disposal container, a component called a basket side cover, shaped as a segment of a circle, fills the space between the fuel assemblies and the curved wall of the container. Since the basket degrades before the containment barriers fail mechanically, the bottom layer of fuel assemblies can settle into the space originally occupied by the bottom basket side covers, and the overlying assemblies can also settle. Accordingly, the drop height was taken to be twice the height of a basket side cover. For the standard disposal container, the basket side cover is a segment of a circle with radius 711.7 mm and chord length 733 mm. From these dimensions, the height of the side cover is calculated to be 101.6 mm, so the drop height is 203.2 mm.

If the bottom surface of a falling block had a flat surface, the energy of the block would be spread over as many rods as are exposed to the impact; this is the diameter of the block divided by the rod pitch. Since the blocks will be irregular, however, this description is not realistic. To provide greater realism, two geometries were considered that are intended to simulate the effects of irregular block surfaces. In both geometries, the bottom surface of the block is taken to have a rigid, massless protrusion called a punch. The entire energy of the falling block is concentrated onto the rods that lie under the punch. The punch is taken to be sufficiently long so that only the punch contacts the fuel; the rods that lie under the remainder of the area of the block are not loaded. For calculating the amount of fuel exposed, the cladding is taken to be completely removed from the portion of a broken fuel rod that lies under the punch.

Two types of punches are considered (see Figure 6-21). The first is a circular punch. The ratio of the diameter of the punch to the diameter of the block is called the focusing parameter. To provide maximum energy transfer, the punch may be considered to be coaxial with the block. The second type is a linear punch. Two parallel chords of equal length and the two arcs that connect them define the outline of a linear punch. A linear punch is defined by two variables: the focusing parameter and the angle. The focusing parameter is the ratio of the distance between the two chords to the block diameter. The angle is simply the angle between a chord and the fuel rods. For both types of punch, a focusing parameter of one corresponds to a flat-bottomed block. Focusing parameters near zero describe a block with either a slender pin (circular punch) or a blade (linear punch) on the bottom. The circular and linear punches are intended to simulate blocks that fall on their vertices or their edges, respectively.

When a block strikes the fuel, the number of rod breaks can vary from zero (if there is not enough energy to begin breaking rods) to the number of rods under the punch. The number of breaks is determined as a weighted average over the number of assemblies of each type and the distribution of block sizes.

The number of breaks is calculated by considering the energy of the falling block. The block will accumulate kinetic energy as it falls freely toward the fuel rods. It will release additional potential energy as it deforms the fuel rods, but at the same time the deformation of the rods will consume energy. If the block has sufficient energy, it will break fuel rods. After the first layer of rods is broken, the energy consumed for each additional layer is constant. Again, there will be additional release of potential energy as the block continues to fall. After the number of breaks is determined, the number of broken rods is calculated by a probabilistic approach. These two quantities can differ because a single rod can be broken in several places.

To estimate the exposure of fuel, the length of each broken rod that lies under the punch is assumed to have its cladding entirely removed.

The fraction of fuel rods broken and the fraction of fuel exposed were calculated for both circular and linear punches with several values of the focusing parameter ranging from 1 to 0.01. The results are documented in Tables 6-24 and 6-25 (CRWMS M&O 1998b). The results of most interest are those in columns labeled "95 percent typ. + 5 percent hi-burn," which contain arithmetic weighted means for a repository that contains 95 percent typical fuel and 5 percent high-burnup fuel. All results in the tables account for the distribution of block sizes and the number of assemblies of each type.

Results for blocks with a circular punch are shown in Table 6-24. The number of breaks per rod and the fraction of fuel rods broken increase as the focusing parameter decreases. A smaller punch apparently makes the block more effective in breaking rods. The largest reported values of the number of breaks per rod and the fraction of rods broken are 0.2845 and 0.2341, respectively. Both of these values are reached at a focusing parameter of 0.1. In contrast to these results, the amount of fuel exposed is nearly independent of the focusing parameter over the range 1.0 to 0.4, then decreases at smaller values of the focusing parameter. The maximum fraction of fuel exposed is 0.0114 at a focusing parameter of 0.6.

Another result of interest for calculations with a circular punch is the punch aspect ratio. This is the ratio of the depth of penetration of the punch to the width of the punch. Here, depth of penetration is defined as the number of layers of rods broken times the effective rod pitch. Different combinations of block size and assembly type will yield different punch aspect ratios. The values reported in Table 6-24 are arithmetic means for blocks that break rods. (For blocks that do not break rods, the punch aspect ratio is zero.) Since it is improbable that a block will have a very long, slender protrusion on its bottom surface, large punch aspect ratios indicate an unrealistic focusing of energy onto a few rods. Table 6-24 shows that the punch aspect ratio increases as the focusing parameter decreases. Since the punch aspect ratios are fairly large for a focusing parameter of 0.1, it is expected that the actual number of breaks per rod and fraction of rods broken will be smaller than the values reported above.

For a linear punch, the results depend on the angle between the punch and the rods. The rubble blocks in a drift will be randomly oriented. As a discrete approximation of a random orientation, the fraction of rods broken and the fraction of fuel exposed were calculated for eight orientations ( $0^\circ$ ,  $22.5^\circ$ , ...  $157.5^\circ$ ), and the arithmetic mean was taken. The results for this composite orientation are shown in Table 6-25. As with a circular punch, the number of breaks per rod and the fraction of rods broken both increase as the focusing parameter decreases from 1 to 0.1. The largest reported values are 0.1507 (linear) and 0.1052 (circular). However, the dependence on the focusing parameter is much weaker than with a circular punch. The fraction of fuel exposed has a more complicated dependence on the focusing parameter, with a maximum at 1, a minimum near 0.2, and a second maximum at 0.1. The maximum fraction of fuel exposed is 0.0110 at focusing parameters of 0.9 and 1.0.

The two models provide substantially different results for the fraction of rods broken. With a linear punch, the largest reported value is 0.1052 for a focusing parameter of 0.1; with a circular punch, the largest reported value is 0.2341, again for a focusing parameter of 0.1. The two

models agree more closely at larger focusing parameters. However, it may be that the circular punch simply represents a more severe loading configuration as regards the number of rods broken.

As regards the amount of fuel exposed, the agreement between results for a circular punch and a linear punch is much closer. With a linear punch, the maximum fraction of fuel exposed is 0.0114; with a circular punch, 0.0110 is exposed. These values are reached at fairly large values of the focusing parameter, 0.6 (linear) and 0.9 to 1.0 (circular). These results indicate that only a small fraction of fuel will be exposed by mechanical failure.

Energies for breaking fuel rods of BWR assemblies have not been calculated. For most of these, the fuel rods will be protected from both impacts and static loads by the flow channels. It would be conservative to assume that the number of breaks per rod and the fraction of fuel exposed are the same for PWR and BWR fuel.

#### **6.3.1.1.7.3 Abstraction of Model**

The development of the model is in itself the process of abstraction. An elastic-plastic beam theory is used to calculate the force-displacement behavior of a fuel rod. A curve is fitted to those results to provide an empirical force-displacement equation. That equation in turn is used to develop a one-dimensional continuum model for the energy absorbed in breaking rods. Finally, the fraction of fuel exposed is calculated by accounting for the distribution of block sizes and the number of fuel assemblies of each type. Further abstraction by taking a maximum value is recommended in the next section.

#### **6.3.1.1.7.4 Recommended Model for Mechanical Failure of Cladding**

For the abstraction in the RIP analysis, the maximum and minimum values of fuel exposed are specified and the RIP code samples between these values. For the geometries considered in this analysis, the maximum fraction of fuel exposed by mechanical loading is 11 percent, representing all high burnup fuel being struck by flat-bottomed rocks. This is the maximum value given in Tables 6-24 and 6-25 for fraction of fuel exposed. Until a sufficient number of patches open up to permit rocks to fall on the fuel (about 100,000 years, see Figure 6-11) little fuel would fail by rock drops and therefore 0.18 percent is conservatively used for the initial plateau value.

The model does not predict the time at which mechanical failure of the container (and thus cladding failure) occurs. For the RIP abstraction, the fraction of exposed fuel was increased from 100,000 years to one million years after the first WP penetration as shown in Figure 6-5. The delay of 100,000 years is to represent the time necessary for both the basket and corrosion resistant barrier to deteriorate sufficiently to permit rocks to strike the fuel.

The fuel in the broken rods will have different degrees of exposure. In the current model, the fuel exposed in crushed sections of fuel rods is taken to be fully exposed as fragments, but the fuel in intact sections of broken rods is not exposed at all. A more realistic model would have some degree of exposure for all fuel in the broken rods.

Although treatment of the fuel exposure may not be conservative, other aspects of the model of dynamic loading contain numerous conservatisms:

- The block fall height is essentially an upper limit. There is no accounting for possible deformation of the containment barriers before complete collapse.
- Blocks are assumed to fall freely; there is no accounting for blocks that encounter friction or are partially supported.
- There is no accounting for energy absorbed in deforming the remnants of the containment barriers.
- There is no reduction of block size to account for breakage when the blocks fall onto the intact disposal container or other rubble.
- There is no accounting for energy absorption by crushing of the spacer grids. That process would also increase the flexibility of the rods and thus increase the energy they could absorb before breaking.
- Falling blocks are assumed to cover the entire exposed area of the assemblies.
- Rod breakage is likely to cause only a few guillotine breaks in the cladding, but the amount of fuel exposed is assumed to be that in the entire length of the rod under the block.
- The neutral axis is taken to be at the surface of the rod. This location minimizes energy absorption.
- No credit is taken for the protection of BWR fuel rods by their flow channels. Because of these conservatisms, the reported values of the number of breaks per rod and the fraction of fuel exposed are believed to be conservative.

#### **6.3.1.1.8 Stress Corrosion Cracking**

During SCC, a crack will propagate at a local stress concentration when chemicals (in cladding, possibly iodine or cesium fission products) concentrate at the crack tip. An example of SCC is the cracking of certain stainless steels under tension and in a chlorine environment. In operating reactors, SCC can occur in locations where the cladding is being pressed against the pellet producing pellet-clad interaction (PCI). For nuclear fuel, these terms (PCI and SCC) are sometimes used interchangeably. In early fuel designs, the pins were not pressurized and the cladding crept against the pellets (due to the reactor operating pressure on the order of 2,200 psi). The cladding tended to fail at the pellet ridges where during rapid power changes, the fuel expanded faster than the cladding, causing high local stresses and PCI or SCC. Limiting reactor maneuvering, pressurizing the pins during manufacturing, and shaping the pellet edges eliminated the PCI problems during operation.

SCC or PCI is not expected to be a problem in dry storage or in the repository. After reactor operation, the fuel pellet, which is hotter than the cladding, contracts away from the cladding and does not interact with the cladding. During the hot dry storage time, if anything occurs, the cladding creeps further away from the fuel pellets (creep is the predicted failure mode although it has not been observed in dry storage). Therefore, PCI does not occur in dry storage. Einziger et al. conducted two series of tests (1982, 1984) of pins in dry storage, conditions identical to repository conditions but not as long. It turns out that cladding damage occurs in the first 20 years, when the temperature spike occurs, so that dry storage tests are good measures of repository conditions. He then looked at cladding and saw no internal attack. The cladding is not under stress against the fuel pellets so that SCC is not expected. SCC is associated with trace halogens. Rothman (1984) summarizes corrosion properties of Zircaloy fuel failure mechanisms in dry storage and concluded that SCC was not a problem. Pescatore et al. (1989) also looked at fuel side SCC and concluded that it was not important. The U.S. Nuclear Regulatory Commission (NRC) is looking only at creep failures for dry storage (NRC 1997, NUREG-1536). Cunningham et al. (1987), also concludes that Iodine-induced SCC is not considered a significant degradation/cladding breach mechanism. Tasooji et al. (1984) analyzed this effect and also concluded that SCC was not a major failure mechanism. Billaux (Letter to E.R. Siegmann, 9/24/97), at Siemens Power looked at spent fuel in the repository using the SIERRA code. This is a state-of-the-art fuel design code that also looks at pellet and cladding life. He found no SCC and very low strains. He reported no significant cladding degradation.

Yau and Webster (1987, p. 718) note that zirconium is resistant to SCC in many environments such as NaCl, HCl, MgCl<sub>2</sub>, NaOH and H<sub>2</sub>S. They note that the high SCC resistance of zirconium can probably be attributed to its high repassivation rate. They also note that SCC is possible in certain environments (FeCl<sub>3</sub>, CuCl<sub>2</sub>, CH<sub>3</sub>OH and HCl mixture and some others). However, these conditions are not expected to occur under repository conditions. Yau (1984, p. 140/1 – 140/8) published results of SCC tests with zirconium in concentrated acids to simulate concentrated geothermal salts. Both welded and non-welded samples were exposed to U-bend SCC tests. Tests were conducted both at room temperature and at high temperature/pressure autoclave conditions. The pH was between 2.3 and 3 (measured at room temperature). The U-bend samples showed no cracking after 60 days of testing.

In summary, SCC is not expected to play a role in cladding degradation in the repository.

#### **6.3.1.1.9 Cladding Unzipping**

The cladding that has failed during reactor operation, or from creep rupture, and DHC generally has small cladding perforations and very small areas of fuel exposed to the near-field environment. When the WP fails, the inert atmosphere inside the WP is replaced with the oxygen and steam from the near-field environment. At an early period, the near-field environment is almost completely steam and dry oxidation is not expected. In the dry oxidizing conditions and with perforated cladding, the UO<sub>2</sub> phase in the spent fuel can oxidize in two stages, first to U<sub>4</sub>O<sub>9</sub> and then to the U<sub>3</sub>O<sub>8</sub> phase (see Section 6.3.1.2) causing an increase of the spent fuel matrix volume. These are nominal formulas only and do not necessarily describe the actual stoichiometry of these oxides. The stress from the volume increase can unzip the clad, causing a gross rupture of the clad and exposing the fuel inside. The fuel also has an increase in surface area and dissolution rate, the combined factor being 150 (Gray and Wilson 1995). If the

fuel oxidizes under wet conditions, cladding unzipping has not been observed. Dry fuel oxidation has been experimentally studied by Einziger et al. (1982) and Hanson (1998). McEachern and Taylor (1997) summarize the work of others.

For the clad unzipping, Section 6.3.1.2 recommends using the activation energy for  $U_3O_8$  formation of 38.4 kcal/mol. This value was obtained by averaging the 36.8 kcal/mol reported by McEachern and Taylor (1997), which was from their review of unirradiated  $UO_2$  oxidation by numerous authors, and the 40.1 kcal/mol from the Waste Form Characteristics Report (WFCR), based on Einziger's data on spent fuel. It is important to remember that the  $U_4O_9$  to  $U_3O_8$  transition has a higher activation energy than the  $UO_2$  to  $U_4O_9$  transition. However,  $U_4O_9$  will not affect the clad. Still, the higher activation energy should only be used to calculate the time for  $U_4O_9$  to turn into  $U_3O_8$ . Hanson (1998) and Einziger et al. (1982) work is on spent fuel. The Section 6.3.1.2 recommendation is an average of Einziger's spent fuel work and McEachern's review of unirradiated  $UO_2$  work. In this case, the unirradiated  $UO_2$  activation energy is conservative (it is slightly smaller) and does not account for any burnup dependence.

The models developed in Section 6.3.1.2 were used for cladding unzipping calculations. The cladding unzips in two phases, an incubation phase and an unzipping phase. In the incubation phase, the oxidized spent fuel phase ( $U_3O_8$ ) builds up just inside the perforation until unzipping of the cladding starts. This incubation time is described by the following equation (see Section 6.3.1.2 for derivation):

$$T_i (\text{Unzip}) = 3.47E-17 \exp[38.4 \text{ kcal/mol} / RT] \quad (6-18)$$

where

- Ti = the incubation or unzipping time (years) from WP failure
- R = the universal gas constant (1.987E-3 kcal/mol·K)
- T = temperature (K)

Using the temperature profiles for the peak pin in the average and design WP (Figure 6-10), the peak pin would unzip if the WP failed before 50 years (average WP) or 200 years (design WP). This calculation was performed by using trapezoidal integration and integrating the time to unzipping backward from one million years. Thus, little or no cladding unzipping and  $U_3O_8$  formation is expected in the repository.

For defective WPs (assumed to have failed at emplacement), it is possible to unzip the cladding of the pins that are perforated. This will probably not actually occur because the environment is mostly steam and the  $O_2$  partial pressure is low at this early time. Therefore, dry oxidation is unlikely. If you assume that dry oxidation does occur, then the degree of unzipping for defective WPs can be estimated. The combination of defective WPs, which is taken as 0.02 percent (Doubt 1984, p. 30) with premature pin failure, 1.25 percent including the stainless steel cladding, gives the fraction of pins expected to be converted to  $U_3O_8$  to be  $2E-6$  ( $2E-4 * 1.25E-2$ ). Overall, when considering the presence of steam, timing of WP failures and decreasing temperatures, it is expected that only very small fractions of fuel are expected to be converted to  $U_3O_8$  and these small fractions will not affect the PA (see Figure 6-22).

Hypothetically, cladding could unzip in a wet environment. As the  $\text{UO}_2$  is converted to secondary phases such as schoepite and Na-boltwoodite, volume increases. Possibly, these phases will only form where there is available liquid volume, or alternatively they might be able to form at solid surfaces and tear the cladding. Cladding unzipping has not been observed in spent fuel pools where fuel has been stored for tens of years as noted by the IAEA (1988) and Johnson et al. (1987, 1980). The Canadians tested a defective pin in a steam autoclave for ten years and did not measure any cladding strain (Wasywich et al. 1986). While these observations are encouraging, the time periods are very short compared to the repository scale and a form of liquid oxidation and secondary phase formation might tear the cladding. In the current model, wet unzipping will have only a minor impact if it is found to occur and is added to the model. The current model assumes that all cladding that is failed during reactor operation has no cladding (that is, no cladding credit) and local corrosion exposes large quantities of fuel for dissolution. Only mechanical failure from rock drops would be effected and that percent is not large (maximum is 11 percent of fuel). Other failure mechanisms that could cause cladding perforation has been found to not be applicable at YMP conditions.

#### 6.3.1.1.10 Source Term From Cladding Effects

Intact cladding prevents the dissolution of the  $\text{UO}_2$  fuel after the WP fails. After the cladding fails, it still restricts the release of fission products. Most of the fuel that has failed during reactor operation contains cladding that is only perforated or contains small cracks (EPRI 1997). Fuel that might fail from creep rupture or DHC also contains small holes. The one pin that failed in the Nevada Test Site dry storage program has a hole of about 0.1 square micron in area (Johnson et al. 1987, p. 52). In a high temperature creep burst test, Lorenz et al. (1980, p. 131) measured a  $2 \text{ mm}^2$  hole. Pitting or crevice corrosion would also produce small holes (see Section 6.3.1.1.2.8). Surveys of spent fuel storage operation have not shown any cladding failure propagation. Even failure of the rod by a rock drop or hydride embrittlement would produce long sections of cladding that would limit release.

Radionuclides would have to diffuse through the holes or cracks in the cladding. The release rate would be isotope dependent because of differences in solubilities, diffusion rates, and absorption into secondary phases. Wilson (1985) performed fuel dissolution tests on fuel with defective cladding. The degree of cladding damage varied between bare fuel pellets (cladding laying next to fuel), cut slit  $0.015 \times 2.54 \text{ cm}$  (representing a crack), two drilled holes of 0.02 cm diameter (representing perforations), and intact cladding. The samples were placed in deionized water, open to hot cell atmosphere and temperature. After 250 days, the samples were removed from the water, placed in fresh water, testing then continued for another 128 days. Table 6-26 gives the release fraction of the inventory of each isotope in the sample after both test intervals. The table shows that the effectiveness of the cladding to retain radionuclides varies from isotope to isotope. It also shows that with the exception of  $^{137}\text{Cs}$ , damaged cladding will still significantly inhibit the release of most isotopes.

Wilson (1987), later performed a second series of tests using the same selection of defective cladding but used J13 water instead of deionized water and the samples were open to the hot cell atmosphere. The first two cycles of this test lasted for over a year. Wilson's Series 3 tests (Wilson 1990b) were again conducted with various defective cladding samples in J13 water but in this test, the sample holder was sealed from the hot cell atmospheres. The Series 3 tests lasted

for over 1.2 years. Both of these tests showed that the effectiveness of the cladding to retain radionuclides varies from isotope to isotope and that damaged cladding will still significantly inhibit the release of most isotopes.

Currently, the EBS transport model is too coarsely discretized to model the diffusion-limited release of isotopes from defected fuel rods. The abstraction of the cladding effect was by limiting the fraction of fuel exposed for dissolution. Future modeling may address the release of specific isotopes by diffusion, sorption, and other mechanisms that are isotope dependent. Better modeling of dissolution from perforated cladding will change both the timing and quantities of radionuclides that are released, and is likely to reduce the dose because of the low release of neptunium.

#### **6.3.1.1.11 VA Abstraction of Cladding Degradation**

Most commercial nuclear fuel is encased in Zircaloy cladding which isolates it from the environment. Models were developed to describe cladding degradation from creep, corrosion, and mechanical failure (rock falls). No cladding credit was taken for the stainless steel clad fuel (1.15 percent of inventory) or fuel with defective cladding from reactor operation (0.1 percent). Figure 6-3 shows the various cladding degradation mechanisms and Figure 6-5, Cladding Abstraction, shows the fraction of the fuel in a WP that is available for fuel dissolution as a function of time. Both the maximum and minimum values are shown. The RIP code samples between the maximum and minimum values using a log uniform distribution. Before 60,000 years, the stainless steel and defective fuel is available for dissolution when the WP becomes penetrated. At about 100,000 years, both mechanical failures and corrosion start to expose more fuel for dissolution. At one million years, about 50 percent of the fuel is available for dissolution. Both creep and DHC were modeled but neither contribute significantly to the amount of fuel availability for dissolution.

The RIP abstraction contains three components: juvenile failures, corrosion, and mechanical failure. For each failure mode, a fraction of fuel exposed for dissolution in RIP is estimated.

Eight of the earlier reactors used stainless steel clad fuel containing a total of 723 metric tons of uranium. This represents 1.15 percent of the estimated 63,000 metric tons of commercial fuel to be placed in the repository. No cladding credit is taken for stainless steel and it is assumed that this fraction of the fuel is exposed for dissolution when the WP fails. The model currently spreads the stainless steel cladding over all WPs in the repository. This model is conservative because it results in a probability of 1 that early-breached WP will contain stainless steel-clad, maximizing the release of solubility-limited isotopes such as Np. Had the stainless steel-clad packages been separated into their own WP group, there would have been fewer but larger release pulses of high-solubility isotopes, and much smaller total release of solubility-limited isotopes.

The commercial Zircaloy clad fuel has improved with time. Early cores (up to 1985) had a pin failure rate from 0.02 percent to 0.07 percent. After 1985, the pin failure rate decreased to 0.006 percent - 0.05. The overall pin failure rate for both time periods is 0.01 percent - 0.05 percent. For this analysis, it is conservatively assumed that 0.1 percent of all the pins are damaged to some degree. The analysis assumes that the fuel that is failed from reactor operation

(0.1 percent of total fuel) has no cladding and is available for dissolution. This is added to the stainless steel fuel so that a total of 1.25 percent of the commercial fuel is available for dissolution when the WP fails.

In the early stages of postclosure (first 50 years), the cladding could be damaged by creep or strain failure if the temperature (and therefore cladding stress) is high enough. This failure mode leads to a pinhole or hairline crack. It is not predicted to occur for pins in the peak pin in either the average or design (hot) WP and does not significantly contribute to the source term. Delayed hydride cracking, creep, and general corrosion (surface oxidation) were modeled but none of these contribute significantly to the amount of fuel available for dissolution.

Corrosion of Zircaloy was modeled with the WAPDEG code. This model was developed to represent corrosion in some unknown and unexpected chemical condition or other failure mechanisms that have not been identified but might occur after 100,000 years. Experimental results are available for corrosion of zirconium and C22 type alloys under very severe conditions of hot, concentrated acids. Corrosion rates for the zirconium tend to be from fifty times to tens of thousands of times slower than C22 type alloys under extreme acid conditions. The WAPDEG model calculated the fraction of patches of cladding that are corroded 75 percent through using the C22 general corrosion model with the corrosion rate decreased by a factor of between 10 (upper limit) and 1,000 (lower limit). For each RIP realization, corrosion starts at the first penetration of the WP and the fuel area exposed (fraction of patches failed) is calculated as a function of time. Fuel starts to become exposed about 30,000 years after the first patch penetrates the WP. After one million years, the range of fuel exposed is from 0.2 percent (lower limit) to 40 percent (upper limit).

Mechanical failure is caused by rocks falling onto the fuel as the WP structurally fails. The sequence is that rocks fall onto the WP upper surface and rest there. Then the WP inner supports fail and the fuel is lowered to the WP bottom. Rocks fall 20 cm from the top of the WP to the top of the fuel. A statistical analysis (described in Section 6.3.1.1.7) of dropping rocks predicts a range of 2.28 percent to 11 percent of the fuel fraction is exposed. It is assumed that mechanical failures occur starting at 100,000 years after initial WP breach, when the number of patches in open WPs starts to increase and continues linearly with the log of time out to one million years (see Figure 6-5). RIP assumes a log uniform distribution and samples between the maximum and minimum value for the mechanical failure of fuel.

Because of the large uncertainties in the cladding performance in the repository, sensitivity studies were performed for effects of cladding. Cases were analyzed with 100 percent of the cladding failing in 10,000 years, 100,000 years, and 1 million years. In addition, a comparison of the 95 percent and 50 percent cases with the base case was performed. These sensitivity studies are presented in Section 5 of the VA.

### **6.3.1.2 Spent Fuel Air Oxidation Models**

Model concepts and parameters for spent fuel oxidation are given in the WFCR (Stout and Leider 1997) and in a Canadian review (McEachern and Taylor 1997). The oxidation is a two-step process—oxidation of  $UO_2$  to  $U_4O_9$  and oxidation of  $U_4O_9$  to  $U_3O_8$ . These are nominal formulas only and do not necessarily describe the actual stoichiometry of these oxides. The cited

papers find that these steps have rates with temperature dependence given in terms of activation energies. The discussion in this section extends that review work to (1) specify error bars for the parameters, and (2) discuss the "plateau" region in the oxidation to  $U_3O_8$ , one of the model areas with relatively greater variability. In the final model, not all steps need be included; some may be conservatively assumed to have zero duration, and the model for time duration will use only some of the steps.

The same type of temperature dependence is seen in the time to initiation of cladding splitting driven by air oxidation of the spent fuel inside a small breach. Hence we associate the experimental information on activation energies for oxidation developed in several types of oxidation experiments, and use one activation energy per oxidation end point (i.e.,  $U_4O_9$  or  $U_3O_8$ ).

Oxidation of spent fuel proceeds first to a  $U_4O_9$  lattice structure with an oxygen/metal (O/M) ratio (the metal is mostly uranium; the change in oxygen is actually measured) of 2.40 to 2.42 and a specific volume about 2 percent smaller than the original  $UO_2$ . In this first step, the process and oxidation product just stated apply to spent fuel and to  $UO_2$  doped with  $\geq 4$  percent simulated fission products, but are different for pure  $UO_2$  (McEachern and Taylor 1997), hence experiments on  $UO_2$  are irrelevant. The process then proceeds to  $U_3O_8$  with an O/M limit of about 2.75 and about 28 percent larger specific volume than the initial  $UO_2$ . The oxidation to  $U_4O_9$  proceeds first rapidly along grain boundaries, and then more slowly into the grains. The oxidation progress into the grains shows a  $(\text{time})^{1/2}$  dependence, an indication that the rate-limiting factor is the diffusion of oxygen through the  $U_4O_9$  lattice. The oxidation from  $U_4O_9$  to  $U_3O_8$  generally proceeds in an s-shaped oxidation progress curve; first in a plateau or nucleation phase, and then in a growth phase. But the plateau is not seen in all experiments.

#### 6.3.1.2.1 Spent fuel with $UO_2$ oxidizing to $U_4O_9$ .

The oxidation to  $U_4O_9$  proceeds more rapidly along grain boundaries than into the individual grains. The oxidation rate into individual grains is reviewed first, since it is slower and hence the main limiting step in complete oxidation to  $U_4O_9$ .

##### Oxidation to $U_4O_9$ in grains

First, individual data sets are reviewed, then parameter and uncertainty values are recommended.

(a) For the oxidation rate into a grain, Einziger et al. (1992) give the width  $W(t)$  of the oxidized zone in  $\mu\text{m}$  as

$$W(t) = (2kt)^{1/2} \quad (6-19)$$

$$k (\mu\text{m}^2/\text{h}) = k_9 \exp(-Q_9 / RT) \quad (6-20)$$

where

$t$  = time in hours

$k_9$  =  $1.04\text{e}+8 (\mu\text{m}^2/\text{h})$

- $Q_9$  = activation energy, with a value of 24 (kcal/mole)  
 $R$  = the gas constant,  $1.986 \times 10^{-3}$  kcal/mole-°K,  $T$  in °K

The subscript 9 indicates the chemical step with the end product  $U_4O_9$ .

They base this on data obtained on individual grains in a matrix by oxidation followed by etching and microscopic photography. Looking at the uncertainty in the slopes of Einziger's Figure 5 to fit through the upper 85th or 90th percentile of the data, the uncertainty in the 24 kcal/mole is  $(24 \pm 2)$  kcal/mole and the uncertainty in  $k_9$  is about  $\pm 10$  percent, i.e.,  $k_9 = (1.04 \pm 0.1)e+8$  ( $\mu m^2/h$ ).

(The data points in Einziger's Figure 5, aside from the upper-bounding-line ones, do not quite match a  $t^{1/2}$  law, so there is some modeling uncertainty also in applying a  $t^{1/2}$  law to this data. This small uncertainty is insignificant in this application, as the oxidation model plays a very minor role in radionuclide releases.)

(b) Several other data sets give independent measurements of  $Q_9$  for oxidation to  $U_4O_9$ . From another set of Einziger et al. data, their Figure 9 for time to oxidize the spent fuel samples to an oxygen to metal atom ratio (O/M) of 2.4,

$$t_{2.4} \text{ (h)} = 2.6E-9 \text{ (h)} \exp(26.6 \pm 7 \text{ (kcal/mole)} / RT) \quad (6-21)$$

The leading factor depends on the grain sizes. The  $Q_9$  value should be a more universal property of oxidation to  $U_4O_9$ .

(c) Another set of data referenced from their earlier work gives  $Q_9 = 27 \pm 4$  (kcal/mole).

For the data going into (a), the estimated error in  $Q_9$  is (25 to  $26 \pm 10\%$ ), which more specifically is  $25.5 \pm 2.6$ . McEachern and Taylor (1997) give an average over different measurements for  $U_4O_9$  of  $Q=106$  kJ/mole, which is 25.3 kcal/mole.

(There are 4.186 Joules per cal.)

Overall, McEachern and Taylor's central value of  $Q_9 = 106$  kJ/mole (25.3 kcal/mole), with an error  $\sigma$  of  $\pm 10$  percent, is recommended. If one is using  $Q_9$  to extrapolate to rates or times at lower temperatures than in the data, it would be reasonably conservative to use the mean minus one standard deviation.

For the rate constant  $k_9$ , the data set going into (a) above is used. The value of  $k_9$  has to be adjusted for the use of  $Q_9 = 25.3$  kcal/mole in place of the one-experiment-specific  $Q_9 = 24$  kcal/mole. (The data on which this  $k_9$  is based are centered at  $T = 458^\circ K$ .) Hence, after re-fitting (Einziger's Figure 9) with this revised  $Q_9$ ,  $k_9$  is found to be 4.18 times larger. The 10 percent uncertainty in  $k_9$  from (a) carries over. Hence in Equation (6-20):

$$Q_9 = (25.3 \pm 2.5) \text{ kcal/mole} \quad (6-22)$$

$$k_9 = (4.34 \pm 0.43)e+8 \text{ } (\mu m^2/h) \quad (6-23)$$

Recall that the  $Q_9$  is a property of the oxidation process to  $U_4O_9$ , and the rate constant  $k_9$  depends also on the distribution of grain sizes and is taken from a series of experiments using a spent fuel sample with one distribution of grain sizes.

**Volume Oxidation Rate**—The conversion from grain surface oxidation rate to a volume-oxidized progress uses geometry. The correspondence depends on grain size. The model is given in the WFCR.

**The Intergranular Progress of Oxidation to  $U_4O_9$  is More Variable**—Thomas et al. (1991) show an example where the oxidation progress from the pellet outer edge has progressed 1.2 mm while oxidation from an exposed inner crack surface has progressed 0.04 mm after 1,826 h at 175°C. A zone of partially oxidized grains extends back about 0.08 mm from the deep front coming in from the outer edge and 0.04 mm from the 0.04-mm deep front. The photomicrographs in the paper are just one snapshot in time (i.e., after 1,826 hours). The more rapid intergranular oxidation in the outer third of the pellet may be correlated with the circumstance of the temperature gradient in a pellet during reactor operation. This gradient causes compression in the inner part of the pellet and circumferential tension in the outer part, and induces some fission gas migration to the grain boundaries and toward the outer edge of the pellet.

The relatively rapid intergranular oxidation step may be conservatively neglected in a predictive model by assuming infinitely fast intergranular oxidation through the entire bulk sample. But in interpreting experiments, the effect and variability of the intergranular oxidation should be kept in mind.

#### 6.3.1.2.2 Second Step, $U_4O_9 \rightarrow U_3O_8$

The transition from  $U_4O_9$  to  $U_3O_8$  is generally accepted to proceed in two stages. This gives a sigmoidal curve of change in oxygen ratio (or an s-shaped curve visually). McEachern and Taylor (1997) call these a nucleation stage and a growth stage. Einziger et al. (1992) state that in oxidation from  $UO_2$  to  $U_3O_8$  there is first the oxidation phase  $UO_2 \rightarrow U_4O_9$  to completion, then a plateau, then oxidation  $U_4O_9 \rightarrow U_3O_8$ . The growth stage shows a linear increase of depth with time;  $U_3O_8$  has a larger specific volume than  $U_4O_9$  or  $UO_2$ , and dust-sized particles loosen from the advancing reaction surface, and so oxygen transport through the  $U_3O_8$  layer is not constrained. The  $U_3O_8$  oxidation advance levels off when the oxidation of the grains nears completion.

The data sets vary substantially. Many data sets are reviewed in McEachern and Taylor (1997). Many data sets are presented in the YMP WFCR (Stout and Leider 1997) and the references cited therein. In many data sets the s-shaped curve is seen clearly, but in some data sets (such as WFCR [Stout and Leider 1997, Figures 3.2.2-5 to 3.2.2-8]) the s-shape is not seen. Hence this nucleation stage is highly variable in the experiments, and for a model of time duration one may conservatively neglect this stage and model the duration of the growth stage only.

Some activation energy ( $Q_8$ ) values observed for the growth stage are 36.8 kcal/mole (154 kJ/mole) (McEachern and Taylor 1997) and 40.1 kcal/mole [Stout and Leider 1997, based on Einziger data]. A central value is:

$$Q_8 = (38.4 \pm 3) \text{ kcal/mole} \quad (6-24)$$

where

the subscript 8 indicates the chemical step with the end product  $U_3O_8$ .

The  $Q_8$  value for the  $U_3O_8$  oxidation growth stage is considerably higher than the  $Q_9$  value for  $U_4O_9$  oxidation, so at low temperatures the  $U_3O_8$  oxidation time duration will be much longer than the  $U_4O_9$  oxidation duration.

The  $U_3O_8$  oxidation rate is steady with time. The WFCR gives the equation:

$$W(t) = k_8 \cdot \exp(-Q_8 / RT) \cdot t \quad (6-25)$$

where

$$k_8 = 8.58 \text{ e}+13 \text{ } \mu\text{m/h}$$

$$Q_8 = 40.057 \text{ kcal/mole}$$

Using the  $Q_8$  value of 38.4 kcal/mole based on a broader set of oxidation data, one then has to refit  $k_8$  to the revised  $Q_8$ , resulting in a revised  $k_8$  value of 2.02 e+13  $\mu\text{m/h}$ .

Some of the parameter mean values used in this analysis differ slightly from those in the WFCR. The small changes in activation energies ( $Q$  values) between the values here and the values in the WFCR are within the error bars developed here.

**Volume oxidation rate**—The conversion from grain surface oxidation rate to the rate of reduction of unoxidized solid volume in the grains uses geometry. The correspondence depends on grain size. The model is given in the WFCR. Spherical, cubic, or pyramidal assumed grain shapes give the same volume-rate results for the same characteristic linear size.

**Nucleation or plateau phase**—It is difficult to quantify the plateau or nucleation phase, and in the end we will conservatively omit it. McEachern and Taylor (1997) say that the time period for nucleation seems to get shorter with increased surface roughness. For spent fuel, greater roughness is correlated with smaller grain size, since the grains are first oxidized to  $U_4O_9$  with a small decrease in grain volume, opening up the grain boundaries. McEachern and Taylor say that different experiments indicate different temperature dependencies for the nucleation time period, ranging from constant with temperature to an Arrhenius temperature dependence with about the same  $Q$  as for the growth period. Einziger et al. (1992) state that it is difficult to measure the plateau, other than that it gets very long at low temperature and vanishingly short at high temperature. The WFCR and several papers by Einziger indicate that the plateau is caused in part or entirely because the second oxidation step to  $U_3O_8$  does not start until the step to  $U_4O_9$  is complete. But McEachern and Taylor (1997) find that the two processes may go in parallel. The  $U_3O_8$  step may require only a surface layer of  $U_4O_9$  before it starts its nucleation stage. At low temperatures the second step is slow enough that one sees the first step clearly by itself. In experiments, as noted, sometimes one does not see the plateau. Hence for conservative predictions, the plateau is omitted until further data clarify its behavior.

### 6.3.1.2.3 Application to Unzipping of Spent Fuel Rods

Einzigler and Strain (1986) show measurements of time to initiation of cladding splitting in a breached spent fuel rod. Their data, reproduced in Figure 6-23, show a time dependence with an activation energy closely similar to the activation energy developed above for oxidation to  $U_3O_8$ . Applying the latter  $Q_8$  value as the slope, and fitting their data to determine an intercept, the curve is found which is shown as the longer solid line in the figure. This is felt to be a better predictive model for extrapolation, because the  $Q_8$  value is derived from a wider set of experiments. This  $Q_8$  value is also slightly lower than the one found by Einzigler and Strain (1986) from their single set of data. Since it is lower, it is relatively more conservative when used for extrapolation to lower temperatures.

### 6.3.1.3 Aqueous Dissolution of Spent Fuel

**Introduction**—When water can get inside fuel rod cladding, a fraction of certain elements is accessible just inside the cladding (see below). These elements were volatile in the hot temperatures during reactor operation, and they are also highly soluble in water. Further, the water gradually dissolves the spent fuel matrix, making its contained radionuclides accessible to the water.

The purpose of this section is to determine the quantities and rates at which radionuclides become accessible to water. The question of solubility limits are addressed later in Section 6.4.1.

The model in this section is simply a numerical estimate or range, for the quantities accessible immediately inside the cladding, based on data and using a relatively conservative selection of numerical values. Elements in the spent fuel matrix are gradually exposed as spent fuel dissolves. For the dissolution model, an equation form is selected consistent with chemical nonequilibrium thermodynamics, the coefficients of the equation determined by a linear regression analysis of a series of experiments done by the YMP.

#### 6.3.1.3.1 Fuel-Cladding Gap Fraction of Elements

The instantaneous release mode consists of species in the gap between fuel pellets and cladding, and species on fuel grain boundaries. These species are referred to here as gap-inventory species and include  $^{14}C$ ,  $^{135}Cs$ ,  $^{137}Cs$ ,  $^{129}I$ ,  $^{99}Tc$ , and  $^{79}Se$ . The species are characteristically mobile and highly soluble in water. Being volatile at high temperatures, a fraction of these elements moves out from the  $UO_2$  grains and deposits in the pellet-cladding gap, since the cladding is cooler than the  $UO_2$  pellets during reactor operation. The fraction of these volatile elements in this location is typically a factor of 8 to 10 smaller than the fraction of fission gases available in the cladding gap and other void spaces (Stout and Leider 1997, 2.1.3.4-4). The available fission gas fraction is in most cases in the range 0.1-2 percent (Stout and Leider 1997, 2.1.1.5-4) with some cases up to 23 percent for unpressurized BWR fuel rods (Stout and Leider 1997, 2.1.1.5-16). In more recent designs of BWR fuel rods as well as PWR fuel rods, there is an initial helium gas pressurization (DOE 1987) so the fission gas release is expected to be in the low range for all recent and future fuel designs. The fractions of the spent fuel inventory projected through 2020 expected to have fission gas releases less than 2 percent and greater than 2 percent is given in Stout and Leider (1997, 2.1.1.5-1).

The gap-inventory species and their gap fractions used in TSPA-1995 are in Table 6-27. The same values are used in TSPA-VA. All other radionuclides in the inventory are assumed to be located in the spent fuel matrix. The gap fractions of gap-inventory species are assumed to be available for immediate release as soon as both WP container and cladding fail. The value of 2 percent for cesium, iodine, technetium, and selenium is conservative as an average, given the fractions of spent fuel with fission gas releases less than and greater than 2 percent, and given that the volatiles released from the matrix to the cladding gap are a factor of 8 to 10 smaller than the gas release.

The distribution of the  $^{14}\text{C}$  gap inventory in Table 6-27 represents the uncertainty of  $^{14}\text{C}$  inventory in the gap and the oxidation layer on the cladding surface, and is the same as used in TSPA-1993 (Andrews et al. 1994). Van Konynenburg et al. (1985) reported that about 65 percent of the total  $^{14}\text{C}$  inventory is present in cladding, crud, and other fuel assembly hardware. However, only the  $^{14}\text{C}$  in the gap and the grain boundary of the spent fuel matrix (about 1 percent), and in an oxidation layer on the surface of the cladding is available for instantaneous release. The release rate for the rest of the  $^{14}\text{C}$  is considerably slower (Barnard et al. 1992). The release of  $^{14}\text{C}$  is calculated assuming that all the  $^{14}\text{C}$  available at a given simulation period migrates out of the EBS as a gas and then dissolves in the aqueous phase (i.e., no gaseous transport in the geosphere is considered).

#### **6.3.1.3.2 Spent Fuel Matrix Forward Dissolution Rate**

The approach for dissolution rate model development uses concepts from nonequilibrium thermodynamics. The objective is to derive function forms for the dissolution rate that are consistent with quasi-static thermodynamic processes. These function forms will contain thermodynamic chemical potentials of both the solid (spent fuels) and the solution (water chemistries) along with a set of coefficients and parameters that can be evaluated by numerical regression of dissolution test data. Currently, detailed knowledge is not available for the atomic (mechanistic) steps and the sequence of chemical/electrochemical reaction steps to describe the dissolution process over the range of spent fuel inventory, potential water chemistries, and temperatures. The existing approach is to obtain an experimental database (flow-through tests) of dissolution rates for a subset of specific spent fuels approved testing materials (ATMs) over a range of controlled, aggressive water chemistries and temperatures. With a numerical regression algorithm, these data are used to evaluate empirical parameters in a rate law for each specific spent fuel ATM (Gray et al. 1992; Steward and Gray 1994). (The final regression analysis is presented later in this section.) The function form of this rate law is a product polynomial involving the bulk water chemistry concentrations and temperature (Stumm and Morgan 1981). In its present form, this function form does not explicitly depend on the thermodynamic properties of the uranium oxide waste form. It does, however, have an approximate representation of the fission products and actinides together in the form of a burnup factor.

The spent fuel waste form dissolution/release rate responses impact both design and performance assessment evaluations and consequences of the substantially complete containment time period (SCCTP) (NRC 10CFR60.113) and the controlled release time period (CRTP) (NRC 10CFR60.113). These two regulatory requirements are coupled because WP failures during the SCCTP will potentially expose spent fuel waste forms to atmospheric conditions in the repository. During this time, the waste forms may be altered by oxidation and/or water vapor adsorbed to the spent fuel surface and dissolution and release of radionuclides from the waste

form as a result of wetting by water. In these cases, alteration, hydration and dissolution of the spent fuel waste-form lattice-structure will take place. The development of a thermodynamically based dissolution and release model relates to the design requirements, as well as the subsystem release and TSPA model development needs.

A release rate model is more complex than a dissolution rate model. The release model includes dissolution rates, precipitation rates, colloidal kinetics, and adsorption rates. At this time, the approach is semi-empirical and depends strongly on the unsaturated testing experiments to provide data and chemical process models. The release model is discussed in Section 6.4.3.

A nonequilibrium thermodynamic approach to the intrinsic dissolution rate model is presented in the WFCR Section 3.4.2 (Stout and Leider 1997). Several functional forms presented there are consistent with the nonequilibrium thermodynamic theory. Two of these forms were the basis of trial linear regression analyses, described in the WFCR, to fit the suite of YMP test data.

The test data for dissolution response were best represented by the currently accepted intrinsic dissolution model, which has the form of the Butler-Volmer equation used in correlation of corrosion and electrochemical rate data. The normal derivation of the Butler-Volmer equation assumes that the electrochemical processes are near thermodynamic equilibrium. In the WFCR approach, thermodynamic nonequilibrium was assumed for the dissolution process. Also, the functional form to relate the dissolution velocity to the ratio of nonequilibrium configurational entropy was assumed. By substituting the traditional chemical potentials that include a logarithmic dependence on activities or concentrations for the chemical potential changes in the Butler-Volmer-like model form, the classic chemical kinetic rate law (Stumm and Morgan 1981) was derived:

$$\text{Rate} = k[A]^a[B]^b[C]^c \dots \exp(E_a/RT) \quad (6-26)$$

The parameters A, B, C, etc. are a generic representation of chemical activities, concentrations, or other parameters. Burnup was represented as a concentration term as well, because it is proportional to the aggregated production and concentration of fission products. For regression, logarithms of each side formed a linear model. The equation is considered an expansion of the theoretical equation about a point in its input space, hence quadratic and cross terms may be added to fit the reaction rate over a broad range of input values. These terms represent nonlinearities and interactions.

This Butler-Volmer type model describes some features of the chemical dissolution processes far from thermodynamic equilibrium and provides a reasonably good fit to the available data. However, because the model is nonlinear, extrapolation beyond the measured independent variable space could cause large prediction errors and should be used with caution.

### **The Final Regression Equation**

The data set for the fit is given in the WFCR (Stout and Leider 1997, Tables 2.1.3.5-4 and 2.1.3.5-4a). The measurements were flow-through tests on dissolution of UO<sub>2</sub> and spent fuel. The flow-through condition gives a forward reaction rate controlled by the water and is not affected by buildup of solutes or reprecipitation. The measurements span ranges of carbonate,

oxygen, and pH values. Most of the spent fuel measurements are at burnups of 30 to 31 MWd/kgU, but several measurements are at higher burnups.

The form of the fitting equation starts with Equation (6-26), where A, B, C, ... represent chemical species concentrations, and one of these terms represents burnup. Logarithms of both sides are taken to form a linear sum of terms. In preliminary fitting, several quadratic and cross terms are added. The final quadratic and cross terms are given in the equation below; the support for these terms is the t-statistic in the regression results, to be discussed below. Before the regression analysis, the terms are shifted to zero-mean by subtracting their means. This makes no essential change to the regression equation, but makes the interpretation of the associated error equation simpler.

Equation (6-26) is transformed into a linear equation by taking logarithms (logarithms to base 10 are used in this numerical analysis):

$$\log(\text{Rate}) = \log(k) + a \log(A) + b \log(B) + c \log(C) + \dots + (E_a/R) \times (1/T) \quad (6-27)$$

The constants  $\log(k)$ ,  $a$ ,  $b$ ,  $c$ , ...  $(E_a/R)$  were determined by a statistical analysis of the experimental data set. These constants are the coefficients of the equation. Note that the equation is linear in these coefficients. The equation has the general form

$$\text{Output} = \sum a_i \times f_i(\text{inputs})$$

including  $f_0 = 1$

A, B, C, ... are chemical concentrations or burnup, which is a combined representation of chemical concentrations in the solid matrix. In particular, the relevant chemical concentrations are:

$\text{CO}_3$ , the carbonate ion concentration (in mole/liter), where  $\text{CO}_3$  is a shorthand for the ion  $\text{CO}_3^{2-}$ ;

$\text{O}_2$ , the oxygen concentration in the gas above the water (in percent of atmosphere), which is assumed to control the concentration of oxygen in the water for a given temperature; and

pH, which is already a logarithmic parameter (i.e., it is the negative of the  $\log_{10}$  of the hydrogen ion concentration).

Burnup, in MWd/kgU

The spent fuel burnup is treated as a multiplicative factor in the rate. This is done because the concentration in the solid matrix of fission products and actinides is roughly proportional to the burnup. Other possible contributing physical features roughly proportional to burnup are fission gas accumulation in the grain boundaries and radiation field due to decay. Hence, burnup is a good stand-in for any of these features.

A possible counter argument is that an important factor in the dissolution rate may be the  $\text{UO}_2$  lattice grain structure, which undergoes a change in grain size because of thermal heating during

reactor operation. This heating occurs early and is not a function of burnup. Additional measurements at other burnups are desirable to improve knowledge of the burnup dependence, and some such measurements are in progress in the YMP.

Because a zero value of burnup is not compatible with a logarithm, burnup value is shifted to a low non-zero value (a nominal value of 1 MWd/kgU was chosen). Later discussions address the use of a different non-zero value on predicting a result for an intermediate burnup value.

Because of the model uncertainty just discussed on the treatment of burnup using the "all data" data set, a second linear regression analysis was done using the "high-burnup" experimental data set, i.e., the data with burnups of 30 MWd/kgU and above. Each regression analysis will be discussed in turn.

Prior to linear regression analysis, the input and output variables from the data set were transformed consistent with the form of Equation (6-27). Transformation involved taking the logarithms of the Rate and of the chemical concentrations, and transforming temperature into the form (1/T).

Next, these variables were transformed further by subtracting their means over the data set. This was done to simplify the interpretation of the coefficient error terms. Also, the first coefficient,  $a_0$ , becomes the mean of the outputs in the data set.

Thus, the transformed input variables are:

$$\begin{aligned}x_0 &= 1 \\x_1 &= 1/T \text{ (where T is in } ^\circ\text{K)} - (\text{Mean of } 1/T) \\x_2 &= \log(\text{CO}_3 \text{ concentration}) - (\text{Mean of } \log\text{CO}_3) \\x_3 &= \log(\text{O}_2 \text{ concentration}) - (\text{Mean of } \log\text{O}_2) \\x_4 &= \text{pH} - (\text{Mean of pH})\end{aligned}$$

When linear regression analysis is performed on the no-burnup  $\text{UO}_2$  data alone, and on the higher-burnup spent fuel alone, burnup is not a variable in each of these analyses. The burnup is constant for the  $\text{UO}_2$  data set, and is nearly constant in the spent fuel data set, since most of the data are at burnups of 30 to 31 MWd/kgU. The input variables are (1/T),  $\log\text{CO}_3$ ,  $\log\text{O}_2$ , and pH.

To accommodate different burnups and to allow intermediate values of burnup,  $\log$  Burnup can be added and second-order terms introduced into the predictive equation (i.e., terms where the  $f_i$  are  $x_1 * \log$  Burnup,  $x_2 * \log$  Burnup,  $x_3 * \log$  Burnup, and  $x_4 * \log$  Burnup). The rationale for considering the addition of second-order terms is that Equation (6-27) is an approximation about a point in input space. For approximate applicability to a broad range of input space, the equation may be extended by using second-order terms.

Even more second-order terms may be added if the experimental data set supports them. The qualitative decision criterion is whether the added terms improve the fit significantly more than would be expected from a random effect (where, if there are more terms to adjust, then there is more curvature) and so can more closely fit a given N data point. A quantitative criterion giving guidance related to this qualitative criterion is the t statistic. The linear regression procedure calculates the t statistic routinely for each coefficient. If the absolute value of this statistic is high, then the term is supported. A threshold value for acceptance of the term and its coefficient is a t-statistic absolute value of about 1.0 to 1.5. After examining possible additional cross terms, the following two terms were added:

$$(\log \text{CO}_3)^2 - \text{Mean}(\log(\text{CO}_3))$$

$$(1/T)(\log \text{O}_2)$$

The support for these terms is given by the t statistic tabulated in the results (Table 6-28a).

Raw inputs:

- Temperature, degrees K
- $\text{CO}_3$ , the carbonate ion concentration (in mole/liter)
- $\text{O}_2$ , oxygen concentration in the gas above the water (in % of an atmosphere)
- pH is already a logarithmic parameter; it is the negative of the  $\log_{10}$  of the hydrogen ion concentration
- Burnup in MWd/kgU

Also, an input to the regression procedure is the experimental output:

- Spent fuel dissolution rate,  $\text{mg}/\text{m}^2\text{-day}$ , where mg refers to mass of the spent fuel matrix, or of the  $\text{UO}_2$  matrix for unirradiated fuel

Transformed input variables and higher-order terms are:

$$f_0 = 1$$

$$f_1 = 1/T - (\text{Mean of } 1/T)$$

$$f_2 = \log(\text{CO}_3 \text{ concentration}) - (\text{Mean of } \log \text{CO}_3)$$

$$f_3 = \log(\text{O}_2 \text{ concentration}) - (\text{Mean of } \log \text{O}_2)$$

$$f_4 = \text{pH} - (\text{Mean of pH})$$

$$f_5 = \log(\text{Burnup}) - \text{Mean of } \log \text{ Burnup}$$

$$f_6 = f_1 \cdot f_5$$

$$f_7 = f_2 \cdot f_5$$

$$\begin{aligned}
f_8 &= f_3 \cdot f_5 \\
f_9 &= f_4 \cdot f_5 \\
f_{10} &= f_2 \cdot f_2 - (\text{Mean of } f_2 \cdot f_2) \\
f_{11} &= f_1 \cdot f_3
\end{aligned}$$

The transformed output variable is

$$y = \log(\text{Spent fuel dissolution rate})$$

where log is  $\log_{10}$ .

The Means are the means over the specific data set used in a regression analysis.

This yields the predictive equation, where the input is a vector of parameter values:

$$y(\text{input}) = \sum a_i \times f_i(\text{input})$$

where  $i$  ranges from 0 to 11, and the equation is applicable to one of the experimental inputs or to a new input within the range spanned by the experimental data set, and the uncertainty in a predicted value is given by the variance:

$$\text{Var. } (y(\text{input})) = (\text{Residual mean-square error}) + \sum (\text{S.D. of } a_i)^2 * f_i(\text{input})^2 \quad (6-28)$$

where S.D. means standard deviation.

The coefficients  $a_i$  are from the coefficients column in Table 6-28a, and the coefficients (*S.D. of  $a_i$* ) are from the standard error column in Table 6-28a. The residual mean-square error is found in the ANOVA (analysis of variance) sub-table in Table 6-28a, at the entry for residual row and MS column. This residual mean-square error is the square of the standard error found in the first sub-table of Table 6-28a.

Finally, the long-term dissolution rate of the spent fuel per unit surface area, in units of  $\text{mg/m}^2\text{-day}$ , is

$$U\_DissRate = 10^y \quad (6-29)$$

Where  $U\_DissRate$  has a lognormal distribution, since  $y$  has a normal distribution with the variance given in Equation (6-28).

Equation (6-27) depends on having terms  $f_i$  which have zero means and zero correlations. If this is not true, then Equation (6-27) becomes more complicated, although Equation (6-27) is unchanged in form. Hence, the mean values were subtracted explicitly before doing the regression analysis. The experimental data set is fairly well balanced; hence, the correlations between the terms are quite low. Thus, it was decided that it was not worth the extra computational effort to transform the parameters further to get the correlations to exactly zero. Therefore, Equation (6-27) is only approximately correct. But since the uncertainty is dominated

by the residual error (see calculation below), then the relative error introduced into the uncertainty value is small.

The results of the linear regression analysis for all data are given in Table 6-28a. The means to be used in Equation 6-27 and the coefficients  $a_i$  are labeled as means and coefficients, respectively. The standard deviations are labeled "Standard Error." The residual mean-square error of Equation 6-28 is given under column "MS," row "Residual." The t-statistic is labeled "t Stat;" the larger the absolute value, the more statistically significant is a non-zero value of the coefficient. In this respect, the coefficient of pH is not statistically significantly different from zero, but we retain the term because we have a quadratic term with pH.

The predicted versus measured values for the experimental data set are shown in Figure 6-24. The amount of scatter about a diagonal line shows the effect of the residual error. The model represents most of the input data within a factor of two and all of the input data within an order of magnitude. Given the relatively rapid dissolution of SNF compared to the time steps in TSPA-VA, uncertainties in this model have little impact on performance.

Predictions for several hypothetical traces through parts of the input range are evaluated, using the coefficients and an explicit calculation of the predictive Equation (6-27). The traces extend  $\pm 60$  percent beyond the measured data range. These predictions are done with two error evaluations, first including only the errors in the coefficients (the sum part on the right side of Equation [6-28]) and second including the residual error as well (thus the full Equation [6-28]). These calculations are shown in Figures 6-25 and 6-26. For points near the center of the data range, the residual error is considerably larger than the error due to the errors in the coefficients. Near and beyond the limits of the actual data range used in the regression, the error due to the coefficients grows larger, particularly the error associated with second-order terms.

The treatment of burnup as a multiplicative term in the Equation (6-27) and the shift of zero burnup to a 1 MW-day/kgU value to allow a logarithmic treatment are judgment calls taken in light of the present limited data. Hence it is interesting to examine the effect of this assumed burnup dependence in the results. Figure 6-27 shows the dissolution rate on a linear scale, with the other parameters at their average values for the measured data set, for three alternate values of the non-zero lower end of the burnup range. The rate of change of dissolution rate with burnup is rather small for the medium to higher burnups (i.e., for the spent fuels with most of the total inventory of radionuclides). In this burnup range, the amplitude of the dissolution rate changes slightly with the assumed lower-end value of the burnup data range (i.e., a small difference compared to the residual error [square root of the residual mean-square error]).

A second linear regression analysis was done using data for the "high-burnup" data set alone, i.e., the data with burnup of 30 MW-day/kgU and above. The same transformed input variables and higher-order terms were used as in the "all-data" regression analysis described above, except that the terms dependent on burnup were omitted. The results are given in Table 6-28b. The omission of a burnup variable means that the resulting predictive equation does not depend on burnup. The "all data" regression model is consistent with a low or nearly-zero variation with burnup in this range, as was illustrated in Figure 6-27.

For use in this TSPA-VA analysis, the "high-burnup" regression model was selected. The performance of spent fuel in the higher-burnup range has a greater impact on repository performance than does low-burnup spent fuel, because there is more of it. When weighted by radionuclide content, it is even more predominant. The "high-burnup" model is based on data within this range, and does not use the data at low burnups far from this range.

### **6.3.2 DOE-Owned Spent Nuclear Fuel, Navy Fuel, and Pu Disposition Wastes**

This section addresses the representation of DOE-owned spent fuel, Navy fuel, and waste from the disposition of excess weapon grade plutonium. Additional discussion and analyses are in Appendix A and Appendix B.

#### **6.3.2.1 DOE-Owned Spent Fuel**

As noted in Section 6.2.1.3, the DSNF Program has categorized the more than 250 types of spent fuel into 16 categories based on similar performance characteristics (see Table 6-5). The performance of the first 13 categories was analyzed in 1997 (CRWMS M&O 1997a). Category 14 (sodium-bonded spent fuel) will be treated and is not addressed here. Because the total inventory of DSNF is about 2,496 MTHM, the inventory was reduced by approximately 7 percent to obtain the 2,333 MTHM for the base case.

The 1997 analyses (CRWMS M&O 1997a) indicated that of the first 13 categories of DSNF only Categories 1, 4, 5, 6, 8, and 11 contributed significantly to dose, and that the dose from a composite of 13 categories was about 2 orders of magnitude below that of the commercial spent fuel in the repository (63,000 MTHM). This would be expected, because it was also shown that the dose from the composite of DSNF was nearly the same as that from an equivalent amount of commercial spent fuel on an MTHM basis.

Based on the 1997 analyses, the radionuclide inventory for a surrogate DSNF was developed for the base case using a weighted average (based on MTHM) of the radionuclide inventories of Categories 1, 4, 5, 6, 8, and 11. Category 15, Navy fuel, was evaluated separately using a WP release term provided by Bettis Atomic Power Laboratory (Beckett 1998). Category 16 is not expected to contribute significantly to the dose because of the small amount of miscellaneous spent fuel. The radionuclide inventory of the surrogate is similar to Category 1 spent fuel because of the large amount of fuel in that category (1979.88 MTHM composed largely of N Reactor spent fuel). Because most of the fuel in the surrogate is metallic (Categories 1 and 6, Table 6-5) that would be expected to leach at a faster rate, the metallic spent fuel dissolution model was assumed for the surrogate.

The surrogate DSNF is assumed to be packaged in 2,418 packages, which is the number of packages used for the six categories that define the surrogate (Categories 1, 4, 5, 6, 8, and 11). The assumption could have been made that the surrogate was packaged in fewer packages because of its similarity to Category 1. However, fewer packages may artificially lower the release of solubility limited radionuclides (i.e., neptunium) and would not be conservative.

Two conservative assumptions are built into the surrogate DSNF using the approach described. The first is using the metallic spent fuel dissolution model for the surrogate because of the faster

dissolution rate for the nonmetallic fuels in the surrogate. This conservatism was put into the base case because in certain scenarios the DSNF could significantly contribute to total dose from the repository. Even though prior analyses show that the dose from DOE fuel in the repository is 2 orders of magnitude below that of the commercial spent fuel, a significant contribution might occur at higher fluxes thorough the repository horizon if combined with advective release from the WP. The contribution of metallic spent fuel to total dose from the repository will be evaluated in the sensitivity analyses for TSPA-VA. The second conservatism is even distribution of the surrogate spent fuel over the large number of packages. In some of the categories that make up the surrogate there will be considerably more fuel in the packages than there would be if a surrogate had not been used. As these packages fail, the duration of release of solubility limited radionuclides will be longer and this could increase the neptunium dose. Before using the approach described above, results were obtained from the model used in the 1997 analyses (CRWMS M&O 1997a) to evaluate the amount of conservatism, and the results indicated that the assumptions made in the formulation of the surrogate are not overly conservative. More details of dose attributable to each category are in Appendix A of this chapter.

### 6.3.2.1.1 DOE-Spent Fuel Degradation Models

Dissolution models for metallic, carbide, ceramic, and oxide (commercial) spent fuel, and for HLW glass are presented below. The metallic and carbide models were taken from the analysis of DSNF done by Sandia National Laboratories (Rechard 1995), the models for commercial spent fuel and HLW were used in TSPA-1995 (CRWMS M&O 1995), and the ceramic model was used in the evaluation of plutonium waste forms (CRWMS M&O 1997a). All of these dissolution models were also used to assess the performance of INEEL spent fuels (INEEL 1997). Figure 6-28 compares the glass and spent fuel models described below. The analyses for this figure were done using the base-case model except no cladding is present on the spent fuel. This figure indicates that the largest dissolution rate over time is for metallic spent fuel and the slowest is for carbide spent fuel. The dissolution rates in order from fastest to slowest are metallic spent fuel under wet oxidic conditions, metallic spent fuel under humid oxidic conditions, oxide spent fuel, HLW glass, ceramic, and carbide spent fuel. The change in rate over time is caused by the buildup of corrosion products on the surface of the waste form, which slows the rate of dissolution. Initially there are about 7 orders of magnitude difference between the fastest and slowest waste form dissolution rate (i.e., metallic and carbide), and after 100,000 years there are about 5 orders of magnitude difference in dissolution rate between these models.

#### Metallic Spent Fuel

The model for metallic spent fuel (uranium metal and uranium metal alloy) used in this study was taken from the 1994 performance assessment of DSNF (Rechard 1995). The model is based on the equation that follows:

$$M = Ae^{-B/T} (t_2^C - t_1^C) D \cdot E \cdot SA \quad (6-30)$$

where

- $M$  = mass of layer corroded in a time step (kg)
- $A$  = Arrhenius-type pre-exponential term (kg/m<sup>2</sup>s)

- $B$  = Arrhenius-type activation energy term (K)
- $t_2$  and  $t_1$  = time at the beginning and end of the time step in seconds
- $C$  = time dependence term
- $D$  = saturation dependence term, which is 0, 1, or  $1 - e^{(-\alpha \cdot (Sat - TS))}$

where

- $\alpha$  =  $\ln(.01)/(S_{99} - TS)$
- $Sat$  = fracture water saturation
- $TS$  = threshold fracture saturation below which wet corrosion does not occur
- $S_{99}$  = fracture saturation where the wet corrosion rate is 99 percent of the corrosion rate at 100 percent saturation
- $E$  = oxygen concentration dependence term
- $SA$  = surface area of the layer (m<sup>2</sup>)

Wet oxid conditions are assumed when the temperature in the repository is below 100°C and humid oxid conditions are assumed at all other times. The parameter values used for metallic spent fuel analyses are:

- $A$  =  $9.4 \times 10^3$  kg/m<sup>2</sup>s for wet oxid conditions
- $A$  =  $1.35 \times 10^2$  kg/m<sup>2</sup>s for humid oxid conditions
- $B$  = 7970 K for wet oxid conditions
- $B$  = 7240 K for humid oxid conditions
- $C$  = 1 for wet and humid oxid conditions
- $D$  = 1 which is assumed to be conservative
- $E$  = 0.2, the oxygen concentration term has been approximated by  $x_{air}$  which is the mass fraction of air within the gas phase

### Carbide Spent Fuel

The model for carbide spent fuel used in this study was taken from the 1994 performance assessment of DSNF (Rechard 1995). The 1994 assessment used a model based on the equation that follows:

$$M = A e^{-B/T} (t_2^C - t_1^C) D \cdot E \cdot M_{layer} \quad (6-31)$$

For silicon carbide coatings:

- $A$  =  $3 \times 10^{-12}$  /s
- $B$  = 0 K
- $C$  = 1

- $D$  = 1 which is assumed to be a conservative assumption  
 $E$  = 0.2  
 $M_{layer}$  = the mass of the layer at time zero

The equation above can be used to calculate the mass corroded at any time step. To obtain the dissolution rate, the mass of the layer at time zero and the surface area must be known. For carbide spent fuel, the surface area of the silicon carbide is assumed to be 1,325 m<sup>2</sup> and the mass of the layer is assumed to be  $M_{layer} = 126$  kg. The surface area is not used to evaluate the mass release, but was used to estimate the initial mass of the coatings. This model describes the dissolution of the silicon carbide coatings on the fuel particles, and does not represent the fuel itself. Once the coating has failed, the fuel reacts rapidly with water, releasing the inventory of the fuel particle. Thus, the model only applies to Category 8 SNF, which has silicon carbide coating.

**Ceramic Spent Fuel**—The dissolution model for ceramic was extracted from Lappa (1995). The composition of the ceramic is assumed by Lappa (1995) to be similar to that of Synroc-C, a titanate ceramic. Reeve et al. (1989) propose the cumulative release from Synroc to be:

$$Q = Q_0 + \theta + SFt/A \quad (6-32)$$

where

- $Q$  = the release per unit surface area (g/m<sup>2</sup>)  
 $Q_0$  = the instantaneous release from grain boundaries and metastable phases (g/m<sup>2</sup>)  
 $\theta$  = a complex kinetic function that accounts for ionic diffusion, selective matrix attack, etc (g/m<sup>2</sup>)  
 $S$  = the solubility of matrix (g/m<sup>3</sup>)  
 $F$  = the groundwater flow rate (m<sup>3</sup>/day)  
 $A$  = the surface area (m<sup>2</sup>)  
 $t$  = time (days)

Lappa (1995) states that it is likely that the long-term release from the Synroc is controlled by the third term in the cumulative release equation. Existing data indicate that  $S$  is less than or equal to 0.007 g/m<sup>3</sup> based on a long-term leaching rate of less than or equal to 10<sup>-4</sup> g/m<sup>2</sup>/day when SA/V is 10 m<sup>-1</sup> at 70°C in deionized water (Lappa 1995). The leaching rate also increases with increasing temperature (Ringwood et al. 1988). This temperature effect is described by:

$$R = \alpha 10^{-\beta (1000/T)} \quad (6-33)$$

where

- R = the leaching rate (g/m<sup>2</sup> day)
- T = temperature (degrees K)
- $\alpha, \beta$  = are constants

Based on the Synroc data in Ringwood et al. (1988),  $\beta \approx 1.0$  K and  $\alpha \approx 0.082$  g/m<sup>2</sup>/day if the long-term leaching rate is assumed to be  $10^{-4}$  g/m<sup>2</sup>/day at 70°C. These are the same conditions as assumed in TSPA-1995 for the HLW glass. The release rate can be calculated by multiplying R by the surface area (S) and the elapsed time (t). The radionuclides are released from the waste based on its alteration rate, and are then transported at a rate dependent on whether they are alteration-controlled or solubility-limited radionuclides.

The alteration/dissolution rate used for ceramic is for a monolithic form, and when cracked along grain boundaries may be substantially different and should be measured in the ongoing research and development program to provide a more realistic rate for the repository environment. However, the ceramic model is only used for Category 12 spent fuel that is less than 2 percent of the total amount of DOE SNF on an MTHM basis. Because of this, the Category 12 spent fuel could be easily bounded using the metallic or oxide models.

**High-Level Waste Glass**—The high-level waste glass dissolution model is the same as that described in Section 6.3.3 for DHLW glass dissolution.

**Oxide Spent Fuel**—The oxide spent fuel dissolution model is the same as that described in Section 6.3.1 for CSNF dissolution.

#### 6.3.2.1.2 DOE-Spent Nuclear Fuel Physical Properties

Fuel properties were determined by the judgment of those personnel most familiar with the fuel inventory, and a consensus on the values was gained by review among the local spent fuel programs at the DOE sites (Cresap 1997). The grouping of fuel into categories, based on chemical fuel form, aided in assigning common properties to each category. The physical properties used in the PA were supplied by the National Spent Nuclear Fuel Program (Stroup 1998), and are presented in Table 6-29 for each category of DOE spent fuel.

Table 6-29 provides estimates of fuel dissolution rate, surface area, cladding failure, free radionuclide inventory, radionuclide inventory in the gap between the fuel and cladding, fuel area, and fuel volume. The fuel area and volume are the current fuel matrix surface area in a plane perpendicular to the groundwater flux and the current total fuel matrix volume, respectively. Because the physical properties for the categories of DSNF are uncertain, the effects of a range of physical properties on performance was examined (Appendix A).

### **6.3.2.2 Navy Fuel**

Navy fuel was considered separately. A source term defined at the edge of the WP was provided by Bettis Atomic Power Laboratory (Beckett 1998). This source term was provided in the form of a look-up table of mass release rate from a WP for each radionuclide as a function of time. Comparative dose contributions from Navy fuel may be seen in Appendix A.

### **6.3.2.3 Pu Disposition Wastes**

Two waste forms were considered to represent the disposition of excess weapons grade Pu, in keeping with the current dual path approach to this issue. MOX is assumed to have the same physical characteristics as commercial spent fuel. The same degradation models were used for MOX fuel as for CSNF (see Section 6.3.1). Direct disposition of Pu was represented by the can-in-canister approach, where a Pu-bearing ceramic form is placed in small canisters and placed into the DHLW glass pour canister before filling them with DHLW glass. The models used for this form are the same as for ceramic DOE fuel (see Section 6.3.2.1.1 above) and DHLW glass (see Section 6.3.2). Further discussion of these waste forms and their radionuclide inventories can be found in Appendices A and B of this chapter.

## **6.3.3 Defense High-Level Waste Glass**

This section addresses the aqueous forward dissolution rate of the DHLW glass waste form. Section 6.4 addresses solubility limits and precipitates, and the net dissolution rate and release rates under limited-flow or zero-flow conditions. In principle the scope of the present section includes the glass pour container and vapor-phase alteration of the glass surface. But these processes are not used in the model. Thus the aqueous alteration rate is the only process relied on in the present model to provide a limited rate of exposure of the radionuclides in the glass matrix to water, after the WP is breached.

### **6.3.3.1 Canister**

No credit is taken in the present model for a period of containment by the stainless steel pour canister, as the potential for nucleation of sites for long-term low temperature sensitization of the austenitic structure exists due to the thermal cycle during glass pouring.

### **6.3.3.2 Defense High-Level Waste Glass Alteration Conceptual Model**

The model assumes aqueous conditions on the surface of DHLW glass once the WP has breached. This is because 1) aqueous conditions were needed on the WP to sustain corrosion processes, and 2) relative humidity is high in the drift at times following WP failure and will result in adsorbed water films on the hygroscopic glass alteration products. The model defers to future consideration the rare cases of vapor phase exposure at temperatures above the boiling point, which would occur only when a WP experiences a juvenile failure.

Experimental and modeling work on aqueous alteration of borosilicate glass shows that the most important parameters that need to be considered in order to predict glass alteration rates are temperature, exposed surface area, solution pH, and dissolved silica concentration in solution

(Bourcier 1994; O'Connell et al. 1997). Long-term dissolution models for borosilicate glass employ a rate equation which includes these parameters and which is consistent with transition state theory (see below). The rate equation indicates that the dissolution rate will slow down under low-flow conditions as the dissolution process of the borosilicate glass adds to the silica (SiO<sub>2</sub>) in solution. As the glass dissolves, secondary phases begin to precipitate. A fraction of the silica contained in the glass will be trapped in the secondary phases. Thus only some fraction of silica in altered glass actually dissolves in the solution. That fraction depends on the types and amounts of alteration minerals that form during the glass alteration process.

The experimental data for several glass compositions show that even when the solution is saturated with silica after a long period of time, a residual dissolution rate persists, evidenced by the continuously increasing concentrations of certain highly soluble elements of the glass composition (Grambow 1987). Therefore an additional parameter must be included in the rate equation ( $k_{long}$ ) that accounts for this residual reaction rate under silica saturated conditions.

This formulation for glass dissolution differs from the one implemented in previous TSPA models in three significant ways: (1) This model uses a more accurate regression equation to provide the rate constant for glass dissolution as a function of temperature and pH (i.e., a maximum over two linear equations rather than one quadratic equation), (2) this model has an additional long-term rate coefficient in the rate equation which provides for residual reaction rates under silica-saturated conditions, and (3) this model uses a revised glass surface area estimate based on analysis of fracture densities of Defense Waste Processing Facility (DWPF) pour canisters.

The model developed for TSPA-VA is similar to those used previously, but updated with current experimental data. The DHLW dissolution rate (g/day) is:

$$R = s \left[ k \left( 1 - \frac{Q}{K} \right) + k_{long} \right] \quad (6-34)$$

where  $s$  is the effective surface area of the glass in m<sup>2</sup>,  $k$  is a rate coefficient (g/m<sup>2</sup>-day) that is dependent on temperature and pH,  $Q/K$  is an affinity term consisting of the silica concentration in the aqueous phase divided by the solubility of silica in the aqueous phase and  $k_{long}$  is the long-term rate at constant temperature. The values of  $k$  and  $k_{long}$  are determined from experimental data.

Glass reaction (Figure 6-29) initiates with water diffusion into the glass and with alkali ion exchange. Evidence for water diffusion comes from secondary ion mass spectroscopy and ion probe profiling of reacted glasses which show diffusion profiles for water in a surface zone generally less than 1 micron thick (Abrajano and Bates 1987; Oversby and Phinney 1992). Ion exchange is indicated by the early rapid release of alkalis relative to other glass components, which is commonly observed in glass dissolution tests. Hydration and ion exchange form two layers on the glass surface (see Figure 6-29): an inner diffusion layer where concentration gradients for alkalis and water are observed, and an outer hydrated gel layer where network hydrolysis (breakage of Si-O-Si bonds) takes place. The gel layer is depleted in alkalis and boron and enriched in insoluble elements such as Al, Ca, Sr, and heavy metals such as actinides.

With time, some elements released into solution reprecipitate on the hydrated glass surface and elsewhere as a variety of secondary phases. These phases are commonly clays, zeolites, and metal oxides and hydroxides. The reaction of glass to form secondary phases is driven by the thermodynamically unstable nature of glasses. Water allows glass to react and transform into a set of crystalline phases, which are thermodynamically more stable. Under anhydrous conditions, geologic evidence shows that even glass compositions that are relatively nondurable in water are stable for millions of years.

Steady-state conditions are commonly observed during glass dissolution where the rates of water diffusion and ion exchange are equal to the rate at which the glass network dissolves. Steady-state conditions are evidenced by the tendency for the glass diffusion layer to remain constant in thickness while the glass dissolves away and the mass of secondary phases increases with time (Abrajano et al. 1986). In open system experiments, the rate of release of most elements is approximately constant or slowly decreases with time. In closed system experiments, the release rates slow down more rapidly with time due to saturation effects, the buildup of dissolved glass species in solution (Figure 6-30). Increased silica concentrations are the primary reason for decreased dissolution rates (Chick and Pederson 1984) although other elements have an effect as well (Stout and Leider 1997, Section 3.5.2). Elemental releases from glasses in closed system tests also show non-stoichiometric behavior, some elements are released much more rapidly than others (Figure 6-30). Most of this non-stoichiometry is due to the precipitation of the less soluble glass components as secondary mineral phases, although a small amount is accounted for in the formation of leached layers.

Nuclear magnetic spectroscopy (NMR) shows that network dissolution reactions taking place in the gel layer are complex. <sup>17</sup>O-doped experiments show that both breakage and re-formation of Si-O-Si linkages are taking place (Bunker et al. 1988). Hydrolysis of the highly stressed glass structure allows relaxation and removal of incompatible elements. The original glass is transformed into a hydrous silica-rich phase plus local areas enriched in transition and other heavy metals such as actinides which eventually crystallize into a variety of solid phases, or are released into solution as dissolved species or colloids. In some flow-through glass dissolution tests, the gel layer appears to serve as a transport barrier that limits the overall dissolution rate (Grambow 1987). However, in most closed-system experiments, elemental release data and electron microscopic examination of the surface layers show that the overall reaction rate is not controlled by diffusion of elements through the alteration layers (Chick and Pederson 1984; Murakami et al. 1988; Abrajano et al. 1990).

The types and amounts of secondary phases are important because most of the radionuclides initially in the glass will be transferred into these mineral phases. This is especially true of the insoluble actinides, and to a lesser extent for some of the fission products. The glass alteration model described here provides the rate at which these radionuclides in glass are available for release. However, actual release rates will be substantially smaller than the value provided by the glass alteration model because of the partitioning of the radionuclides into alteration minerals and alteration layers. The alteration minerals which form during the glass reaction will depend on the composition of the incoming fluid, which in turn depends on previous reactions with other repository materials. Although alteration tests of glass provide qualitative information on types of alteration phases that form, their compositions and the partitioning of radionuclides into them

will also depend on other repository-fluid interactions and so cannot be predicted from the glass alteration model alone.

Rates of glass dissolution may also be strongly affected by certain dissolved elements. For example, dissolution rates of silicate glasses strongly decrease in the presence of dissolved Mg, Pb, and Zn, and are strongly enhanced, under some conditions, by dissolved Fe (McVay and Buckwalter 1983; Barkatt et al. 1989; Bourcier et al. 1992). Likewise, anions such as phosphate and sulfide are known to affect mineral dissolution rates and may affect glass dissolution rates. Depending on the specific metal, these effects may be attributed to several processes: the formation of surface complexes, the precipitation of a surface layer providing a transport barrier, or the reaction of dissolved glass species with the dissolved metals, causing the precipitation of colloids or secondary phases that affect the glass dissolution affinity (McVay and Buckwalter 1983). These types of effects are potentially important in repository environments where a variety of dissolved species derived from other repository materials will be present.

In summary, a thorough model for borosilicate glass dissolution must account for the following processes: (1) kinetically-controlled network dissolution, (2) precipitation of secondary phases, (3) ion exchange of selected elements, (4) in some cases, rate-limiting diffusive transport through a hydrous surface reaction layer, and (5) specific glass surface interactions with dissolved cations and anions. This set of coupled processes should be able to quantitatively predict observations of glass dissolution which include the saturation effect (glass dissolution rate slows down as dissolved glass species build up in solution), the increase in pH which accompanies glass dissolution in closed-system tests, the variability of glass dissolution rate as a function of glass composition, and rate-affecting interactions of the glass surface with dissolved cations and anions.

### **6.3.3.3 Defense High-Level Waste Glass Model Abstraction**

The model for PA of the glass forward alteration rate concentrates on the steady rate observed in experiments after the initial higher rate has decreased to a steady rate. As discussed above, this rate is understood to be a condition where the glass diffusion layer remains constant in thickness while the glass dissolves away, as water and ions diffuse through this layer. The model fits the steady-state data with an equation of the form of Equation (6-33). This form is consistent with transition state theory discussed below.

This model is an evolution of earlier models as is consistent with ongoing testing and initial production and analysis of DHLW glass. The glass dissolution test data given below were for a simplified preliminary glass composition (SRL-165). However, more recent data show a similar rate and a similar rate dependence on pH and temperature for the current SRL-202 formulation. Currently, the SRL-165 data set is the most complete and was therefore used in the regression. Available data for the SRL-202 glass will replace the SRL-165 data in TSPA-LA.

The entire phenomenology of the glass alteration process described above in Section 6.3.3.2 cannot be incorporated directly into a PA model, because it would necessitate tracking too many system variables and also because several of the relationships between glass reaction rate and solution chemistry cannot yet be quantified with available experimental data. It is therefore important to prioritize the processes described above in order to generate a simplified glass

model amenable for incorporation into PA calculations. Of those parameters mentioned above, those most important for controlling the rate of glass reaction are temperature, fluid pH, fluid silica concentration, and reactive glass surface area. The current analysis ignores the effects of adsorbed species such as iron and magnesium and any potential armoring effect of surface layers, either as a transport barrier or as a means to generate altered local chemical environments at the glass-solution interface. Work continues on quantifying the effects of dissolved species such as iron and magnesium. Iron species may be present in abundance because of the iron oxide products from the outer container and the slow corrosion of the inner container of the waste package. These effects can be added to the glass model later. The potential impact of iron ions is not expected to be large, because even with the conservative assumption of all glass surface exposed to aqueous dissolution upon WP failure, EBS release is not strongly sensitive to the glass dissolution model.

We use a rate equation for glass reaction consistent with transition state theory. The rate law is given by (Aagaard and Helgeson 1982; Lasaga 1984):

$$\frac{dn_i}{dt} = A v_i k \prod_j a_j^{-n} \left( 1 - e^{-\left(\frac{A}{\sigma R T}\right)} \right) \quad (6-35)$$

where  $n_i$  is the number of moles of species  $i$  in solution released from the glass,  $t$  is time,  $A$  is the reactive surface area of glass,  $v_i$  is the concentration of species  $i$  in the glass,  $k$  is the rate coefficient for the glass,  $\prod_j a_j^{-n}$  is the product of the activities (concentrations) of dissolved

aqueous species which make up the activated complex of the rate-limiting microscopic dissolution reaction,  $A$  is the reaction affinity defined as  $RT \ln(Q/K)$  where  $Q$  is the activity product and  $K$  the equilibrium constant for the rate-determining glass dissolution reaction,  $\sigma$  is a stoichiometric factor that relates the rate-controlling microscopic reaction to the overall solid dissolution reaction (usually it is assumed  $\sigma = 1$ ),  $R$  is the gas constant, and  $T$  is the temperature in Kelvin. The form of (Equation 6-35) predicts that the dissolution rates of solids have the following characteristics: (1) the amount of solid dissolved is proportional to exposed surface area, (2) the dissolution rate slows down as the liquid approaches saturation, and (3) the dissolution rate is constant under conditions far from saturation ( $Q/K \ll 1$ ).

The rate law is further simplified to include only the four effects mentioned above ( $T$ ,  $pH$ ,  $SiO_2$  and surface area) which is then given as:

$$\frac{dn_i}{dt} = A v_i k(pH) \left( 1 - \left(\frac{Q}{K}\right) \right) \quad (6-36)$$

where the product term  $\prod_j a_j^{-n}$  is reduced to include only the  $pH$  dependence of the rate coefficient, and the affinity expression is simplified and re-expressed in terms of the saturation index ( $Q/K$ ) of the dissolving solid. In this application,  $Q$  is the activity (concentration) of dissolved silica and  $K$  is a fitting parameter with a value equal to the silica saturation level for a

particular glass composition.  $K$  is obtained from experimental data. This form of rate law is commonly used as an expression to which experimental elemental release data are fitted, i.e., values of  $k$  and  $K$  are determined by regression of experimental data. The assumption is that  $\sigma = 1$ . Sufficient experimental data currently do not exist to allow better estimates of this parameter (Bourcier et al. 1994).

**Final Recommended Model for TSPA**—The simplified rate equation to be used in TSPA-VA, now expressed in mass units of grams, and which now includes an additional long-term rate parameter  $k_{long}$  (see below), is given by:

$$R = s \left[ k \left( 1 - \frac{Q}{K} \right) + k_{long} \right] \quad (6-37)$$

where

$R$  = alteration rate of glass (g/yr)

$s$  = surface area ( $m^2$ )

$k$  = glass surface alteration rate constant ( $g/m^2/yr$ ), a function of temperature and pH of the solution

$Q$  = concentration of dissolved silica ( $g/m^3$  water)

$K$  = a quasi-thermodynamic parameter for glass equal to the silica saturation value for the glass ( $g/m^3$  water)

$k_{long}$  = long-term dissolution rate determined from test data

**Model Parameters**—The rate constant,  $k$ , has been measured over a range of pH and temperature conditions. Table 6-30 shows the results of  $k$  in units of  $g/m^2/day$  from flow-through experiments by Knauss et al. (1990). These data are plotted in Figure 6-31. These data are for a simplified preliminary glass composition (SRL-165). However, more recent data show a similar rate and a similar rate dependence on pH and temperature for the current SRL-202 formulation. Currently, the SRL-165 data set is the most complete and was therefore used in the regression. Available data for the SRL-202 glass will be used to replace the SRL-165 data in TSPA-LA.

A regression analysis of the data from Table 6-30 yields the following relations for  $k$  in units of  $gm/m^2/year$ :

$$k = 365 \times 10^m \quad (6-38)$$

$$m = \max(m_a, m_b)$$

$$m_a = (-1.5775 + 0.1681N_{a0}) + (-0.6381 + 0.0265N_{a1})(pH - 3.19) \quad (6-39)$$

$$+ (-2991.7706 + 225.8962N_{a2})(1/(T+273.15) - 0.003109)$$

$$m_b = (-2.4138 + 0.1059N_{b0}) + (0.4721 + 0.0141N_{b1})(pH - 9) \quad (6-40)$$

$$+ (-4502.9765 + 142.1147N_{b2})(1/(T+273.15) - 0.003109)$$

where  $T$  is solution temperature ( $^{\circ}\text{C}$ ),  $pH$  is the pH of the water, and  $N_{a0}$ ,  $N_{a1}$ ,  $N_{a2}$ ,  $N_{b0}$ ,  $N_{b1}$ , and  $N_{b2}$  represent uncertainty, as sampled from a standard normal distribution  $N(0,1)$ .

The error in the constant term includes the residual error.

The major effect of groundwater chemistry on the glass dissolution rate, other than pH, is through the concentration of dissolved silica. For the TSPA-VA model,  $Q$  equals the concentration of dissolved silica in the water contacting the glass. The local groundwater chemistry in the vicinity of the repository will likely be dominated by the host rocks and the silica concentration is therefore expected to be close to cristobalite saturation at the ambient temperature. Cristobalite is a common constituent of the host rocks at Yucca Mountain. Table 6-31 lists concentrations of silica in equilibrium with cristobalite at temperatures from  $0^{\circ}\text{C}$  to  $150^{\circ}\text{C}$  (Johnson et al. 1992).

$K$  in Equation (6-36), the silica saturation value for the waste glass, is assumed equal to the equilibrium constant for amorphous silica.  $K$  actually varies as a function of glass composition and experimental conditions, but for most waste glass compositions, the experimentally determined value of  $K$  is of the same general magnitude but slightly less than the value of  $K$  for amorphous silica. Our simplification therefore gives conservative estimates. This assumption involving amorphous silica is made because there is currently no mechanistic quantitative understanding of how  $K$  varies with glass composition and experimental test conditions. Table 6-31 lists values of  $\log_{10}K$  (in molality) for temperatures from 0 to  $150^{\circ}\text{C}$ .

The ratio of  $Q$  and  $K$  for temperatures between  $0^{\circ}\text{C}$  and  $100^{\circ}\text{C}$  is given by the equation:

$$Q/K = (0.272749 + 0.0107N_{i0}) + (0.001958 + 0.000082N_{i1})(T - 70.83) \quad (6-41)$$

where  $N_{i0}$  and  $N_{i1}$  represent uncertainty as sampled from the standard normal distribution  $N(0,1)$ .

It has been observed experimentally that even when the solution is saturated with silica after a long time, dissolution rate is still non-zero. Considering the current lack of a mechanistic model that can predict the variation of the long-term rates with environmental parameters, an averaged value of  $k_{long} = 0.002$  g glass/ $\text{m}^2/\text{day}$  is recommended for SRL-202 glass. This value was obtained from glass corrosion tests at  $90^{\circ}\text{C}$  (an averaged value for data shown in Table 2-5 of Cunnane et al. 1994). For other temperatures, the same temperature dependency is assumed for  $k_{long}$  as that measured for  $k$  (the forward rate constant). That is:

$$k_{long} \approx 365 \times 10^d \text{ g/m}^2/\text{yr} \quad (6-42)$$

$$d = (-4.31 + 0.15N_{g0}) + (-4502.9765 + 142.1147N_{b2})(1/(T+273.15) - 0.003109) \quad (6-43)$$

for basic conditions (pH > 7); see Figure 6-31. The error in the constant term is primarily the error in estimating the long-term rate at 90°C from the tests.  $N_{g0}$  represents uncertainty, sampled from the standard normal distribution.

In applying equation 6-36, for conditions where  $Q > K$ , the term  $(1-Q/K)$  should be set equal to zero. The glass reaction rate is then simply  $R = s k_{long}$ .

The reactive surface area of glass in a DWPF pour canister is increased above its simple geometric value through two processes (Wicks 1985). The first is thermal fracturing. As the waste glass cools after pouring, thermal gradients induce stresses which cause the glass to crack. Figure 6-32 shows the relative increase in actual surface area over the geometric surface area as a function of cooling rate. The faster the glass cools, the higher the surface area due to cracking. For typical cooling rates for the DWPF, the factor is around 10 to 15 (Smith and Baxter 1981; Baxter 1983). The glass area increases a minor amount due to production of fines generated during thermal cracking. These fines do not appear to contribute significantly to total surface area, and based on leaching studies of cracked glasses (Perez and Westsik 1980), and measurements of fines generated (Ross and Mendel 1979), these fines can be ignored.

The second process which may potentially increase glass surface area is impact cracking. If the glass canister is dropped or has a collision, the glass will crack (Smith and Ross 1975). Data are available which show the increase in surface as a function of collision velocity. For example, at an impact velocity of 117 feet per second (80 mph), the glass surface area is increased by a factor of about 40.

For both types of cracking, the actual increase in glass reaction rate is actually less than proportional to the increase in surface area (Perez and Westsik 1980). Presumably this is due to a combination of restricted water mobility through tight cracks, solution saturation effects, and swelling due to precipitation of hydrous alteration phases. Generally, a factor of 10 increase in surface area gives only a factor of 3 to 5 times faster reaction rate in a static leach test (Wicks 1985). Based on these data, a conservative surface area value of roughly 21 times geometric area for typical DWPF glass is recommended. To obtain this value, assume 1 percent of all canisters suffer severe damage during transit so that their surface areas are increased a factor of 40 times above the normal value of air-cooled glass. For 100 canisters, the one damaged canister has a surface area of  $40 \times 15 = 600$  times geometric and the other 99 have a surface area of 15 times geometric. The total surface area is

$$40 \times 15 \times 1(\text{damaged}) + 15 \times 99(\text{undamaged}) = 2085/100 = 20.85 \text{ times}$$

We do not take credit for the lack of scaling between observed increase in surface area and a lesser increase in glass reaction rate.

A typical filled canister of SRL-202 glass has about 1,680 kg of glass with a density of 2.7 g/cm<sup>3</sup>. The volume of the glass log is therefore  $1,680,000/2.7 = 622,000 \text{ cm}^3$ . The inside diameter of the canister is about 60 cm. Therefore the glass cylinder has a height of:

$$\pi r^2 \times \text{height} = \text{volume} \tag{6-44}$$

$$\text{height} = 622,000 \text{ cm}^3 / \pi 900 \text{ cm}^2 = 220 \text{ cm} \tag{6-45}$$

with total surface area:

$$2 \pi r^2 + 2 \pi r \times \text{length} = 5,655 + 41,469 = 47,124 \text{ cm}^2 = 4.7 \text{ m}^2$$

Therefore an average DWPF canister has a glass surface area of  $21 \times 4.7 = 99 \text{ m}^2$

**Model Limitations**—This simple glass alteration rate model ignores all solution chemistry other than pH and silica concentration. It is known from a variety of experiments that species such as dissolved Mg and Fe can change glass dissolution rates by up to a few orders of magnitude. We do not account for effects such as these in this model. We also do not consider the effects of vapor phase alteration of the glass. If a canister containing glass is breached and humid air reaches the glass, the glass will react and form an alteration rind composed of hydrated glass and secondary phases. The durability of this material with respect to later contact with liquid water differs from that of the unaltered glass. Quantitative information needed to incorporate this phenomenon into the model is not currently available, although experiments are in progress to address this issue.

This model of the forward dissolution rate is only one step in the net release rate. As with SNF, the dissolution rate model provides an upper bound on the rate at which radionuclides become potentially available for mobilization. For most radionuclides, this bound is conservative due to the expected and observed formation of secondary phases, which retain a significant fraction of the radionuclides. Diffusion of radionuclide out of the glass matrix to the surface and preferential dissolution of these radionuclides is not addressed at this time. Similar to SNF, many radionuclides are limited by aqueous solubility to mobilization rates below the dissolution bounded availability rate. Significant colloid formation is expected from the glass waste form. Solubility, colloids, and net release rate are discussed in Section 6.4. Sensitivity results in Section 6.6.1.2 show only minor sensitivity of release rates to variation in the DHLW dissolution rate model.

## 6.4 RADIONUCLIDE MOBILIZATION

Degradation of the waste form, as discussed in the previous section, frees radionuclides from the waste form matrix and makes them potentially available for transport. Not all of these radionuclides are immediately mobile, however. In this section, the processes and limitations on radionuclide mobilization will be addressed. Three processes that may control mobilization are: (1) radionuclide solubility limits, (2) colloid (or other mobile particulate) formation, and (3) retention of radionuclides in secondary phases and are the subject of the subsections that follow.

In TSPA-VA, aqueous conditions are assumed on the surface of the waste form after failure of the WP and cladding/canister. This is due to the high relative humidity throughout nearly all of the near-field environmental scenarios and the expected formation of microporous alteration layers on the waste form surfaces. Under these aqueous conditions, highly soluble radionuclides are assumed to be mobilized at the rate they become available from the waste form dissolution model. Less soluble radionuclides are assumed to be mobilized at their elemental solubility limit. An exception to this is the potential for colloidal mobilization, which could exceed the solubility limit, and is applied in a preliminary model for Pu only. The potential for retention of

significant radionuclide inventory in secondary phases that form on the waste surface is also represented in a preliminary way in sensitivity studies, but not in the TSPA-VA base case.

This analysis does not include gaseous mobilization of radionuclides. Previous studies have considered gaseous releases (Wilson et al. 1994). An abstracted approach to considering gas phase release for  $^{14}\text{C}$  is to allow gas transport into the host rock where ion exchange returns the  $^{14}\text{C}$  to aqueous phases prior to significant transport. The mobilization and near-field transport abstractions in this TSPA-VA, where mobile radionuclides are assumed to be in rapid diffusive communication with available advective flow paths gives analogous results for  $^{14}\text{C}$  in either aqueous or gaseous near-field pathways.

#### **6.4.1 Radionuclide Solubility**

The primary controlling process for many radionuclides is their elemental solubility in waste flowing through the repository. Because of uncertainties in the chemistry, temperature, and controlling phases, these solubilities are represented by distribution functions. This section will address the development of the solubility distribution functions used in this analysis.

##### **6.4.1.1 Goal**

The term solubility refers to the equilibrium concentration of a solid phase that is dissolved in a solvent phase at a fixed set of system conditions (e.g., chemical compositions of solid and solvent, temperature, and pressure). The purpose in determining radionuclide solubilities is to define the upper bounds of the radionuclide concentrations that can exist in dissolved form in the flowing groundwater within a nuclear waste repository under a given set of system conditions. Thus, when the fluid flow rate and radionuclide solubilities are known, the maximum rate of release of radionuclide mass to the flowing groundwater in the form of dissolved solutes can be directly calculated. The relation between solubility of a solute phase and its constituent elemental concentrations in the saturated solution is given by the stoichiometry of the solute phase. At the solubility limit, the solution concentration of any particular solute element is dependent upon the solvent composition, including pH, the initial concentration(s) of any other solute constituent(s), and complexing agents. The elemental solubility refers to the solution concentration of an element controlled by the equilibrium solubility of a saturated phase containing that element.

##### **6.4.1.2 Conceptual Model: Solubility-Limited Aqueous Radionuclide Concentrations**

Calculated bounds on the aqueous concentration of radionuclides in groundwater that has reacted with the waste form are derived initially from the waste form dissolution model. Subsequently, another filter is applied which compares the dissolution-based aqueous radionuclide concentration with a solubility-limited value that is sampled from either a distribution of solubility limits for radionuclide-bearing minerals, or a functional form for the solubility limit for each radionuclide considered. If the sampled solubility-limited value is lower for a given radionuclide than its concentration derived from the waste form dissolution, then the aqueous concentration is set to the solubility-limited value and the difference in mass is calculated to precipitate out of solution. These solubility-limited values place constraints on the aqueous

concentration of the particular radionuclide *element* considered, with each isotope of that element present in proportion to its isotopic abundance.

This analysis does not include solubility limits with all their functional dependencies explicitly represented. These dependencies include temperature (and, to a lesser extent, pressure) and compositional parameters of both the concentration-limiting solid phase and the aqueous solution (e.g., pH, oxygen fugacity, concentrations of other metals and ligands). In TSPA-1995 (CRWMS M&O 1995), experimental studies of the steady-state concentration limits for some of the radionuclides (Np, Pu, and Am) in J-13-like water compositions (Nitsche et al. 1993) were used to derive empirical relations describing the temperature and pH dependence for their aqueous concentrations. As discussed below, the apparent metastable nature of the Np phases formed in that study result in a conceptual inconsistency in the TSPA model if the solubility-limited distribution for Np based on those results is applied. Because of this, the Np distribution has been revised as described below and the functional form derived for Np in TSPA-1995 is no longer considered. These results derived for Am and Pu may still be used to evaluate the release of these radionuclides with explicit dependence on both pH and temperature. These relations may be used to evaluate how sensitive results are to various cases using samples over the distributions. The base-case distributions and functional forms for Am and Pu radionuclide solubility limits are discussed below in detail.

There may be periods of time in the system when fluid compositions reacting with the waste forms are different enough from J-13-like fluids that radionuclide solubility limits may be controlled very differently than for the J-13 fluid composition. Delineating such potential fluid composition scenarios is part of the Near-Field Geochemical Environment (NFGE) effort in PA as discussed in Chapter 4. The NFGE includes changes to gas, water, and solid compositions in the potential emplacement drifts resulting from thermal perturbations, reactions with introduced materials (including the waste forms), and potential microbial activity. Ongoing work for waste form degradation is addressing the derivation of solubility-limited concentration distributions that are dependent on specific fluid composition scenarios, and the stable radionuclide-bearing phase(s) for those compositions, for a number of radionuclides. Part of this work is to review the current distributions given below for the J-13-like case, and to synthesize these distributions with the conceptual models developed for PA of radionuclide dissolution, mobilization, and release from waste forms. The current state of this work is discussed below in subsection "Strategies for Additional Distributions and Concentration Constraints," but is not yet complete enough to include in base-case calculations.

#### 6.4.1.3 Input Data and Assumptions

**Base-Case Distributions**—The concentration of aqueous radionuclides in groundwater reacting with spent fuel or glass waste has a complex dependence on the composition and phase assemblage of the solid waste material, the composition of the aqueous phase (e.g., pH, dissolved carbonate, oxygen fugacity), and the conditions at which the reaction occurs (e.g., temperature, pressure). For many of the radionuclides considered in this analysis, explicit representation of these dependencies is not currently possible in a comprehensive manner. In addition, constraints on the system conditions which would affect aqueous radionuclide concentrations are not currently fully defined/quantified. The description of the NFGE is becoming more detailed and

definition of scenarios of water compositions should facilitate strategies for encompassing some of the large-scale variability in system conditions within the various conceptual models directly.

To account for some of these uncertainties, the ranges of possible radionuclide concentrations that would be controlled by radionuclide-bearing mineral equilibration with groundwater (solubility-limited concentrations) are generally represented as probability distributions. By randomly sampling these distributions of solubility-limited aqueous radionuclide concentrations in each realization, PA can *implicitly* encompass a range of possible system conditions and assess the potential consequences. This can be done whether the distribution is a result of actual system variability or uncertainty in what the actual system will be. If much of the system variability and/or conceptual uncertainty can be encompassed with various conceptual models, then the distribution applicable to any one of those models should be more tightly constrained than a single distribution that also tries to include all the conceptual possibilities and uncertainties.

Distributions of solubility-limited concentrations for the radionuclides of Ac, Am, Cm, Cs, Nb, Ni, Np, Pa, Pb, Pd, Pu, Ra, Se, Sm, Sn, Tc, Th, U, and Zr are in Table 6-32 and discussed below in this section. Many of these distributions result from an elicitation of project experts for values applicable to ambient system fluids with some variability considered, whereas some others are taken from a number of sources that generated very broad distributions to represent very uncertain conditions. Table 6-32 lists the radionuclide, the type of distribution used, the variable of the distribution as either concentration or log(concentration), the parameters for the distribution in units of  $\text{g/m}^3$  and molarity, and the source of the information. As discussed in Section 6.2.2, only nine radionuclides ( $^{14}\text{C}$ ,  $^{99}\text{Tc}$ ,  $^{129}\text{I}$ ,  $^{79}\text{Se}$ ,  $^{231}\text{Pa}$ ,  $^{234}\text{U}$ ,  $^{237}\text{Np}$ ,  $^{239}\text{Pu}$ ,  $^{242}\text{Pu}$ ) were used in the base case analyses and many of the sensitivity analyses.

As stated above, many of the distributions of concentration limits given in Table 6-32 are based primarily on an elicitation of project chemical/geochemical experts held at Sandia National Laboratories on April 13, 1993 (Wilson et al. 1994). Judgment of the project-expert panel was based on both empirical studies and modeling results, but did not include consideration of distributions used in the 1991 TSPA (Barnard et al. 1992). The results of the project expert elicitation were reviewed by the SolWoG, which recommended only two modifications to the distributions of Np and Pu. These were incorporated into the TSPA-1995 analyses.

The assumptions behind the project expert's development of the distributions are (1) the unsaturated zone water composition is between the composition of J-13 well water and that of UE-25p#1, (2) the solubility-limits will be determined by the far-field groundwater environment, (3) the environment is oxidizing, and (4) future climate changes will cause groundwater compositional changes. As discussed below and shown in Table 6-32, a number of additional sources were used to further constrain distributions of solubility limits for the radionuclides used in this analysis.

In addition, a major modification has been made to the solubility-limited concentration distribution for Np based on an analysis by Sassani and Siegmann (CRWMS M&O 1998a) of the applicability of the data on which the original distribution was constructed. This is not a case of analytical error with the original measurements of Nitsche et al. (1993). Rather because of the apparent metastable nature of the phases formed in that study, the measured values are not

expected to apply to the case of J-13-like fluids, based on experiments conducted on dissolution of spent fuel. This revision is discussed below.

**C, Cl, and I**—The project elicitation results (Wilson et al. 1994, p. 9-1 through 9-11) indicate that the solubility limits on aqueous concentrations for these elements were all very high and would probably result in high dissolved concentrations. A reasonable value was given as 1 mole per liter (1 molar) for each of these, which would place them into the dissolution controlled regime. These elements, and hence their releases from WP, are controlled by their presence in the gap-fraction and by waste-form dissolution, not by solubility limits. These radionuclides (C-14, Cl-36, and I-129) are then treated as unretarded dissolved species throughout the transport calculation and ultimately contribute to the calculated dose. The release of C-14 along gaseous pathways was evaluated in TSPA-1993 (Andrews et al. 1994), but because dose calculations were based on drinking well water, that radionuclide did not contribute to those calculated doses. In TSPA-VA, only aqueous transport pathways were considered.

**Ac, Am, and Sm**—A single uniform distribution is used for each of these elements as a result of the 1993 project elicitation (Wilson et al. 1994, p. 9-1 through 9-11). The project experts indicated that both Ac and Sm should be taken as analogous to Am. The distribution chosen was based on the range of values from the recent measurements of steady-state Am concentrations in both J-13 and UE-25p#1 groundwaters (Nitsche et al. 1993 1994). The distribution parameters are in Table 6-32. For this uniform distribution of concentrations, 90 percent of samples from this distribution come from concentrations between  $1 \times 10^{-7}$  and  $1 \times 10^{-6}$  molar.

**Cm**—As was done for Cm in TSPA-1993 (Andrews et al. 1994), the measured concentrations of Cm in J-13 groundwater from Wilson's dissolution experiments ( $1.2 \times 10^{-5}$  gm/m<sup>3</sup> at 25°C, and  $2.4 \times 10^{-9}$  gm/m<sup>3</sup> at 85°C) were used. In the absence of any estimate of the error, a log-triangular distribution was assumed that extended 1 order of magnitude in each direction from each measured value. The temperature at which the solubility limit was switched from one distribution to the other was selected to be 55°C, the midpoint of the two temperatures. The parameters for these distributions are in Table 6-32.

**Cs, Se, and Tc**—For Cs, Se, and Tc, the solubility-limits were constrained by the project elicitation (Wilson et al. 1994, p. 9-1 through 9-11) to be large to the extent that release of these radionuclides would probably be controlled by dissolution of the waste form. In addition, log-triangular distributions for these elements (see Table 6-32) were taken from the compilation of Golder Associates (1993), which was based in part on the literature evaluation done by Shaw (1992). These ranges of values allow this analysis to encompass implicitly a variety of possible conditions. Because these distributions encompass elemental concentrations controlled by highly soluble salts, they result in dissolution limited release for these radionuclides in general. Very soluble salts have uncertain application to constraining dissolved elemental concentrations in natural systems unless there is a large source of such salts driving high concentrations of the element (i.e., the solubility limiting phase for an element is its least soluble, not its most soluble). It may therefore be possible in the future to constrain further the distributions of solubility limits for these elements.

**Nb**—The project elicitation (Wilson et al. 1994, p. 9-1 through 9-11) based the log uniform distribution for solubility-limited Nb concentrations on the data given in Andersson (1988). The parameters for this distribution are in Table 6-32.

**Ni**—The project elicitation (Wilson et al. 1994, p.9-1 through 9-11) based the log beta distribution for solubility-limited Ni concentrations on the data given in Andersson (1988) and data from the caisson experiment at Los Alamos National Laboratory (Siegel et al. 1993). The parameters for this distribution are in Table 6-32. In TSPA-1993 (Andrews et al. 1994) this distribution was approximated by a log normal distribution which was replaced in TSPA-1995 (CRWMS M&O 1995) with the log beta distribution in Table 6-32.

**Np**—Between the 1991 (Barnard et al. 1992) and 1993 TSPA analyses (Andrews et al. 1994; Wilson et al. 1994), incorporation of new project data resulted in revisions to both dissolution rates and solubility limits. These changes resulted in higher calculated Np releases and these were also seen in TSPA-1995 analyses (CRWMS M&O 1995). As discussed below, the data on which the revised solubility constraints are based probably represent metastable equilibrium between the aqueous fluids and metastable Np-phase(s) (i.e., Na-neptunyl carbonate hydrates and  $\text{Np}_2\text{O}_5$ : [Nitsche et al. 1993, 1994]). In addition, at the relevant conditions the calculated stable N-phase  $\text{NpO}_2$  corresponds to Np concentrations many orders of magnitude lower than these metastable phases. However, simply using the calculated  $\text{NpO}_2$  solubilities to constrain the solubility-limited Np concentration may be objected to on grounds that kinetic barriers could prevent the formation of the  $\text{NpO}_2$  phase. The analysis in CRWMS M&O (1998a) addresses these issues and presents revisions to the current solubility-limited Np concentration distribution.

In Section 6.4.1.4, the current re-evaluation of Np solubility, is presented along with a summary of the detailed analysis from CRWMS M&O (1998a). This includes (1) the constraints used in each of the TSPA analyses, (2) the Np concentration constraints derived from spent fuel dissolution studies, (3) the applicability of the data used in TSPA-1995 to constrain Np concentrations for the case of J-13-like fluid, and (4) the revisions to the solubility constraints on Np concentrations to be used in the future (CRWMS M&O 1998a).

**Pa**—The project elicitation (Wilson et al. 1994, p. 9-1 through 9-11) based the range of the log uniform distribution for solubility-limited Pa concentrations on the data given in Andersson (1988). A log uniform distribution was assigned because the panel agreed that Pa should be less soluble than suggested by the range of values, and that the distribution should have a large variance and be skewed to low values. The distribution parameters are in Table 6-32.

**Pb**—The project elicitation (Wilson et al. 1994, p. 9-1 through 9-11) based the log beta distribution for solubility-limited Pb concentrations on the data range given in Andersson (1988) and other previous work on this element (Tien et al. 1985). It was noted also that the concentration of dissolved Pb is sensitive to the amount of dissolved carbonate. The parameters for this distribution are in Table 6-32. In TSPA-1993 (Andrews et al. 1994), this distribution was approximated by a log normal distribution which was replaced with the log beta distribution in TSPA-1995 (CRWMS M&O 1995) that is also in Table 6-32.

**Pd**—The distribution of solubility-limits for Pd given by Golder Associates (1993) is a uniform distribution with a minimum of  $1 \text{ g/m}^3$  and a maximum of  $1 \times 10^5 \text{ g/m}^3$ . This was given as an

estimated distribution to cover a large range of concentrations because there was a lack of readily available data. Because Pd is one of the noble metals and belongs to the platinum-group elements (PGE), this range of values appears extremely high (PGE limits on their aqueous concentrations tend to be generally lower than limits of many other metals see Sassani [1992] and references therein, or Cotton and Wilkinson [1980] for a general discussion). For the TSPA-1995 (CRWMS M&O 1995) analysis, the maximum value for the Pd-distribution was reduced to  $1 \times 10^4 \text{ g/m}^3$  ( $9.4 \times 10^{-2}$  molar), a value that corresponds to a 1 percent by mass Pd solution and is still viewed here as conservative.

Additional justification that this lowered maximum is conservative comes from comparing the other estimated distributions given by Golder Associates (1993) for Nb, Pa, and Pb and the corresponding distributions for these elements given by the project elicitation (Wilson et al. 1994, p. 9-1 through 9-11). The project expert elicitation values are from 5 to 8 orders of magnitude lower compared to those estimated by Golder Associates (1993). The modified distribution parameters are in Table 6-32. Further refinement of the distribution of solubility limits for Pd will likely lead to much lower values in future TSPAs.

**Pu**—The distribution for solubility-limited Pu concentrations used in TSPA-1995 represented a minor modification (as recommended by SolWoG) of the original distribution given by the project elicitation. The project elicitation (Wilson et al. 1994, p. 9-1 through 9-11) assigned an original uniform distribution identical to that for Am, and this was used in TSPA-1993 (Andrews et al. 1994; Wilson et al. 1994). In reviewing the proposed distributions, the SolWoG suggested that the minimum value be changed from  $1 \times 10^{-10}$  to  $1 \times 10^{-8}$  molar (Dyer 1993; Wilson et al. 1994), based on the range of values from the recent measurements of steady-state Pu concentrations in both J-13-like and UE-25p#1-like groundwaters (Nitsche et al. 1993, 1994). Because the values below  $1 \times 10^{-8}$  molar would have represented only about 1 percent of the samples for the unmodified distribution, this change is not expected to substantially impact the results. The modified distribution parameters are in Table 6-32. For this uniform distribution of Pu concentrations, 90 percent of samples from this distribution come from between concentrations of  $1 \times 10^{-7}$  and  $1 \times 10^{-6}$  molar.

**Ra**—The project elicitation (Wilson et al. 1994, p. 9-1 through 9-11) based the log beta distribution for solubility-limited Ra concentrations on the calculations done by Kerrisk (1984), noting that these limits should be similar to those for Ba and dependent upon the presence of sulfate in the groundwater. It was noted in the project elicitation that Ra should only form a single cation and that the solubility limits should be relatively unaffected by compositional variations in the groundwater. The elicited distribution parameters are in Table 6-32.

**Sn**—The project elicitation (Wilson et al. 1994, p. 9-1 through 9-11) noted that the elemental solubility of Sn is very low and based the uniform distribution for solubility-limited Sn concentrations on the data range given in Andersson (1988) and the consensus that any value was equally likely. The elicited distribution parameters are in Table 6-32. For this uniform distribution of Sn concentrations, 90 percent of samples from this distribution come from concentrations between  $1 \times 10^{-8}$  and  $1 \times 10^{-7}$  molar.

**Th**—The project elicitation (Wilson et al. 1994, p. 9-1 through 9-11) noted that the elemental solubility of Th should be generally less than either Am or Pu, making it relatively dilute, and

that the range of values were well defined, similar to Am. The project elicitation indicated that the lower values are more probable, and thus derived a log uniform distribution for solubility-limited Th concentrations. The elicited log uniform distribution parameters are in Table 6-32.

U—The project elicitation (Wilson et al. 1994, p. 9-1 through 9-11) noted that the elemental solubility of U should be higher in general than either Am or Pu but also that it was not expected that solubility limits for U would be a factor in release of U in Yucca Mountain even though the groundwater has silica, which could cause uranium silicates to precipitate. The project elicitation panel indicated that the data for U (Grenthe et al. 1992) have a wide range with a central tendency between  $1 \times 10^{-5}$  and  $1 \times 10^{-4}$  molar and about 1 order of magnitude spread (Wilson et al. 1994, p. 9-1 through 9-11). Based on this information, the project elicitation resulted in a log beta (skewed log normal) distribution for solubility-limited U concentrations. The parameters for this distribution are in Table 6-32.

Zr—The project elicitation (Wilson et al. 1994, p. 9-1 through 9-11) noted that the elemental solubility of Zr is very low and based the log uniform distribution for solubility-limited Zr concentrations on the data range given in Andersson (1988). The project elicitation panel selected a logarithmic distribution to emphasize the probability of the lower values, which they concluded were more likely. The elicited log uniform parameters are in Table 6-32.

#### 6.4.1.4 Results of Conceptual Model – Np Solubility Re-evaluation

**Previous TSPA Treatment of Solubility-Limited Np Concentrations**—The analysis performed in 1991 (Barnard et al. 1992) calculated Np-237 releases based on a solubility-limited source-term for Np-237. To represent the solubility-limited concentrations (in units of moles/liter, M), TSPA-1991 used a log-uniform distribution with a minimum of -10.23, a maximum of -7.72, and an expected value of -8.48. This distribution was generated from a selected nominal value for Np concentration of  $5.9 \times 10^{-9}$  M. This nominal value was the highest steady-state value observed in the spent-fuel studies of Wilson (1987, 1990a, 1990b). A variability range of 2 orders of magnitude below and 0.5 orders of magnitude above was applied to this nominal value to generate the final distribution (Barnard et al. 1992, 4-30).

Two sets of TSPA analyses were performed in 1993 (Wilson et al. 1994; Andrews et al. 1994). Both of these analyses incorporated new project data for constraining the dissolved concentration of Np in the source-term provided by an elicitation of project experts (Wilson et al. 1994, p. 9-1 through 9-11). The project-expert elicitation distribution for Np (Wilson et al. 1994, p. 9-1 through 9-11) is based on the Nitsche et al. (1993, 1994) studies of solubility-limited Np concentrations. The distribution was given as log beta with a minimum value of -8, a maximum value of -2, an expected value of -4, and a coefficient of variation of 0.2 (Wilson et al. 1994, p. 9-1 through 9-11). In one case (Wilson et al. 1994), the distribution for solubility-limited Np concentrations (M) was taken directly as that given by the project experts. In the other TSPA-1993 analysis (Andrews et al. 1994), the Nitsche et al. (1993, 1994) studies were also used to develop additional constraints on Np concentration as functions of temperature and pH. In both cases, the solubility-limited Np concentrations were increased beyond those used in TSPA-1991 by about 2 to almost 6 orders of magnitude.

In addition to raising the solubility-limited Np concentrations, these TSPA-1993 analyses also incorporated modified waste-form alteration/dissolution rate models. These revised dissolution-rate models were based on the flow-through experiments of Gray et al. (1992), which are applicable for far-from equilibrium conditions for the dissolution reaction. Because these rates represent far-from equilibrium conditions, the reaction rates are higher than for close-to equilibrium conditions. These far-from equilibrium dissolution rates provide conservative bounds for the dissolution-rate limited aqueous release of radionuclides into dilute, J-13-like fluids. In contrast to the TSPA-1991 analysis, these models incorporated functional dependence on the system parameters of temperature, pH, and dissolved carbonate (Wilson et al. 1994; Andrews et al. 1994).

Although the solubility-limited Np concentrations were raised for TSPA-1993 analyses, the addition of far-from equilibrium dissolution rates resulted in solubility-limited source-terms for Np-237 because of transport limitations. Because of such high solubility-limited Np concentrations and the inclusion of greater-than-10,000 year time frames, Np was a major contributor to the total, long-term releases in the results of TSPA-1993 analyses.

The peak doses at long-times in the 1995 TSPA analyses were caused mainly by Np-237 (CRWMS M&O 1995), as was the case in TSPA-1993 (Wilson et al. 1994; Andrews et al. 1994). This result was driven mainly by the high values for the solubility-limited concentrations of NP used in those analyses as given by the project-expert elicitation (Wilson et al. 1994, p. 9-1 through 9-11). The distribution for solubility-limited Np concentrations used in the TSPA-1995 study represents a minor modification (as recommended by the SolWoG [Dyer 1993]) of the original distribution given by the internal project elicitation.

The previous distribution for solubility-limited Np concentrations used in TSPA-1995 represented a minor modification (as recommended by SolWoG (Dyer 1993) of the original distribution given by the project elicitation. The project elicitation (Wilson et al. 1994, p. 9-1 through 9-11) based the original log beta distribution on the range of values from the measurements of steady-state Np concentrations in both J-13-like and UE-25p#1-like groundwaters (Nitsche et al. 1993, 1994), and ongoing research at Los Alamos National Laboratory. In reviewing the proposed distributions, SolWoG suggested that the minimum value be changed from  $1 \times 10^{-8}$  to  $5 \times 10^{-6}$  molar (Dyer 1993), but did not indicate how to adjust the coefficient of variation or the expected value. It was decided for TSPA-1995 that a reasonable procedure was to adjust these values so that the shape of the modified distribution was similar to that of the original distribution, except for the lack of a tail at low values of log (Np concentrations). The change made in TSPA-1995 makes the moderate values more probable at the expense of the probability of very low values of log (Np concentration).

As was found in TSPA-1993, the TSPA-1995 results indicate that Np release is the dominant release/dose contributor at long time frames and, therefore, constraints on dissolved Np concentrations in J-13-like fluids warrant critical examination. Comparison of aqueous Np concentrations in J-13-like fluids derived from dissolution studies, solubility studies, and thermochemical calculations allows an assessment of the applicability of the data set used to construct the distribution of Np solubility limits given by the project-expert elicitation.

**Values for Dissolved Np Concentration Derived from Spent Fuel Dissolution Studies**—The project-elicited solubility limits are based on a set of solubility experiments that approached steady-state conditions from oversaturation and formed a highly metastable Np-bearing phase. That is, highly concentrated Np solutions were prepared using very soluble Np-salts, and these were allowed to precipitate Np-solids from this highly unstable state in order to try to identify upper limits on Np concentrations in J-13-like fluids. Aqueous Np concentrations measured in dissolution experiments are directly relevant to evaluating the applicability of such experimental results for a system which will approach its steady-state conditions from undersaturation. If spent-fuel dissolution cannot provide Np concentrations high enough to even approach saturation of the metastable phase (even over a large range of fluid-flow rates), then there is no reason to expect such a phase would form and control Np concentrations at longer time-frames.

The data below are summarized from the sections of CRWMS M&O (1998a) that present a synthesis of a number of spent-fuel dissolution-rate studies that have variable flow rates. The flow rates range from none (batch studies) to fast (flow-through studies). These studies have been used to constrain the dissolved concentrations of Np in the resultant fluids. The Np concentration values derived from these studies are used to evaluate current solubility limits for Np used in TSPAs. In addition to variable flow rates, the dissolution-rate studies were done over a range of conditions such as temperature, fuel sample, and time.

Table 6-33 summarizes four sets of experiments that determined  $^{237}\text{Np}$  dissolution rates from spent fuel into J-13-like water. Two sets of test series (Wilson 1990a, b) are steady-state experiments in which the samples were immersed in water and the solution was sampled at various time intervals. In the third set (Finn et al. 1995), EJ-13 water (i.e., J-13 water equilibrated with tuff at the temperature of the experiment) was dripped on the samples every 3.5 days. A fourth set of experiments (Gray and Wilson 1995) analyzed uranium dissolution rates in a flow-through apparatus, but did not measure Np-237 directly. These four sets of tests are evaluated below to examine the relations between the different testing methods, and to derive additional constraints on the aqueous concentrations of Np for J-13-like fluids starting out at zero Np content. Values taken from these sources and the conversion methods used to derive corresponding dissolved Np concentrations are in CRWMS M&O (1998a, Tables 2-1a and 2-1b), and the derived values of that study (CRWMS M&O 1998a, Tables 2-2 and 3-1) are reproduced in Table 6-33. Also shown in Table 6-33 for comparison are the value ranges of the elicited distribution and the data upon which they were based.

All four experimental studies were performed with J-13-like water and spent nuclear fuel. The fluid flow rates ranged from 0.0 (steady-state tests) to 0.144 L/d (flow-through tests). The temperatures of the experiments ranged from 22° to 90°C. Results for both the first time cycle and last time cycles in the experiments are discussed by CRWMS M&O (1998a). In general, the concentrations are higher in the first cycle of any experimental study and decrease later. All four experimental studies give fairly consistent results for the latter cycles (reproduced in Table 6-33), even though they encompass about 4 orders of magnitude difference in flow rate. The data suggest that temperature dependency is weak and there is only a slight, negative dependence on the flow rate. In the section below, the derived values are discussed and used to evaluate the applicability of the project expert elicited values for the case of J-13-like water compositions.

#### 6.4.1.5 Abstraction and Implementation into RIP

The waste form module in RIP initially uses the dissolution rate equation to calculate upper and lower boundary values on the aqueous concentration of radionuclides in water that has reacted with the waste form. Subsequently, these values are filtered by comparing them with solubility-limited values sampled from the distribution function for each radionuclide. If the sampled solubility limited value is lower than the concentration derived from the dissolution model, then the aqueous concentration is set to the solubility-limited value and the difference in mass is calculated and treated as precipitated out of solution. This precipitated inventory is still available for future mobilization. The process places constraints on the aqueous concentration of each radionuclide element considered, with each isotope of that element present in proportion to its isotopic abundance.

#### 6.4.1.6 Representation/Validity

**Applicability of the TSPA-1995 Np Concentration Distributions for J-13-like Fluid**—This discussion is also a summary of that given in CRWMS M&O (1998a). As discussed above, the range of solubility-limited Np concentrations used in TSPA-1995 is based primarily on the range of the data of Nitsche et al. (1993, 1994). These ranges are shown in Table 6-33 with the values of aqueous Np concentrations derived from the spent-fuel alteration/dissolution studies. For additional comparison, the project-elicited distribution range, the data from Nitsche et al. (1993), and the values derived in this study from the dissolution studies are shown in Figure 6-33. It appears clear from Figure 6-33 that the dissolved Np concentrations in the resultant fluids of these studies are all well below those of the metastable solubilities measured by Nitsche et al. (1993, 1994). These dissolution studies show that Np reached these lower concentrations in very short time (at most a few years) relative to that expected for geological disposal. It seems unlikely that the metastable phases observed in the oversaturation experiments of Nitsche et al. (1993, 1994) would form at all for the case of J-13-like water interaction with the waste form.

The highest value derived in CRWMS M&O 1998a from the spent-fuel studies ( $1.4 \times 10^{-7}$  M, see Section 2.1.3 of CRWMS M&O 1998a) is only about 3 percent of the minimum value in the TSPA-1995 solubility-limit range. In addition, this highest value ( $1.4 \times 10^{-7}$  M) is an average from Finn et al. (1995) data that include the measured values from all the cycles in the experiments. The values in the early portion of the tests were much higher than the later ones. The values were high in the first cycle using ATM-103 (Finn et al. 1995) and decreased for the latter cycles to a value of  $9.9 \times 10^{-10}$  M (Table 6-33), which is about 2 orders of magnitude smaller than the average given above. This indicates even further that it is highly unlikely that J-13 water reacting with spent fuel will achieve concentrations of Np high enough to even approach saturation of the metastable phases on which the project-elicited solubility limits are based. The next highest value in Table 6-33 is that of  $5.9 \times 10^{-9}$  M is the high value reported by Wilson (1990a, b). This value is only 0.12 percent of the minimum value of the project-expert elicited range. Thermochemical analyses of the Nitsche et al. (1993, 1994) studies have evaluated the degree of metastability in those tests.

The degree to which the fluids from the Nitsche et al. (1993, 1994) studies were supersaturated with respect to  $\text{NpO}_2$  was calculated by Janecky et al. (1994). Comparing those values to the range of Np concentrations used by the project expert elicitation (CRWMS M&O 1998a), shows

that  $\text{NpO}_2$  is calculated to be about 5 to 10 orders of magnitude supersaturated in the Nitsche et al. (1993, 1994) studies, depending on the experimental conditions. Calculation of the stable Np phase and its solubility in J-13-like water at other conditions (Wilson and Bruton 1990; Wilson 1990b; Wolery et al. 1995) has also shown that the dissolved Np concentration set by  $\text{NpO}_2$  equilibrium is orders of magnitude lower than those observed for the metastable phases formed in supersaturation experiments (Nitsche et al. 1993, 1994). Additional calculated values providing similar information are discussed in CRWMS M&O (1998a).

Using calculated  $\text{NpO}_2$  solubilities (or values for  $\text{NpO}_2$  as a solid solution component) for direct constraints on solubility limits for TSPA requires the assumption that kinetic inhibitions to precipitation would not be prohibitive on geologic time scales (i.e., one must assume that the metastable phase does not precipitate and deter the systems approach to equilibrium). Although this is the case for any solubility limiting phase, this assumption is more difficult in the case of Np. This difficulty comes from a theoretical standpoint. Because the aqueous Np is pentavalent and the Np in  $\text{NpO}_2$  tetravalent, precipitation therefore requires a reduction of the aqueous Np. At low temperature, reduction reactions are generally slow reactions even at reduced conditions in hydrothermal pressurized experiments.

In addition, metastably elevated silica concentrations in the Yucca Mountain groundwater indicate that disequilibrium can persist on geologic time scales. However, for any metastable phase to first precipitate, the solution must become saturated (or even slightly supersaturated) with that phase. In the case of silica in Yucca Mountain groundwaters, there are highly metastable silica-source phases (e.g., volcanic glass) that are dissolving and contributing higher-than-equilibrium concentrations to the fluid. Phases such as opal-CT and cristobalite, which are metastable relative to stable quartz, precipitate and impose silica concentrations that are about 2 to 3 times those of the equilibrium concentration (Duffy 1993).

As discussed above, it appears that spent fuel dissolution studies in J-13-like water may have been able to (super)saturate with respect to  $\text{NpO}_2$  (or its corresponding solid-solution phase). However, none of the spent fuel dissolution studies resulted in Np concentrations apparently required to reach saturation of the metastable sodium-neptunyl-carbonate-hydrate phases or  $\text{Np}_2\text{O}_5$  phases observed in the Nitsche et al. (1993, 1994) studies. These dissolution tests then indicate that highly metastable concentrations are not developed at laboratory time scales and should not be expected over longer time frames, because Np is being controlled by more stable phases (and possibly as a solid solution component) even on these short time scales. In addition, if the Np occurs as a  $\text{NpO}_2$  solid solution in the spent fuel, or as minute discrete  $\text{NpO}_2$  solids, then nucleation kinetics should not be a major factor to formation of the more stable Np phases.

**Revisions to the Solubility-Limited Np Concentration Distribution for TSPA-VA-CRWMS M&O (1998a)** presents a synthesis of Np concentrations as constrained by the spent fuel alteration/dissolution studies and calculational studies of  $\text{NpO}_2$  solubility with the conceptual framework of a performance assessment model that uses a far-from equilibrium dissolution rate combined with solubility-limited dissolved radionuclide concentrations. Based on the derived values and analysis of the experimental systems, CRWMS M&O (1998a) recommended that the current distributions for solubility limited Np concentrations be shifted lower by 2 orders of magnitude with preservation of the shape or variance, of the distribution. This shifted range for

the distribution is shown in Figure 6-33 for comparison to the range of the previous distribution and the values derived in CRWMS M&O (1998a).

Based on the values discussed above and shown in Figure 6-33, this is a relatively conservative adjustment and still encompasses a portion of the range provided by the project expert elicitation, even though there is little or no possibility that for J-13-like water these values will ever apply. For the beta distribution of  $\log_{10}(\text{Np})$  given in TSPA-95 (CRWMS M&O 1995; Table 6.3-1), this revision amounts to shifting the expected value of  $\log_{10}(\text{Np})$  (in mole/L) from -3.85 to -5.85, and the minimum and maximum values from -5.30 and -2.0, to -7.30 and -4.0, respectively. Because the variance, and thus the standard deviation, remain the same for the revised distribution, the coefficient of variation (i.e., the standard deviation divided by the mean) becomes 0.099. The parameters for the modified distribution are in Table 6-33.

This adjustment is supported also by lower values measured for the concentration of Np in J-13-like fluids in ongoing oversaturation studies at Los Alamos National Laboratory (Efurd et al. 1996). These tests were conducted under conditions slightly different from the Nitsche et al. (1993) study and determined lower steady-state Np concentrations, but also have precipitated apparently metastable Np solids.

As fluid compositional scenarios are defined in the performance assessment near-field geochemistry model, all the solubility-limit distributions will need to be reevaluated and revised for each specific fluid-composition scenario in preparation for TSPA-LA.

Assessing how solubility-limit distributions are changed by new data is facilitated by a well-defined paradigm for building the distribution. A suggested approach is to define, for each element, the stable, solubility-limiting phase for each specific fluid scenario. For the identified stable phase, its equilibrium dissolved radionuclide concentration would be used to constrain the expected value of the distribution. For the case of Np in J-13-like fluids, calculated or measured  $\text{NpO}_2$  solubilities should be used for the expected value. Such a value may still even provide a conservative estimate for dissolved Np concentrations if Np is controlled primarily as a trace component in solid solution with precipitating phases. This latter possibility could be handled in terms of uncertainty of the expected value.

Construction of a distribution around such a value would entail encompassing sources of uncertainties associated with the identification of the stable solid phase and the derivation of the solubility-limited value, as well as conceptual uncertainties buried in this approach. These sources include (1) parameter uncertainty on the experimental measurements or the thermochemical data used to delineate the radionuclide concentration, and (2) conceptual model uncertainties primarily regarding a) potential kinetic barriers to stable phase formation, b) potential misidentification of the actual stable phase(s), and c) incorporation of radionuclides as trace solid solutions in other phases. Some of the magnitudes of conceptual uncertainties could be assessed by constraints on solubility limits of metastable phases and natural analog for geochemical behavior of radionuclides. The first of these three sources of conceptual error generally adds uncertainty at values greater than the expected value, whereas the latter two generally lead to greater uncertainty lower than the expected value. Such distributions would also be used to incorporate uncertainty/variability in the fluid compositions, although major

processes affecting water composition should be addressed via different water composition scenarios.

It is envisioned that improvements to future TSPA analyses would result from further analysis of the data from spent fuel alteration/dissolution studies in order to derive relations between concentration and flow rate. These could then be used to define values of radionuclide concentrations for specific flow rates in conjunction with the source-term concentrations derived solely from the far-from equilibrium studies. Such limits would specifically apply to the water composition(s) and temperature(s) of the studies. As discussed in Section 6.4.3, data from the dissolution studies can provide constraints to dissolution model development in order to account for reprecipitation observed in laboratory experiments. Applying such data directly for time periods in which secondary phases are forming is a direct approach to using such data, in addition to the above evaluation of the conceptual applicability of solubility limits.

**Strategies for Additional Distributions and Concentration Constraints**—The solubility-limited radionuclide distributions discussed above were given, in many cases, for specific consideration of fluid compositions and system conditions that apply most directly to the ambient system at the site. In some cases, the conditions for which the distribution applies are wider ranging. The basic hypothesis regarding solubility-limited concentrations is that for some radionuclides, stable solid-phase formation will occur over geologic time scales and will provide an upper bound to the dissolved radionuclide concentration. Such solids may be pure phases of the radionuclide of interest or possibly phases in which the radionuclide is incorporated as a trace solid solution component. In either case, the stability of solid phases will depend on the temperature (and to a lesser extent pressure) and compositional parameters of both the concentration-limiting solid phase and the aqueous solution (e.g., pH, oxygen fugacity, concentrations of other metals and ligands). Because potential perturbations to the system may affect these parameters for some time, consideration of additional solubility-limited radionuclide distributions for conditions outside those for which the above distributions apply will facilitate evaluation of the potential impacts to performance caused by these expected changes. In addition, a systematic strategy for defining the distributions used in probabilistic safety analyses facilitates interpretation of results and revisions to analyses as additional data are collected.

One of the waste form workshop activities focused on the application of such solubility limits in PAs. The overall goal of such an activity is to derive constraints on dissolved radionuclide concentrations based on the long-term interactions with the perturbed and geologic environment for use in TSPA calculations. The basic hypotheses behind using such constraints to develop distributions are (1) given geologic time frames, stable equilibrium is approached and kinetic constraints become less controlling and can be represented by the uncertainty associated with the stable thermochemical equilibrium; (2) values and/or variations in major element fluid composition are provided by the fluid compositional scenarios from the near-field geochemical environment (see Chapter 4) tasks; (3) parameter and conceptual uncertainties can be used directly in the distributions; and (4) uncertainties regarding temperature dependencies will either be addressed explicitly or incorporated via parameter uncertainties reflecting different temperatures.

As fluid compositional scenarios are defined in the performance assessment near-field geochemistry model, all the solubility-limit radionuclide concentration distributions will need to

be reevaluated and revised for each specific fluid-composition scenario. Assessing how solubility-limit distributions are changed by new data is facilitated by a well-defined paradigm for building the distribution. The suggested approach is to define, for each element, the stable, solubility-limiting phase for each specific fluid scenario. For the identified stable phase, its equilibrium dissolved radionuclide concentration would be used to constrain the expected value of the distribution. For the case of Np in J-13-like fluids, calculated or measured  $\text{NpO}_2$  solubilities should be used for the expected value. Such a value may still even provide a conservative estimate for dissolved Np concentrations if Np is controlled primarily as a trace component in solid solution with precipitating uranium phases. This latter possibility is one aspect that could be handled in terms of uncertainty of the expected value.

Construction of a distribution around such a value would entail encompassing sources of uncertainties associated with the identification of the stable solid phase and the derivation of the solubility-limited value, as well as conceptual uncertainties that are buried in this approach. These sources include (1) parameter uncertainty on the experimental measurements or the thermochemical data used to delineate the radionuclide concentration, (2) conceptual model uncertainties primarily regarding a) potential kinetic barriers to stable phase formation, b) potential misidentification of the actual stable phase(s), and c) incorporation of radionuclides as trace solid solutions in other phases. Some of the magnitudes of conceptual uncertainties could be assessed by constraints on solubility limits of metastable phases and natural analogues for geochemical behavior of radionuclides. The first of these three sources of conceptual error generally adds uncertainty at values greater than the expected value, whereas the latter two generally lead greater uncertainty lower than the expected value. Such distributions would also be used to incorporate uncertainty/variability in the fluid compositions, although major processes affecting water composition should be addressed via different water composition scenarios.

Within the performance assessment analyses, these distributions act as a filter to the dissolved concentrations generated on each waste-form surface (SNF and DHLW glass) before being fed to transport and release. An additional application could account for spatial variability of fluid composition where specific distributions could be used to check for concentration limits at other points within the EBS, the geosphere, or any other place where a different geochemical environment is expected.

The approach to deriving these additional constraints is being performed in a graded manner. This started with an assessment of the current solubility limited distributions of the radionuclides used in TSPA-95 for the TSPA-1995 "ambient" system, (i.e., J-13-like fluid and atmospheric gas pressures). This was done in order to identify the needed revisions to the base-case distributions discussed above in terms of this revised strategy, prioritize the revisions, and evaluate the required level of effort to accomplish such work. Below is a summary of the status of this activity.

Project staff began this task by reviewing the distributions used in previous performance assessment analyses and assessing the priority for revising some of those distributions relevant to the ambient fluid composition cases, which is changing based on new work on the NFG. What has been accomplished so far:

- Reviewed the TSPA-1995 solubility-limited concentration distributions to assess the range of values and identify the primary elements for revision in the TSPA-VA for the “J-13” fluid composition case.
- Identified a list of first priority elements to have distributions for ambient fluids revised based on one or more of the following criteria:
  - a. The range of values seemed inappropriate for the defined conditions/fluid composition (i.e., dilute J-13 or UE-25). For more detail, see the discussion regarding Np above.
  - b. A comprehensive review of thermochemical data for that element is being completed by the Nuclear Energy Agency (NEA) or the YMP.
  - c. The NRC has questions regarding the range of values used in TSPA-1995, or the values diverge substantially (i.e., >2-3 orders of magnitude) from the chosen values in the NRC performance assessments.
  - d. The element is a substantial portion of resultant peak releases/doses in total system performance calculations and, as such, its values should be scrutinized.
  - e. There are outstanding questions regarding the capacity for gaseous transport of the element.

The following elements were chosen for reevaluation/revision for the identified reasons above

<u>Element</u>	<u>Reasons</u>
Am	b
I	d, e
Nb	c
Ni	b
Np	a, b, d
Pu	b
Se	b
Tc	b, c, d, e
U	a, b, c
Zr	b

The next step was to begin revising the distribution of these elements for ambient fluid (i.e., ~J-13). Project staff identified possible data sets to be used in thermochemical calculations of the stable phase for these elements in specific water composition scenarios. In some cases, more than one data set is available. Calculations with various data sets will allow evaluation of parameter uncertainties as well as conceptual uncertainties if the data sets contain different solid phases for a specific element. The data sets identified below for each element will be used to calculate stable phase and solubility of that phase in ~J-13 water. (The J-13 water composition

used will be that identified as the base case at ambient conditions resulting from the NFGC activities.)

As an example of the first step in this strategy, preliminary calculations were performed for three of these elements being considered within base-case performance assessment calculations (U, Np, and Pu). These example calculations have been done for the incoming ambient water compositions (equilibrated J-13) at three temperatures (31°C, 60°C and 90°C) with imposed atmospheric oxygen and 1,000 ppm carbon dioxide gas partial pressures. The calculated water compositions, detailed in the NFGC section of the TSPA-VA, with these imposed gas compositions are appropriate at 31°C, and 60°C, however, at 90°C the carbon dioxide content of the gas phase is expected to be lower.

Element	Dataset	Reference	Location
Am	NEA Am Dataset	Silva et al. 1995	GEMBOCHS
I	EQ3/6 Sup Data set	Johnson et al. 1992	GEMBOCHS
Nb	Not identified		
Ni	LLNL Data set Milestone	SPL4DM4	TBI GEMBOCHS
Np	EQ3/6 COM Data set		GEMBOCHS
	LANL SIIT aqueous	MS 3792	TBI GEMBOCHS
	NEA Draft 12/97	VOL II	TBI GEMBOCHS
Pu	EQ3/6 COM Data set		GEMBOCHS
	LANL SIIT aqueous	MS 3792	TBI GEMBOCHS
	NEA Draft 12/97	VOL III	TBI GEMBOCHS
Se	Defer until NEA Phase-2 data are ready		
Tc	Defer until Rard/NEA Data set ready		TBI GEMBOCHS
U	NEA U Data set	Grenthe et al. 1992	GEMBOCHS
Zr	LLNL Data set Milestone	SPL4DM4	TBI GEMBOCHS

All of these example solubility calculations were performed using the EQ3NR code (Wolery 1992) in the EQ3/6 code package Version 7.2c (TBV-581) and the com (composite) R6 (Revision 6, December 3, 1996) data file that is part of the EQ3/6 code package. The plutonium dataset from Lemire and Tremaine (1980), the Np dataset from Lemire (1984), and the U data from the NEA source data of Grenthe et al. (1992) are the sources of the data in the EQ3/6 Version 7.2c (TBV-581) com data file. These data and the code are not qualified, and the results of these calculations are not used in TSPA-VA component models. The results of these preliminary example calculations are in Table 6-34. (DTN: MO9811MWD0EQ36.008).

#### 6.4.2 Colloid Mobilization

Colloidal systems may be defined as those in which the component phases are highly dispersed; the phases range in size from 1 nm to 1 μm, approximately. "Pseudocolloids" form when

radionuclides are adsorbed onto existing colloids, such as those present in natural groundwaters, primarily clays and iron oxy-hydroxides. (Colloids are "surface active," meaning that under most conditions they readily adsorb metal ions of high ionic charge, such as transition metals and actinides.) "Real" colloids, or intrinsic, or true colloids form from the hydrolysis of highly charged ions in solution, followed by polymerization of metal ions, which leads to the formation of colloids.

Colloids may be important to performance for two reasons: they may increase the release of radionuclides from the waste package, and they may increase the transport velocity of radionuclides. When a radionuclide concentration is solubility limited, transport on mobile colloids increases the release of the radionuclide from the waste package. The transport velocity of radionuclides attached to colloids may be faster than that of dissolved radionuclides because colloids may travel in the faster parts of the flow paths, and colloids may sorb to host rock less than dissolved radionuclides.

#### **6.4.2.1 Goal**

Colloid-associated radionuclides have been observed and studied for some time. Methods for describing their generation, stability, and transport have been developed. These methods, however, are quite computationally intensive, and require a large database of site specific information in order to generate reliable results. For this first attempt at modeling colloid effects in DOE's TSPA, the goal was to bound the possible behavior of colloid-bound plutonium using simple, fast-running models.

While many radionuclides have the potential for colloidal transport, this initial colloid analysis focused on plutonium. Plutonium has low solubility and high sorption onto the host rock, and is thus one of the radionuclides most likely to be affected by colloidal transport. In addition, the proposed repository has high inventories of plutonium isotopes with half-lives short enough to pose a dose danger but also long enough to allow transport over distance. Americium and thorium, with their low solubilities and high sorption are also associated with colloids, but their inventories and half-lives make them less likely than plutonium to affect repository performance. As more data are obtained, colloidal transport of additional radionuclides will be investigated.

#### **6.4.2.2 Conceptual Model**

In order for colloids to affect repository performance, the colloids must first be generated in significant quantities, be stable within the EBS and far-field environments, and carry a significant radionuclide load and must transport readily. Each of these processes is discussed below.

**Colloid Generation**—Many types of colloids are expected to be generated within the Yucca Mountain repository system. Colloids may be produced in the far field, the near field, and at the waste form. Far field colloids are those produced in the geosphere, from the soil zone to the water table. The types of these colloids may include: microbe bodies, organic colloids (such as humic and fulvic acids), and mineral colloids (such as goethite, hematite, clays, etc.) In the near field, additional colloids may be produced from the degradation of EBS components, including steel, concrete, and other components. At the waste form, additional colloids are produced

during the degradation of the waste form. Colloid generation during degradation of each of the three main waste form types is discussed next.

**DHLW**—Laboratory investigations have demonstrated that the corrosion of DHLW glass can result in the formation of colloids e.g., Bates et al. 1992; Feng et al. 1994). Experimental results suggest that primary colloids can result from the “spallation” of the surface layers formed from the degradation of the glass waste form (Bates et al. 1994, p. 92) under a range of experimental moisture conditions (water vapor tests, drip tests, and immersion tests). It has been shown that smectite clays may nucleate in solution, forming colloids, in immersion tests (Feng et al. 1994, p. 205). The clay colloids can in turn provide sites for adsorption of radionuclides.

Mineralogically the colloids have been shown to be primarily smectite clays and uranium silicate, probably weeksite (Bates et al. 1994, p. 94), with other phases containing dolomite, calcium phosphate, and silica-rich uranium-titanium oxide and manganese-rich oxide components. Colloids formed from the degradation of DHLW glass have been shown to incorporate more than 99 percent of the available mobile Pu and Am, (i.e., less than 1 percent of the mobile Pu and Am occurs as aqueous Pu and Am in the solution). Experiments suggest that Np is not incorporated into the colloids to the degree that Pu and Am are but largely remains in solution (Bates et al. 1992, p. 650).

The rate at which the colloids are produced in the experiments appears to be a function of the ratio of the surface area of the glass to the solution volume, or SA/V (Bates et al. 1993, p. 88). Similarly, SA/V appears to control how long the colloids stay in suspension; it has been observed that the quantity of colloids in the leachate increases steadily and then decreases with time. This is because tests conducted at higher SA/V result in greater glass corrosion and high ionic strength of the solution, which in turn results in compression of the diffuse counter-ion atmosphere (electric double layer) toward the surface of the colloid, causing the particles to agglomerate by van der Waals attraction and settle out of solution (Bates et al. 1993, p. 88; Feng et al. 1994, p. 210). If the solution is diluted, double layer compression is reduced, and the colloids can re-disperse.

This effect of ionic strength of the solution on colloid agglomeration rate is countered by the effect of pH, which serves to increase the interparticle repulsion by increasing the negative surface charge of the colloids. As pH of the solution increases with increasing SA/V, the colloids are effectively stabilized, in spite of the high ionic strength (Bates et al. 1993, p. 88).

Because the repository environment is expected to be nearly static, with minimal groundwater in contact with the glass, the glass corrosion will produce a leachate of high ionic strength and high pH. This would result in lower colloid concentrations and less colloid-assisted transport of radionuclides. Conversely, if increased rates of infiltration result in increased amounts of groundwater in contact with the waste, precipitated colloids would become resuspended and transport would increase (Feng et al. 1994, p. 210-211).

**CSNF**—Colloids have been observed in UO<sub>2</sub> (Wronkiewicz et al. 1992) and spent fuel dissolution tests (Wilson 1990b). Wronkiewicz et al. (1992, p. 125) note that “spallation” of UO<sub>2+x</sub> granules are released from the UO<sub>2</sub> matrix, and that the amount of U released in the experiments appears to be largely controlled by the “migration of the fine-grained particulate matter.” They state

further that, in consideration of this, "the migration of other radionuclides contained in the  $\text{UO}_2$  matrix of spent fuel (Pu + Am) may be controlled by particulate dispersion rather than by solubility of the  $\text{UO}_2$  matrix or the individual radionuclides alone" (p. 125).

Finn et al. (1994a) describe leaching of two types of spent nuclear fuel under unsaturated condition. Colloids ranging in diameter from 50 to 100 nm were produced as highly disordered or amorphous secondary phases; based on elemental compositions these have been identified as schoepite, a uranyl hydrate, and soddyite, a uranyl silicate (Finn et al. 1994a, p. 203). Other calcium and silica rich phases have been identified as palygorskite clay and amorphous silica (Finn et al. 1998a). Some of these clay particles may have been present in the added equilibrated J-13 water used in the leach tests, and others may have formed from super-saturation during the experiment.

**DSNF**—The rapid corrosion of the more unstable DOE spent fuels such as the metallic uranium fuels will favor colloid production. Corrosion of metallic fuels in water is characterized by the production of copious amounts of fine-grained black precipitates containing various uranium oxides and hydrides (Wilkinson 1962) It is expected that some of these fine particulates will be in the colloidal range, but these colloids have not been studied for their stability or transportability. These uranium minerals are quite dense, which will enhance sedimentation of the larger colloids.

Of these many types, four were chosen for explicit modeling within the PA because they may be present in significant concentrations and have enough attached plutonium to affect repository performance: clay, iron corrosion products, spent fuel colloids, and glass waste colloids. The spent fuel and glass waste colloid types refer to all colloids that are produced during the degradation of the waste forms containing these waste types. The effect of these colloids on performance, however, will depend on the transport properties of the colloids, for example, velocity, filtration, and sorption, and the reversibility of the plutonium attachment to colloids.

**Colloid Stability**—In order for a colloid to affect performance, the colloid must have significant stability for the time frame of transport, and must carry significant amounts of radionuclide. Transport times can range from minutes for transport out of a failed WP under a large seep, to hundreds of thousands of years for retarded transport to the accessible environment. Thus, some relatively unstable colloids generated at the waste form may persist long enough to transport out the waste package, increasing the radionuclide release from the package, but not traveling a significant distance away from the repository. The more stable colloids, however, may remain suspended for years and travel a much greater distance. Section 4.4.3.3 of Chapter 4 of this document discusses the stability of natural colloids in some detail. The silica and clay colloids observed in the CSNF and HLW dissolution experiments may have similar stability to natural silica and clay colloids. The stabilities of the other colloid types observed, however, are not known.

**Radionuclide Attachment**—Colloids are only important to repository performance when radionuclides attach to them. Attachment may occur by a number of mechanisms and may be reversible or irreversible in the time frame of transport. Figure 6-34 shows the possible interactions of radionuclides, colloids, and stationary materials. Some of the mechanisms of attachment include coprecipitation, surface sorption, and ion exchange. The rate of attachment,

detachment, and transport determine the “effective reversibility” of the attachment. When the attachment is fast and reversible, transport on colloids will be controlled by local equilibrium, and simple models using effective partition coefficients do a good job describing the radionuclide behavior. When attachment is irreversible or detachment is slow relative to transport times, then local equilibrium models fail – resulting in over- or under-predictions of transport. See Section 8.5.2.5 of Chapter 8 of this document for a discussion of the importance of sorption and desorption kinetics in colloid-assisted radionuclide transport.

Lu et al. (1998) have studied the sorption/desorption of plutonium (IV) and plutonium (V) on hematite, goethite, clay and silica colloids. Their work shows that attachment is fast and detachment is slow, but at least partially reversible in several months’ experiments. Therefore, at least part of the sorption of dissolved plutonium onto the major near- and far-field colloids is expected to be reversible on the time scale of transport to the accessible environment (hundreds to millions of years). The reversibility of attachment to waste form colloids, however has not been established. Coprecipitation, in particular, has the potential to create colloids that have radionuclides encapsulated by stable minerals. These colloids may be able to move large distances without giving up their radionuclides. It is not clear what fraction of the waste form colloids may have irreversibly attached radionuclides. Experiments are planned to address this issue.

**Transport**—Besides the reversibility of attachment of the radionuclide to the colloid, other processes important to transport include: retardation of the colloid by reversible or irreversible attachment of the colloid to solid surfaces, filtration of colloids in small pore spaces, attachment of the colloid to water-air interfaces.

#### 6.4.2.3 Implementation in RIP

Based on experiments and observations to date, plutonium attachment to colloids can vary from relatively fast and reversible to effectively irreversible. However, the necessary parameter values for modeling plutonium attachment to all types of colloids that may affect repository performance are not all available. In addition, the performance assessment computer codes for modeling radionuclide transport currently cannot easily accommodate the complexity needed for these calculations. (See Section 8.5.2.5 for a discussion of scoping reactive transport modeling of colloid-assisted radionuclide migration.) Instead, plutonium attachment to colloids has been modeled using the two extremes: instantaneously reversible attachment and totally irreversible attachment as discussed in Chapter 3 of this TSPA-VA TBD. Partitioning of plutonium into these two categories is treated as a sampled parameter and is done at the hand-off between the EBS and UZ.

**The Reversible Pu Attachment Model**—The reversible model assumes instantaneous equilibrium between dissolved radionuclides and colloid particles and was available within the RIP code (Version 5.19.01, CSCI 30055 V.5.19.01) for use in the near field and the Finite Element Heat and Mass (FEHM) code (TBV-564) for use in the far field (see Chapter 8). The RIP model defines the amount of radionuclide mobilized in colloidal form as the product of the dissolved radionuclide concentration, the dissolved-colloid sorption partitioning coefficient ( $K_d$ ), and the colloid concentration. The colloid concentration was calculated as a function of the ionic strength of the fluids as described in the NFG Chapter 4. The FEHM model combines the  $K_d$

and colloid concentration parameters into a single parameter—the aqueous-colloid partitioning coefficient,  $K_c$ . The parameter ranges used in the calculations are summarized below and discussed further.

<b>Parameters Used in Reversible Attachment Model</b>		
	$K_d$ (ml/g)	Effective $K_c$
<b>Near-field colloids</b>		
Clay	$10^5 - 10^7$	$\sim 10^{-3} - 1$
Iron oxy-hydroxy colloids	$10^6 - 10^8$	$\sim 10^{-2} - 10$
Spent fuel waste form colloids	$10^2 - 10^8$	$10^{-5} - 1$
Glass waste form colloids	$10^2 - 10^9$	$10^{-5} - 10$
<b>Far-field colloids</b>		
		$10^{-5} - 10$

**bold: as input, italic: effective value in calculation**

NOTE: (DTN SNT05080598002.001)

The  $K_d$ 's were based on early data from desorption experiments of Pu(IV) and Pu(V) on hematite, goethite, and smectite in J-13 well water (reported in Lu et al. 1998). These early results showed initial desorption  $K_d$ 's for the iron colloids in the  $10^4$  to  $10^6$  ml/gm range and for smectite clays in the range of  $10^3$  to  $10^5$  ml/gm. These were expected to be maximum  $K_d$ 's because further desorption would reduce these figures. The use of maximum  $K_d$ 's yields maximum calculated colloid-assisted radionuclide releases and is thus conservative. However, due to the conceptual model uncertainty associated with assuming equilibrium  $K_d$ 's, when it is known that desorption is much slower than sorption, the  $K_d$ 's ranges were raised another two orders of magnitude for use in the near field where transport times are short. This is shown in the table of the  $K_d$ 's used for clay and iron colloids in the near field. Note that these higher  $K_d$ 's result in effective  $K_c$ 's that range over 1, and thus may result in enhanced transport of radionuclides due to the colloids. Had the ranges not been shifted up, the colloids could have only made a fractional difference in the transport of radionuclides.

The  $K_c$ 's for the waste form colloids and far-field colloids were more difficult to estimate. For the lower bound of the far-field,  $K_c$ , the original low  $K_d$  of  $10^3$  ml/gm for smectite clay was used. When this  $K_d$  is combined with the low range for colloid concentration in J-13 well water, a  $K_c$  of about  $10^{-5}$  is obtained. For the upper range, the following summary of recent data from Argonne's testing of HLW and CSNF was used (Finn et al. 1997b).

### Observed Behavior for Spent Fuel and High-Level-Waste Glass in Unsaturated Tests

	Leachate EJ-13	Waste Form Spent Fuel <sup>a</sup>	HLW Glass <sup>b</sup>
Type of Colloid	Clay observed	Clay assumed	Clay observed
Total Pu (M)	----	10 <sup>-8</sup>	10 <sup>-6</sup>
Colloid Pu (%)	----	≤50	≥90
Ionic Strength (M)	0.004 <sup>c</sup>	0.0012 <sup>c</sup>	0.02 <sup>d</sup>
pH	8-8.5	6.8-7.2 <sup>e</sup>	4.5-5.5 <sup>f</sup>

NOTE: (DTN SNT05080598002.001)

<sup>a</sup> High-drip-rate test at 90°C, nominal 0.75 ml every 3.5 days.

<sup>b</sup> High-level waste glass at 90°C, nominal 0.075 ml every 3.5 days.

<sup>c</sup> Depends primarily on sodium, silicate, and carbonate concentration.

<sup>d</sup> Dominated by sodium and carbonate concentration.

<sup>e</sup> After three years of reaction and measured at 20°C in stainless steel vessel.

<sup>f</sup> Measured at 20°C in stainless steel vessel.

These data suggest  $K_c$ 's of up to 1 for spent fuel and at least 9 for HLW. Combined with an expected Pu solubility of  $5.1 \times 10^{-7}$  M these  $K_c$ 's would suggest maximum total mobile Pu concentrations of up to  $1.02 \times 10^{-6}$  M for spent fuel and  $5.1 \times 10^{-6}$  M for glass, consistent with the observed concentrations. However, it is not known how stable or transportable these colloids are. In these tests, the plutonium moved with water droplets about 2 cm into the catch basin. The colloids were collected and characterized after they had remained in the catch basin for periods up to six months and then cooled to room temperature. In the proposed repository, the transport pathway through the EBS will offer significantly more distance and chance for coagulation and filtration. However, this data is valuable in that it provides an upper bound for the  $K_c$ . For spent fuel the upper bound of 1 was used, and for HLW the upper bound of the  $K_c$  was rounded to 10.

The reversible model was implemented into RIP with four types of colloidal solids: clay, iron corrosion products, spent fuel colloids, and glass waste colloids. The colloid concentrations for all four colloid types were based on the equations provided in the NFGE chapter. Colloid masses within the RIP cells were calculated from the colloid concentrations and the volume of water within the cells. For clay and iron colloids, the  $K_d$ 's were sampled log-uniformly within the ranges shown above.  $K_c$ 's were independently sampled log-uniformly from  $10^{-5}$  to 1 for spent fuel colloids and  $10^{-5}$  to 10 for HLW colloids and far-field colloids. "Effective"  $K_d$ 's were calculated for the waste form colloids from the sampled  $K_c$  divided by the colloid concentration.

Relative diffusivities of the colloids relative to water were estimated using the Stokes-Einstein equation:

$$D_w = kT / (6\pi r \mu) \quad (6-46)$$

where  $D_w$  is the colloid diffusion coefficient in water,  $k$  is Boltzman's constant,  $T$  is the absolute temperature,  $r$  is the colloid radius, and  $\mu$  is the fluid viscosity. Using the following values,

$$\begin{aligned} k &= 1.3 \times 10^{-23} \text{ J/K} \\ T &= 298 \text{ K} \\ \mu &= 8.9 \times 10^{-4} \text{ Kg/m-s} \end{aligned}$$

$$\begin{aligned} r &= 1 \times 10^{-7} \text{ m (i.e., a 200 nm diameter colloid)} \\ \text{yields } D_w &= 2.3 \times 10^{-12} \text{ m}^2/\text{s} \end{aligned}$$

Dividing by the reference diffusivity within RIP,  $10^{-9} \text{ m}^2/\text{s}$ , yields a relative diffusivity of  $2.3 \times 10^{-3}$ . The relative diffusivities will be higher for smaller colloids and lower for larger colloids. Average size and densities for colloids that are found to travel well in the geosphere are about 200 nm and 2 gm/ml (see Chapter 4, Section 4.4.3.3), but within the short travel distances of the EBS, larger or denser colloids may play a role. With larger denser particles, gravitational settling of colloids may be an important transport mechanism, exceeding diffusion by orders of magnitude. Because RIP does not model settling, this process could be added by raising the upper range of relative diffusivities to incorporate the uncertainty in this phenomenon. Because of lack of conceptual models and data for gravitational settling within the WP and EBS materials, the relative diffusivity was conservatively left at 1 for the base case.

**The Irreversible Pu Attachment Model**—The irreversible model was also included in the calculation to capture the possibility of a fraction of the radionuclides moving rapidly through the transport system irreversibly attached to colloids. At the Benham nuclear test site at the Nevada Test Site, rapid transport of colloid-associated plutonium may have occurred (Thompson et.al. 1998, p. 13 and 18). At 1.3 km from the blast site,  $1 \times 10^{-14} \text{ M}$  colloid-associated plutonium was detected 30 years after the blast. It is not clear what fraction of the transport was due to transport on colloids, injection through fractures at the time of the blast, or transport as dissolved Pu. However, fracture injections have not been observed to extend beyond a few hundred meters, and dissolved plutonium is expected to sorb strongly to the fracture surfaces. In fracture systems, colloids that are repelled from the host material walls may move even faster than non-sorbing dissolved species because they remain in the faster flowing portions of the flow paths. This behavior was seen in a fraction of specially designed colloids pumped through 32 m of fractured tuff near Yucca Mountain (CRWMS M&O 1997e). These observations suggest that some small fraction of colloid-associated plutonium may travel relatively quickly through water-filled fractures, but these observations do not adequately define the uncertainty in this process. Specifics of colloid properties such as surface charge, size distribution, and stability in expected groundwaters, and of the transport and filtration properties in the pathways within the fractured tuff, are not adequately known for accurate prediction at this time. These observations, however, were used to guide selection of a large range for sensitivity studies. Based on the expected value Pu solubility of  $5 \times 10^{-7} \text{ M}$  and the observed  $1 \times 10^{-14} \text{ M}$  colloidal Pu concentration 1.3 km from the blast site, it was estimated that about  $1 \times 10^{-7}$  of the Pu has attached irreversibly to colloids and also moved quickly. Since this estimate is quite uncertain and since the applicability of this estimate to the transport within the Yucca Mountain site is unknown, a three order of magnitude range was added to either side of this estimate. Thus a log-uniform range of  $10^{-10}$  to  $10^{-4}$  was used. While this fraction includes effects from both source term and transport, it was implemented into the calculations at the EBS-natural barrier system interface. The “irreversible Pu” mass flux from the EBS to the UZ was calculated as the “reversible Pu” mass flux times this irreversible Pu fraction. Once passed to far field, the “irreversible Pu” was treated as a non-sorbing, slowly diffusing tracer.

#### 6.4.2.4 Colloid Results

There were three main colloid parameters with the potential to affect Pu release at the accessible environment: the fraction of Pu irreversibly attached to fast moving colloids, the  $K_c$  for the reversible model, and the effective porosity in volcanic layers of the saturated zone for both models. The system showed different sensitivity to each of these parameters.

The irreversible fraction, sampled from  $10^{-10}$  to  $10^{-4}$ , showed almost no effect on the total dose. A set of expected value runs (100,000 year and 1 million-year) were performed with the irreversible fraction set to  $10^{-4}$ . While the early time  $^{239}\text{Pu}$  and  $^{242}\text{Pu}$  releases were somewhat increased, the releases were too small a fraction of the total dose to show any effect on the total dose curves.

In the reversible model, the expected values for both the  $K_c$ , and effective porosity in the saturated zone result in colloid facilitated transport that is more noticeable in the full TSPA base case. The expected values of the  $K_c$ 's are listed below for the seven time periods.

Expected Values:

End of time period (yrs.)	Ionic Strength (M)	Colloid conc.(kg/m <sup>3</sup> )	$K_c$ clay	$K_c$ Fe-col	$K_c$ HLW	$K_c$ SF	$K_c$ Total
200	2.6E-2	1.1E-5	2.4E-2	2.4E-1	7.2E-1	8.7E-2	1.1E+0
1,000	1.6E-2	2.4E-5	5.2E-2	5.2E-1	7.2E-1	8.7E-2	1.4E+0
2,000	1.9E-2	1.9E-5	4.1E-2	4.1E-1	7.2E-1	8.7E-2	1.3E+0
4,000	3.2E-3	6.5E-5	1.4E-1	1.4E+0	7.2E-1	8.7E-2	2.4E+0
10,000	4.7E-3	5.8E-5	1.2E-1	1.2E+0	7.2E-1	8.7E-2	2.2E+0
100,000	6.4E-3	5.1E-5	1.1E-1	1.1E+0	7.2E-1	8.7E-2	2.0E+0
1,000,000	2.5E-3	6.9E-5	1.5E-1	1.5E+0	7.2E-1	8.7E-2	2.4E+0

The maximum total  $K_c$  is 2.4, so the maximum mobilized concentration for Pu is 3.4 times the solubility limit, thus increasing the release rate from the waste package. The SZ effective retardation factor,  $R_{eff}$ , including the effect of reversible colloids is



where  $R_{aq}$  is the retardation for aqueous species, and  $R_c$  is the retardation of the colloidal particles conservatively set to 1 in this analysis. Because the  $R_{aq}$  for Pu is much greater than the far-field expected value  $K_c$  of 0.72, the equation reduces to approximately  $R_{aq}/(1.72)$ . In addition, the expected value for the effective porosity in the volcanic layers of the saturated zone of  $10^{-4}$  was a factor of between 30 and 40 times lower than the expected values for dissolved species, which reduces the net retardation by another factor of 30 to 40 in those layers. Thus, in the expected value run, the source term for Pu is calculated to be elevated by a factor of about 3.4, and the retardation in the volcanic layers is calculated to be reduced by a factor of about 60 due to colloids. Even so, the retardation is still large enough to delay the Pu from becoming a significant contributor to dose until after about 340,000 years in the expected value run (see Volume 3 Section 4.2 of DOE 1998). The contribution of Pu to the total dose only exceeds that

of Np during periods immediately following the superpluvial climates, and at other times is about one-tenth that of Np. In several realizations of the probabilistic runs, however, the high sampled  $K_c$ 's and low sampled effective porosities resulted in Pu dominating the dose in the one-million year TSPA runs.

### 6.4.3 Secondary Phase Formation/Radionuclide Retention

Waste packages disposed of in an unsaturated hydrogeologic repository would in time suffer container and cladding failures, exposing the spent fuels to air and water. The objective of this development of unsaturated spent fuel release rate models is to quantify and bound the rates of release of radioactive materials from the spent fuels to the flowing air and water under unsaturated environmental conditions. The focus of this modeling work is on the combined processes of oxidation, dissolution, and redeposition that take place when spent fuel is simultaneously exposed to both air and to small amounts of groundwater. The incorporation of all of these processes concurrently distinguish the spent fuel release models for unsaturated conditions presented in this section from the forward dissolution rate models for spent fuel previously presented in Section 6.3.1.3. In contrast to the unsaturated release rate models presented here, in forward dissolution rate models the amount of oxygen is limited to that dissolved in water, the amount of flowing water is substantial, and the dissolved products become unavailable for subsequent processes because of the high water flow rates that rapidly transport dissolved products away from the site of reaction.

In Section 6.4.3.1 below, the unsaturated release rate models for interpreting and extracting the minimum number of parameters that could represent the experimentally observed releases in drip tests are presented. No attempt is made here to provide a detailed predictive capability based on more fundamental thermodynamic and kinetic properties of the underlying chemical species and reactions. Detailed prediction of the release rate from fundamental thermodynamic and kinetic properties using a full-fledged reactive transport model are in Section 6.4.3.2, together with a discussion of the uncertainties inherent in such an approach due to lack of data at the level of detail required to adequately support these analyses. Because the unsaturated release rate models incorporate dissolution as one of the active processes, detailed prediction of release rates from fundamental considerations will require use of the forward dissolution rate of spent fuel obtained from fully saturated flow-through dissolution tests, as one of the many required thermodynamic and kinetic parameters. This basic kinetic dissolution rate parameter is usually obtained from laboratory flow-through tests conducted under dissolution rate limited saturated flow conditions at high water flow rates (Steward and Gray 1994) as previously described in Section 6.3.1.3. Furthermore, because secondary mineral phases are formed and redeposited from solution during spent fuel dissolution under unsaturated conditions at low flow rates, the release rates under unsaturated drip-test conditions are generally smaller by orders of magnitude than the release rates predicted by a forward dissolution rate model for saturated high flow rate conditions.

**Formation of Secondary Phases**—Most of the U released to solution during the dissolution of  $UO_2$  combines with silicon, sodium, potassium, calcium, and magnesium derived from synthetic J-13 water to form secondary alteration phases. In experiments, these phases precipitate on the samples and surrounding surfaces. Both natural and experimental U-based systems display a paragenetic sequence of mineral phase formation that is characterized by the following general trend (Stout and Leider 1997):  $UO_2 \Rightarrow$  uranyl oxide hydrates  $\Rightarrow$  alkali- and alkaline-earth uranyl

oxide hydrates  $\Rightarrow$  uranyl silicates  $\Rightarrow$  alkali- and alkaline-earth uranyl silicates + palygorskite clay as indicated in Table 6-35. Specifically, mineralization in the paragenetic sequence of alteration phases is  $\text{UO}_2 \Rightarrow$  dehydrated shoebite  $\Rightarrow$  compregnacite + becquerlite  $\Rightarrow$  soddyite  $\Rightarrow$  boltwoodite + uranophane + palygorskite clay (Wronkiewicz et al. 1997). This trend appears to be controlled by precipitation kinetics and is nearly identical to alteration patterns observed during the weathering of naturally occurring uraninite, such as that which occurs at the Nopal I U deposit in Chihuahua, Mexico. This resemblance suggests that the conditions in the experimental tests have replicated an environment that may be representative of that occurring during uraninite alteration in natural oxidized systems.

The alkali- and alkaline-earth uranyl silicates represent the long-term solubility-limiting phases for U in the  $\text{UO}_2$  tests and the natural U deposits at Nopal. This similarity suggests that the experiments and the natural analog reactions may simulate the long-term reaction progress of spent  $\text{UO}_2$  fuel following disposal at the proposed YMP repository. The actinide concentration in water contacting actinide-bearing phases is the major determinant of release rates from the repository. Uranium transport generally occurs in oxidizing surface and groundwaters as uranyl ( $\text{U}^{+6}$ ) species, most often as  $\text{UO}_2^{+2}$  or uranyl fluorides, phosphate, hydroxyl, or carbonate species. The background U concentration in United States streams is about 0.1 ppb. In uraniferous areas, U ranges from 1-10 ppb in surface waters and 1-120 ppb in groundwaters. More importantly, the range is typically 15 to 400 ppb U in uranium mines (Fix 1956; Langmuir 1978). This is similar to concentrations seen in spent fuel dissolution experiments (Wilson 1990a; Stout and Leider 1997).

#### **6.4.3.1 Secondary Phase Formation/Radionuclide Retention: Interpretive Models for Unsaturated Drip Flow Tests**

In experiments of spent nuclear fuel dissolution with limited water flow, secondary phases are seen to develop. These phases retain a significant fraction of the radionuclides contained in the reacting matrix. These same phases are seen in natural analogs and have retained some radionuclides for geologic times. In this analysis, the program has begun to develop models to reflect this retention process. These models have not been incorporated into the TSPA-VA base case, but have been used for sensitivity analyses intended to point toward future development of these models.

##### **6.4.3.1.1 Goal**

In this section, models for interpreting and extracting radionuclide release rate model parameters from laboratory experimental data gathered in the unsaturated spent fuel release drip tests conducted at the Argonne National Laboratory (Finn et al. 1994a; Finn et al. 1994b; Bates et al. 1995b; DTN LL980813151021.052) are presented. The goal of this work is to directly extract from this test data the minimum number of model parameters required to estimate the radionuclide release rate under unsaturated drip flow conditions that are expected to be representative of the environmental conditions in the YMP reposition. An important aspect of this work is to determine this minimum set of model parameters from this series of tests without requiring additional, generally unavailable, data. This task was performed as a part of activity D-20-43 of the LLNL Spent Fuel Scientific Investigation Plan of the YMP (Stout and Leider 1997, Stout 1996).

#### 6.4.3.1.2 Conceptual Model

An idealized representation of the experimental configuration used in the drip flow tests is shown in Figure 6-35. In these tests, approximately 6 g of spent fuel fragments were placed within a closed vessel on a Zircaloy screen. Groundwater was allowed to drip onto the fuel fragments at one of three flow rates (no drip, low drip, and high drip). After contacting the fuel, the water drained into the bottom part of the vessel, which served as a collection tank. A mass of water in excess of that required to saturate the entire vessel with water vapor was initially placed in this collection tank. The entire vessel was maintained at a constant temperature of 90°C. At the low-drip rate, one drop (approximately 0.05 ml) of water contacted the fuel every 3.5 days. The high drip rate was 10 times higher than the low drip rate. In addition to the external drip-water, there was water evaporated from the bottom of the container, recirculating through the screen to the top portion of the container as water vapor, contacting and condensing on the surfaces of the fuel fragments, mixing with drip water, and draining down into the collection tank. In the no drip (or vapor) test, no external water dripped onto the fuel, but radionuclides in the collection tank indicated that condensed vapor-water was draining and transporting radionuclides into it. The water used for these tests was J-13 well water equilibrated with tuffaceous rock from the YMP repository site. Samples of two standard spent fuels, ATM-103 and ATM-106, with burnups of 30 MWd/kg and 40 MWd/kg, respectively, were tested in these experiments. Consequently, the fission product content and radioactivity of the ATM-106 spent fuel was higher than that of the ATM-103 spent fuel.

**Physical Transport Phenomena**—The conceptual model for spent fuel release under unsaturated low flow rate conditions assumes that the region occupied by the fuel fragments can be divided into two zones: a drip water contact zone and a condensed vapor-water contact zone. This is indicated in Figure 6-35. In the drip water zone, droplets of water intermittently drip onto the fuel fragments. When the small droplets contact the fuel fragments, they collect in patches of water on the surface and spread out into a thin film of water covering the fuel surface. In addition, localized patches grow thicker until capillary forces are exceeded; then they drain along the surfaces of the fuel fragments in intermittent rivulets. Thus, most of this water quickly flows away from the collection of fuel fragments in rivulets while a small part of the water remains trapped by surface tension at the surfaces of contact between fuel fragments. The void space between fuel fragments occupied by the flowing and/or trapped drip water at any instant of time is assumed to be occupied by air saturated with water vapor. Thus, the surfaces of the fuel fragment in this region are contacted by a film of condensed water vapor when it is not in contact with drip water.

In the vapor zone, which is not directly contacted by the dripping water, the fuel fragments are in an atmosphere saturated by water vapor. The water vapor is assumed to condense on the surface of the fuel fragments to form a thin film of water that covers the entire external surface of each fuel fragment. Surface patches of water may also grow thicker, and coalesce into larger droplets on the surfaces of the fuel fragments, then drain away as rivulets as in the drip zone, but at a much slower rate.

The liquid film in the vapor contact regions is assumed to flow under the action of gravity along the surfaces of the fuel fragments. The rate of drainage of solution will depend on the film thickness/drop size, and the combined action of surface tension, viscous and gravitational forces.

A pool of drained water is always assumed to exist in the neighborhood of the fuel fragments so that there is always sufficient water to saturate the void spaces. Consequently, the condensation rate of water on the fuel fragments is assumed to exactly equal the rate of water drainage from the condensed vapor film, and the process is in a steady state with respect to the evaporation and condensation of water vapor and drainage of liquid water.

In the areas contacted by the drip water, the rapidity of drainage of the drops will not permit sufficient time for the chemical reactions of dissolution to act to any significant extent with the intermittent falling droplets. Instead, the significant processes will be the mixing of the drip water with the existing vapor-water film and the mechanical entrainment of colloidal particles from the contacted surface into the droplets as they drain away from the fuel fragments (Finn et al. 1994b). The degree of entrainment of the colloidal particles is likely to be much more significant in the drip region than in the vapor region, because the drip water volume is locally much greater and faster flowing than the water vapor-water film. When each drop has rapidly drained away, the dissolution process reverts to that of a vapor test. In essence, then the drip region behaves similarly to the vapor region with the addition of short periods of rapid transport and liquid mixing that coincide with the release of a drop onto the fuel fragments. In this model of release under unsaturated drip conditions, the differences in chemistry will primarily become evident in the change in chemistry of the residual liquid film along the path of drip water passage.

In both regions, the water in the films will react with the fuel fragments and will diffuse into their interiors. However, unlike the surfaces exposed only to water vapor, the surfaces contacted by the drip water will also be affected by reactions with chemical components dissolved in the original groundwater. Some of the reactants will dissolve and diffuse back into the water film, so the film will consist of a solution of water and dissolution products.

**Chemical Transformation Phenomena**—The chemical reactions between the water contacting the fuel fragments and the fuel transform the fuel fragment surfaces through a sequence of chemical transformations that involve oxidation to more soluble phases, dissolution and removal of the oxidized phases, precipitation of secondary mineral phases from solution, sorption of colloidal matter in the solution phase, redissolution of the secondary mineral phases and reprecipitation as other alteration mineral phases. These complex transformations occur not only at the nominal exposed surface of the altering fuel fragments, but also to some distance into the interior of fuel fragment along grain boundaries that dissolve preferentially. The paragenetic sequences observed in both natural and experimental systems follow the general trend (Stout and Leider 1997) of uranium dioxide  $\Rightarrow$  uranyl oxide hydrates  $\Rightarrow$  alkali- and alkali-earth uranyl oxide hydrates  $\Rightarrow$  uranyl silicates  $\Rightarrow$  alkali- and alkaline-earth uranyl silicates + palygorskite clay. The specific mineral phase sequence usually observed is uranium dioxide  $\Rightarrow$  dehydrated schoepite  $\Rightarrow$  compreignacite + becquerelite  $\Rightarrow$  soddyite  $\Rightarrow$  boltwoodite + uranophane + palygorskite clay (Wronkiewicz et al. 1997).

Observation of the mineral transformations that take place in the drip tests indicate that the dissolved minerals in the incoming groundwater would affect only the surfaces directly contacted by the drip water, and this effect is significant only at relatively high flow rates that bring substantial amounts of these dissolved minerals. The dominant mineral phases observed in these tests over a time period of approximately 3.5 years are given in the order in which they form in

Table 6-35 (Wronkiewicz 1997). The alkali- and alkaline-earth uranyl silicates represent the long-term solubility limiting phases for U in these tests and in natural U deposits in natural oxidizing systems. From this table, it can be seen that the mineral transformations that occur under vapor test (condensed vapor-water flow only) and low drip test (condensed vapor-water and low-drip-water flow rate) conditions are similar over the entire testing time period, but they differ significantly from those of the high drip test (condensed vapor-water and high drip water flow rate), particularly at late times. Accordingly, the assumption that the same mineral phases form over the entire time period in vapor and low drip conditions may be used to simplify and consolidate the analysis models for these two conditions. More recent data, however, indicate that the same alteration phases observed in the high drip test are slowly beginning to form in the low drip test. However, within the time period analyzed, the dominant sequence of mineralization is that given in Table 6-36.

**Interpretive Model for Vapor and Drip Tests**—A mathematical model was developed to analyze the laboratory vapor and drip tests conducted on two standard spent fuels (ATM-103, ATM-106) by the Argonne National Laboratory. The water used for these tests was J-13 well water equilibrated with tuffaceous rock from the YMP repository site. As previously stated, this model is not intended to enable detailed predictions of the radionuclide releases as a function of the chemistry of the groundwater and the temperature of the environment. Instead, it was developed for the limited purpose of extracting the radionuclide concentrations released as a function of the drip water rate for the given groundwater composition and temperature, while allowing for the formation of secondary minerals under unsaturated low flow rate conditions.

In these tests, as indicated in Figure 6-34, the experimental test condition is the same for the drip test and the vapor test experts that in the drip test, the drip groundwater chemical composition differs from the initial water used in the vapor test. The interpretation of the drip tests is more complicated than the interpretation of the vapor tests due to the uncertainty regarding the spatial distribution of the drop water and the area of contact between the drop water the spent fuel fragments. A similar uncertainty would exist in application to a repository, in that the spatial extent of the drip water contact zone would have to be estimated.

The mass balance for the  $\alpha$ -th chemical element in the liquid phase in the fluid film can be expressed as (Rate of accumulation of chemical element in the liquid-phase) = (Rate of dissolution of spent fuel) x (Mass fraction of element in spent fuel) + (Rate of dissolution of altered materials) x (Mass fraction of element in altered materials) – (Rate of precipitation from dissolved solutes and suspended colloids) – (Rate of convective transport of element  $\alpha$  out of the liquid film). Accordingly, the mass balance for the liquid film in the drip and vapor zones are given by the equations:

$$\frac{d}{dt} (f_d A_t d_d C_{fd}^\alpha) = V_{sd} A_{sd} \rho_{sd} X_{sd}^\alpha + \sum_a (V_{ad} A_{ad} \rho_{dv} X_{ad}^\alpha) - \sum_p (V_{pd} A_{pd} C_{fd}^\alpha) - f_d A_t V_{td} C_{fd}^\alpha \quad (6-47)$$

$$\frac{d}{dt} ((1-f_d) A_t d_v C_{fv}^\alpha) = V_{sv} A_{sv} \rho_{sv} X_{sv}^\alpha + \sum_a (V_{av} A_{av} \rho_{av} X_{av}^\alpha) - \sum_p (V_{pv} A_{pv} C_{fv}^\alpha) - (1-f_d) A_t V_{tv} C_{fv}^\alpha \quad (6-48)$$

The time derivative on the left side of each these two equations represents the rate of accumulation of the  $\alpha$ -th chemical element in the drip zone (subscript  $d$ ) and vapor zone

(subscript  $v$ ), respectively. In these terms,  $C_{fd}^\alpha, C_{fv}^\alpha$  are the mass concentrations of the  $\alpha$ -th chemical element in the liquid films of the drip and vapor zones accounting for mass in both dissolved solute and suspended colloid forms,  $f_d$  is the fraction of the total liquid transport surface area  $A_t$  associated with the drip zone, and  $d_d, d_v$  are the average thicknesses of liquid films in these zones. The first and second terms on the right side of these equations represent the rates of dissolution of the spent fuel (subscript  $s$ ) and alteration materials (subscript  $a$ ) with the summation sign  $\Sigma_a$  signifying summation over all solid alteration phases. In these terms,  $V_s, V_a$  are the corrosion velocities (i.e., the forward mass dissolution rate divided by mass density),  $A_s, A_a$  the corresponding corrosion surface areas,  $\rho_s, \rho_a$  the densities of spent fuel and the alteration products, and  $X_s^\alpha, X_a^\alpha$  are the mass fractions of the  $\alpha$ -th chemical element in the spent fuel and the alteration products. The third term on the right side of each equation represents the loss of mass of the  $\alpha$ -th chemical element from the liquid phase to the non-mobile solid phases through precipitation and sorption. In these terms,  $V_p$  is the velocity of precipitation,  $A_p$  is the corresponding precipitation surface area, and the sign  $\Sigma_p$  signifies summation over all precipitating/sorbing minerals (subscript  $p$ ) that contain the  $\alpha$ -th chemical element. The fourth, and last, term on the right side of these two equations represents the mass release rate, or the rate at which mass is advected out of the drip and vapor zone liquid films by the moving fluid. The advective velocities in the vapor and drip zones are given by  $V_{vd}$  and  $V_{dv}$ , respectively.

The above equations may be considerably simplified by making several assumptions. If the advective velocity of the flowing fluid is large enough to dominate the mass accumulation term on the left side of each equation, the net mass transferred to the liquid phase would be transported out by the flowing fluid and the left side of these equations can be set equal to zero. Under this assumption (that is not valid for stagnant liquid phase tests without convective transport), the above two equations can be recast in the following form:

$$r_{sd}^\alpha f_d A_t (1 - C_{fd}^\alpha / C_{fmd}^\alpha) - f_d A_t V_{vd} C_{fd}^\alpha = 0 \quad (6-49)$$

$$r_{sv}^\alpha (1 - f_d) A_t (1 - C_{fv}^\alpha / C_{fmv}^\alpha) - (1 - f_d) A_t V_{dv} C_{fv}^\alpha = 0 \quad (6-50)$$

where, the 'effective dissolution rates'  $r_{sd}^\alpha, r_{sv}^\alpha$  for the vapor and drip zones are defined by:

$$r_{sv}^\alpha(t) \equiv [V_{sv} A_{sv} \rho_{sv} X_{sv}^\alpha + \Sigma_a (V_{av} A_{av} \rho_{av} X_{av}^\alpha)] / A_t \quad (6-51)$$

$$r_{sd}^\alpha(t) \equiv [V_{sd} A_{sd} \rho_{sd} X_{sd}^\alpha + \Sigma_a (V_{ad} A_{ad} \rho_{dv} X_{ad}^\alpha)] / A_t \quad (6-52)$$

and the 'equilibrium film mass concentrations,' for which the dissolution and precipitation/sorption rates would be equal, are defined by:

$$C_{fmd}^\alpha(t) \equiv [V_{sd} A_{sd} \rho_{sd} X_{sd}^\alpha + \Sigma_a (V_{ad} A_{ad} \rho_{dv} X_{ad}^\alpha)] / [\Sigma_p (V_{pd} A_{pd})] \quad (6-53)$$

$$C_{fmv}^\alpha(t) \equiv [V_{sv} A_{sv} \rho_{sv} X_{sv}^\alpha + \Sigma_a (V_{av} A_{av} \rho_{av} X_{av}^\alpha)] / [\Sigma_p (V_{pv} A_{pv})] \quad (6-54)$$

for the drip and vapor zones, respectively. The effective dissolution rates represent the rate of transfer of the  $\alpha$ -th chemical element through the dissolution of the spent fuel and all stationary alteration phases present in solid form. The equilibrium film mass concentrations represent the concentration of the  $\alpha$ -th chemical element in the fluid phase, arising from dissolution of the spent fuel and stationary alteration phases of solid form, at which the mass transfer due to backward reactions that lead to redeposition of alteration materials onto the solid phase exactly balances the rate of mass transfer of that chemical element to the liquid phase due to the forward reactions of dissolution. These effective dissolution rates and equilibrium film mass concentrations can be computed from a more detailed combined speciation and reaction kinetics model in which the parameters that appear on the left sides of these equations would be computed from more fundamental thermodynamic and kinetics considerations. With these definitions, the mass balance Equations (6-49) and (6-50) for the two zones can be solved for the actual film mass concentrations to yield the expressions:

$$C_{fd}^{\alpha}(t) = \frac{r_{sd}^{\alpha} C_{fmd}^{\alpha}}{r_{sd}^{\alpha} + V_{td} C_{fmd}^{\alpha}} \quad (6-55)$$

$$C_{fv}^{\alpha}(t) = \frac{r_{sv}^{\alpha} C_{fmv}^{\alpha}}{r_{sv}^{\alpha} + V_{tv} C_{fmv}^{\alpha}} \quad (6-56)$$

**Film Mass Concentration for Transport and Reaction Rate Limited Regimes**—The film mass concentrations given by Equations (6-55) and (6-56) exhibit the following limiting behaviors. For transport limited conditions when the advective transport of mass is negligible compared to the effective rate of dissolution (as in typical unsaturated laboratory drip release rate tests):

$$C_{fd}^{\alpha}(t) \rightarrow C_{fmd}^{\alpha} \quad \text{if } V_{td} C_{fmd}^{\alpha} \ll r_{sd}^{\alpha} \quad (6-57)$$

$$C_{fv}^{\alpha}(t) \rightarrow C_{fmv}^{\alpha} \quad \text{if } V_{tv} C_{fmv}^{\alpha} \ll r_{sv}^{\alpha} \quad (6-58)$$

For reaction rate limited conditions when the dissolution rate is much smaller than the mass transport rate (as in typical saturated laboratory flow-through dissolution tests):

$$C_{fd}^{\alpha}(t) \rightarrow \frac{r_{sd}^{\alpha}}{V_{td}} \quad \text{if } V_{td} C_{fmd}^{\alpha} \gg r_{sd}^{\alpha} \quad (6-59)$$

$$C_{fv}^{\alpha}(t) \rightarrow \frac{r_{sv}^{\alpha}}{V_{tv}} \quad \text{if } V_{tv} C_{fmv}^{\alpha} \gg r_{sv}^{\alpha} \quad (6-60)$$

**Total Mass Release Rate**—An equation can now be developed from these equation for the total mass  $\Delta M^\alpha$  released from the vapor and drip zones in a given time increment  $\Delta t$ :

$$\Delta M^\alpha \equiv A_t (1 - f_d) V_{iv} C_{fv}^\alpha \Delta t + A_t f_d V_{id} C_{fd}^\alpha \Delta t \quad (6-61)$$

where the vapor and drip zone mass concentrations  $C_{fv}^\alpha, C_{fd}^\alpha$  are given by Equations (6-55) and (6-56), respectively. This general equation may be applied to unsaturated and saturated tests (by appropriately choosing the area fraction  $f_d$ ) and to low flow rate and high flow rate conditions. For interpreting the drip tests, the drip zone liquid flow velocity  $V_{id}$  can be expressed more conveniently in terms of the condensed vapor-water flow velocity  $V_{iv}$  and the drip water volume flow rate  $q_d$  by the equation:

$$V_{id} = V_{iv} + q_d / (A_t f_d) \quad (6-62)$$

In summary, for conditions in which advective transport is sufficiently large for the advective mass transport to dominate the rate of mass accumulation in the liquid phase, the general Equation (6-55) and (6-56) give the variation of film mass concentration with fluid flow rate while including the dissolution of spent fuel, formation of alteration products, and dissolution of the alteration products. Only two time-varying constitutive properties appear in each equation for the film mass concentration  $C_{fd}^\alpha$  or  $C_{fv}^\alpha$  of a particular chemical element  $\alpha$ , namely, the effective rate of dissolution  $r_{sd}^\alpha$  or  $r_{sv}^\alpha$  and the equilibrium film mass concentration  $C_{fmd}^\alpha$  or  $C_{fmv}^\alpha$ . Therefore, in interpreting mass release data from drip tests using this interpretive model, the task is to determine the condensed vapor water circulation rate  $V_{iv}$ , the effective dissolution rates  $r_{sd}^\alpha$  and  $r_{sv}^\alpha$ , and the equilibrium film mass concentrations  $C_{fmd}^\alpha$  and  $C_{fmv}^\alpha$ , given the drip water flow rate  $q_d$ , the incremental mass released  $\Delta M^\alpha$  in the time increment  $\Delta t$ , the total transport surface area  $A_t$  (i.e., the total fuel fragment surface area), and the drip zone area fraction  $f_d$ . For an experiment that involves as many as 10 measured chemical elements, this is a feasible, but formidable, challenge.

**Mass Release Under Advective Transport Limited Conditions**—If the water flow rate is sufficiently low for the advective transport of mass to be the mechanism limiting mass release, the general Equation (6-61) for the mass released simplifies to the form

$$\Delta M^\alpha \equiv A_t (1 - f_d) V_{iv} C_{fmv}^\alpha \Delta t + A_t f_d V_{id} C_{fmd}^\alpha \Delta t \quad (6-63)$$

that is independent of the effective rates of dissolution  $r_{sd}^\alpha, r_{sv}^\alpha$  and is a function only of the equilibrium film mass concentrations  $C_{fmd}^\alpha, C_{fmv}^\alpha$ . This approximation is valid if the flow velocities are sufficiently small that expressions (6-57, 6-58) are satisfied.

The mass released can be expressed in an even more convenient form if it is assumed that, for the flow rates satisfying Equations (6-57) and (6-58), the alteration products being formed are essentially the same in the vapor and drip zones. Under this assumption, the equilibrium film

mass concentration would be the same (i.e.,  $C_{fmd}^\alpha = C_{fmv}^\alpha \equiv C_{fm}^\alpha$ ) in these two zones and Equation (6-63) simplifies to the form:

$$\Delta M^\alpha = (A_t V_{tv} + q_d) C_{fm}^\alpha \Delta t \quad (6-64)$$

Therefore, in interpreting mass release data from drip tests using this advective transport limited approximate model, the task is to determine the condensed vapor water circulation rate  $V_{tv}$  and the equilibrium film mass concentrations  $C_{fm}^\alpha$ , given the drip water flow rate  $q_d$ , the incremental mass releases  $\Delta M^\alpha$  in the time increment  $\Delta t$ , and the transport surface area  $A_t$  (i.e., the total fuel fragment surface area). In this approximation, it is not necessary to independently specify the transport surface area fraction  $f_d$  because it is assumed that the same chemical transformations occur in the drip and vapor zones. When compared to the full interpretive model for mass release given by Equation (6-61), the number of parameters that must be determined from the drip test data is much smaller in this approximate model. These parameters are the single value of the condensed vapor water circulation rate  $V_{tv}$ , and the equilibrium film mass concentration  $C_{fm}^\alpha$  for each radionuclide at each measurement time.

**Mass Release Under Reaction Rate Limited Drip Zone and Advective Transport Limited Vapor Zone Conditions**—If the water drip rate is sufficiently high and mass release is reaction rate limited in the drip zone and advective transport limited in the vapor zone, the general Equation (6-61) for the mass released simplifies to the form

$$\Delta M^\alpha = A_t (1 - f_d) V_{tv} C_{fmd}^\alpha \Delta t + A_t f_d r_{sd}^\alpha \Delta t \quad (6-65)$$

that is independent of the equilibrium film mass concentration  $C_{fmd}^\alpha$  in the drip zone and the effective rate of dissolution  $r_{sv}^\alpha$  in the vapor zone. It is a function only of the effective rate of dissolution  $r_{sd}^\alpha$  in the drip zone, and the equilibrium mass concentration  $C_{fmv}^\alpha$  in the vapor zone. This approximation is valid if the flow velocities in the drip and vapor zones are such that the Equation (6-59) is satisfied in the drip zone while the Equation (6-58) is satisfied in the vapor zone. If, in addition, the flow domain is completely saturated, then by setting  $f_d = 1$  it is possible to eliminate the first term on the left side of Equation (6-65), and recover the expression applicable to saturated high flow rate flow-through dissolution tests. Under these circumstances, it is also likely that no alteration products would be formed and the effective dissolution rate is the dissolution rate for the spent fuel itself.

### 6.4.3.1.3 Input and Assumptions

**Methodology for Extracting Model Parameters from Experimental Data**—The release rate model presented above was used to extract data from the unsaturated drip tests performed at the Argonne National Laboratory. In these tests, two standard fuel types (ATM-103 and ATM-106) were tested at three levels of drip rate in zero-drip ( $\beta=1$ ), low-drip ( $\beta=2$ ), and high-drip ( $\beta=3$ ) drip rate tests. The method adopted to fit the data was to assume that the effective dissolution rates and equilibrium film mass concentrations defined as model parameters in the unsaturated

release rate model varied with fuel type, released chemical element, experimental time, and drip rate.

By substituting Equations (6-56) in Equation (6-61), the following equation is obtained for the incremental mass release  $\Delta M_i^{\alpha\beta}$  of  $\alpha$ -th chemical element in the  $\beta$ -th flow-rate test during the time interval  $\Delta t_i^\beta$ :

$$\Delta M_i^{\alpha\beta} = \frac{A_t^\beta (1 - f_d^\beta) V_{tv} r_{svi}^{\alpha\beta} C_{fmvi}^{\alpha\beta} \Delta t_i^\beta}{r_{svi}^{\alpha\beta} + V_{tv} C_{fmvi}^{\alpha\beta}} + \frac{(A_t^\beta f_d^\beta V_{td} + q_{di}^\beta) r_{sdi}^{\alpha\beta} C_{fm di}^{\alpha\beta} \Delta t_i^\beta}{r_{sdi}^{\alpha\beta} + (A_t^\beta f_d^\beta V_{tv} + q_{di}^\beta) C_{fm di}^{\alpha\beta}} \quad (6-66)$$

The data fitting task is to find the set of unknown parameters  $Z \equiv (C_{fm di}^{\alpha\beta}, C_{fm vi}^{\alpha\beta}, r_{sdi}^{\alpha\beta}, r_{svi}^{\alpha\beta}, V_{tv})$  given the measured values of  $\Delta M_i^{\alpha\beta}$ ,  $q_{di}^\beta$ ,  $\Delta t_i^\beta$  and  $A_t^\beta$ . The general method adopted was to minimize with respect to the values of the unknown parameters the square error between the experimentally measured mass release and the mass release predicted by the above equation summed over all chemical elements, measurement times, and tests. That is, minimize the error  $E$  defined by:

$$E(Z) \equiv \sum_{\beta} \sum_{\alpha} \sum_i (\Delta M_i^{\alpha\beta} |_{predicted} - \Delta M_i^{\alpha\beta} |_{measured})^2 \quad (6-67)$$

with respect to each member  $Z_n$  of the set of unknown parameters by setting:

$$\frac{dE}{dZ_n} = \left\{ \sum_{\beta} \sum_{\alpha} \sum_i (\Delta M_i^{\alpha\beta} |_{predicted} - \Delta M_i^{\alpha\beta} |_{measured}) \frac{d(\Delta M_i^{\alpha\beta} |_{predicted})}{dZ_n} \right\} = 0 \quad (6-68)$$

This procedure yields a set of  $n$  coupled non-linear algebraic equations that were solved for the  $n$  unknowns by a suitable iterative method (successive substitution, Newton-Raphson, sub-space projection/iteration methods, etc.). A macro was developed within the Microsoft Excel 97 spreadsheet program for this purpose.

Generally, to solve the problem the number of distinct measurements must equal or exceed the number of unknown parameters. If the effective rates of dissolution and the equilibrium film mass concentrations are allowed to vary with time and remain different in the vapor, low-drip, and high-drip tests, then the number of measurements available was not sufficient to determine all unknown parameters. Furthermore, the greater the number of measurements above the minimum required, the more reliable and accurate are the fitted parameters. For these reasons, it was decided to verify the applicability and adopt the approximate model given by Equation (6-64) for advective transport limited conditions, and the additional assumption of equal equilibrium film mass transfer concentrations in the vapor and low-drip tests. The high-drip test, in which the alteration products from those observed in the vapor and low-drip tests, was excluded from the parameter fitting procedure. That is, the vapor test and low-drip test data were used to determine the vapor-water circulation rate  $V_{tv}$ , and the time varying equilibrium film

mass coefficients  $C_{fm}^\alpha$  for each chemical element at each experimental measurement time. For this case, Equation (6-66) reduces to:

$$\Delta M_i^{\alpha\beta} = (A_i^\beta V_{id} + q_{di}^\beta) C_{fmi}^\alpha \Delta t_i^\beta \quad (6-69)$$

The equations solved for the equilibrium film mass concentrations  $C_{fm}^\alpha$ , obtained by applying Equation (6-68) to Equation (6-69), are given by:

$$\sum_{\beta} (\Delta M_i^{\alpha\beta} |_{predicted} - \Delta M_i^{\alpha\beta} |_{measured}) q_{di}^\beta \Delta t_i^\beta = 0 \quad (6-70)$$

Similarly, the equation for the vapor-water recirculation rate  $V_v$  is given by:

$$\sum_{\beta} \sum_{\alpha} \sum_i (\Delta M_i^{\alpha\beta} |_{predicted} - \Delta M_i^{\alpha\beta} |_{measured}) A_i C_{fmi}^\alpha \Delta t_i^\beta = 0 \quad (6-71)$$

These nonlinear algebraic equations were simultaneously solved for the constant value of  $V_v$  and the unknown equilibrium film mass concentrations  $C_{fm}^\alpha$  at each measurement time.

**Model Application Assumptions**—Although the effect of drip rate on mass transport was explicitly represented in the model, additional dependence of these two constitutive parameters on drip rate (through effects of dissolved chemicals in the incoming drip water) was recognized because different types of alteration minerals were formed in the later stages of these experiments. As shown in Table 6-36, the high-drip rate tests, in particular, showed the formation of boltwoodite as the dominant mineral at long times, whereas schoepite was the predominant mineral formed in the vapor and low-drip tests. These differences in long time response were particularly important because the response at long times, and possible emergence of these minerals as stable end states, are of greater relevance to repository performance than the responses at short times. More recent data, not included in the data sets that were analyzed, show the slow emergence in the low drip test of the same alteration phases that had already been observed in the high-drip test. This indicates that at longer times, the end states of the alteration minerals may be independent of flow rate at sufficiently small flow rates that would allow sufficiently high solute concentrations in the fluid phase for reprecipitation from solution.

For this reason, the vapor and low-drip tests data ( $\beta=1,2$ ) were analyzed together using Equation (6-71) for the vapor-water flow rate and the species film concentrations. Another reason for combining the analyses of the vapor and low-drip test data was that it is impossible to determine the unknown vapor-water flow rate and the species concentrations for the vapor test using the vapor test data alone, because they appear in the vapor-test equations as a single product term. The low-drip and high-drip tests do not have this difficulty because the equations have a known drip flow rate. The high-drip data set was then analyzed separately using the vapor-water flow rate determined from the combined analysis of the vapor and low-drip tests. The vapor-water flow rate was not separately determined from the separate low-drip and high-drip test data sets because the vapor-water flow rate, being the only flow rate present in the vapor test, is a sensitive parameter in the vapor test but not in the low drip and high drip tests where it is

dominated by the drip flow rate. Therefore, it is better estimated in the combined analysis of the vapor and low-drip tests rather than from separate analysis of the low-drip and high-drip data sets. From a physical standpoint, this is a valid procedure because the vapor-water flow rate is primarily a function of the temperature at which the tests are performed, and this was the same (90°C) in all tests.

#### 6.4.3.1.4 Results of Conceptual Model

**Parameters for Release Rate Models for Unsaturated Low Flow Rate Conditions With Secondary Phase Formation**—This section includes the constitutive parameters fitted to the release rate model for unsaturated low flow conditions that account for the formation of alteration mineral products. The approximate model for mass release given by Equation 6-62 was used to analyze the vapor and low-drip test data. This model is valid when the release rate is limited by advective transport, and the alteration minerals formed in the vapor and drip zones are of the same composition and have the same equilibrium film mass concentrations.

The equilibrium mass concentrations and vapor-water recirculation velocities that were fitted to the vapor and low-drip test data are in Tables 6-37 and 6-38 for ATM-103 and ATM-106 spent fuels, respectively. The equilibrium mass concentrations determined in this way are plotted against time in Figures 6-36 and 6-37 for ATM-103 and ATM-106 spent fuels, respectively. The first important aspect of these results is that all equilibrium film mass concentrations decrease in value with increasing time by many orders of magnitude. This is important because it implies that the formation of alteration products reduces radionuclide releases far below the initial short-term levels. The second important feature is that the equilibrium film mass concentrations appear to approach constant values (*within the order of magnitude experimental data fluctuations*) at long times. This is important because constant long-term values would imply that stable alteration minerals are being formed. The calculated equilibrium film mass concentrations indicate that the mass releases are not congruent, although dissolution of spent fuel itself may be congruent. That is, the radionuclides are not released proportional to their mass abundance in the fuel matrix; therefore, they are not released congruent with the dissolution process. Finally, the relative magnitudes of the equilibrium film mass concentrations for different chemical elements cannot be explained solely on the basis of their pure element solubilities, possibly underscoring the importance of preferential substitutional incorporation of elements in alteration minerals.

An important aspect of the equilibrium film mass concentrations presented here is that in the advective transport limited analysis model, the concentrations are the actual film mass concentrations of the chemical elements and, therefore, can be compared directly to the pure-element solubilities previously recommended in TSPA-1995 for bounding the radionuclide mass releases from spent fuel. The long-term equilibrium film mass concentrations and the TSPA-1995 recommended average, minimum and maximum solubilities are in Table 6-39 and are plotted in Figure 6-38 for comparison. The comparison shows that the equilibrium film mass concentrations are many orders of magnitude smaller than the average recommended TSPA-1995 values, and are often many orders of magnitude smaller than the minimum solubilities recommended in TSPA-1995. Thus, the formation of alteration minerals under unsaturated slow flow conditions appears to reduce the release of radionuclides into the flowing groundwater by many orders of magnitude. If these preliminary results can be confirmed with additional

experiments and analysis, and can be shown to be applicable to repository performance over long time periods, then secondary phases may be a key feature in the success of an oxidizing, unsaturated repository.

**Colloid Formation**—Colloids have been observed in numerous spent fuel dissolution tests (see Section 6.4). In the analyses given above, the species concentrations in the fluid phase include the species masses that exist both as dissolved solutes and as colloid particles suspended in the fluid phase. As such, these concentrations represent the total radionuclide masses that were released in the tests and they should be used to estimate the total releases that would occur under unsaturated drip-flow conditions in a geologic repository.

#### 6.4.3.1.5 Abstraction/Implementation into RIP

The results of this interpretation of experimental data has been incorporated into specific sensitivity analyses, but not into the TSPA-VA base case. The sensitivity analysis used the average of the calculated thin film concentrations for Pu, U, Tc and Np from Tables 6-37 and 6-38 in place of the solubility distributions for those elements. This is a simplistic initial representation of the secondary phase retention process. Results are discussed in Section 6.6.

#### 6.4.3.1.6 Representation/Validity

**Applicability of Results to Repository Performance**—The applicability of the results of laboratory experiments performed over very short time periods of 3 to 4 years to the long term (1,000-100,000 years) release of radionuclides under repository conditions can strictly be assessed only by examining the thermodynamic stability of the alteration phases under the changing hydrological and geochemical conditions in the near field of the repository over time scales representative of the repository performance period. Because such long term experiments are impossible to perform, releases over the performance period must be estimated on the basis of the persistence of the alteration products and mechanisms of their formation over long time intervals. If the environmental conditions (e.g., water saturation, temperature, water composition) are assumed to be fixed, then the temporal evolution of the mineral phases to a thermodynamically stable end state may be assessed with less difficulty. Subject to the availability of the relevant thermodynamic data, the thermodynamic stability of different mineral phases as end states may be accomplished through the use of geochemical speciation computer programs such as EQ3 (Wolery 1992), and the rates at which the transformations occur may be estimated using geochemical kinetics computer programs such as EQ6 (Wolery 1992). With less certainty, confirmatory assessments of the stability of the alteration phases can be obtained through comparison against the mineral phases that presumably have persisted over very long times in natural field analogs at many sites throughout the world.

It is also important to recognize that the mineral phases formed in multi-component water chemistries of thin films on spent fuel surfaces will not always be ideal. That is, the different elements in the actinide series of radionuclides can become substitutional atoms in precipitated mineral phases. Furthermore, passive product elements, which may form a set of minerals, can also be adsorbed on the surfaces and become substitutional atoms in mineral phases. Thus, idealized thermodynamic equilibrium evaluations, that do not account for these phenomena, may

not be in full agreement with available experimental data or with observations made in field analogs.

#### **6.4.3.2 Secondary Phase Formation/Radionuclide Retention: Detailed Numerical Modeling**

Another approach to representing the retention of radionuclides in secondary phases was taken using reactive transport modeling of low water flow rate alteration of spent fuel. This approach was also used for sensitivity analyses, and not in the TSPA-VA base case. It is expected that future evolution of models such as these will be usable in future TSPA analyses.

##### **6.4.3.2.1 Conceptual Model**

In this section, the results of detailed numerical modeling of radionuclide release from dissolving spent fuel and secondary phases are presented together with a discussion of the underlying assumptions of the analysis and the adequacy and quality of available data used in the analysis.

As water seeps into failed WPs, it will react with CSNF. CSNF will dissolve and secondary-uranium minerals will precipitate. Since both laboratory experiments (Buck et al. 1998) and theoretical study (Burns et al. 1997) show Np (maybe Pu, too) will be incorporated into secondary uranyl minerals (coprecipitation), the releases of Np (Pu) could possibly be controlled by the formation and dissolution of secondary minerals. The formation/dissolution of secondary phase is determined by many factors, such as the pH and other chemical parameters of the water seeping into WPs, the partial pressure of CO<sub>2</sub>, temperature, hydrogeological condition, and cladding failure. Considering these controlling factors, this section presents an alternative model of Np release by secondary phase dissolution.

The model is mechanistic based on the general reactive-transport simulator AREST-CT Version 1.2, CSCI 30019 V.1.2. AREST-CT was developed at Pacific Northwest National Laboratory (Chen et al. 1995; Chen et al. 1996; Chen et al. 1997a, b), and modified at Performance Assessment Operation of CRWMS M&O (Chen 1998). The code considers chemical interactions among solid, gaseous, and aqueous phases under flow conditions. The underlying mathematics of AREST-CT is a set of coupled, nonlinear, partial differential equations that describe the time change rate of the solute concentrations of pore water in a porous medium, and the alteration of solid phases. The current Version accounts for the following processes:

- Kinetic dissolution of solid phases
- Kinetic precipitation and dissolution of secondary phases
- Aqueous equilibrium speciation
- Gas-aqueous equilibria
- Redox reactions
- Advection
- Diffusion
- Dispersion
- Nucleation thresholds for precipitation of new solids

Other physical and chemical features in the code are:

- 1-D or 2-D simulation domains
- General interface to take user-specified chemistry
- Nonisothermal or isothermal chemistry
- Ionic strength correction according to modified B-dot equation (Wolery 1992)
- Spatially varying distribution of solid phases
- Effective reaction surface depending on texture of solids

The primary output of AREST-CT consists of:

- Concentrations of aqueous species as a function of time and space
- The chemistry of aqueous solution exiting the simulation domains
- pH changes
- Radii, surface areas, and volume fractions of solids as a function of time and space
- Dissolution/precipitation rates of solids
- Porosity changes

The computer code takes a number of input parameters. One type of input is the system parameters relevant to the design and hydrological/geochemical conditions of the repository. The other is thermodynamic and kinetic parameters measured or calculated according to the fundamental sciences that quantify the chemical reactions.

To avoid confusion, in the following discussion, the computer code of AREST-CT used to build the model is referred to as *the code*. The integrated product, including the conceptualization of the processes, assumptions adopted, and input parameters along with the code, is referred to as *the model*.

The model consists of two submodels. One is the spent fuel dissolution and secondary mineral formation for the first 1,000 years after WPs are breached, named the Step-1 submodel. The other is Np release from secondary-phase dissolution following CSNF disappearance, named the Step-2 submodel. Ideally, the two submodels should be integrated. However, they are presented separately this time, as the first round of the study. The Step-1 submodel should be regarded as a part of the model validation activity. Only the results of the Step-2 submodel go into TSPA analyses.

#### **6.4.3.2.2 Step-1 Submodel**

The Step-1 submodel starts when WPs fail. The purpose of the Step-1 submodel is model validation (or confirmation). It compares the model predictions to observations of Argonne National Laboratory's drip tests (Wronkiewicz et al. 1992; Finn et al. 1994a; Finn et al. 1998b), which simulate the corrosion of CSNF under repository conditions.

##### **6.4.3.2.2.1 Input and Assumptions**

**Physical Configuration of the Simulation Domain**—The model treats WPs of CSNF as a 1-D column, as shown in Figure 6-39. Column length is 1.56 m (CRWMS M&O 1995, p. 3-13,

Table 3.5-1), the inner diameters of 21-PWR WPs. Dripping water enters the column at the top and exits at the bottom. The volume fraction of CSNF is 14 percent, equal to the waste form volume in a WP divided by the void space of the WP (CRWMS M&O 1998c). Cladding and basket materials occupy 21 percent of the space and they are assumed inactive. Thus, the porosity of a WP is 65 percent.

**Pore-water Velocity**—According to the model results for the long-term average seepage into drift model (see Chapter 3) and the average patch failure area of WPs (see Chapter 5), the average pore-water velocity of water seeping into WPs is set to 3.36 cm/year. Water saturation in WPs is assumed to be 70 percent.

**Incoming Water Composition, Gas Fugacity, and Temperature**—Preliminary predictions by the WAPDEG model show that, under dripping conditions, WP failure starts at 4,000 years after emplacement. (Final WAPDEG results show WPs start failure at 2,700 years under dripping conditions [see Chapter 5]. Future work needs to address different water and gas chemistry.) Based on the gas compositions and thermal history, six periods (A-F) were defined for the base NFGE (see Chapter 4). Period E covers 4,000 to 10,000 years, and Period F covers 10,000 to 100,000 years. Therefore, it is expected that CSNF will be subject to the environments of Periods E and F. Table 6-40 lists the relevant conditions of Period E and Period F given by NFGE study (see Chapter 4). The temperature is 70°C for Period E and 30°C for Period F. For the Step-1 submodel, Period E conditions are used, for it is closer to those of the drip-tests.

**Spent Fuel Available to React and Cladding Failure**—As predicted by the cladding corrosion model (cf. Section 6.3.1.1), some of the CNSF in the WP would be protected by the Zircaloy cladding and would not be exposed to the seeping water. The available amount of CSNF is assumed to be linearly proportional to the fraction of failed cladding. For the Step-1 submodel, 11 percent cladding failure, the maximum amount caused by mechanical forces, is considered. Consequently, the volume fraction of the available CSNF in a WP at the start of the simulation is 1.54 percent. The rest of CSNF is assumed inactive. The specific surface area of spent fuel was set to 39.6 cm<sup>2</sup>/g, the value used in the base case for TSPA-VA.

**System Components, Species, and Equilibrium Reactions**—The system consists of eight components: H, O, CO<sub>2</sub>, SiO<sub>2</sub>, Ca, Na, Cl, and U. Based on the criterion that under the pH conditions of interest, the major species of those components should be accounted for, 26 aqueous species and 2 gaseous species are included in the model. A pH value of 8.0 was used for species choice. As shown later, because reactions with spent fuel and secondary phases in the WP do not cause the pH to deviate significantly from 8, the selected species would sufficiently represent the system. Sixteen aqueous equilibrium reactions and 2 gaseous-aqueous equilibrium reactions are constructed among those species. Reaction construction is according to EQ3/6 database (Version 7.2b, CSCI LLNL # UCRL-MA-110662) (Wolery 1992). Reactions have been rearranged to eliminate unselected species. Those equilibrium reactions are listed in Table 6-41. The equilibrium constants data used in the simulations are taken from EQ3/6 database data0.com.R22a (Wolery 1992), and fitted into fourth-order polynomial functions of temperature. The coefficients of the polynomial functions are also listed in Table 6-41.

**Spent Fuel Dissolution**—Chemically, spent fuel is treated as pure  $\text{UO}_2$ . The reaction of spent fuel dissolution is in Table 6-42. The equilibrium constant of uraninite ( $\text{UO}_2$ ) (Wolery 1992) is assigned to spent fuel.

The dissolution of spent fuel is treated as kinetically controlled. As a mechanistic geochemical code, AREST-CT assumes kinetic reactions obey the general form of Transition-State Theory (TST) rate law. Therefore, a rate equation consistent with TST rate law is required by the code.

Gray et al. (1992) studied the dissolution kinetics of CSNF under oxidizing conditions by flow-through experiments. Since oxidizing conditions are currently expected to prevail in WPs once they are breached and gas composition will be similar to that of atmosphere (DOE 1998, Chapter 4), Gray's experiment is relevant to the YMP repository. Several dissolution rate equations are given in that article. Based on the same data set, other rate equations are derived to account for burnup and other factors (Stout and Leider 1997). However, among those rate equations of CSNF dissolution, only Equation (1) of Gray (Gray et al. 1992, p. 50, Table 3) is consistent with the general form of TST rate law. Therefore, it was implemented in AREST-CT. Gray's Equation (1):

$$\log R = 7.45 + 0.258 \log[C] + 0.142 \log[H] - 1550/T \quad (6-72)$$

where  $R$  is the dissolution rate of  $\text{U}$  in  $\text{mg}/[\text{m}^2\text{-day}]$ ,  $C$  stands for the total of  $\text{CO}_3^{2-}$  and  $\text{HCO}_3^-$  concentrations,  $H$  stands for the concentration of  $\text{H}^+$  (both in mole/kg water), and  $T$  is the temperature in Kelvin. In AREST-CT, it is implemented as the forward dissolution rate in the form

$$R' = 0.00137 \times e^{\frac{29697}{RT}} a_{\text{CO}_2}^{0.258} a_{\text{H}^+}^{0.142} \quad (6-73)$$

where  $R'$  is the dissolution rate of spent fuel in  $[\text{mole}/\text{m}^2\text{-sec}]$ ,  $R$  is the gas constant,  $a_{\text{CO}_2}$  and  $a_{\text{H}^+}$  are activities of  $[\text{HCO}_3^- + \text{CO}_3^{2-}]$  and  $\text{H}^+$ , respectively.

**Secondary Uranyl Minerals**—As discussed in Section 6.4.3, about 10 secondary uranyl minerals are identified as the product of CSNF dissolution. They are grouped into three categories: (a) uranyl-oxide hydrates, including schoepite, dehydrated schoepite, compregnacite, and becquerelite; (b) uranyl silicate hydrate (soddyite); and (c) uranyl alkaline silicate hydrate, including uranophane, boltwoodite, Na-boltwoodite, and sklodowskite. In this set of modeling studies, four are included in the model: schoepite, soddyite, uranophane, and Na-boltwoodite. The first two represent the first two categories and the last two represent the third category. The choice is mainly based on their abundance observed in laboratory experiments (Wronkiewicz et al. 1992) and natural analogs (Percy et al. 1994, p. 725, Figure 8). Another consideration in choosing those secondary minerals is the availability of thermodynamic and kinetic data. Their reactions, according to EQ3/6 database (Wolery 1992), are listed in Table 6-42.

Their equilibrium constants ( $K^{\text{eq}}$ ) listed in the EQ3/6 database are estimated values, except for schoepite. Nguyen and his colleagues (Nguyen et al. 1992, p. 374, Table 6) gave different values for soddyite, uranophane, and sodium-boltwoodite in their solubility experimental study. Since we believe the data obtained from experimental study have higher quality than the estimated

values, the  $K^{eq}$  values for uranophane, soddyite, and Na-boltwoodite from Nguyen are used in the model calculation.

Their rate constants are derived from the experimental results reported by Casas et al. (1994, p. 62-64), Bruno et al. (1995, p. 635, Table 1), and Perez et al. (1997, p. 571, Equation 9) by assuming that forward dissolution rate equals

$$R = k_0 e^{-\frac{E_a}{RT}} a_{H^+}^{v_{H^+}} \quad (6-74)$$

where  $v_{H^+}$  is the stoichiometric coefficient of  $H^+$  in the dissolution reactions for those minerals as given in the EQ3/6 database (Wolery 1992). Since the experiments were carried out at one temperature, there is no information to derive the activation energy  $E_a$  from, and the exponential term was incorporated into the rate constant. Table 6-43 lists their rate constants.

Two types of rate constants are in the table. One is in the unit of  $\text{mol}/\text{m}^2\text{-sec}$  and the other in  $\text{m}/\text{sec}$ . They are equivalent to each other under the assumption solids are in spherical shape. The rate constant for Na-boltwoodite is guessed from uranophane data, since they are similar in crystal structures and chemical compositions.

#### 6.4.3.2.2 Results of Simulations for Step-1 Submodel

The simulations were carried out for 2,000 years. The calculated dissolution rate and volume changes of spent fuel are shown in Figure 6-40. Figure 6-40a shows that the dissolution rate of CSNF is almost constant, both spatially and temporally. Figure 6-40b reveals that available CSNF is totally consumed in less than 500 years.

The development of secondary phases throughout the one-dimensional column of CNSF is shown in Figure 6-41. Schoepite is the major secondary uranyl-mineral and distributes almost uniformly within the WPs. Except for the top portion ( $\sim 0.2$  m) of the WP, after 1,000 years about 4 percent (volume fraction of the WP) schoepite precipitates uniformly across the WP. The ratio of schoepite to the originally available spent fuel is about  $4/1.54 = 2.597$ . The number is very close to the expansion factor of molar volumes from  $\text{UO}_2$  to schoepite, that is  $66.08 \text{ cm}^3/\text{mol} : 24.618 \text{ cm}^3/\text{mol} = 2.684$  (Wolery 1992). That means, more than 90 percent of  $\text{UO}_2$  is converted to schoepite. The rest has either formed uranophane or soddyite, or has been removed by transport. After 500 years, schoepite starts dissolving at the entrance to the one-dimensional column.

As shown in Figure 6-41b, uranophane precipitates mainly at the top of the WPs. That is because the precipitation reaction rapidly depletes Ca in the incoming water. For a similar reason, soddyite precipitates at the top of the WP, due to the consumption of Si. However, soddyite redissolves after spent fuel has been consumed because of the decrease in U concentration. In contrast to soddyite, uranophane keeps growing even after spent fuel disappears. Na-boltwoodite is not observed in the simulation.

The reactive-transport model is based on the average of many solid grains and does not provide meaningful results for individual grains. Therefore, the simulation results do not represent, in a strict sense, the paragenetic sequence of secondary minerals. However, a general sequence of mineral formation can still be derived from movements of reaction fronts. For example, scrutinizing the development of the precipitation fronts of secondary minerals reveals that the growth of uranophane is at the expense of schoepite and soddyite. Figure 6-42 is the derived formation sequence summarized based on the simulation results. A dashed line means metastable phase. Both schoepite and soddyite become metastable after the spent fuel is consumed.

Figure 6-43 shows the pH and U(total) concentration at the bottom of the WP as functions of time. The pH drops initially and then reverses to its initial value, though the change is quite small (only 0.25 pH unit). The concentration of U(total) increases first and then decreases, due to the precipitation of secondary minerals. The final U concentration is about  $6 \times 10^{-5}$  mole/kg.

#### 6.4.3.2.2.3 Model Validation

Model validation has different meanings to different individuals. Model validation here means, according to OCRWM Quality Assurance Requirement Document (QARD) (OCRWM 1998, p. 3), "...comparing analysis results against data acquired from laboratory or field experiments, natural analogue studies, or observations that were not used in the original development of the model."

The laboratory observations used to do the comparison are from the drip tests done at Argonne National Laboratory (Wronkiewicz et al. 1992, Finn et al. 1994b, Finn et al. 1998a, Finn et al. 1998b). Although the drip tests are not set up for model validation, they are comparable in several aspects: (1) both the model and experiments are flow-through systems consisting of spent fuel; (2) the composition of incoming water in both cases is J-13-like water reacted with tuff rock; and (3) the temperature for drip tests is 90°C, while that of the simulation is 70°C. Thus, the drip tests are good benchmarks for validating the model. However, disparities between them in other aspects and limited quantitative information measured in the experiments determine that the comparison can be done only on a semi-quantitative basis. An example for the former case is that the drip tests are in much smaller scales in time and space. The example for the latter case is that the water-solid ratio cannot be determined for the tests from the information presented in the papers. Therefore, the validation can be only partially accomplished.

The modeling results and corresponding experimental observations, along with comments/explanations are listed below in four categories.

#### Dissolution Rate of Spent Fuel

*Modeling Result*—the dissolution rate of spent fuel varies less than 15 percent with time and space.

*Lab Observation*—"either that the reaction pathways have been constant during this time or that the contribution from multiple reaction pathways has not varied over time" (Finn et al. 1998b, p. 129, paragraph 2).

*Comments*—the modeling results and laboratory observations match each other quite well.

*Modeling Result*—spent fuel is totally consumed in less than 500 years. In other words, more than 0.2 percent spent fuel dissolves each year.

*Lab Observation*—“<sup>99</sup>Tc release fraction should reflect the minimum matrix dissolution rate” (Finn et al. 1998b, p.129, paragraph 1) and “0.03 of the total <sup>99</sup>Tc inventory has been released after 3.7 years of reaction” (Finn et al. 1998b, p. 129, paragraph 2) That is, 0.81 percent spent fuel dissolves each year.

*Comments*—the predicted average dissolution rate of CSNF is of the same order as the observed rate, but lower by a factor of 4. The lower temperature used in the model calculation may contribute to the difference.

### **Abundance and Distributions of Secondary Minerals**

*Modeling Result*—schoepite is the major secondary phase and distributes evenly in the WP.

*Lab Observation*—“dehydrated schoepite is the dominant alteration phase” (Wronkiewicz et al. 1992, p. 115, paragraph 4).

*Comments*—They match each other very well, if the distinction between schoepite and dehydrated schoepite is disregarded.

*Modeling Result*—uranophane mainly precipitated at the top of the WP.

*Lab Observations*—“Uranophane is the most common phase observed on the top surface ... but is conspicuously absent from the sides and bottoms of these samples” (Wronkiewicz et al. 1992, p. 118, paragraph 5).

*Comments*—The simulation results correctly reproduce the same phenomenon observed in the experiments. They reflect the mechanism that the rapid precipitation of uranophane consumes Ca in the incoming water.

*Modeling Result*—a small amount (<0.5 percent) of soddyite has been precipitated at a time of 10 years. It re-dissolves after CSNF disappears.

*Lab Observation*—“Soddyite has been identified as a minor alteration product” (Wronkiewicz et al. 1992, p. 118, paragraph 4).

*Comments*—Soddyite redissolution cannot be observed in the experiments as CSNF matrix is present throughout the experiment.

*Modeling Result*—No Na-boltwoodite precipitates.

*Lab Observation*—“Like uranophane, boltwoodite is found only on the top surfaces of samples” (Wronkiewicz et al. 1992, p. 118, paragraph 5). “The major alteration product in the high-drip-rate tests was determined to be Na-boltwoodite” (Finn et al. 1998b, p. 125, paragraph 3).

*Comments*—Several reasons can cause the discrepancy. One guess is that the equilibrium constant data for Na-boltwoodite used in the simulation, which is measured at 30°C, is not an accurate approximation for 70°C. As it is believed that uranyl minerals have the tendency of retrograde solubility (Murphy 1997), the solubility of Na-boltwoodite at 70°C should be lower than that at 30°C. Therefore, Na-boltwoodite may appear if its equilibrium constant at higher temperature is available and used. As uranophane and Na-boltwoodite have very similar

chemical composition and crystal structures, the discrepancy should not be regarded as evidence that the model is invalid.

### **Paragenetic Sequence**

*Modeling Result*—As outlined in Figure 6-42, the paragenetic sequence of secondary phases is schoepite (uranium oxide hydrate)->soddyite->uranophane (uranium alkali silicate).

*Lab and Field Observation*—Wronkiewicz (1992, p. 122, Figure 7) summarized the paragenetic sequence of drip tests as uranium oxide hydrates->soddyite->uranium alkali silicate. Murphy (1997, p. 718, paragraph 2) also summarized the paragenetic sequence of uranyl minerals at the natural analog site at Pena Blanca as schoepite->soddyite->uranophane.

*Comments*—The good match in paragenetic sequence between simulation results and laboratory and field observations suggests that the model qualitatively reproduce the replacement relations among uranyl minerals. It suggests the thermochemical and kinetic data used in the model can correctly reflect the phase relations, at least qualitatively.

### **Water Chemistry at Bottom of WP**

*Modeling Result*—As shown in Figure 6-43, pH at the exit drops first, followed by an increase. The change is quite small, from 8.2 to 7.95.

*Lab Observations*—“the pH (of the dripping water) was 8.4” (Finn et al. 1994b, p. 197, paragraph 5). “the leachate had a pH of 6.0 at 57 d and 6.3 at 120 d” (Finn et al. 1994b, p. 190, paragraph 4).

*Comments*—the simulation correctly reproduces the trend of pH changes, though the change is much smaller. Possible explanations for the small change in pH include: (1) the water-solid ratio of the simulation is larger than that of the experiments, (2) radiolysis effects are not included in the model, and (3) the simulation does not catch the large pH change at the early stage because the first recorded time slice was set too large (10 years).

*Modeling Result*—U(total) concentration at the exit increases first, then decreases. After 10 years, the concentration is between  $10^{-5}$ – $10^{-4}$  mol/kg.

*Lab Observation*—the average U concentration of the leachate reported by Wronkiewicz et al. (1992, p. 108, Table 1, column 4) is 3.2 µg/ml =  $1.34 \times 10^{-5}$  mol/kg.

*Comments*—the calculated U concentration matches the experiments very well.

It is worth pointing out that the simulation was not calibrated by those laboratory and field observations. It is a blind prediction, and no data were manipulated. The only exception is that the observations of secondary mineral abundance have been used to choose which uranyl minerals to include in the model.

The above comparison demonstrates the model reproduces experimental results and field observations in many aspects. More important is that no contradiction among them has been found yet. It strongly indicates that the model, (consisting of the computer code, the conceptualization, and the data used in the simulation), is a reasonably good representation of the real system.

The above validation, though still partial and preliminary, shows the capability of the model in predicting the behavior of waste form under the repository conditions. It gives a certain degree of confidence to say a working spent fuel dissolution model has been established. While it is highly desirable to continuously build confidence by obtaining high quality thermodynamic and kinetic data and fine-tuning the model, the objective is to use the model to investigate radionuclide mobilization in WPs.

#### 6.4.3.2.3 Step-2 Submodel

As discussed above, both laboratory observation and simulation results show CSNF will be totally consumed and converted to secondary uranyl minerals in  $10^2 - 10^3$  years. For the time frame of performance assessment,  $10^2 - 10^3$  years can be considered an instant. In other words, CSNF will quickly convert to secondary uranyl minerals once WPs are breached. Therefore, for the long-term performance of the repository, the period after CSNF has been converted to secondary minerals is more important. The Step-2 submodel is developed to analyze the dissolution behavior of secondary minerals, and Np (and other actinides) release from the dissolution of secondary phases.

##### 6.4.3.2.3.1 Input and Assumptions

The input parameters for the Step-2 submodel are very similar to the Step-1 submodel. Only the differences and additions will be discussed in the following text.

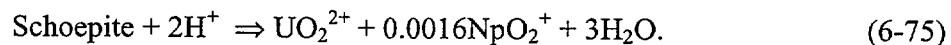
**Physical Configuration of the Simulation Domain**—The basic configuration is the same as in the Step-1 submodel. However, the starting time is set to the point when spent fuel has been totally converted to secondary phases. As seen in the results of the Step-1 simulation, schoepite is the major secondary uranyl mineral and forms evenly within the WP. It is taken as the surrogate of all secondary minerals, and is assumed to be uniformly distributed throughout the WP. Furthermore, it is assumed all the available CSNF has been converted to schoepite; i.e., the amount of schoepite in the WP equals the amount of available CSNF times the expansion factor of molar volumes from  $UO_2$  to schoepite (2.684). Consequently, the porosity of the WP =  $1 - V_{\text{schoepite}} - V_{\text{unavailable CSNF}} - 0.21$ , where 0.21 is the volume fraction of inert components, including cladding and basket materials. Two scenarios (named Scenario-1 and Scenario-2 in the following), with 4.13 percent and 0.38 percent schoepite, are considered in the Step-2 submodel. They correspond to 11 percent and 1 percent cladding failure cases (the maximum and minimum of mechanical cladding failure), respectively. The radius of schoepite is arbitrarily assumed to be 1 mm, with a specific surface area of  $6.15 \text{ cm}^2/\text{g}$ .

**System Components, Species, and Equilibrium Reactions**—In the Step-2 submodel, one more component, Np, is added. The Np component comprises 12 aqueous species, including Np(IV), Np(V), and Np(VI) species. Eleven aqueous Np equilibrium reactions are included in the Step-2 submodel. The total number of aqueous species is 38 plus 2 gaseous species. There are 25 complexation reactions, 2 redox reactions, and 2 gaseous-aqueous equilibrium reactions (see Table 6-44).

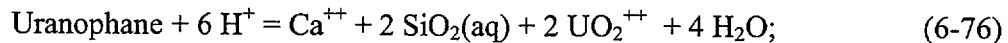
**Np Incorporation into Uranyl Minerals**—Based on an analyses of the crystal-chemical properties of U-O bond, Np-O bond, and Pu-O bond, Burns and his colleagues (Burns et al.

1997) predict that “the substitutions  $\text{Pu}^{6+} \leftrightarrow \text{U}^{6+}$  and  $(\text{Np}^{5+}, \text{Pu}^{5+}) \leftrightarrow \text{U}^{6+}$  are likely to occur in most  $\text{U}^{6+}$  structures” (Burns et al. 1997, p. 8, paragraph 5). Later, Buck and his colleagues at Argonne National Laboratory (Buck et al. 1998) confirmed the prediction by TEM (transmission electron microscope) analyses of the corrosion product of spent fuel drip tests. In their study, Np is found incorporated into dehydrated schoepite (Buck et al. 1998, p. 91). Therefore, it is reasonable to assume Np will not be totally released into the aqueous phase during the period of CSNF corrosion. Instead, some of the Np will be segregated into the secondary schoepite.

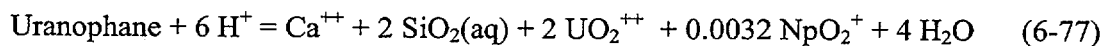
Since the purpose for the Step-2 submodel is to analyze the release of Np after CSNF has been totally converted to secondary minerals, it is conservative to assume that the Np inventory remains with schoepite, the surrogate of secondary uranyl minerals. Furthermore, the inventory of  $^{237}\text{Np}$  was adjusted to include both  $^{241}\text{Pu}$  and  $^{241}\text{Am}$ , because they quickly decay to  $^{237}\text{Np}$ . ATM-103 fuel with a burn-up of 30 MWd/kg, and 10 years out of core is used as the reference. The inventory for  $^{237}\text{Np}$ ,  $^{241}\text{Pu}$ ,  $^{241}\text{Am}$  for this fuel is listed in Table 6-45. According to the inventory, the molar ratio of  $\text{U} : ^{237}\text{Np}$  is 1:0.0016. Therefore, for these analyses, one mole of schoepite contains 0.0016 mole of Np. The dissolution reaction for schoepite is approximately written as



As schoepite dissolves, other more stable uranyl minerals (uranophane, soddyite, and Na-boltwoodite, called tertiary minerals) will precipitate. Although it is believed Np can also be incorporated into tertiary minerals (Burns et al. 1997), it is yet to be confirmed by laboratory analysis. Let us consider two hypotheses: Hypothesis-1 is that Np does not incorporate into tertiary minerals. Hypothesis-2 is that Np incorporates into tertiary minerals congruently with U. For example, for Hypothesis-1, uranophane reaction is



For Hypothesis-2, the corresponding reaction is:



Hypothesis-2 also implies that in aqueous phase, Np should have a congruent relation with U. This hypothesis is supported by several laboratory observations. Sassani and Siegmann (CRWMS M&O 1998a, p. 7, paragraph 3) concluded that “The data suggest that Np enters the aqueous phase congruently with U as the fuel dissolves” by analyzing Series 2 steady-state tests results (Wilson 1987, 1990a). Bruno and his colleagues (Bruno et al. 1998, Slide 9) also observed the congruent relation between Np and U. Therefore, Hypothesis-2 does have experimental evidence to support it, although direct evidence is needed to confirm it.

**Incoming Water Composition, Gas Fugacity, and Temperature**—Both Period E and Period F conditions were considered in the Step-2 submodel, referred to as Condition-1 and Condition-2.

**Eight Combinations of Scenarios, Hypotheses, and Conditions**—There are eight possible combinations for the above described scenarios, hypotheses, and conditions. These eight combinations are listed in Table 6-46 and represent the eight simulations. These simulations are referred to as Case-1 through Case-8 in the table, and in the following discussion.

#### 6.4.3.2.3.2 Results of Simulations for Step-2 Submodel

The results of the eight simulations are quite similar. Case-1 will be discussed in detail. Figure 6-44 and Figure 6-45 are the profiles for schoepite and uranophane. They show that schoepite is dissolved with time and replaced by uranophane. Schoepite dissolution and uranophane precipitation take place across the whole WP before 10,000 years. After 10,000 years, the replacement is localized to the dissolution/precipitation front that advances from upstream to downstream. At about 50,000 years, schoepite is totally replaced by uranophane. Soddyite and Na-boltwoodite are not observed.

Figure 6-46 shows the calculated concentration of U for Case-1. It increases with depth into the WP and reaches its maximum ( $\sim 2 \times 10^{-5}$  mole/kg) at the bottom of WP. The U concentration at the bottom does not change much until 50,000 years, when schoepite has been totally replaced by uranophane. It appears that before 50,000 years, the controlling mineral for U concentration is schoepite. After that, the controlling mineral is uranophane.

Figure 6-47 is the calculated concentration of Np for Case-1. Its behavior is very similar to U. Its maximum concentration is about  $3.7 \times 10^{-7}$  mol/kg.

Figure 6-48 shows the Np concentration curves at the bottom of the WP of all 8 simulations, with Np range for the TSPA-VA base case included for comparison. From the figure, the following phenomena can be observed:

**Hypothesis-1**—Np concentration for the cases of Hypothesis-1 (Cases 1-4, curves without symbols) ranges from  $10^{-8}$  to  $10^{-6}$  mole/kg. The upper-bound is about a factor of 100 lower than that of the TSPA-VA base case Np solubility distribution, which ranges from  $10^{-7.3}$  to  $10^{-4}$  mole/kg (cf. Section 6.4.1). The lower-bound is about 5 times lower than that of the TSPA-VA base-case value. It suggests that if the assumption of Np hold up by schoepite is correct, even without invoking Hypothesis-2, this alternative model yields lower effective Np concentration.

**Hypothesis-2**—Np concentration for the cases of Hypothesis-2 (Cases 5-8, curves with symbols) ranges from  $10^{-9}$  to  $10^{-7}$  mole/kg. This is almost 1,000 times lower than the TSPA-VA base-case value. If the hypothesis of Np incorporation into uranophane and other uranyl minerals could be confirmed, then the effective concentration of Np should be much lower than the solubility value used in TSPA-VA.

For Case-5 and Case-7 (Hypothesis-2, 11 percent cladding failure, 70°C and 30°C, respectively), Np concentrations decrease at a later time by at least 10 times. That is because schoepite is consumed and the release rate from uranophane dissolution is lower than from schoepite dissolution.

*Cladding Credit*—As one can expect, the percentage of cladding failure has a large effect on Np concentration. Np concentrations for cases with 1 percent cladding failure are about 10 times lower than that for cases with 11 percent cladding failure. The exception is for the pair of Hypothesis-1 cases at 30°C, where the difference is smaller. The cause of this is unclear and will be investigated in the future.

*Temperature Effect*—For most time, Np concentrations for the cases at 30°C are higher than for cases at 70°C, with a difference of less than 1 order of magnitude. This is because of the retrograde solubility of schoepite. Moreover, the effect is smaller for the cases of Hypothesis-2 than for the cases of Hypothesis-1. In general, the temperature effect is not as strong as the effect of Hypothesis-1 vs. Hypothesis-2, or that of cladding failure percentage.

#### 6.4.3.2.4 Abstraction/Implementation into RIP

Although it is believed that Hypothesis-2 is more likely than Hypothesis-1 and shall carry more weight, without direct laboratory evidence, they are assumed to be equally possible. Since the number of simulations are very limited, it is difficult to elaborate the distribution form of Np concentration in all the possible conditions from the results. Therefore, a log-uniform distribution for Np is proposed here for TSPA-VA sensitivity analysis. The range of Np concentration is the upper-bound and the lower-bound given by those 8 simulations; i.e., ( $10^{-9}$  –  $10^{-6}$ ) mole/kg. The expected value is  $10^{-7.5}$  mole/kg.

Comparing with Np solubility distribution used in the TSPA-VA base case, this Np concentration range is more than 10 times lower. It may suggest the TSPA-VA base-case value for Np solubility is conservative. Furthermore, if the incorporation of Np into uranophane and other tertiary phases can be confirmed, an even lower Np distribution would be expected. Since Np is the major dose contributor, the benefit of using this alternative model and taking credit for Np incorporation into secondary and tertiary uranyl-minerals in future TSPA iterations is apparent; that is, we would be able to replace the (over)-conservative values by more realistic values with a well-justified basis.

#### 6.4.3.2.5 Caveats

As noted in the beginning of this discussion, this analysis is the first attempt to apply the new approach to study CSNF dissolution and radionuclide mobilizations. The needed data are rare and the quality of existing data is yet to be fully evaluated. The hypothesis of Np incorporation into secondary uranyl minerals needs to be further confirmed by laboratory observations. The results should be regarded as preliminary. The following caveats are advised.

- Np incorporation into uranyl minerals has not been well characterized. This introduces a big conceptual uncertainty into the modeling results.
- The thermochemical and kinetic properties of uranyl minerals have not been well measured. The effects of inaccuracy in those parameters on Np concentration have to be evaluated.
- The effects of corrosion of basket material and inner layer of waste containers on the water chemistry is not considered in the model. Its effects should be investigated in the next round of analyses.
- As the simulation shows, schoepite precipitates rapidly. As pointed out by Bourcier (CRWMS M&O 1998d, Appendix D, p. 7, paragraph 3), “rapidly precipitating mineral phases often contain higher concentrations of trace and minor elements than

do phases that form more slowly, or the phases they will eventually age into. It is conceivable that the uranium alteration minerals could expel their guest Np contents at some later time when they recrystallize." That recrystallization phenomenon is not considered in the model.

- Radiolysis effects are not included in the model and should be analyzed.
- Since the number of simulations are very limited, the effects of the incoming water composition, its velocity, and other factors have not been analyzed. A number of analyses for various environmental boundary conditions should be done in the future.

#### 6.4.3.2.6 Summary and Recommendations

This alternative model for spent fuel dissolution and radionuclide mobilization has been validated partially and qualitatively by comparing modeling predictions against laboratory experiments. Applying the model to the dissolution of schoepite yields a much lower Np concentration than what is used in the TSPA-VA base-case (at least 10 times lower). It suggests the Np solubility value used for TSPA-VA base-case analysis may be overly conservative. It is demonstrated that this alternative model would bring a large benefit in calculating the performance of the repository if Np incorporation into secondary and tertiary phases is further confirmed.

It is recommended that the following issues be addressed in the next Version of TSPA.

**Conceptual Model**—Incorporation of Np into schoepite and other uranyl minerals needs to be well characterized.

**Numerical Model**—It is the first time the new reactive-transport model is applied to this type of analysis. Because the theory and algorithms of reactive-transport modeling are immature, the uncertainty associated with the numerical model needs to be evaluated.

**Kinetic Data**—The dissolution kinetic data of uranyl minerals used in this analysis are the only available data to us. Although the data appear high quality, it needs to be fully evaluated. The project needs to carry out its own experimental program to obtain higher quality data and fully quantify the kinetic behavior of the uranyl minerals. As far as we know, the kinetics of Naboltwoodite have not been studied. Since it is the major secondary mineral in Argonne National Laboratory high-drip tests (Finn et al. 1998b), starting a kinetic experimental study on Naboltwoodite is highly recommended.

**Thermodynamic Data**—The quality of the thermodynamic data for some uranyl minerals need to be improved. Their temperature dependency has to be determined. Such data can affect the accuracy of these analyses, and more fully constrained values would decrease the uncertainty with them.

## 6.5 ENGINEERED BARRIER SYSTEM TRANSPORT

The EBS is the first barrier for radionuclide release in a geologic repository system. The EBS is comprised of two major components: the WPs that encase waste forms and the concrete invert

below the waste packages. The release of radionuclides into the natural environment is controlled by the transport of the radionuclides out of the WPs and through the concrete invert. Key factors affecting the transport of radionuclides through the EBS are: the performance of the waste package, the protection provided by cladding, the matrix dissolution rate, the entry and movement of water through waste packages, colloidal transport of radionuclides and the sorption affinity of radionuclides to the concrete below the waste packages. These factors and their effect on EBS transport and release will be discussed in the following section.

### **6.5.1 Overview of the Conceptual Model**

The current repository design concept calls for cylindrical WP that contain the waste to be placed in drifts within the potential repository. The WP will be comprised of a 10 cm carbon steel corrosion allowance material outer layer, a 2 cm high nickel alloy corrosion resistant material inner layer, and various handling and spacing materials holding waste forms in place. The WP will be placed on top of pedestals composed of carbon steel and concrete that will be placed on top of a concrete invert emplaced from pre-formed concrete sections (see Figure 6-49). In addition, a drift liner will be emplaced to prevent rock fall during the repository operational time.

After emplacement of the waste packages, the radioactive decay of the waste will heat the drifts and disturb the normal percolation of water through the mountain. As the drifts cool, some of the ground water percolating through the mountain may drip into the drifts and onto some of the waste packages. Through time, the components of the engineered barrier are expected to degrade. The metallic materials of the WP and pedestals are expected to undergo humid and wet corrosion (see Chapter 5 of this document) and the concrete materials are expected to undergo hydrothermal degradation. As the materials deteriorate, the drift liner will fall onto and around the WP and the pedestals will collapse lowering the WP toward the floor. The WP are expected to undergo humid corrosion, and if wetted by dripping or high relative humidity to undergo aqueous corrosion. Under aqueous conditions, depending upon the chemical conditions, the metallic materials may undergo localized or generalized corrosion, which may result in small or large breaches of the WPs.

Once a WP is breached, water may enter the WP as water vapor or as drips. If handling packages and cladding are also breached, radionuclides may start to dissolve in the water. The radionuclides mobilized into the water as dissolved or colloidal species may then be transported by advective flow of the water and by diffusion through breaches in the WPs. Once outside of the package, the radionuclides will be transported through the concrete invert by diffusion or with the movement of water through the invert.

This section describes how radionuclides move from inside the waste package, through corrosion products, pedestal and possible drift-liner rubble, and through the degraded invert to the host rock. In reality, this process will be quite complicated and many scenarios may be envisioned. Each WP will have its own thermal history and degradation history. One package may experience dripping all over the entire waste package, another may have a drip only on one end, and another may never experience dripping. One package may fail by generalized corrosion, and another may fail by a single spot of localized corrosion. One may have water flow through just one section, while the next one may fill with water before corrosion at the bottom lets the water out. Late time rock fall may cause severe damage to the clad within an already corroded waste

package, and another may never experience significant rock fall damage. In addition, the advective and diffusive pathways through the EBS will change with time. Soon after WP breach, the pathway for radionuclide transport from a pin hole breach in a fuel rod to the part of the WP where water is flowing may be long and tortuous. At later times, the fuel rods may have ruptured and settled into a mass of corrosion products and the pathway may be described as a nearly saturated porous medium. These details were difficult to capture in the TSPA and conservative or bounding simplifications were made.

First, the packages within the potential repository were divided into groups by fuel type (CSNF, HLW and DSNF) and into six repository regions for performance analysis. The repository was divided into six regions based on the infiltration and thermal behavior differences within the repository. Each package group was further divided into sub-groups based on the dripping environment of a set of packages. Drips into the drift will not be uniformly distributed so not all packages will see drips. In addition, three separate climate states were modeled during the 1,000,000 years after waste emplacement. The climates include the current dry climate (DRY), a long-term average (LTA) climate with increased infiltration and a superpluvial climate (SP) during which even greater infiltration occurs. As infiltration increases, the number of packages that see drips also increases. Based on the dripping and climates, four environments were defined. The first environment was defined for the packages that see drips during all times, including during the present dry climate. This environment was labeled "DRY" because dripping occurred even in the dry climates. Packages that see drips during the long-term average climate and during the superpluvial climate were grouped in the second environment called the "LTA" environment. Packages that only see drips in the superpluvial climate were grouped in the "SP" environment sub-group. Packages that never encounter drips were grouped in the "NDR" (Never Drip) environment. Each package sub-group (72 in all with 6 regions, 3 WP types and 4 environments) was associated with a unique set of parameters that affect WP release and EBS transport. The transport of radionuclides through the invert was modeled separately for each package sub-group.

Second, the diffusive and advective pathways from the WP to the invert were defined using the output of the WP degradation (Chapter 5) and seepage model (Chapter 2). The seepage model provided the fraction of WP that were under seeps, and volume of water flowing onto the WP per year for each seep. The WAPDEG assumed that a package under a seep was completely covered by the water, and provided a time history of the number of small breaches (pits) from localized corrosion and larger breaches (patches) from generalized corrosion for the packages that had been breached. A separate time history was provided for packages assumed to be under a drip or not. From this information, four pathways were defined between the WP and the invert: advective transport through pits, advective transport through patches, diffusive transport through pits, and diffusive transport through patches (see Section 6.5.2.2 for further discussion.)

Third, in the base case it was conservatively assumed that after water enters the waste package, it contacts all exposed waste and exits the WP with no time delay. This assumption is very conservative because it maximizes calculated releases and results in the earliest releases. In a more realistic and less conservative model, (the "bathtub" models), locations of individual breaches are specified and a delay in release is seen as the package fills with water up to the breach height. These models typically treat the waste under the water line as a mixing cell and the waste above the water line as less available to advective transport. At later times when the

bottom of the package breaches, these models show a pulse release as the water drains from the package. In the TSPA-VA analysis, the WP model did not attempt to specify the location of individual pits and patches and a bathtub model was not attempted. Section 6.6.1.4 discusses a less conservative water contact model.

Finally, it was assumed that the invert surrounds the bottom half of each WP (see Figure 6-50), and that the properties of the invert will remain that of relatively intact concrete. The WP will be emplaced on pedestals that separate them from the invert, but with time the pedestal will degrade, lowering the WP possibly to the invert floor. Any remaining gap between the WP and the invert will probably fill with corrosion products, degraded concrete liner, and rock fall. Thus the assumption of contact of invert material with the bottom half of the WP is conservative in that it maximizes contact and minimizes diffusive transport lengths. The assumption that the properties of the invert material will remain that of intact concrete, however, is likely very conservative for diffusive transport, and non-conservative for advective transport. Thermal hydrology calculations (see Chapter 3) show that intact concrete, with a porosity of about 0.1, will dry out and then return to a saturation of about 0.998 long before the WP breach. A material with a porosity of 0.1 and a saturation of 0.998 will offer only moderate diffusive resistance. If the properties were instead those of coarse rubble, it is expected that the saturation would remain much lower, affording an effective diffusive barrier. For advective transport, intact concrete surrounding the package offers a large mass of sorbing material to delay break-through of the contaminant plume, while rubble or fractured concrete may offer fast paths with little sorptive interaction with the concrete. Therefore the assumption of intact concrete is probably quite conservative for diffusive transport, and may be non-conservative for advective transport.

## **6.5.2 Implementation of Conceptual Model into RIP**

Like clad degradation, waste form degradation, and radionuclide mobilization, EBS transport was abstracted and modeled within the RIP code. A quick overview of the capabilities of the code is presented, followed by a quick overview of the implemented base-case model. A more complete discussion of the RIP base case will be published following completion of the TSPA-VA.

### **6.5.2.1 RIP Code**

RIP is a transport code with built-in features for source term including WP failure, clad failure, and waste form degradation. Solubilities and suspended particulate loads limit concentrations. Reversible sorption is included in the form of linear  $K_d$ 's. The code also has built-in features for representing uncertainty in a probabilistic way. Transport can be modeled with three types of pathways: mixing cell, pipe or external function. The EBS transport model was built with RIP cells and advective and diffusive connections between the cells. The parameters used to define the model are listed below as they are organized in the RIP user interface, and are indicative of the level of detail in the transport model. For further details see the RIP Users Manual (Golder Associates 1998).

1) Materials

Species:

name

element

MW (gm/mole)

decay rate (/yr)

specific activity (Ci/gm) (calculated by RIP from decay rate)

Daughter 1

stoichiometric ratio for decay equation

fraction to daughter 1

daughter 2

stoichiometric ratio for decay equation

decay radioactive?

40CFR191 limit (Ci/MTHM)

additional data

Media:

name

description

type

Solid

porosity

tortuosity

Kd ( $m^3/kg$ )

relative particulate diffusivity

Fluid

reference diffusivity

species

solubility ( $g/m^3$ )

relative diffusivity

2) Source Term

name

description

# of containers

rewet condition

matrix degradation rate

primary failure definition

description

start when rewet?

Start time

probability

aging rate

distribution type (Weibull, exponential, uniform, log uniform, degenerate, user defined, F(age))

failure mode

secondary failure definition  
     description  
     start when container fails?  
     Start time  
     probability  
 distribution type (Weibull, exponential, uniform, log uniform, degenerate, user defined, F(age))  
     failure mode  
 inventory  
     species  
     Ci/container  
     outer container fraction  
     inner container fraction  
     waste matrix fraction  
 associated cells  
     fraction of inventory in each associated cell  
 local environments  
     fraction of packages in each local environment

### 3) Pathways (Cells)

name  
 description  
 media  
     name  
     for solids: mass (kg), suspended solid concentration (kg/m<sup>3</sup>)  
     for fluids: volume( m<sup>3</sup> for fluids)  
 connections for this cell (see connections)  
 environment  
 inventory

### 4) Connections

diffusive:
 

connection area	
<u>from</u> cell	<u>to</u> cell
fluid	fluid
porous medium	porous medium
length in pathway (m)	length in pathway (m)
diffusivity (m <sup>2</sup> /sec)	diffusivity (m <sup>2</sup> /sec)

 advective:
 

<u>from</u> cell	<u>to</u> cell
medium flowing	
flow (m <sup>3</sup> /yr for fluids, kg/yr for solids)	

RIP parameters may be constants, distributions, functions, tables, or calls to external codes, giving the code great flexibility. The source term parameters and the fluid material parameters have been discussed in the WP Chapter (5) and the waste form Sections 6.2 through 6.4. The solid materials, pathways and connection parameters are discussed here.

### 6.5.2.2 The Base Case Model

Figure 6-49 shows a representation of the potential water flow within the EBS and 6-50 shows a schematic of part of the base case EBS model. Only the CSNF sub-group of one region is shown in detail in Figure 6-50, but the HLW and DSNF sub-groups are analogous. Each package sub-group (72 in all with 6 regions, 3 WP types and 4 environments) is associated with a unique set of parameters that affect WP release and EBS transport. The transport of radionuclides through the WP and invert is modeled separately for each package sub-group as required by the conceptual model. Thus the flux "qdrip" in Figure 6-50 actually represents four qdrips, one for each environment, and it is a function of time as the climate changes. The packages were allotted to each of the six regions based on the regional areas. The three types of waste were assumed to be uniformly distributed throughout the repository. The number of WP within the sub-groups were calculated using the fraction of packages that see drips (seepage fraction) in each climate state in each region. In addition, the seepage fractions in the different environments were positively correlated in order to ensure the wetter climates always had higher number of packages seeing seeps.

While all 72 sub-groups were modeled separately in the EBS transport model, it should be noted that this was not the case for the WP degradation abstraction. The WP degradation histories for the 6 regions were found to be sufficiently similar that the degradation history for only the northeast region was used. In another simplification, only two environments were used in the WP degradation modeling, the always-dripped on and the never-dripped on environments (see Chapter 5 for discussion of these simplifications.)

In addition to 18 (6 regions, 3 wastes) WP groups that breach by corrosion degradation of waste packages, the base case includes the effect of early or "juvenile" waste-package failures by non-corrosion processes such as materials defects, seismic activity, and human-induced factors, such as welding, handling, and transportation. Unlike the other groups, this group was defined with only one environment, the wettest one. The juvenile failure is assumed to cause a single patch opening in a commercial spent fuel nuclear fuel package in a dripping environment, in the southeast region (region 3). This is implemented within RIP by adding a source term group in addition to the eighteen source term groups. The expected-value base case assumes a single juvenile failure at 1,000 years. The probabilistic base case uses a log-uniform distribution for juvenile failures from 0.001 percent to 0.1 percent of the repository packages, all occurring at 1,000 years after closure. For these few packages (one in the expected value run), the single patch failure at 1,000 years was the only failure modeled, with no further degradation modeled.

As shown in Figure 6-49, only a portion of the seepage that falls on a package is modeled to enter the package. In the base case, the WP degradation modeling used the assumption that the seeps move with time, thus wetting the entire WP surface. This assumption would preclude the fraction of water entering the package from approaching 1, at least until the WP is seriously degraded. However, it is also recognized that if the seep does not move with time, the WP will preferentially degrade under the seep, and most of the seep will enter the package as soon as a significant opening is produced. In order to remain consistent with the WP abstraction, the fraction that enters the package is assumed to be proportional to the fraction of the WP surface that has failed. However, this fraction is also multiplied by a parameter sampled from 1 to 10 for patches and 0 to 2 for pits to acknowledge the uncertainty in this assumption, and also the

uncertainty in how much water may enter very tiny openings.  $Q_{\text{patch}}$  and  $q_{\text{pit}}$  in Figure 6-50 are the advective flow calculated to enter the packages through the patch and pit openings. Figure 6-51 shows the fraction of the seepage that enters the package through patch openings over one million and 20,000 years in the expected value case. The fraction that enters through pits never exceeds  $10^{-7}$ . In addition to the two advective pathways between the waste form and invert cells, there were also two diffusive pathways, one each through the pits and patches. Diffusive transport is modeled in RIP using a simple 1-D approximation defined with a diffusive area, path length and material. For diffusion through the pits, the diffusive length was assumed to be the thickness of the collision resistant material inner layer, 0.02 meters. The area was the number of pits time the single pit area,  $3.8 \times 10^{-7} \text{ m}^2$ , and the material was assumed to be corrosion products with a porosity of 0.4 and tortuosity of one. In order to simulate the reduced effective diffusion coefficient in an unsaturated medium, the equation for diffusion in a partially saturated medium of Conca and Wright (1990 and 1992) was implemented as a RIP external call (CRWMS M&O 1998e). This function required the saturation of the diffusive medium. The saturation of the corrosion products was determined by drift-scale thermal hydrologic modeling as a function of time, and was found to return to 99.8 percent by the time the packages failed. For diffusion through the patches, the area was equal to the number of patches times the patch area,  $0.031 \text{ m}^2$ . Because the patch was much larger, it was not assumed that the corrosion products would be trapped within the WP breach, and the WP was conservatively assumed to lie directly on the invert. Thus the path length was one half the first invert cell width and was assumed to consist of intact invert with porosity of 0.1 and saturation of 0.998.

The third assumption of the conceptual model can be seen in the use of a single mixing cell to represent the waste form within the WP in Figure 6-50. This cell is scaled in size to the number of packages that have breached within that WP sub-group. As more packages breach, the size of the single WP cell increases to account for the volume and inventory of the newly breached package. Cells within RIP are defined with a volume of water and mass of solid materials associated with the cell. The amount of water in the waste form cell is assumed to be equal to the pore space of the rind of alteration products that forms as the  $\text{UO}_2$  is converted into secondary minerals. The volume of the rind is calculated to increase as a function of time, but is not allowed to exceed the original fuel matrix volume. The solid materials within a cell are defined for batch sorption, and for particulate mobilization. The sorptive solids within the waste form cells, such as secondary uranium minerals and degraded basket materials were conservatively not included. The mass of colloids within the WP cells was calculated by multiplying the concentration of colloids by the volume of water within the cell. The concentration of colloids was provided by the Near Field Geochemical Environment abstraction (see Chapter 4).

The final assumptions of the conceptual model are also shown in Figure 6-50. The invert cells are shown to wrap around the waste form cell. The invert was divided into three cells to decrease numerical dispersion. Each invert cell contained water, concrete invert, and colloids. The mass of the invert within each cell was determined by multiplying the bulk density of concrete ( $2100 \text{ kg/m}^3$ ) by the physical volume of the invert cell. The volume of the water within each invert cell was determined by multiplying the porosity of the concrete invert (10 percent) by the physical volume of the cell. As in the waste form cells, the mass of colloids within a cell is determined by multiplying the colloid concentration by the volume of water in the cell. Two connections, one advective and one diffusive, were defined between adjacent invert cells. The flow value for the

advective connection was set to the seepage through the drift and is not scaled to the area of the pits and patches on the WP. The diffusive area was based on the physical area between the two invert cells while the diffusive length is equal to the sum of half the thickness of the adjacent invert cells as shown in Figure 6-50. The effective diffusion coefficient values were based on the porosity and liquid saturation of the invert. The liquid saturation values were obtained from drift-scale thermal hydrology modeling.

Past the invert cells there is a single cell ("SF last" in Figure 6-50) used to implement the "swept-away" boundary condition. An advective and diffusive connection was defined between the third invert cell and this last cell. The volume of water in the "SF out" cell was small compared to the flow of water ( $1 \times 10^6 \text{ m}^3/\text{yr}$ ) out of the cell, so that almost all of the radionuclide mass that reached this cell was instantly swept away. This created a zero concentration boundary condition at the edge of the EBS. This conservative approach assured the largest concentration gradient between the WP and the edge of the EBS.

At the edge of the EBS, six more cells were defined (labeled "out" in Figure 6-50). Each of these cells collected the radionuclide releases from all of the WP groups and environments within a single repository region. The six mixing cells are used to combine the release from the different waste forms so that only six mass flux values are passed to the UZ. The volume of water in each of these cells is small ( $1 \times 10^{-6} \text{ m}^3$ ) compared to the flow of water out of the cells to assure that there is almost no residence time for the radionuclides moving through the cell. An advective connection was defined between each of the six cells and the UZ representing the release of radionuclides from the EBS regions into the UZ. The fraction of the plutonium which was assumed to be irreversibly attached to colloids and highly mobile, was applied at the edge of the EBS to the mass of plutonium leaving the EBS and entering the UZ. This fraction was sampled from a log-uniform distribution.

Some of the base case parameters for the EBS transport model are presented in Table 6-47. These parameters have been discussed in this section or other sections of chapter, however the  $K_d$ 's for sorption onto EBS materials requires further discussion.

Site-specific studies and modeling of sorption onto corrosion products and the concrete invert are being carried out (Hardin et al. 1998, Section 6.4). This work was not abstracted into simple form in time for inclusion into the TSPA. For this reason, sorption onto corrosion products was conservatively left out of the EBS transport model and the following placeholder  $K_d$ 's for sorption onto the invert were used.

<u>Element</u>	<u><math>K_d(\text{m}^3/\text{kg})</math></u>	<u>Rationale</u>
C, I, Se, Tc	0	conservative
Np	0 - .2	conservative to minimum of Albinsson et al. (1993)
Pu	0 - 1.2	conservative to minimum of Albinsson et al. (1993)
U	0 - .1	conservative to minimum of Albinsson et al. (1993)
Pa	0 - .1	range for tuff (Triay et al. 1997)

NOTE: (DTN SNT05080598002.001)

Minimum values for all invert  $K_d$ 's were set to 0 because of the possibility of fast fracture flow through cracks in the invert. Upper ranges were set to the minimum reported in Albinsson et al.

(1993) because of the uncertainty in the water chemistry within the invert during the 1000 year to million-year time frame. Albinsson reported  $K_d$ 's for Portland cements of varying composition in contact with a variety of synthetic pore waters, (pH about ~13) of varying ionic strengths higher than J13. The pH within the invert is not expected to be as high as reported in Albinsson, particularly after the invert is fully carbonated. The range of  $K_d$ 's reported by Triay et al. (1997) for Pa on tuff was also used for the invert. These  $K_d$ 's have been called placeholder, because  $K_d$ 's have not been measured over the range of chemical conditions expected in the invert in the 1000 to million-year time frame. Without further data it is difficult to assess if these ranges are conservative or non-conservative although preliminary work by Hardin et al. (1998, Section 6.4.4.3) suggest that they may be conservative. Hardin et al. have looked at sorption onto hydrothermally altered concrete. At equilibrated pH's of 10.8+/- .1, preliminary conservative  $K_d$ 's for U and Np were reported on the order of 10 m<sup>3</sup>/kg.

### 6.5.3 Behavior of RIP Expected Value Base Case Model

The behavior of the expected value RIP near field release model is presented here in detail for one waste and one sub-area. CSNF contains the largest inventory and region 6 has the largest flows and second largest number of WP and so were chosen for more detailed examination. Figure 6-52 shows the EBS release of <sup>237</sup>Np from the region 6 CSNF from the four environments in 400,000 years. 400,000 years was chosen because the peak dose typically occurs at about 290,000 years during the first superpluvial climate. After 400,000 years doses typically decline. There are no releases from the CSNF from environments 3 and 4 in Figure 6-52, because the RIP model uses package breach histories for never-dripped-on packages for these environments. The never-dripped-on packages don't breach until after 700,000 years in the expected value run. Environments 1 and 2 both use the package breach history for always-dripped-on packages and thus start breaching at about 4480 years. Environment 2 has 486 packages and so it shows higher releases than environment 1, which has only 87 packages. Therefore environment 2 was chosen for more detailed examination. <sup>99</sup>Tc was chosen as the most important highly soluble radionuclide and <sup>237</sup>Np was chosen as the most important low solubility radionuclide.

Figure 6-53a shows the release of <sup>99</sup>Tc from the CSNF in region 6, environment 2, in the expected value run for the first 20,000 years. During this time, 9 WPs breach, which is clearly seen in the peaks in the <sup>99</sup>Tc releases. The Tc releases are presented with a log scale so that the relative releases for the four connections between the waste form and invert are visible. The first release is diffusive release that occurs at package breach at 4,480 years. The first package breaches before 5,000 years because the always-dripped-on WAPDEG results were used, however, the flux is zero until the LTA climate starts at 5,000 years, at which time advective releases start. At 5,000 years, the fraction of water calculated to enter the package through the patches is 2,657 times greater than the fraction of water calculated to enter the package through the pits, resulting in release that is 2,657 times larger from the patches than from the pits. The diffusive releases are not proportionately scaled to the size of the patch and pit breaches because of the different assumed porosities and path lengths for the two pathways as shown here.

**Base case diffusive pathways:**

**Pits:**

<u>from</u> WF cell	<u>to</u> Invert cell
fluid: water	fluid: water
porous medium: none	porous medium: Corrosion products
length in pathway (m): 1e-12	length in pathway (m): 0.02

**Patches:**

<u>from</u> WF cell	<u>to</u> Invert cell
fluid: water	fluid: water
porous medium: none	porous medium: Invert
length in pathway (m): 1e-12	length in pathway (m): 0.075

The porosity of the corrosion products was 0.4 and the invert was 0.1. When Conca's equations were used to calculate effective diffusion coefficients, these porosities resulted in very different diffusion resistance values. The expected-value base case results are repeated in Figure 6-54a, and the results of the base case run with the diffusive pathways defined more consistently are shown in Figure 6-54b.

**More consistent diffusive pathways:**

**Pits and Patches:**

<u>from</u> WF cell	<u>to</u> Invert cell
fluid: water	fluid: water
porous medium: Corrosion products	porous medium: Invert
length in pathway (m): 0.1	length in pathway (m): 0.075

Notice that adding the 0.1 m of corrosion products to the pathway within the waste form cell did not change the diffusion release from the patches. This is because the high porosity and saturation of the corrosion products results in little modeled transport resistance. Changing the pit diffusion pathway within the invert cell from corrosion products to invert made a large difference in the pit diffusive release. The 0.075 m of porosity 0.1 invert material adds significant diffusive resistance and results in much lower diffusive releases. For completeness sake, further work is suggested to provide more realistic porosities for both the corrosion products and the invert as it degrades. However, because advective release through the patches is at least an order of magnitude more important than diffusive release through either the pits or patches, definition of the diffusive release pathways is low priority.

The Np releases are shown with a linear scale in Figure 6-53b to compare with the fraction of qdrip that enters the package in Figure 6-51. Because the Np release is solubility limited, the Np release rate is directly proportional to the waste flow rate per package and the number of packages breached. This is seen in the steps in the Np release rate as each package breaches and the slopes of the "stair treads" as the fraction of the seepage entering the package increases with time.

Figure 6-55 shows the expected-value run releases from all four waste form connections and also from the EBS in 400,000 years. The dry climates at 95,000, 195,000, 295,000 and 395,000 years are clearly seen in the release curves. Release during the dry climate falls due to lack of flow, but in the Tc release, there is a spike in release at return to long-term-average climate. This is due to build-up of Tc released from clad and package breaches that occurred during the dry period. When flow is reestablished, the built-up Tc is flushed from the waste form. Note that there is no delay between the release of Tc from the waste form to release from the EBS system; however, a delay is seen in the Np releases. This is due to sorption of Np in the invert. Notice also, that the Np release from the waste form does not spike at return to long term average climate at 105,000 and 205,000 years because the release at those times is solubility limited. The superpluvial climate at 285,000 is not seen in the Tc release, because the Tc release is inventory limited. As long as a modest flow is maintained, Tc release rate is determined by the rate at which packages and cladding breach. The superpluvial climate is, however, seen in the spike of EBS release of Np. This spike is due to flushing of Np from the invert. The drop in the Np release rate after about 225,000 years is due to the change from solubility control to inventory control. This is why, during the superpluvial climate there is no spike in the Np release from the waste form but there is a spike in the Np waste form release at the 305,000 year return to long-term-average climate.

## 6.6 SENSITIVITY

A number of sensitivity studies have evaluated the impact of the uncertain parameters and conceptual models discussed in this section. These sensitivity studies compare results from variations in features, parameters, alternative conceptual models, and assumptions. Some of the analyses were done with the entire TSPA-VA analysis code suite and compare results in dose at the accessible environment over time. Other analyses were done with a subset of the models up to and including the EBS modules in RIP. These compare results in terms of release rate from the EBS for specific radionuclides over time. The EBS release calculations are much more computationally efficient and capture all of the processes of waste form degradation, radionuclide mobilization, and transport of radionuclides through the EBS.

### 6.6.1 Sensitivity Calculations—Base Case Waste Forms

During development of the TSPA-VA base case, and after the base case was finalized, a number of comparative analyses were conducted using the base case waste inventory.

#### 6.6.1.1 Cladding Credit

The cladding model used in the base case is a recent development, and significant uncertainties remain in the very long time degradation processes. To explore the impact of variation in the cladding performance, analyses were run with no cladding credit, and with forced failure of the cladding by  $10^5$  and  $10^6$  years. Failure by “ $10^5$  years” was implemented with an exposure of 0.0001 of the fuel at 1,000 years and 1.0 of the fuel at 100,000 years. All times in between are interpolated using a log-log (failure-age) interpolation scheme. Similarly, “failure by  $10^6$  years” was implemented with exposure of 0.0001 of the fuel at 1,000 years, 0.01 at 10,000 years, 0.1 at 100,000 years and 1.0 at 1,000,000 years. All times in between are interpolated using a log-log (failure-age) interpolation scheme. In all cases, the juvenile failure fraction of 0.0125 was used.

Note that both these forced failure cases model significantly more exposure by 100,000 years than the base case which has only 0.0125 exposed by 100,000 years, and both cases expose all fuel in the million year runs while the base case exposes less than 50 percent. The results of these analyses are shown in Figure 6-56 compared to the base case. The no-cladding case results in dose rates nearly 2 orders of magnitude higher at early time ( $10^4$  years), virtually no difference around  $2 \times 10^5$  years, and about 1 order of magnitude at long times ( $10^6$  years). The results are dominated at early times by highly soluble Tc being released proportional to the fraction of SNF exposed. The convergence at 200,000 years is probably dominated by Np and other actinides being released at solubility limits regardless of the SNF exposure fraction, with the details at long times influenced by differences in the time of Np depletion.

#### 6.6.1.2 Dissolution Models

Implementation of the revised SNF dissolution rate model in the base case fixed a number of the new parameters (burnup,  $O_2$  partial pressure) or with limited variation (pH,  $CO_3$ ). With this implementation, a comparison to the TSPA-95 model shows no significant difference in results as seen in Figure 6-57 for dose rates and Figure 6-58 for EBS release. The impact of the revised dissolution model could be more significant in scenarios where WPs fail at earlier times, since burnup effects (radiation dose rates),  $O_2$ , and water chemistry all vary more at early times.

The new HLW glass dissolution model was also compared to the TSPA-95 model (Rev.0 in Figure 6-59). The new glass dissolution model shows a reduction in Tc release rates of 50 to 100 percent. This reduction is generated by the new fit to the dissolution rate data for the TSPA-VA. This fit closely matches the data in the pH range of 7 to 8, as shown in Figure 6-31. The pH range of 7 to 8 is important, because it is typical of that for tuff-water interactions with J-13 groundwater. The previous curve fit for TSPA-95 is higher than the data points by of 10 to 500 percent in this range of pH and for temperatures between  $25^\circ C$  and  $50^\circ C$ . This overestimate of the dissolution rate leads to higher releases of Tc with the TSPA-95 model.

Note that Np releases are identical with either dissolution model, because Np release is solubility limited for this calculation.

#### 6.6.1.3 Solubilities and Secondary Phases

The effect of radionuclide retention in secondary phases during SNF dissolution is not represented in the base case. Two models were developed to begin assessing the potential for significant reduction in calculated dose if credit can be taken in the future for this process. The calculation of observed film concentrations for selected radionuclides in low drip rate testing was incorporated into a sensitivity comparison to the base case by fixing the effective concentration at the calculated values instead of that calculated from the solubility limit. The "effective concentration" of Pu was changed from  $0.12 \text{ g/m}^3$  in the expected value run to  $1.6E-5 \text{ g/m}^3$ ; from  $1.2E+4$  to  $7.9E-4$  for Tc; and from  $3.4E-1$  to  $1.1E-6$  for Np. This comparison in Figures 6-60 and 6-61 shows a factor of 5 to 20 reduction in the dose, as other radionuclides dominate the dose. A similar calculation for Np-dose only is shown in Figure 6-62, using the concentrations calculated by reactive transport for Np during secondary phase precipitation and dissolution. In this calculation the effective Np solubility was reduced from  $0.34 \text{ gm/m}^3$  in the base case to  $0.0075 \text{ gm/m}^3$  for the secondary phase controlled case. This two order of magnitude decrease in

concentration limit results in much lower dose from Np at early times when the release is solubility controlled. After the superpluvial climate, however, the base case Np release is no longer solubility controlled, but inventory controlled, so the two curves start to converge. After about 700,000 years there is sufficient flushing of the packages that even with the lower solubility limit, the secondary phase controlled runs switch from solubility limited to inventory limited Np release.

These results suggest that the base case analysis has significant conservatism in neglecting the retention of radionuclides in secondary phases. If sufficient confidence can be obtained to represent this process in future analyses, significant improvement in modeled performance may be obtained.

#### 6.6.1.4 Water Contact

For an initial look at the importance of water contact with the waste form on EBS performance, three processes were examined: clad failure, drip entry into the WP, and waste form discretization. Each of these three significantly affects the modeled contact of water with the waste form and thus examination of all three together is required for a full understanding of the modeled system. In each case two extremes were examined as abbreviated below:

cc	clad credit
nc	no clad
sd	split drip
fd	full drip
sw	split waste form
fw	full waste form

The "clad credit" model was the base case clad model. For the "no clad" case, all of the cladding is assumed to have failed by the time a WP first breaches. The "split drip" model was the base case model, which used a "qdrip" (dripping flux) that was proportional to the fraction of the surface area of the WP that was breached. In the "full drip" model, all of the dripping flux associated with a WP flows through the WP. In the "full waste form" model, the water entering the WP contacts all the exposed radionuclides in a single mixing cell. The "split waste form" model more finely discretizes the waste form and requires further discussion.

**Split Waste Form**—Earlier modeling (not presented) in which the waste form was split into two cells showed very little effect on the results due to the coarse discretization and strong diffusive connection between the two cells. For this scoping study, several finer discretizations were tried and compared. Two discretizations are presented here, a 9-cell model and a 21-cell model. To model the axial diffusive transport within the partially failed fuel rods, the cells were defined as cylindrical sections of the waste package. Diffusive transport was assumed to begin between adjacent cells throughout the entire package at the time of first breach, but advective transport was modeled to occur only through local breaches. For computational efficiency, the WP was more finely divided within the sections of the waste package that would experience local breaches within the 400,000 year simulation, and more coarsely divided elsewhere.

The 9-cell model was composed of eight cells, each 5 percent of the WP length (0.2668 m), and a ninth cell with the remaining 60 percent of the length (3.2 m). Thus, when the first breach occurs, only 5 percent of the waste was assumed to be exposed to dripping flux, and as successive cells experience local failure, only 5 percent additional inventory was exposed to dripping. The package surface area covering a 5 percent slice is 1.395 m<sup>2</sup>, ( $2 \cdot \pi \cdot 0.832 \text{m} \cdot 0.2668 \text{m}$ ), which is about 45 surface corrosion patches as defined by the WP degradation abstraction.

The WP degradation abstraction gives the timing of patch breaches but does not give the spatial distribution of patch breaches. If drips are stationary, then patch breaches will start at the location of the drip and grow outward from there. If drips move randomly with time, then patch breaches would occur more randomly over the WP. For this calculation, it was assumed that dripping would not be random and that patch breaches would spread out from the first breach. However, it was not assumed the entire surface of a WP cell is covered with breached patches before patches start to breach on the adjacent cell. Instead, it was assumed that the first 11 patches (about 1/4 of the patches covering the first cell) would breach over the first cell, the next 11 patches would breach over the second, etc. The WP was modeled using a mirror plane through the middle of the first cell. Thus, the second cell and subsequent cells were modeled as two half-cells (thickness .1334 m) on either side of the first cell. The final cell containing 60 percent of the waste was two half-cells of 1.60 m thickness at the two ends of the package.

The time of first patch failures for the first 6 cells in the simulations is given below, and Figure 6-63 shows the advective release of <sup>237</sup>Np through the patches to the invert for the first 6 waste form cells of this run (ccsdsw). Figure 6-63(a) shows a linear release scale for comparison with Figure 6-55(b) and Figure 6-63(b) shows the log release so that the first releases from each cell are visible.

<u>Cell</u>	<u>Year at first patch failure</u>
1	5,000
2	181,000
3	228,000
4	282,000
5	331,000
6	384,000

For the diffusive connections, the assumed geometry, effective porosity, tortuosity, and saturation of the material within the waste form cells must be defined. In a physical WP these will change with time as the internal structures corrode, fuel rods collapse and breach, and UO<sub>2</sub> alters to larger specific volume secondary minerals. For this sensitivity study, it was assumed that the cladding would remain substantially complete and that all diffusion from one cell to the next would occur within the fuel rods. At early times, this is consistent with the base case conceptual model, which assumes no filling of the WP with water, only 1.25 percent of the rods failed and no clad unzipping. For a package with 21 - 15 x 15 B4 assemblies, there are 4368 fuel

rods, (17 rods per assembly contain non-fuel materials). With an outer diameter of .43" and clad thickness of .0265", the combined inside cross sectional area of the fuel rods in a package is about .315 m<sup>2</sup>. This area was doubled to account for diffusion through both circular ends of the cells to get .63 m<sup>2</sup>. This simplification is conservative, since diffusion can occur through the entire cross-section of the rods instead of through just the failed rods. The tortuosity was set to 1, and the effective porosity was set to the ratio of the gap volume to total volume (as manufactured) -- 5 percent. Conca and Wright's equations (1990 and 1992) were used to calculate the effective diffusion coefficients within this assumed unsaturated porous medium. The saturation was set to 0.998, the expected value of the invert saturation after the initial thermal pulse. At early times, or if the WP does not fill with water, these assumptions result in an overestimation of the rate of diffusion between waste form cells and thus an overestimation of the release of solubility controlled radionuclides. At late times, or if the WP does fill with water, these assumptions result in an underestimation of the rate of diffusion between waste form cells and an underestimation of the release of those radionuclides from the WP.

Comparing Figures 6-63(a) and 6-55(b) one sees that the calculated releases in the first 400,000 years drop dramatically when the waste form cell is more finely discretized and when there is significant diffusive resistance to transport between WF cells. Instead of solubility limited releases in the first 225,000 years as in the base case, the split waste form shows inventory limited releases. This is seen in the drops in releases at times other than the dry climates and the spikes in release at the return to long-term-average climate. The drops are due to inventory depletion within the flow path cells, and the spikes are due to build-up of inventory during the dry climates. The exact height and time of the peaks in Figure 6-63 are directly due to the assumed size of the waste form cells.

Figure 6-64 compares the Np releases from this 9 cell run with the more finely discretized 21-cell run. For the run shown in 6-64b, 20 - 2 percent cells were used with the remaining 60 percent of the waste in a single cell. This figure shows how the peaks in the more finely discretized runs are due to the opening of new patches over successive cells, and how after a patch over a cell has opened, the Np in the cell is rapidly depleted. Figure 6-65(a) shows the total waste form Np advective release for the base case, the 9-cell case and the 21-cell case, while 6-65(b) shows the cumulative releases for these cases. The cumulative Np releases at the time of the superpluvial climate calculated with the 9-cell and 21-cell models are about a factor of four smaller than calculated with the base case single cell model. Thus the single cell model is conservative for Np release, and the 9-cell model captures the full benefit of the assumed axial transport resistance.

**The Eight Cases**—The 9-cell model was used for the split waste form cases in this section. Eight cases were created from all combinations of the extremes for the three water contact process: cc/nc, sd/fd; and sw/fw. The eight cases were examined at two time scales. 20,000-year simulations with 20-year time steps show the breach of the first 9 waste packages. 400,000-year simulations with 1,000-year time steps show the EBS behavior during the time of expected peak dose.

The early time results are shown in Figures 6-66 to 6-68. In Figure 6-66, there is a spike in the Tc EBS release associated with each WP failure. Because of the numerous spikes, only four cases could be presented on each plot. The greater water flow in the full-drip runs results in the

faster flushing of the available Tc and the low valleys between the peaks as shown in Figure 6-66(a). This is especially true of the full-drip-full-waste cases where all waste is in contact with the advective flow. The full-drip-split-waste cases have lower peaks and higher valleys because less waste is in the advective path but diffusion from adjacent cells allows continued release. The valleys are even shallower in the split-drip cases, Figure 6-66(b), especially at the earliest times when the fraction of the dripping flux entering the packages is quite low (see Figure 6-51). In contrast to the two full-drip-split-waste cases, the two split-drip-full-waste cases show shallow valleys, indicating that with the low flow, the flushing is not as effective. As expected, the no-clad releases are higher than the clad-credit releases, the split drip releases are lower than the full drip cases, and the full waste releases are greater than the split waste cases. This is especially easy to see in the cumulative release curves shown in Figure 6-67. The split drip cases approach the full drip cases as the fraction of the drips entering the packages increases. For the first 20,000 years, the Tc release is most sensitive to the clad model, then the waste form model, and not very sensitive to the dripping model.

In contrast, the Np release at 20,000 years is most sensitive to the dripping model, and less sensitive to the waste form and clad models as seen in Figures 6-67(b) and 6-68. In fact, for the split drip cases, neither cladding nor waste form model make any difference, because the release rate is driven by the solubility limit and flow rate. The Np release in Figure 6-68(a) shows three types of behavior. With both no clad and full drip, there is plenty of Np available and lots of flow, so the release is high and shows a simple stair step as new packages breach. The stair step pattern is indicative of the solubility-limited release. With the split drip cases, much lower release is seen with the stair steps ramped up as the flow into the packages increases with time. Between these extremes are the two clad credit-full drip cases. In these cases, because the amount of Np available is low from the clad credit, and the flow rate is high, the Np becomes depleted within the advective flow path. The depletion occurs earlier for the split waste form case than the full waste form case because there is less Np in contact with the advective flow, and thus the cumulative releases are lower. An artifact of the way RIP scales up the size of a cell as more packages breach can be seen in the width of the plateaus in the Np release in the ccfdw case. The time before depletion gets smaller with each breach. This is because when RIP breaches a package, it adds the inventory, and flow of the newly breached package to the cell. For example, when one package is breached, there is the inventory of one package and the flow of one package. When the second package breaches, there is the flow of two packages and the inventory of two packages, however, since the available inventory from the first package is already flushed away, the inventory from the second package effectively sees twice the flow as the first package. This artifact results in Np releases that are conservatively high when inventory limits take effect.

Figure 6-68(b) shows the smoothing-out and delay in Np release from the EBS compared to the release from the WF due to sorption in the invert. The peaks in the release from the ccfdsw and ccfdw are smoothed, and in all eight cases, the rate of Np release is reduced especially at early times. The Np accumulates within the invert until it reaches the limit set by the  $K_d$  and the solubility limit. Once this limit is reached, the model passes Np through the invert unretarded. By 20,000 years, Np is no longer retarded by the model in the ncfdw and ncfdsw cases, but significant retardation is still evident in split drip cases.

At later times, Np dominates the release. Figure 6-69 shows the releases from the same eight cases for Np over 400,000 years. The ccfds<sub>w</sub> curve crosses the four split drip cases around 50,000 years, because with clad credit as well as split waste form, the exposed inventory within the advective path is depleted by 50,000 years. Looking at the cc<sub>s</sub>ds<sub>w</sub> and ccfds<sub>w</sub>, it is seen that when inventory is exposed, it is flushed out earlier in the full drip case, resulting in higher early releases and lower later releases. The split drip model results in lower release rates than the full drip model within the 10,000 year time frame, but higher peak release rates in some cases, in the 400,000 year time frame.

During the superpluvial climate, both of the clad credit/split waste cases perform slightly better than the base case. The base case with split drip performs the same as the full drip case during the superpluvial climate, because by that late time, the Np has become inventory limited in the cases with cladding credit. All four no clad cases perform significantly worse than the base case during the superpluvial period.

In summary, at early times Np is solubility limited so reducing the flow into the packages makes the most difference. When no clad credit is taken, and the drips are split, splitting the waste form makes no difference. When no clad credit is taken, and all drips enter the package, splitting the waste form makes a large difference. During the superpluvial climate, release from the EBS is determined by clad credit and previous inventory depletion. After the superpluvial climate, inventory depletion becomes a major determinant.

#### **6.6.2 Sensitivity Calculations: DOE-Spent Nuclear Fuel, Navy Fuel and Pu Disposition Wastes**

The information presented in this section summarizes the complete analyses DSNF listed in Appendix A.

The analyses described here were done using the TSPA-VA base-case model, placing each category of DSNF (one at a time) in the environment of the base case, and calculating the expected-value dose history 20 kilometer downgradient from the repository. For each category of spent fuel, the results were obtained for the DSNF and codisposed HLW (where appropriate), the DSNF alone, and an equivalent amount of CSNF (for comparison). For the comparison of DSNF to an equivalent amount of CSNF, the CSNF was assumed to be packaged in the same number of WPs as the DSNF. The same number of WPs was assumed so that there would be equivalent release of solubility controlled radionuclide (<sup>237</sup>Np) because there was the same number of failed WPs of both spent fuels. No credit was taken for the cladding of the CSNF. This was done because some of the DOE spent fuel has cladding that is expected to be short lived, is disrupted or damaged, and the assumption produces a fuel-to-fuel comparison. For the analyses, the WP were assumed to be disposed in Region 6 of the base case repository, the region with the highest UZ flux.

Most analyses discussed in Appendix A were conducted for the total amount of DSNF (2,496 MTHM of spent fuel) to assess the full impact of disposing of all DSNF and codisposed HLW. The TSPA-VA base case contains 2,333 MTHM of DSNF and 4,667 of HLW so that the base case repository is below the 70,000 MTHM limit. For this reason selected analyses of DSNF

were also conducted to show the difference between the base case and that of disposing of all of the DSNF.

Where uncertainties in packaging or physical properties of the DSNF exist because of criticality considerations or lack of laboratory testing, respectively, sensitivity analyses were done to determine how this uncertainty affects dose history. These sensitivity analyses also provide guidance for future testing of DSNF.

#### **6.6.2.1 Dose From Defense Spent Nuclear Fuel**

The dose history at 20 kilometers for Categories 1 through 7 of DSNF are shown in Figure 6-70 for the total amount of DSNF in each category. The results for Categories 8 through 13, 15, and 16 are shown in Figure 6-71. No results are included on these figures for Categories 2 and 10 DSNF, because each of these categories contained too few packages (5 and 8, respectively) for there to be an expected package failure in the first 100,000 years. For these categories, all of the packages were assumed to fail at once and these failures were compared to an equivalent amount of CSNF. The results indicated that these two categories would produce doses less than an equivalent amount of CSNF when the packages fail (Appendix A).

The expected-value total dose history from the spent fuel in Categories 1 through 7 is plotted in Figure 6-70. Categories 1 and 6 contribute the highest dose from these 7 categories. Category 2 does not contribute because packages are not expected to fail in the first 100,000 years. Category 3 has a dose history about 3 orders of magnitude below that of the other spent fuels shown on Figure 6-70. The dose history for Categories 8 through 13, 15, and 16 are shown in Figure 6-71. Category 10 has no dose history because no packages are expected to fail in the first 100,000 years. Comparing Figures 6-70 and 6-71, it appears that Categories 1, 4, 5, 6, 7, 8, 11, and 16 will contribute significantly to the dose from all DSNF. The analyses conducted in 1997 (CRWMS M&O 1997a) found that Categories 1, 4, 5, 6, 8, and 11 contributed significantly to the dose from a composite of the first 13 categories of DSNF. The current analyses indicate that Category 7 has been added to the group of fuels that contribute significantly to the dose from all DOE spent fuels. The reason for this increase is that the radionuclide inventory for Category 7 was increased because of additional ORIGEN (Version 2.1, CSCI # A00000000-02268-1200-20027 v 2.1) analyses for this category. Category 16 is also added to the group, but had not been previously analyzed.

The dose from Navy spent fuel (Category 15) is about 2 orders of magnitude below that of the more significant dose-producing categories of DSNF, Categories 1 and 6 (Figure 6-70 and 6-71). The dose from Navy spent fuel is due to the release from the crud on the outside of the Zircaloy cladding. The cladding is not expected to fail for over a million years (Beckett 1998). Because of this, the dose from the Navy spent fuel is more than 2 orders of magnitude below that from an equivalent amount of CSNF (Appendix A).

**Combined Waste Forms**—Figure 6-72 compares the expected value dose history from a composite of all DSNF to that of an equivalent amount of CSNF. The analysis of CSNF is for unclad fuel disposed in Region 6 of the base case repository. Both types of spent fuel are packaged in the same number of WP. The reason for the difference in roughness is because of how the two curves were derived. The CSNF curve is from 3,456 packages that contain an equal

amount of spent fuel in each package, and with this large number of packages, there are enough package failures so that the curve is smooth. The curve for DSNF is a composite of the categories that contribute significantly to the dose from all DSNF. Several of the categories have few enough packages that package failures appear as spikes in  $^{99}\text{Tc}$  and  $^{129}\text{I}$  dose, and the roughness of the DSNF curve results from these spikes (i.e., Category 1, see Appendix A).

Figure 6-73 compares 2,333 MTHM of unclad CSNF, 2,333 MTHM of the metallic surrogate spent fuel used in the base case, and 2,333 MTHM of DSNF. For the analyses of both the surrogate and the commercial, the WPs are disposed in Region 6. This figure indicates that the surrogate metallic spent fuel is a good average for the DSNF. The surrogate curve appears as a best-fit curve through the spikes of the DSNF curve, but at later time, it bounds the spikes (after about 70,000 years). The 2,333 MTHM of unclad commercial appears to be a good bound for the DSNF, it is above all of the spikes on the DSNF curve created by individual WP failures (Figure 6-73).

Figure 6-74 shows the expected-value dose history for the base case repository, 2,333 MTHM of DSNF, and 9,334 canisters (4,667 MTHM) of HLW. The upper curve is the analysis for the 70,000 MTHM repository of the base case that includes 2,333 MTHM of surrogate DSNF, 63,000 MTHM of clad CSNF, and 4,667 MTHM of HLW. Figure 6-75 shows the comparison of 63,000 MTHM of CSNF with 2,333 MTHM of DSNF, and 2,496 MTHM of DSNF. The peak dose from 63,000 MTHM of CSNF is nearly the same as that from the base case repository (compare Figures 6-74 and 6-75). The expected value dose history from 2,333 MTHM of DSNF is nearly the same as that from 2,496 MTHM of DSNF (Figure 6-75). Here the primary difference between the two loading scenarios stems from the number of WPs in each. The 2,496 MTHM dose curve is somewhat higher and has somewhat different WP failures because it has more WPs.

Two additional algorithms for estimating the MTHM of HLW have been considered: the first is based on a strict interpretation of the Nuclear Waste Policy Act, and a second is based on the toxicity of the HLW. The first algorithm, the HLW waste equivalent to the fuel from which it was produced, would yield about 400 canisters as being equivalent to 4,667 MTHM of HLW. The second, the toxicity basis, would allow codisposal of all of the high- and medium-enriched spent fuel and still remain below the 4,667 MTHM. The HLW waste necessary for codisposal of all of the DSNF is 7,240 10-foot canisters and 7,836 15-foot canisters of HLW. This is equivalent to 18,994 or approximately 19,000 10-foot canisters of HLW. Figure 6-76 shows the expected-value total dose curves for 400, 9,334, and 18,996 canisters of HLW. The 400 and 9,334 canister cases do not have a very significant dose contribution to the entire repository. The 18,996 canisters would affect the dose from the entire repository because of the early contribution from  $^{99}\text{Tc}$  at about 30,000 years and by a lesser amount due to  $^{237}\text{Np}$  at later times. The 18,996 canisters of HLW are the amount needed to codispose the high- and medium-enriched spent fuel in all (2,496 MTHM) of the DSNF.

**Other Sensitivity**—A considerable amount of uncertainty exists both in the long-term repository environment and in the physical characteristics of DSNF. Other fuel properties that are uncertain are the effects of fuel cladding, choice of dissolution model, dissolution rate, and surface area on the calculated dose. In addition, because of criticality considerations, the number of packages of spent fuel for some categories is also uncertain. Analyses of all of these uncertainties are

presented in Appendix A. Analyses of the effect of dissolution rate and surface area on selected categories (selected based on their contribution to total dose) of DSNF show that increases in the assumed dissolution rate and surface area have little effect on the dose. A decrease in dissolution rate or surface area reduces the peak dose. This can be interpreted to mean that overly conservative assumptions have little effect on dose; however, a reduction in the conservatism through additional testing could reduce the dose from categories of DSNF that contribute significantly to the total dose from all categories of spent fuels.

For the analyses of disposal DSNF different dissolution models are used for oxide, metallic, carbide, and ceramic spent fuel and for HLW glass. A comparison of these dissolution models was presented in Section 6.3.2.2 (Figure 6-28). The dissolution rates in descending order are metallic spent fuel, oxide spent fuel, HLW glass, ceramic, and carbide spent fuel. After about 20,000 years, the range of dissolution rate is more than 4 orders of magnitude. In general, the number of orders of magnitude between different dissolution models does not translate into equal orders of magnitude of difference in the resulting dose. This is because the dose from spent fuel is due to three radionuclides ( $^{99}\text{Tc}$ ,  $^{129}\text{I}$ , and  $^{237}\text{Np}$ ). The release of the radionuclides  $^{99}\text{Tc}$  and  $^{129}\text{I}$  is rapid because they are highly soluble regardless of the selected dissolution model (unless the dissolution rate is greatly reduced as in the case of the silicone carbide dissolution model). The release of  $^{237}\text{Np}$  is controlled by its solubility, and as long as there is enough  $^{237}\text{Np}$  in solution to be transported at its solubility limit, the dissolution rate (model) makes little difference.

**Conclusions**—The dose from a composite of all categories of DSNF can be bounded by an equivalent amount, on an MTHM basis, of unclad CSNF.

The largest contributor to dose from all DSNF is Category 1 that is composed primarily of N Reactor spent fuel.

The metallic surrogate spent fuel that represented the DSNF in the TSPA-VA base case appears to be an appropriate average of the composite of the categories of DSNF. Some of the dose spikes from  $^{99}\text{Tc}$  and  $^{129}\text{I}$  caused by individual package failures of Category 1 spent fuel are higher than the dose from the surrogate, but overall the surrogate dose curve is higher including the peak dose that occurs at 100,000 years.

The spike in dose from  $^{99}\text{Tc}$  and  $^{129}\text{I}$  caused by individual package failure of Category 1 spent fuel is sensitive to changes in dissolution rate and surface area. They do not increase as dissolution rate is increased, but are nearly eliminated when dissolution rate is reduced by 3 orders of magnitude. The spikes remain the same for increased surface area and decrease as surface area is decreased. These results indicate the importance of reducing any conservatism in the assumed values of dissolution rate and surface area through laboratory testing.

Categories 1, 4, 5, 6, 7, and 16 are the largest contributors to dose from all DSNF, and Categories 1 and 6 are the largest contributors. All other categories (2, 3, 8, 9, 10, 11, 15, and 16) produce dose more than 2 orders of magnitude below that from all DSNF. Of the lower dose-producing categories, Categories 8, 9, and 11 are highest.

The dose from Category 15, Navy spent fuel, is more than 2 orders of magnitude below that from all DOE spent fuel. Category 15 dose is also more than 2 orders of magnitude below that of an

equivalent amount of CSNF. The reasons for the low dose from Navy spent fuel are that the dose is from crud on the outside of the Zircaloy clad, and that the robust clad is not expected to fail for over a million years.

The spikes in dose from  $^{99}\text{Tc}$  and  $^{129}\text{I}$  caused by individual package failures of Category 1 spent fuel may be artificially increased by model assumptions. Because WPs in the repository cannot be tracked individually, fuel alteration is assumed to begin at time zero (repository closure) rather than at the time of WP failure. For metallic spent fuel that alters rapidly this could cause a large amount of fuel in the WP and hence the spike in alteration-controlled radionuclides. This observation is supported by analyses of failing 5 packages of Category 1 spent fuel at 1,000 years and comparing the results to that of normal Category 1 package failures. The spike for the alteration-controlled radionuclides from the early failure is lower than from a normal failure of a single package. Additional analyses should be done to determine the effects of this assumption.

The dose from approximately 19,000 canisters of HLW that would be needed to codispose the high- and medium-enriched spent fuel in all of the DSNF is less than a factor of 5 higher than the 4,667 MTHM of HLW in the TSPA-VA base case (9,334 canisters).

#### 6.6.2.2 Pu Disposition Wastes

The information presented in this section summarizes the more complete analyses of Pu waste forms that are contained in Appendix B and describe TSPA of selected Pu waste forms.

**Dose From Plutonium Waste Forms**—The expected-value dose history of an individual located 20 kilometers downgradient from the repository was analyzed for each of the Pu waste form, and the results are compared to HLW and CSNF as appropriate. The results for the MOX spent fuel are compared to an equivalent amount of CSNF, and the results for the can-in-canister ceramic are compared to the same number of canisters of HLW.

Figure 6-77 shows the expected-value dose history for disposal of 50 metric tons of surplus Pu disposed as a combination of MOX spent fuel and can-in-canister ceramic (33 tons in MOX and 17 tons in can-in-canister ceramic). The figure also shows the total dose curve that is the sum of the dose from the MOX spent fuel and the can-in-canister ceramic (Figure 6-77).

Figure 6-78 shows the expected-value total dose history for 436 packages of can-in-canister ceramic compared to the same number of packages of HLW. These curves are nearly identical because the ceramic waste form does not contribute significantly to the total dose (Appendix B). The curves differ by about 12 percent due to the decrease of 12 percent of the HLW contained in the packages of can-in-canister ceramic.

Figure 6-79 shows the comparison of expected-value total dose history for 75 packages of MOX spent fuel as compared to 75 packages of CSNF. The two dose curves are nearly equivalent, with the curve for the MOX being somewhat higher than that for the CSNF. This indicates that disposal of 33 tons of Pu as MOX spent fuel would insignificantly affect the dose from the entire repository, especially if it is assumed to replace an equivalent amount of CSNF. If the MOX were assumed to be in addition to the CSNF, the effect would still be insignificant. The difference between the two curves is due to the inventory analyzed in each case. The MOX spent

fuel was packaged with 21 assemblies per package (about 9.7 MTHM per package) and this was compared to average CSNF packages used in the base case that contain about 8.1 MTHM per package.

**Conclusions**—Based on comparisons of analyses of MOX spent fuel and can-in-canister ceramic and the comparison of these waste forms to CSNF and HLW, respectively the following conclusions are drawn.

- The disposal of 50 metric tons of surplus Pu in the repository insignificantly affects the dose from the entire repository.
- The dose from MOX spent fuel is about the same as that from an equivalent amount of CSNF. Any difference is insignificant compared to the dose from the entire repository.
- The dose from either 159 packages or 436 packages of can-in-canister ceramic is nearly identical to that from an equivalent number of HLW packages. Any difference is insignificant compared to the dose from the entire repository.

## 6.7 SUMMARY AND RECOMMENDATIONS

Models have been prepared for use in TSPA-VA to describe relevant processes of waste form degradation, radionuclide mobilization, and transport of radionuclides through the EBS. In many cases these models are evolutionary developments from models used previously. In other cases, these models are being used for the first time in a TSPA. Improvements have been made in the following areas in the TSPA-VA base case:

- Developed cladding performance credit to limit the fraction of SNF matrix exposed as a function of time. This is a new model based on degradation mechanisms and external data, rather than the more arbitrary cladding credit that had been used in TSPA-95 sensitivity studies.
- Updated CSNF intrinsic dissolution rate model, including new dependence on burnup and gas phase oxygen in addition to temperature, pH, and CO<sub>3</sub>, which had been used previously. These new dependencies were not utilized in the TSPA-VA base case, but are available for sensitivity studies.
- Updated DHLW glass dissolution model.
- Revised solubility for Np, with ongoing review of other solubilities.
- Developed initial representation of colloid formation at waste form surfaces.
- Included of DSNF waste forms.
- Revised models for transport of radionuclides through the EBS with coupling to near-field geochemistry.

Additional improvements were made in models used in sensitivity analyses, including:

- Initial use in sensitivity studies of unsaturated CNSF test results to provide an alternative bound for mobilization of certain radionuclides.
- Initial use of reactive transport calculations to provide an alternative bound on Np mobilized concentrations in the presence of secondary phases.
- Initial inclusion of diffusive transport through waste form alteration products.
- Inclusion of Pu disposition waste forms.

These models were developed in cooperation with process experts working with PA staff, to assure acceptance of these models by those responsible for the testing and process model development. Input on these models is being received from several independent review and expert groups. These representations are preliminary and are expected to evolve throughout the TSPA-VA analysis.

#### **6.7.1 Implications for Performance**

The issues in this chapter define the quantity and nature of radionuclides that are released from the EBS. In this function, they constrain the potential doses from the repository. In most scenarios, a reduction in release from the EBS correlates to a similar reduction in dose at the accessible environment. There appears to be several conservative features in these models and assumptions. More realistic representation of these features holds potential for significant reduction in modeled dose rates. Key among these are water contact, solubilities, secondary phase retention of radionuclides, and diffusive transport through the EBS. Several features in this analysis bear additional scrutiny due to the possibility that they are nonconservative and could result in larger releases and dose rates. Key among these are cladding credit at very long times and the temporal averaging of short pulse releases. Two important parameters tying to portions of the near-field environment models include the assumptions regarding water contact modes (including distribution in time and space) and the variations in effective local chemistries for EBS processes.

The sensitivity of certain features and processes is influenced by assumptions, abstractions, and features of other system components. One of these features is the much longer lifetime predicted for the current WP design. This results in low temperatures by the time the waste forms are exposed, resulting in less importance for models such as cladding and SNF oxidation. Assumptions such as allowing aqueous processes upon exposure of waste form surfaces results in more importance to dissolution models and less to early release fractions and vapor phase alteration. Abstractions such as averaging burnup and fixed vapor phase oxygen content resulted in little change in release from improvements to the dissolution model.

#### **6.7.2 Guidance for License Application**

The analyses to date point to several areas that could provide high leverage on performance assessment results and increased confidence if they receive additional attention between the

viability assessment and the LA analyses. The highest leverage for additional information occurs where there is large sensitivity to a feature or process and also high uncertainty in the representation of that feature or process.

**Cladding Credit**—Cladding credit was a new feature of this TSPA. The cladding model provided significant reduction in EBS release rate for most times. The model is preliminary and has significant uncertainties. Additional gathering of industry data, model development, and specific laboratory tests to address the key uncertainties are recommended to provide a more robust representation in future analyses.

**Water Contact**—Ultimately, it is water contact with the waste form that provides a means for radionuclides to escape from the EBS and pose a risk to health and environment. Sensitivity to water contact ranges several orders of magnitude within the range of uncertainty in water flow processes. The details of water contact are improved in this analysis, but are still severely simplified. Integrated testing and modeling of EBS water flow processes are recommended to provide confidence in EBS models.

**Solubilities**—For many radionuclides, the EBS release rate is directly proportional to the elemental solubility used in TSPA. The current solubility distributions vary by many orders of magnitude, representing both data variability and uncertainty in environment and controlling processes. There has been a prioritization for reassessment of solubilities. The first of these priorities was Np, with initial results presented earlier in Section 6.4.1. Further evaluation of existing data, improved modeling, and selected laboratory experiments may allow removal of significant conservatism in future analyses.

Further development in solubility, secondary phase formation, and chemical reaction modeling should converge on a more realistic and more defensible mobilization rate, probably orders of magnitude below the rates used in this base case.

**Colloid Formation, Stability, and Transport**—This TSPA-VA included for the first time the colloidal mobilization and transport of Pu. This is a process that could lead to nonconservative results if ignored or misrepresented. It is also a process seen in field studies. The models in this analysis were extremely preliminary, and additional modeling and experimental work is needed to provide sufficient confidence in future treatment of colloids.

More specifically, it is recommended that the project continue to pursue more realistic and mechanistically based models of colloid-facilitated transport such as the reactive colloid transport model discussed in Chapter 8 Section 8.5.2.5, and to provide data to better constrain the parameters of those models. These parameters include sorption and desorption rates, colloid filtration, and effective porosities, and may require laboratory, field, and site-scale observations to adequately constrain. If desorption rates for some of the colloids such as the waste form colloids are too low to measure, then an irreversible model may be required, and its parameters may also need to be determined.

**Secondary Phase Retention of Radionuclides**—The formation of secondary (and tertiary) phases during SNF and glass dissolution at low water flow rates is a known process. The complexities of the actual mobilization rate of radionuclides in balance with this evolution of

phases is only known in a preliminary fashion, as represented in several sensitivity studies using preliminary models and data. The results indicate that significant reduction in modeled EBS release rates are possible if our understanding evolves to a level sufficient for use in future base-case analyses.

Further development in solubility, secondary phase formation, and chemical reaction modeling should converge on a more realistic and more defensible mobilization rate, probably orders of magnitude below the rates used in this base case.

**Diffusive Transport Through the EBS**—Diffusive transport through EBS materials, particularly through the porous secondary phases resulting from waste form dissolution, is not included in this TSPA-VA base case. Preliminary models indicate the potential for orders of magnitude reductions in aqueous release rates. Improved models and specific laboratory experiments are recommended to explore this process further.

## 6.8 REFERENCES

- Aagaard, P. and Helgeson, H.C. 1982. "Thermodynamic and Kinetic Constraints on Reaction Rates Among Minerals and Aqueous Solutions. Volume I. Theoretical Considerations." *American Journal of Science*, 282 (3), 237-285. New Haven, Connecticut: Yale University, Kline Geology Laboratory. 225516.
- Abrajano, T.; Bates, J.; Ebert, W.; and Gerding, T. 1986. "The Effect of Gamma Radiation on Groundwater Chemistry and Glass Leaching as Related to the NNWSI Repository Site." 88<sup>th</sup>. UCRL-15825, Preprint SANL-510-001. Argonne, Illinois: Argonne National Laboratory. 202939.
- Abrajano, T.A., Jr. and Bates, J.K. 1987. "Transport and Reaction Kinetics at the Glass: Solution Interface Region: Results of Repository-Oriented Leaching Experiments." *Scientific Basis for Nuclear Waste Management X, Materials Research Society Symposia Proceedings, Boston, Massachusetts, December 1-4, 1986*, 84, 533-546. Bates, J.K and Seefeldt, W.B., eds., Pittsburgh, Pennsylvania: Materials Research Society. 238700.
- Abrajano, T.A.; Bates, J.K.; Woodland, A.B.; Bradley, J.P.; and Bourcier, W.L. 1990. "Secondary Phase Formation During Nuclear Waste-Glass Dissolution." *Clays and Clay Minerals*, 38 (5), 537-548. Long Island City, New York: Pergamon Press. 238909.
- Ahn, T.M. 1996. *Dry Oxidation and Fracture of LWR Spent Fuels*. NUREG-1565. Washington, D.C.: Nuclear Regulatory Commission, Office of Nuclear Material Safety and Safeguards. 231667.
- Albinsson, Y.; Andersson, K.; Börjesson, S.; and Allard, B. 1993. *Diffusion of Radionuclides in Concrete/Bentonite Systems*. SKB Technical Report 93-29. Stockholm, Sweden: Swedish Nuclear Fuel and Waste Management Co. 210415.
- Andersson, K. 1988. *SKI Project-90: Chemical Data*. SKI Technical Report 91:21. Stockholm, Sweden: Swedish Nuclear Power Inspectorate. On order.
- Andrews, R.W.; Dale, T.F.; and McNeish, J.R. 1994. *Total System Performance Assessment - 1993: An Evaluation of the Potential Yucca Mountain Repository*. B00000000-01717-2200-00099 REV 01. Las Vegas, Nevada: CRWMS M&O. NNA.19940406.0158.
- ASM International Handbook Committee 1996. *Volume 19 Fatigue and Fracture*. ASM Handbook 10<sup>th</sup> Edition. Metals Materials Park, Ohio: ASM International. 239319.
- Barkatt, A.; Saad, E.E.; Adiga, R.; Sousanpour, W.; Barkatt, A.; Adel-Hadadi, M.A.; O'Keefe, J.A.; and Alterescu, S. 1989. "Leaching of Natural and Nuclear Waste Glasses in Sea Water." *Applied Geochemistry*, 4 (6), 593-603. New York, New York: Pergamon Press. 238911.
- Barnard, R.W.; Wilson, M.L.; Dockery, H.A.; Gauthier, J.H.; Kaplan, P.G.; Eaton, R.R.; Bingham, F.W.; and Robey, T.H. 1992. *TSPA 1991: An Initial Total-System Performance Assessment for Yucca Mountain*. SAND91-2795. Albuquerque, New Mexico: Sandia National Laboratories. NNA.19920630.0033.

Bates, J.K.; Bradley, J.P.; Teetsov, A.; Bradley, C.R.; Buckholtz ten Brink, M.B. 1992. "Colloid Formation During Waste Form Reaction: Implications for Nuclear Waste Disposal." *Science*, 256, 649-651. Washington, D.C.: American Association for the Advancement of Science. 239138.

Bates, J.K.; Bradley, C.R.; Buck, E.C.; Cunnane, J.C.; Dietz, N.L.; Ebert, W.L.; Emery, J.W.; Feng, X.; Gerding, T.J.; Gong, M.; Hoh, J.C.; Mazer, J.J.; Wronkiewicz, D.J.; Bourcier, W.L.; Morgan, L.E.; Newton, L.; Nielsen, J.K.; Phillips, B.L.; Ewing, R.C.; and Wang, L. 1993. *ANL Technical Support Program for DOE Environmental Restoration and Waste Management. Annual Report, October 1991-September 1992*. ANL-93/13. Argonne, Illinois: Argonne National Laboratory. 207129.

Bates, J.K.; Bradley, C.R.; Buck, E.C.; Cunnane, J.C.; Dietz, N.L.; Ebert, W.L.; and Emery, J.W. 1994. *ANL Technical Support Program for DOE Environmental Restoration and Waste Management. Annual Report, October 1992-September 1993*. ANL-94/19. Argonne, Illinois: Argonne National Laboratory. 211863.

Bates, J.K.; Hoh, J.C.; Emery, J.W.; Buck, E.C.; Fortner, J.A.; Wolf, S.F.; and Johnson, T.R. 1995a. "Reactivity of Plutonium-Containing Glasses for the Immobilization of Surplus Fissile Materials." *High Level Radioactive Waste Management 1995, Proceedings of the Sixth Annual International Conference, Las Vegas, Nevada, April 30-May 5, 1995*, 588-593. La Grange Park, Illinois: American Nuclear Society, Inc.; New York, New York: American Society of Civil Engineers. 235083.

Bates, J.K.; Finn, P.A.; Bourcier, W.L.; and Stout, R.B. 1995b. "Reaction Progress Pathways for Glass and Spent Fuel Under Unsaturated Conditions." *High Level Radioactive Waste Management 1995, Proceedings of the Sixth Annual International Conference, Las Vegas, Nevada, April 30-May 5, 1995*, 600-602. La Grange Park, Illinois: American Nuclear Society, Inc. 238001.

Baxter, R.G. 1983. *Description of Defense Waste Processing Facility Reference Waste Form and Canister*. DP-1606 Rev. 1. Aiken, South Carolina: Savannah River Laboratory. 225532.

Beckett, T.H. 1998 (May 8). Letter (Department of the Navy), from Thomas H. Beckett (C), to Dr. J. Russell Dyer, Yucca Mountain Site Characterization Office. Re: Naval Spent Nuclear Fuel Package Source Term Release Data. Arlington, Virginia: Department of the Navy. MOL.19980617.0476.

Bourcier, W.L.; Weed, H.C.; Nguyen, S.N.; Nielsen, J.K.; Morgan, L.; Newton, L.; and Knauss, K.G. 1992. "Solution Compositional Effects on Dissolution Kinetics of Borosilicate Glass." *Proceedings of the Seventh International Symposium on Water-Rock Interaction, Park City, Utah, July 13-18, 1992*, 81-84. Kharaka, Y.K. and Maest, A.S., eds., Rotterdam, The Netherlands: A.A. Balkema. 238352.

Bourcier, W.L. 1994. *Critical Review of Glass Performance Modeling*. ANL-94/17. Argonne, Illinois: Argonne National Laboratory, Chemical Technology Division. 211862.

Bourcier, W.L.; Carroll, S.A.; and Phillips, B.L. 1994. "Constraints on the Affinity Term for Modeling Long-Term Glass Dissolution Rates." *Scientific Basis for Nuclear Waste Management XVII, Materials Research Society Symposium Proceedings, Boston, Massachusetts, November 29-December 3, 1993*, 333, 507-512. Barkatt, A. and Van Konynenburg, R.A., eds., Pittsburgh, Pennsylvania: Materials Research Society. 237858.

Bradley, E.R.; Bailey, W.J.; Johnson, A.B., Jr.; and Lowry, L.M. 1981. *Examination of Zircaloy-Clad Spent Fuel After Extended Pool Storage*. PNL-3921. Richland, Washington: Pacific Northwest Laboratory. 230049.

Bruno, J.; Casas, I.; Cera, E.; Ewing, R.C.; Finch, R.J.; and Werme, L.O. 1995. "The Assessment of the Long-Term Evolution of the Spent Nuclear Fuel Matrix by Kinetic, Thermodynamic and Spectroscopic Studies of Uranium Minerals." *Scientific Basis for Nuclear Waste Management XVIII, Materials Research Society Symposium Proceedings, Kyoto, Japan, October 23-27, 1994*, 353 (1), 633-639. Murakami, T. and Ewing, R.C., eds., Pittsburgh, Pennsylvania: Materials Research Society. 238160.

Bruno, J.; Cera, E.; Eklund, U.B.; Eriksen, T.E.; and Grive, M. 1998. "Some Preliminary Modeling Results of Long Term Radiolytic Mass Balance Experiments." *Presentation at 1998 International Spent Fuel Workshop, Las Vegas, Nevada, May 18-20, 1998*. Barcelona, Spain: Quantisci. 240716.

Buck, E.C.; Finch, R.J.; Finn, P.A.; and Bates, J.K. 1998. "Retention of Neptunium in Uranyl Alteration Phases Formed During Spent Fuel Corrosion." *Scientific Basis for Nuclear Waste Management XXI, Materials Research Society Symposium Proceedings, Davos, Switzerland, September 28-October 3, 1997*, 506, 87-94. McKinley, I.G. and McCombie, C., eds., Warrendale, Pennsylvania: Materials Research Society. 240017.

Bunker, B.C.; Tallant, D.R.; Headley, T.J.; Turner, G.L.; and Kirkpatrick, R.J. 1988. "The Structure of Leached Sodium Borosilicate Glass." *Physics and Chemistry of Glasses*, 29 (3), 106-120. Sheffield, England: Society of Glass Technology. 239215.

Burns, P.C.; Ewing, R.C.; and Miller, M.L. 1997. "Incorporation Mechanisms of Actinide Elements into the Structures of  $U^{6+}$  Phases Formed During the Oxidation of Spent Nuclear Fuel." *Journal of Nuclear Materials*, 245 (1), 1-9. Amsterdam, The Netherlands: North-Holland Publishing Company. 235501.

Casas, I.; Bruno, J.; Cera, E.; Finch, R.J.; and Ewing, R.C. 1994. *Kinetic and Thermodynamic Studies of Uranium Minerals: Assessment of the Long-Term Evolution of Spent Nuclear Fuel*. SKB Technical Report 94-16. Stockholm, Sweden: Swedish Nuclear Fuel and Waste Management Company. 213723.

Charquet, D.; Rudling, P.; Mikes-Lindback, M.; and Barberis, P. 1994. "Hydrogen Absorption Kinetics During Zircaloy Oxidation in Steam." *Zirconium in the Nuclear Industry, Tenth International Symposium, Baltimore, Maryland, June 21-24, 1993*, 80-95. Garde, A.M. and Bradley, E.R., eds., Philadelphia, Pennsylvania: American Society for Testing and Materials. 237257.

- Chen, Y.; Engel, D.W.; McGrail, B.P.; and Lessor, K.S. 1995. *AREST-CT V1.0 Software Verification*. PNL-10692. Richland, Washington: Pacific Northwest Laboratory. 238766.
- Chen, Y.; McGrail, B.P.; and Engel, D.W. 1996. "A Reaction-Transport Model and Its Application to Performance Assessment of Nuclear Waste Disposal." *Proceedings of the 1996 International Conference on Deep Geological Disposal of Radioactive Waste, Winnipeg, Manitoba, Canada, September 16-19, 1996*, 8-21 to 8-30. Ohta, M.M. and Nuttall, K., eds., Toronto, Ontario, Canada: Canadian Nuclear Society. 235084.
- Chen, Y.; McGrail, B.P.; and Engel, D.W. 1997a. "Source-Term Analysis for Hanford Low-Activity Tank Waste Using the Reaction-Transport Code AREST-CT." *Scientific Basis for Nuclear Waste Management XX, Materials Research Society Symposium Proceedings, Boston, Massachusetts, December 2-6, 1996*, 465, 1051-1058. Gray, W.J. and Triay, I.R., eds., Pittsburgh, Pennsylvania: Materials Research Society. 236519.
- Chen, Y.; Chen, W.; Mu, J.; Park, A.; and Ortoleva, P. 1997b. *A General, Coupled Model for Solute Transport and Reactions and Porous Medium Alteration*. Las Vegas, Nevada: Duke Engineering & Services. 238119.
- Chen, Y. 1998. *Software Routine Report for AREST-CT (Version 1.2)*. TSPA:VA6-WFMD. Las Vegas, Nevada: Civilian Radioactive Waste Management System, Management and Operating Contractor. 237968.
- Chick, L.A. and Pederson, L.R. 1984. "The Relationship Between Layer Thickness and Leach Rate for Nuclear Waste Glasses." *Scientific Basis for Nuclear Waste Management VII, Materials Research Society Symposium Proceedings, Boston, Massachusetts, November 14-17, 1983*, 26, 635-642. McVay, G.L., ed., Pittsburgh, Pennsylvania: Materials Research Society. 221404.
- Chin, B.A. and Gilbert, E.R. 1989. "Prediction of Maximum Allowable Temperatures for Dry Storage of Zircaloy-Clad Spent Fuel in Inert Atmosphere." *Nuclear Technology*, 85 (1), 57-65. Hinsdale, Illinois: American Nuclear Society, Inc. 224675.
- Conca, J.L. and Wright, J. 1990. "Diffusion Coefficients in Gravel Under Unsaturated Conditions." *Water Resources Research*, 26 (5), 1055-1066. Washington, D.C.: American Geophysical Union. 237421.
- Conca, J.L. and Wright, J. 1992. "Diffusion and Flow in Gravel, Soil, and Whole Rock." *Applied Hydrogeology*, 1 (1), 5-24. Hanover, Germany: Verlag Heinz Heise. 224081.
- Cotton, F.A. and Wilkinson, G. 1980. *Advanced Inorganic Chemistry: A Comprehensive Text*. Fourth Edition, Completely Revised from the Original Literature. New York, New York: John Wiley and Sons. 217739.
- Cragolino, G. and Galvele, J.R. 1977. "Anodic Behavior and Pitting of Zirconium and Zircaloy-4 in Aqueous Solutions of Sodium Chloride." *Passivity of Metals, Proceedings of the Fourth International Symposium on Passivity*, 1053-1057. Frankenthal, R.P. and Kruger, J., eds., Princeton, New Jersey: The Electrochemical Society. 237155.

Cresap, D. 1997. *Results of Sensitivity Studies on Parameters for INEEL Spent Fuel*. Draft. Idaho Falls, ID: Idaho National Engineering and Environmental Laboratory, National Spent Fuel Program. On order.

CRWMS M&O (Civilian Radioactive Waste Management system, Management and Operating Contractor) 1995. *Total System Performance Assessment - 1995: An Evaluation of the Potential Yucca Mountain Repository*. B00000000-01717-2200-00136 REV 01. Las Vegas, Nevada: Author. MOL.19960724.0188.

CRWMS M&O 1997a. *Total System Performance Assessment Sensitivity Studies of U.S. Department of Energy Spent Nuclear Fuel*. A00000000-01717-5705-00017 REV 01. Prepared for National Spent Nuclear Fuel Program, U.S. Department of Energy, Idaho Operations Office, Idaho Falls, Idaho. Las Vegas, Nevada: Author. MOL.19980618.0474.

CRWMS M&O 1997b. *Waste Form Degradation and Radionuclide Mobilization Abstraction/Testing Workshop Results*. B00000000-01717-2200-00189. Las Vegas, Nevada: Author. MOL.19980602.0479.

CRWMS M&O 1997c. *Waste Quantity, Mix and Throughput Study Report*. B00000000-01717-5705-00059 REV 01. Las Vegas, Nevada: Author. MOL.19980123.0681.

CRWMS M&O 1997d. *Confirmation of Empirical Design Methodologies*. BABEE0000-01717-5705-00002 REV 00. Las Vegas, Nevada: Author. MOL.19980219.0104.

CRWMS M&O 1997e. *Report of Results of Hydraulic and Tracer Tests at the C-Holes Complex (1997f)*. Las Vegas, Nevada: Author. MOL.19971024.0074.

CRWMS M&O 1997f. *Thermal Evaluation of Preliminary 21 PWR UCF Design - Internal Structures*. BBAA00000-01717-0200-00018 REV 00. Las Vegas, Nevada: Author. MOL.19971103.0481.

CRWMS M&O 1998a. *Constraints on Solubility-Limited Neptunium Concentrations for Use in Performance Assessment Analyses*. B00000000-01717-2200-00191 REV 00. Las Vegas, Nevada: Author. MOL.19980213.0484.

CRWMS M&O 1998b. *Design Basis Cladding Analysis*. BBA000000-01717-0200-00054 REV 01. Las Vegas, Nevada: Author. MOL.19980325.0102.

CRWMS M&O 1998c. *AREST-CT Parameter Input: Calculation of Spent Fuel Volume Fraction, Porosity, and Radius*. B00000000-01717-0210-00025 REV 01. Las Vegas, Nevada: Author. MOL.19981030.0236.

CRWMS M&O 1998d. *Waste Form Degradation and Radionuclide Mobilization Expert Elicitation Project*. Rev. 1. Las Vegas, Nevada. Author. MOL.19980804.0099.

CRWMS M&O 1998e. *Fitting of the Data for Diffusion Coefficients in Unsaturated Porous Media*. B00000000-01717-0210-00026 REV 00. Las Vegas, Nevada: Author. MOL.19981014.0003.

Cunnane, J.C.; Bates, J.K.; Bradley, C.R.; Buck, E.C.; Ebert, W.L.; Feng, X.; Mazer, J.J.; Wronkiewicz, D.J.; Sproull, J.; Bourcier, W.L.; McGrail, B.P.; and Altenhofen, M.K. eds., 1994. *High-Level Waste Borosilicate Glass: A Compendium of Corrosion Characteristics*. DOE-EM-0177. Washington, D.C.: U.S. Department of Energy, Assistant Secretary for Environmental Management. On order.

Cunningham, M.E.; Simonen, E.P.; Allemann, R.T.; Levy, I.S.; and Hazelton, R.F. 1987. *Control of Degradation of Spent LWR Fuel During Dry Storage in an Inert Atmosphere*. PNL-6364. Richland, Washington: Pacific Northwest Laboratory. 210249.

DOE (U.S. Department of Energy) 1987. *Characteristics of Spent Fuel, High-Level Waste, and Other Radioactive Wastes Which May Require Long-Term Isolation*. DOE/RW-0184, Vols. 1-6. Washington, D.C.: DOE, Office of Civilian Radioactive Waste Management. 202243.

DOE 1996. *Spent Nuclear Fuel Discharges from U.S. Reactors 1994*. SR/CNEAF/96-01. Washington, D.C.: U.S. DOE, Office of Coal, Nuclear, Electric and Alternate Fuels, Energy Information Administration. 232923.

DOE 1998. *Viability Assessment of a Repository at Yucca Mountain*. DOE/RW-0508. 5 volumes. Washington, D.C.: U.S. Government Printing Office.

Overview (Executive Summary). MOL.19981007.0027.

Volume 1. MOL.19981007.0028.

Volume 2: MOL.19981007.0029.

Volume 3: MOL.19981007.0030.

Volume 4: MOL.19981007.0031.

Volume 5: MOL.19981007.0032.

Doubt, G. 1984. *Assessing Reliability and Useful Life of Containers for Disposal of Irradiated Fuel Waste*. AECL-8328. Chalk River, Ontario, Canada: Atomic Energy of Canada Limited, Chalk River Nuclear Laboratories. 227332.

Duffy, C.J. 1993. *Preliminary Conceptual Model for Mineral Evolution in Yucca Mountain*. LA-12708-MS, Los Alamos, New Mexico: Los Alamos National Laboratory. NNA.19900117.0152.

Dyer, J.R. 1993 (August 2). *Radionuclide Solubility Working Group (SolWOG) Meeting Report*. DOE Letter with Enclosure to LLNL and LANL. Las Vegas, Nevada: TRW Environmental Safety Systems. MOL.19981104.0136.

Efurd, D.W.; Runde, W.; Banar, J.C.; Roensch, F.R.; Clark, D.L.; Palmer, P.D.; and Tait, C.D. 1996. *Measured Solubilities and Speciation of Neptunium and Plutonium in J-13 Groundwater*. LANL Milestone Report 3411. Los Alamos, New Mexico: Los Alamos National Laboratory. 237839.

Einzigler, R.E.; Atkin, S.D.; Stellrecht, D.E.; and Pasupathi, V. 1982. "High Temperature Postirradiation Materials Performance of Spent Pressurized Water Reactor Fuel Rods Under Dry Storage Conditions." *Nuclear Technology*, 57 (1), 65-80. Hinsdale, Illinois: American Nuclear Society, Inc. 237142.

Einzigler, R.E. and Kohli, R. 1984. "Low-Temperature Rupture Behavior of Zircaloy-Clad Pressurized Water Reactor Spent Fuel Rods Under Dry Storage Conditions." *Nuclear Technology*, 67 (1), 107-123. Hinsdale, Illinois.: American Nuclear Society. 216868.

Einzigler, R.E. and Strain, R.V. 1986. "Behavior of Breached Pressurized Water Reactor Spent-Fuel Rods in an Air Atmosphere Between 250 and 360°C." *Nuclear Technology*, 75 (1), 82-95. Hinsdale, Illinois. American Nuclear Society, Inc. 238325.

Einzigler, R.E.; Thomas, L.E.; Buchanan, H.C.; and Stout, R.B. 1992. "Oxidation of Spent Fuel in Air at 175 to 195°C." *Journal of Nuclear Materials*, 190, 53-60. Amsterdam, The Netherlands: North-Holland Publishing Company. 238511.

Einzigler, R.E. 1994. "Preliminary Spent LWR Fuel Oxidation Source Term Model." *High Level Radioactive Waste Management, Proceedings of the Fifth Annual International Conference, Las Vegas, Nevada, May 22-26, 1994*, 2, 554-559. La Grange Park, Illinois: American Nuclear Society, Inc.; New York, New York: American Society of Civil Engineers. 233158.

EPRI (Electrical Power Research Institute) 1997. *The Technical Basis for the Classification of Failed Fuel in the Back-End of the Fuel Cycle*. EPRI TR-108237, 4-1 to 4-3. Palo Alto, California: Electric Power Research Institute. 236839.

Ewing, R.C. and Jercinovic, M.J. 1987. "Natural Analogues: Their Application to the Prediction of the Long-Term Behavior of Nuclear Waste Forms." *Scientific Basis for Nuclear Waste Management X, Materials Research Society Symposia Proceedings, Boston, Massachusetts, December 1-4, 1986*, 84, 67-83. Bates, J.K and Seefeldt, W.B., eds., Pittsburgh, Pennsylvania: Materials Research Society. 240556.

Feng, X.; Buck, E.C.; Mertz, C.; Bates, J.K.; Cunnane, J.C.; and Chaiko, D.J. 1994. "Characteristics of Colloids Generated During the Corrosion of Nuclear Waste Glasses in Groundwater." *Radiochimica Acta*, 66/67, 197-205. Munich: R. Oldenbourg Verlag; New York, New York: Academic Press. 238720.

Finch, R.J. and Ewing, R.C. 1992. "Uranyl Oxide Hydrates and Uraninite Corrosion: Relevance to 'Natural Analogue' Studies of Spent Fuel Corrosion." *High Level Radioactive Waste Management, Proceedings of the Third International Conference, Las Vegas, Nevada, April 12-16, 1992*, 1, 332-337. La Grange Park, Illinois: American Nuclear Society, Inc.; New York, New York: American Society of Civil Engineers. 240557.

Finn, P.A.; Buck, E.C.; Gong, M.; Hoh, J.C.; Emery, J.W.; Hafenrichter, L.D.; and Bates, J.K. 1994a. "Colloidal Products and Actinide Species in Leachate from Spent Nuclear Fuel." *Radiochimica Acta*, 66/67, 189-195. Munich, Germany: R. Oldenbourg Verlag; New York, New York: Academic Press. 238493.

Finn, P.A.; Bates, J.K.; Hoh, J.C.; Emery, J.W.; Hafenrichter, L.D.; Buck, E.C.; and Gong, M. 1994b. "Elements Present in Leach Solutions from Unsaturated Spent Fuel Tests." *Scientific Basis for Nuclear Waste Management XVII, Materials Research Society Symposium Proceedings, Boston, Massachusetts, November 29-December 3, 1993*, 333, 399-407. Barkatt, A. and Van Konynenburg, R.A., eds., Pittsburgh, Pennsylvania: Materials Research Society. 238007.

Finn, P.A.; Hoh, J.C.; Wolf, S.F.; Slater, S.A.; and Bates, J.K. 1995. "The Release of Uranium, Plutonium, Cesium, Strontium, Technetium and Iodine from Spent Fuel Under Unsaturated Conditions." *Migration '95, Fifth International Conf. on the Chemistry and Migration Behavior of Actinides and Fission Products in the Geosphere*, Saint-Malo, France, Sept 10-15, 1995. 238155.

Finn, P.A.; Hoh, J.C.; Wolf, S.F.; Surchik, M.T.; Buck, E.C.; and Bates, J.K. 1997b. "Spent Fuel Reaction: The Behavior of the  $\epsilon$ -Phase Over 3.1 Years." *Scientific Basis for Nuclear Waste Management XX, Materials Research Society Symposium Proceedings, Boston, Massachusetts, December 2-6, 1996*, 465, 527-534. Gray, W.J. and Triay, I.R., eds., Pittsburgh, Pennsylvania: Materials Research Society. 238716.

Finn, P.A.; Wronkiewicz, D.J.; Finch, R.J.; Hoh, J.C.; Mertz, Co; Emery, J.W.; Buck, E.C.; Fortner, J.A.; Wolf, S.F.; Neimark, L.A.; and Bates, J.K. 1998a. *Yucca Mountain Project—Argonne National Laboratory, Annual Progress Report, FY 1997 for Activity WP1221: Unsaturated Drip Condition Testing of Spent Fuel and Unsaturated Dissolution Tests of Glass. ANL-98/12*. Argonne, Illinois: Argonne National Laboratory. MOL.19980818.0230.

Finn, P.A.; Finch, R.; Buck, E.; and Bates, J. 1998b. "Corrosion Mechanisms of Spent Fuel Under Oxidizing Conditions." *Scientific Basis for Nuclear Waste Management XXI, Materials Research Society Symposium Proceedings, Davos, Switzerland, September 28-October 3, 1997*, 506, 123-131. McKinley, I.G. and McCombie, C., eds., Warrendale, Pennsylvania: Materials Research Society. 234677.

Fix, P.F. 1956. "Hydrogeochemical Exploration for Uranium." Contributions to the Geology of Uranium and Thorium by the United States Geological Survey and Atomic Energy Commission for the United Nations Conference on Peaceful Uses of Atomic Energy, Geneva, Switzerland, 1955. Geological Survey Professional Paper 3, 667-671. Page, L.R.; Stocking, H.E.; and Smith, H.B., compilers. Washington, D.C.: U.S. Government Printing Office. 238658.

Garde, A.M. 1986. *Hot Cell Examination of Extended Burnup Fuel from Fort Calhoun*. DOE/ET/34030-11, CEND-427. Windsor, Connecticut: Combustion Engineering, Inc. 237128.

Garde, A.M. 1991. "Enhancement of Aqueous Corrosion of Zircaloy-4 Due to Hydride Precipitation at the Metal-Oxide Interface." *Zirconium in the Nuclear Industry, Ninth International Symposium, Kobe, Japan, November 5-8, 1990*. ASTM Special Technical Publication 1, 566-591. Eucken, C.M. and Garde, A.M., eds., Philadelphia, Pennsylvania: American Society for Testing and Materials. 237129.

Golder Associates 1993. *Application of RIP (Repository Integration Program) to the Potential Repository at Yucca Mountain: Conceptual Model and Input Data Set*. Redmond, Washington: Golder Associates. 235334.

Golder Associates 1998. *RIP Integrated Probabilistic Simulator for Environmental Systems: Theory Manual and User's Guide*. Redmond, Washington: Golder Associates. 238560.

Gould, T. 1998. *Plutonium Immobilization Project, Data for Yucca Mountain Total System Performance Assess.* Letter Report to Sarvajit S. Sareen, TRW Safety Systems, Inc., Vienna, Virginia. January 23, 1998. PIP 98-011 and PIP 98-012. Livermore, California: Lawrence Livermore National Laboratory. MOL.19980617.0472.

Grambow, B. 1987. *Nuclear Waste Glass Dissolution: Mechanism, Model and Application. Report to JSS Project Phase IV*. JSS Project 87-02. Stockholm, Sweden: SKB, Swedish Nuclear Fuel and Waste Management Company. 239007.

Grambow, B. 1998. "Source Terms for Performance Assessment of HLW-Glass and Spent Fuel as Waste Forms." *Scientific Basis for Nuclear Waste Management XXI, Materials Research Society Symposium Proceedings, Davos, Switzerland, September 28-October 3, 1997*, 506, 141-152. McKinley, I.G. and McCombie, C., eds., Warrendale, Pennsylvania: Materials Research Society. 238657.

Gray, W.J.; Leider, H.R.; and Steward, S.A. 1992. *Parametric Study of LWR Spent Fuel Dissolution Kinetics*. UCRL-JC-110160. Livermore, California: Lawrence Livermore National Laboratory. 230492. (See also: Gray, W.J.; Leider, H.R.; and Steward, S.A. 1992. "Parametric Study of LWR Spent Fuel Dissolution Kinetics." *Journal of Nuclear Materials*, 190, 46-52. Amsterdam, The Netherlands: North-Holland Publishing Company. 230492; 238041.

Gray, W.J. and Wilson, C.N. 1995. *Spent Fuel Dissolution Studies FY 1991-1994*. PNL-10540. Richland, Washington: Pacific Northwest Laboratory. MOL.19960325.0421.

Grenthe, I.; Fuger, J.; Konings, R.J.M.; Lemire, R.J.; Muller, A.B.; Nguyen-Trung, C.; and Wanner, H. 1992. "Chemical Thermodynamics of Uranium." *Chemical Thermodynamics Vol. 1*. 714 Wanner, H. and Forest, I., eds., Amsterdam, The Netherlands: North-Holland Publishing Company; New York, New York: Elsevier Science Pub. Company. 224074.

Hanson, B.D. 1998. *Burnup Dependence of Light Water Reactor Spent Fuel Oxidation*. PNNL-11929. Richland, Washington: Hanford Northwest National Laboratory. 238459.

Hansson, C.M. 1984. *The Corrosion of Zircaloy 2 in Anaerobic Synthetic Cement Pore Solution*. SKB-KBS-TR-84-13. Stockholm, Sweden: Svensk Kärnbränsleförsörjning A.B. 206293.

Hardin, E.L.; Blair, S.C.; Bourcier, W.L.; Buscheck, T.A.; Chesnut, D.A.; DeLoach, L.D.; Glassley, W.E.; Johnson, J.W.; Knapp, R.B.; Lee, K.; Meike, A.; Myers, K.; Nitao, J.J.; Palmer, C.E.; Rogers, L.L.; Rosenberg, N.D.; Viani, B.E.; Wittwer, C.; and Wolery, T.J. 1998. *Near-Field/Altered-Zone Models Report*. UCRL-ID-129179 DR, Level 4 Milestone Report SP3100M4. Livermore, California: Lawrence Livermore National Laboratory. MOL.19980504.0577.

- Hillner, E.; Franklin, D.G.; and Smee, J.D. 1998. "The Corrosion of Zircaloy-Clay Fuel Assemblies in a Geologic Repository Environment." *Journal of Nuclear Materials*. WAPD-T-3193. West Mifflin, Pennsylvania: Bettis Atomic Power Laboratory. 237127.
- Huang, F.H. 1995. *Fracture Properties of Irradiated Alloys*. p. 195. Richland, Washington: Avante Press. 224548.
- IAEA (International Atomic Energy Agency) 1988. *Survey of Experience with Dry Storage of Spent Nuclear Fuel and Update of Wet Storage Experience*. Technical Reports Series No. 290. Vienna, Austria: International Atomic Energy Agency. 233246.
- IAEA (International Atomic Energy Agency) 1998. *Waterside Corrosion of Zirconium Alloys in Nuclear Power Plants*. IAEA-TECDOC-996, p. 178. Vienna, Austria: International Atomic Energy Agency. 238879.
- INEEL (Idaho National Engineering and Environmental Laboratory) 1997. *Technical Strategy for the Management of INEEL Spent Nuclear Fuel*. INEL/EXT-97-00387-Vol. 1. Idaho Falls, Idaho: Idaho National Engineering Laboratory, Task Team on Spent Nuclear Fuel. 235028.
- Janecky, D.R.; Duffy, C.J.; Tait, C.D.; and Clark, D. 1994. *Letter Report on Thermochemical Data on Actinides for Modeling*. LANL Milestone Report 4025. Los Alamos, New Mexico: Los Alamos National Laboratory. On order.
- Johnson, A.B., Jr. 1977. *Behavior of Spent Nuclear Fuel in Water Pool Storage*. BNWL-2256. Richland, Washington: Pacific Northwest Laboratories. 234703.
- Johnson, A.B., Jr.; Dobbins, J.C.; Zaloudek, F.R.; Gilbert, E.R.; and Levy, I.R. 1987. *Assessment of the Integrity of Spent Fuel Assemblies Used in Dry Storage Demonstrations at the Nevada Test Site*. PNL-6207. Richland, Washington: Pacific Northwest Laboratory. 230135.
- Johnson, A.B., Jr.; Bailey, W.J.; Schreiber, R.E.; and Kustas, F.M. 1980. *Annual Report - FY 1979. Spent Fuel and Fuel Pool Component Integrity*. PNL-3171. Richland, Washington: Pacific Northwest Laboratory. 229623.
- Johnson, J.W.; Oelkers, E.H.; and Helgeson, H.C. 1992. "SUPCRT92: A Software Package for Calculating the Standard Molal Thermodynamic Properties of Minerals, Gases, Aqueous Species, and Reactions from 1 to 5000 Bar and 0 to 1000°C." *Computers & Geosciences*, 18 (7), 899-947. Oxford; New York, New York: Pergamon Press. 234273.
- Kerrisk, J.F. 1984. *Solubility Limits on Radionuclide Dissolution At a Yucca Mountain Repository*. LA-9995-MS. Los Alamos, New Mexico: Los Alamos National Laboratory. NNA.19870519.0049.
- Knauss, K.G.; Bourcier, W.L.; McKeegan, K.D.; Merzbacher, C.I.; Nguyen, S.N.; Ryerson, F.J.; Smith, D.K.; Weed, H.C.; and Newton, L. 1990. "Dissolution Kinetics of a Simple Analogue Nuclear Waste Glass as a Function of pH, Time and Temperature." *Scientific Basis for Nuclear Waste Management XIII, Materials Research Society Symposium Proceedings, Boston*,

Massachusetts, November 27-30, 1989, 176, 371-381. Oversby, V.M. and Brown, P.W., eds., Pittsburgh, Pennsylvania: Materials Research Society. 203658.

Krauskopf, D.K. and Bird, D.K. 1995. *Introduction to Geochemistry*. Third Edition. New York, New York: McGraw-Hill. 239316.

Kreyns, P.H.; Bourgeois, W.F.; White, C.J.; Charpentier, P.L.; Kammenzind, B.F.; and Franklin, D.G. 1996. "Embrittlement of Reactor Core Materials." *Zirconium in the Nuclear Industry, Eleventh International Symposium, Garmisch-Partenkirchen, Germany, September 11-14, 1995*, 758-782. Bradley, E.R. and Sabol, G.P., eds., West Conshohocken, Pennsylvania: American Society for Testing and Materials. 237256.

Langmuir, D. 1978. "Uranium Solution-Mineral Equilibria at Low Temperatures with Applications to Sedimentary Ore Deposits." *Geochimica et Cosmochimica Acta*, 42 (6), 547-569. Oxford; New York, New York: Pergamon Press. 217857.

Lanning, D.D.; Beyer, C.E.; and Painter, C.L. 1997. *FRAPCON-3: Modifications to Fuel Rod Material Properties and Performance Models for High-Burnup Application*. PNNL-11513-V1, NUREG/CR-6534-V1. Richland, Washington: Pacific Northwest National Laboratory; Washington, D.C.: Nuclear Regulatory Commission, Division of Systems Technology. 238923.

Lappa, D.A. 1995. *Immobilization 1: Greenfield Glass, Preliminary Plutonium Vitrification Schedule is Attached*. Correspondence to D.J. Harrison, U.S. Department of Energy. Livermore, California: Lawrence Livermore National Laboratory. MOL.19970421.0195.

Lasaga, A.C. 1984. "Chemical Kinetics of Water-Rock Interactions." *Journal of Geophysical Research*, 89 (B6), 4009-4025. Washington, D.C.: American Geophysical Union. 224110.

Lee, J.H.; Chambré, P.L.; and Andrews, R.W. 1996a. "Mathematical Models for Diffusive Mass Transfer from Waste Package Container with Multiple Perforations." *Proceedings of the 1996 International Conference on Deep Geological Disposal of Radioactive Waste, Winnipeg, Manitoba, Canada, September 16-19, 1996*, 5:61 through 5:72. Ohta, M.M. and Nuttall, K., eds., Toronto, Ontario, Canada: Canadian Nuclear Society. 240568.

Lee, J.H.; Atkins, J.E.; McNeish, J.A.; and Vallikat, V. 1996b. "Sensitivity of the Engineered Barrier System (EBS) Release Rate to Alternative Conceptual Models of Advective Release from Waste Packages Under Dripping Fractures." *Proceedings of the 1996 International Conference on Deep Geological Disposal of Radioactive Waste, Winnipeg, Manitoba, Canada, September 16-19, 1996*, 8:65 through 8:75. Ohta, M.M. and Nuttall, K., eds., Toronto, Ontario, Canada: Canadian Nuclear Society. 240570.

Lemire, R.J. and Tremaine, P.R. 1980. "Uranium and Plutonium Equilibria in Aqueous Solutions to 200°C." *Journal of Chemical and Engineering Data*, 25 (4), 361-370. Washington, D.C.: American Chemical Society. 222175.

Lemire, R.J. 1984. *An Assessment of the Thermodynamic Behaviour of Neptunium in Water and Model Groundwaters from 25 to 150°C*. AECL-7817, Pinawa, Manitoba, Canada: Atomic Energy of Canada Limited, Whiteshell Nuclear Research Establishment. 238910.

Leslie, B.W.; Percy, E.C.; and Prikryl, J.D. 1993. "Oxidative Alteration of Uraninite at the Nopal I Deposit, Mexico: Possible Contaminant Transport and Source Term Constraints for the Proposed Repository at Yucca Mountain." *Scientific Basis for Nuclear Waste Management XVI, Materials Research Society Symposium Proceedings, Boston, Massachusetts, November 30-December 4, 1992*, 294, 505-512. Interrante, C.G. and Pabalan, R.T., eds., Pittsburgh, Pennsylvania: Materials Research Society. 240571.

Lorenz, R.A.; Collins, J.L.; Malinauskas, A.P.; Kirkland, O.L.; and Towns, R.L. 1980. *Fission Product Release from Highly Irradiated LWR Fuel*. NUREG/CR-0722, ORNL/NUREG/TM-287. Oak Ridge, Tennessee: Oak Ridge National Laboratory for the U.S. Nuclear Regulatory Commission, Office of Nuclear Regulatory Research, Washington, D.C. 211434.

Lowry, L.M.; Markworth, A.J.; Perrin, J.S.; and Landow, M.P. 1981. *Evaluating Strength and Ductility of Irradiated Zircaloy, Task 5. Experimental Data Final Report*. NUREG/CR-1729, BMI-2066, Vol. 1. Columbus, Ohio: Battelle Columbus Laboratories for U.S. Nuclear Regulatory Commission, Washington, D.C. 238074.

Lu, N.; Triay, I.R.; Cotter, C.R.; Kitten, H.D.; and Bently, J. 1998. Reversibility of Sorption of Plutonium - 239 onto Colloids of Hematite, Goethite, Smectite, and Silica. Los Alamos, New Mexico: Los Alamos National Laboratory. MOL.19981030.0202.

Maguire, M. 1984. "The Pitting Susceptibility of Zirconium in Aqueous Cl<sup>-</sup>, Br<sup>-</sup>, and I<sup>-</sup> Solutions." *Industrial Applications of Titanium and Zirconium: Third Conference, A Symposium Sponsored by ASTM Committee B-10 on Reactive and Refractory Metals and Alloys, New Orleans, Louisiana, September 21-23, 1982*. ASTM Special Technical Publication 830, 177-189. Philadelphia, Pennsylvania: American Society for Testing and Materials. 237161.

Mahmood, S.T.; Farkas, D.M.; Adamson, R.B.; and Etoh, Y. 1998. "Post-Irradiation Characterization of Ultra High Fluence Zircaloy-2 Plate." *Twelfth International Symposium on Zirconium in the Nuclear Industry, Program Abstracts, Toronto, Ontario, Canada, June 15-18, 1998*, 19-20. Philadelphia, Pennsylvania: American Society for Testing and Materials. 237270.

Manaktala, H.K. 1993. *Characteristics of Spent Nuclear Fuel and Cladding Relevant to High-Level Waste Source Term*. CNWRA 93-006. San Antonio, Texas: Center for Nuclear Waste Regulatory Analyses. 208034.

Manzel, R. and Coquerelle, M. 1997. "Fission Gas Release and Pellet Structure at Extended Burnup." *Proceedings of the 1997 International Topical Meeting on LWR Fuel Performance, Portland, Oregon, March 2-6, 1997*, 463-470. La Grange Park, Illinois: American Nuclear Society, Inc. 237134.

Mardon, J.P.; Garner, G.; Beslu, P.; Charquet, D.; and Senevat, J. 1997. "Update on the Development of Advanced Zirconium Alloys for PWR Fuel Rod Claddings." *Proceedings of the 1997 International Topical Meeting on LWR Fuel Performance, Portland, Oregon, March 2-6, 1997*, 405-412. La Grange Park, Illinois: American Nuclear Society, Inc. 237167.

Matsuo, Y. 1987. "Thermal Creep of Zircaloy-4 Cladding Under Internal Pressure." *Journal of Nuclear Science and Technology*, 24 (2), 111-119. Tokyo, Japan: Atomic Energy Society of Japan. 237137.

Mayuzumi, M. and Onchi, T. 1990. "Creep Deformation of an Unirradiated Zircaloy Nuclear Fuel Cladding Tube Under Dry Storage Conditions." *Journal of Nuclear Materials*, 171, 381-388. Amsterdam, Holland: Elsevier Science BV. 237136.

Mazer, J.J. 1994. "The Role of Natural Glasses as Analogues in Projecting the Long-Term Alteration of High-Level Nuclear Waste Glasses: Part 1." *Scientific Basis for Nuclear Waste Management XVII, Materials Research Society Symposium Proceedings, Boston, Massachusetts, November 29-December 3, 1993*, 333, 159-165. Barkatt, A. and Van Konynenburg, R.A., eds., Pittsburgh, Pennsylvania: Materials Research Society. 240573.

McDonald, S.G. and Kaiser, R.S. 1985. "The Impact of Metallic Debris on Fuel Performance - A Case History." *Proceedings of American Nuclear Society Topical Meeting on Light Water Reactor Fuel Performance, Portland, Oregon, April 29-May 3, 1979*, 1, 2/3 to 2/19. La Grange Park, Illinois: American Nuclear Society, Inc. 237132.

McEachern, R.J. and Taylor, P. 1997. *A Review of the Oxidation of Uranium Dioxide at Temperatures Below 400°C*. AECL-11335, COG-95-281-I. Pinawa, Manitoba, Canada: Atomic Energy of Canada Limited, Whiteshell Nuclear Research Establishment. 232575.

McKinnon, M.A. and Doherty, A.L. 1997. *Spent Nuclear Fuel Integrity During Dry Storage - Performance Tests and Demonstrations*. PNNL-11576. Richland, Washington: Pacific Northwest Laboratory. 237126.

McMinn, A.; Darby, E.D.; and Schofield, J.S. 1998. "The Terminal Solid Solubility of Hydrogen in Zirconium Alloys." *Twelfth International Symposium on Zirconium in the Nuclear Industry, Toronto, Ontario, Canada, June 15-18, 1998*. American Society for Testing and Materials, West Conshohocken, PA. 238579.

McVay, G.L. and Buckwalter, C.Q. 1983. "Effect of Iron on Waste-Glass Leaching." *Journal of the American Ceramic Society*, 66 (3), 170-173. Columbus, Ohio: American Ceramic Society. 238912.

Murakami, T.; Ewing, R.C.; and Bunker, B.C. 1988. "Analytical Electron Microscopy of Leached Layers on Synthetic Basalt Glass." *Scientific Basis for Nuclear Waste Management XI, Materials Research Society Symposium Proceedings, Boston, Massachusetts, November 30-December 3, 1987*, 112, 737-748. Apter, M.J. and Westerman, R.E., eds., Pittsburgh, Pennsylvania: Materials Research Society. 238903.

Murphy, W.M. 1997. "Retrograde Solutions of Source Term Phases." *Scientific Basis for Nuclear Waste Management XX, Materials Research Society Symposium Proceedings, Boston, Massachusetts, December 2-6, 1996*, 465, 713-720. Pittsburgh, Pennsylvania: Materials Research Society. 238534.

Nguyen, S.N.; Silva, R.J.; Weed, H.C.; and Andrews, J.E., Jr. 1992. "Standard Gibbs Free Energies of Formation at the Temperature 303.15 K of Four Uranyl Silicates: Sodydyte, Uranophane, Sodium Boltwoodite, and Sodium Weeksite." *The Journal of Chemical Thermodynamics*, 24 (1), 359-376. London; New York, New York: Academic Press (Harcourt Brace Jovanovich, Publishers). 238507.

Nitsche, H.; Gatti, R.C.; Standifer, E.M.; Lee, S.C.; Müller, A.; Prussin, T.; Deinhammer, R.S.; Maurer, H.; Becraft, K.; Leung, S.; and Carpenter, S.A. 1993. *Measured Solubilities and Speciations of Neptunium, Plutonium, and Americium in a Typical Groundwater (J-13) from the Yucca Mountain Region*. Milestone Report 3010. LA-12562-MS. Los Alamos, New Mexico: Los Alamos National Laboratory. 206976.

Nitsche, H.; Roberts, K.; Prussin, T.; Müller, A.; Becraft, K.; Keeney, D.; Carpenter, S.A.; and Gatti, R.C. 1994. *Measured Solubilities and Speciations from Oversaturation Experiments of Neptunium, Plutonium, and Americium in UE-25 p#1 Well Water from the Yucca Mountain Region*. Milestone Report 3329. LA-12563-MS. Los Alamos, New Mexico: Los Alamos National Laboratory. MOL.19951006.0171.

NRC (Nuclear Regulatory Commission) 1997. *Standard Review Plan for Dry Cask Storage Systems. Final Technical Report*. NUREG-1536. Washington, D.C.: Office of Nuclear Material Safety and Safeguards, U.S. Nuclear Regulatory Commission. 232373.

O'Connell, W.J.; Bourcier, W.L.; Gansemer, J.; and Ueng, T.S. 1997. *Performance Assessment Modeling for Savannah River Glass HLW Disposal in a Potential Repository at Yucca Mountain*. UCRL-JC-127352 Preprint. Livermore, California: Lawrence Livermore National Laboratory. MOL.19980211.0541.

OCRWM. 1998. *Quality Assurance Requirements and Description for the Civilian Radioactive Waste Management Program*. DOE/RW-0333P, Revision 8. Washington, D.C.: U.S. Department of Energy, Office of Civilian Radioactive Waste Management. MOL.19960925.0063.

Oversby, V.M. and Phinney, D.L. 1992. "The Development of Surface Alteration Layers on SRL-165 Nuclear Waste Glasses." *Journal of Nuclear Materials*, 190, 247-268. Amsterdam, The Netherlands: North-Holland Publishing Company. 238510.

Pearcy, E.C.; Prikryl, J.D.; Murphy, W.M.; and Leslie, B.W. 1994. "Alteration of Uraninite from the Nopal I Deposit, Pena Blanca District, Chihuahua, Mexico, Compared to Degradation of Spent Nuclear Fuel in the Proposed U.S. High-Level Nuclear Waste Repository at Yucca Mountain, Nevada." *Applied Geochemistry*, 9 (6), 713-732. New York, New York: Pergamon Press. 236934.

Peehs, M. and Fleisch, J. 1986. "LWR Spent Fuel Storage Behaviour." *Journal of Nuclear Materials*, 137, 190-202. Amsterdam, The Netherlands, North-Holland Publishing Company. 235595.

Pérez, I.; Casas, I.; Torrero, M.E.; Cera, E.; Duro, L.; and Bruno, J. 1997. "Dissolution Studies of Soddyite as a Long-Term Analogue of the Oxidative Alteration of the Spent Nuclear Fuel Matrix." *Scientific Basis for Nuclear Waste Management XX, Materials Research Society Symposium Proceedings, Boston, Massachusetts, December 2-6, 1996*, 465, 565-572. Gray, W.J. and Triay, I.R., eds., Pittsburgh, Pennsylvania: Materials Research Society. 236533.

Perez, J.M., Jr. and Westsik, J.H., Jr. 1980. "Effects of Cracks on Glass-Leaching." *ORNL Conference on the Leachability of Radioactive Solids, Gatlinburg, Tennessee, December 9, 1980*. PNL-SA-8931, CONF-801206-10. Richland, Washington: Pacific Northwest Laboratory. 240681.

Pescatore, C.; Cowgill, M.G.; and Sullivan, T.M. 1989. *Zircaloy Cladding Performance Under Spent Fuel Disposal Conditions, Progress Report, May 1-October 31, 1989*. BNL-52235. Upton, New York: Brookhaven National Laboratory. NNA.19900710.0055.

Pescatore, C. and Cowgill, M. 1994. *Temperature Limit Determination for the Inert Dry Storage of Spent Nuclear Fuel*. EPRI-TR-103949. Palo Alto, California: Electric Power Research Institute. 102933.

Puls, M.P. 1988. "The Influence of Hydride Size and Matrix Strength on Fracture Initiation at Hydrides in Zirconium Alloys." *Metallurgical Transactions A*, 19A, 6, 1507-1522. Warrendale, Pennsylvania: The Metallurgical Society of AIME; Metals Park, Ohio: American Society for Metals. 237143.

Ravier, G.; Masuy, G.; and Willse, J.T. 1997. "Framatome and FCF Recent Operating Experience and Advanced Features to Increase Performance and Reliability." *Proceedings of the 1997 International Topical Meeting on LWR Fuel Performance, Portland, Oregon, March 2-6, 1997*, 31-36. La Grange Park, Illinois: American Nuclear Society, Inc. 237168.

Rechard, R.P., Editor. 1995. *Performance Assessment of the Direct Disposal in Unsaturated Tuff of Spent Nuclear Fuel and High-Level Waste Owned by U.S. Department of Energy*. SAND94-2563, Vols. 1-3. Albuquerque, New Mexico: Sandia National Laboratories. 237101, 237102, 237103.

Reed-Hill, R.E. 1973. "Fuel in a Tuff Repository" in *Physical Metallurgy Principles*. Second Edition, 797-801. New York, New York: D. Van Nostrand Company. 237154.

Reeve, K.D.; Levins, D.M.; Seatonberry, B.W.; Ryan, R.K.; Hart, K.P.; and Stevens, G.T. 1989. "Fabrication and Leach Testing of Synroc Containing Actinides and Fission Products." *Scientific Basis for Nuclear Waste Management XII, Materials Research Society Symposium Proceedings, Berlin, Germany, October 10-13, 1988*, 127, 223-230. Lutze, W. and Ewing, R.E., eds., Pittsburgh, Pennsylvania: Materials Research Society. 238006.

Ringwood, A.E.; Kesson, S.E.; Reeve, K.D.; Levins, D.M.; and Ramm, E.J. 1988. *Chapter 4, Synroc*. *Radioactive Waste Forms for the Future*, 233-334. Lutze, W. and Ewing, R.C., eds., Amsterdam, The Netherlands; New York, New York: North-Holland Publishing Company; New York, New York: Sole Distributors for the USA and Canada, Elsevier Science Publishing Company. 103525.

Ross, W.A. and Mendel, J.E., eds., 1979. *Annual Report on the Development and Characterization of Solidified Forms for High-Level Wastes: 1978*. PNL-3060. Richland, Washington: Pacific Northwest Laboratory. 229585.

Rothman, A.J. 1984. *Potential Corrosion and Degradation Mechanisms of Zircaloy Cladding on Spent Nuclear Fuel in a Tuff Repository*. UCID-20172. Livermore, California: Lawrence Livermore National Laboratory. 209058.

Sagat, S.; Coleman, C.E.; Griffiths, M.; and Wilkins, B.J.S. 1994. "The Effect of Fluence and Irradiation Temperature on Delayed Hydride Cracking in Zr-2.5Nb." *Zirconium in the Nuclear Industry, Tenth International Symposium, Baltimore, Maryland, June 21-24, 1993*, 35-61. Garde, A.M. and Bradley, E.R., eds., Philadelphia, Pennsylvania: American Society for Testing and Materials. 237158.

Sanders, T.L.; Seager, K.D.; Rashid, Y.R.; Barrett, P.R.; Malinauskas, A.P.; Einziger, R.E.; Jordan, H.; Duffey, T.A.; Sutherland, S.H.; and Reardon, P.C. 1992. *A Method for Determining the Spent-Fuel Contribution to Transport Cask Containment Requirements*. SAND90-2406. Albuquerque, New Mexico: Sandia National Laboratories. 232162.

Santanam, L.; Raghavan, S.; and Chin, B.A. 1992. "Zircaloy Cladding Rupture During Repository Storage." *Nuclear Technology*, 97 (3) 316-322. Hinsdale, Illinois: American Nuclear Society, Inc. 237166.

Sasaki, S. and Kuwabara, S. 1997. "Utility Perspective on Commercial Light-Water Reactor Fuel in Japan." *Proceedings of the 1997 International Topical Meeting on LWR Fuel Performance, Portland, Oregon, March 2-6, 1997*, 11-20. La Grange Park, Illinois: American Nuclear Society, Inc. 237169.

Sassani, D.C. 1992. *Petrologic and Thermodynamic Investigation of the Aqueous Transport of Platinum-Group Elements During Alteration of Mafic Intrusive Rocks*. Ph.D Dissertation. Volumes I-II, St. Louis, Missouri: Washington University; Ann Arbor, Michigan: UMI. 240738.

Sayles, C.W.; Chang, R.Y.; Thomsen, O.J.; and Swoope, S.C. 1994. "4. Use of Axial Cesium Distribution for Failure Identification in San Onofre Units." *Transactions of the American Nuclear Society, New Orleans, Louisiana, June 19-23, 1994*, 70, 76-77. La Grange Park, Illinois: American Nuclear Society, Inc. 236801.

Schneider, K.J. and Mitchell, S.J. 1992. *Foreign Experience on Effects of Extended Dry Storage on the Integrity of Spent Nuclear Fuel*. PNL-8072. Richland, Washington: Pacific Northwest Laboratory. 205836.

Schrire, D.I. and Pearce, J.H. 1994. "Scanning Electron Microscope Techniques for Studying Zircaloy Corrosion and Hydriding." *Zirconium in the Nuclear Industry, Tenth International Symposium, Baltimore, Maryland, June 21-24, 1993*. ASTM Special Technical Publication 1245, 98-115. Garde, A.M. and Bradley, E.R., eds., Philadelphia, Pennsylvania: American Society for Testing and Materials. 237130.

Shaw, R.A. 1992. "Source Term in the EPRI Performance Assessment." *Nuclear Waste Technical Review Board, Las Vegas, Nevada, October 15, 1992*. Palo Alto, California: Electrical Power Research Institute. 238962.

Shi, S.Q. and Puls, M.P. 1994. "Criteria for Fracture Initiation at Hydrides in Zirconium Alloys I. Sharp Crack Tip." *Journal of Nuclear Materials*, 208 (3), 232-242. Amsterdam, The Netherlands: North-Holland Publishing Company. 237135.

Shi, S.Q. and Puls, M.P. 1996. "Advances in the Theory of Delayed Hydride Cracking in Zirconium Alloys," *Hydrogen Effects in Material.*, Thompson, A.W. and Moody, N.R., eds., p 611-621. Warrendale, Pennsylvania: The Minerals, Metals & Materials Society. 239793.

Siegel, M.D.; Ward, D.B.; Cheng, W.C.; Bryant, C.; Chocas, C.S.; and Reynolds, C.G. 1993. "Preliminary Characterization of Materials for a Reactive Transport Model Validation Experiment." *High Level Radioactive Waste Management, Proceedings of the Fourth Annual International Conference, Las Vegas, Nevada, April 26-30, 1993, 1*, 348-356. La Grange Park, Illinois: American Nuclear Society, Inc.; New York, New York: American Society of Civil Engineers. 224543.

Siegmann, E.R. 1998 (October 28). Transmittal of Personal Communications used in Chapter 6, TBD. CRWMS M&O Interoffice Correspondence LV.PA.RLH.10/98-151. Las Vegas, Nevada: CRWMS M&O. MOL.19981029.0262.

Silva, R.J.; Bidoglio, G.; Rand, M.H.; Robouch, P.B.; Wanner, H.; and Puigdomenech, I. 1995. "Chemical Thermodynamics of Americium." *Chemical Thermodynamics 2*. Amsterdam, The Netherlands; Elsevier. 237106.

Smith, T.H. and Ross, W.A. 1975. *Impact Testing of Vitreous Simulated High-Level Waste in Canisters*. BNWL-1903. Richland, Washington: Pacific Northwest Laboratories. 238924.

Smith, P.K. and Baxter, C.A. 1981. *Fracture During Cooling of Cast Borosilicate Glass Containing Nuclear Wastes*. DP-1602. Aiken, South Carolina: E.I. du Pont de Nemours & Co., Savannah River Laboratory. 238536.

Steward, S.A. and Gray, W.J. 1994. "Comparison of Uranium Dissolution Rates from Spent Fuel and Uranium Dioxide." *High Level Radioactive Waste Management, Proceedings of the Fifth Annual International Conference, Las Vegas, Nevada, May 22-26, 1994, 4*, 2602-2608. La Grange Park, Illinois: American Nuclear Society, Inc.; New York, New York: American Society of Civil Engineers. 238004.

Stout, R.B. 1996. "Nonequilibrium Thermodynamical Model for Spent Fuel Dissolution Rate." *High Level Radioactive Waste Management 1996, Proceedings of the Seventh Annual International Conference, Las Vegas, Nevada, April 29-May 3, 1996*, 393-395. La Grange Park, Illinois: American Nuclear Society, Inc.; New York, New York: American Society of Civil Engineers. 233230.

Stout, R.B. and Leider, H.R., eds., 1997. *Waste Form Characteristics Report, Revision 1*. UCRL-ID-108314 Version 1.2. Livermore, California: Lawrence Livermore National Laboratory. MOL.19980512.0133.

Stroup, E.P. 1998. Letter to R.W. Andrews, Duke Engineering and Services, Las Vegas, Nevada, May 4, 1998. Idaho Falls, Idaho: Lockheed Martin, Idaho Technologies Company. MOL.19980616.0308.

Stumm, W. and Morgan, J.J. 1981. *Aquatic Chemistry: An Introduction Emphasizing Chemical Equilibria in Natural Waters*. New York, New York: John Wiley & Sons. 208448.

Sunderland, D.J.; Kennard, M.W.; and Harbottle, J.E. 1994. "2. Identification of Failed LWR Fuel in U.S. Reactors." *Transactions of the American Nuclear Society*, 70, 73-74. La Grange Park, Illinois: American Nuclear Society, Inc. 237153.

Tasooji, A.; Einziger, R.E.; and Miller, A.K. 1984. "Modeling of Zircaloy Stress-Corrosion Cracking: Texture Effects and Dry Storage Spent Fuel Behavior." *Zirconium in the Nuclear Industry, Sixth International Symposium, Vancouver, British Columbia, June 28- July 1, 1982*. ASTM Special Technical Publication 824, 595-626. Franklin, D.G. and Adamson, R.B., eds. Philadelphia, Pennsylvania: American Society for Testing and Materials. 223247.

Thomas, L.E.; Slagle, O.D.; and Einziger, R.E. 1991. "Nonuniform Oxidation of LWR Spent Fuel in Air." *Journal of Nuclear Materials*, 184, 117-126. Amsterdam, The Netherlands: North-Holland Publishing Company. 238355.

Thompson, J.L. ed. 1998. *Laboratory and Field Studies Related to Radionuclide Migration at the Nevada Test Site. October 1, 1996 - September 30, 1997*. LA-13419-PR. Los Alamos, New Mexico: Los Alamos National Laboratory. MOL.19980625.0450.

Tien, P-L.; Updegraff, C.D.; Wahi, K.K.; Siegel, M.D.; and Guzowski, R.V. 1985. *Repository Site Data Report for Unsaturated Tuff, Yucca Mountain, Nevada*. NUREG/CR-4110, SAND84-2668. Washington, D.C.: U.S. Nuclear Regulatory Commission, Office of Nuclear Material Safety and Safeguards, Division of Waste Management, and Albuquerque, New Mexico: Sandia National Laboratories. 217172.

Triay, I.R.; Meijer, A.; Conca, J.L.; Kung, K.S.; Rundberg, R.S.; Strietelmeier, B.A.; and Tait, C.D. 1997. *Summary and Synthesis Report on Radionuclide Retardation for the Yucca Mountain Site Characterization Project - [Milestone 3784M]* LA-13262-MS, Los Alamos, New Mexico: Los Alamos National Laboratory. MOL.19971210.0177.

Uziembo, N.H. and Smith, H.D. 1989. *An Investigation of the Influence of Fluoride in the Corrosion of Zircaloy-4: Initial Report (Draft)*. PNL-6859. Richland, Washington: Pacific Northwest Laboratory. MOL.19980326.0369.

Van Konynenburg, R.A.; Smith, C.F.; Culham, H.W.; and Otto, C.H., Jr. 1985. "Behavior of Carbon-14 in Waste Packages for Spent Fuel in a Repository in Tuff." *Scientific Basis for Nuclear Waste Management VIII, Materials Research Society Symposia Proceedings, Boston, Massachusetts, November 26-29, 1984*, 44, 405-412. Jantzen, J.M.; Stone, J.A.; and Ewing, R.C., eds., Pittsburgh, Pennsylvania: Materials Research Society. 238904.

Van Konynenburg, R.A.; Curtis, P.G.; and Summers, T.S.E. 1998. *Scoping Corrosion Tests on Candidate Waste Package Basket Materials for the Yucca Mountain Project*. UCRL-ID-130386. Lawrence Livermore National Laboratory. MOL.19980727.0385.

Van Swam, L.F.; Strasser, A.A.; Cook, J.D.; and Burger, J.M. 1997. "Behavior of Zircaloy-4 and Zirconium Liner Zircaloy-4 Cladding at High Burnup." *Proceedings of the 1997 International Topical Meeting on LWR Fuel Performance, Portland, Oregon, March 2-6, 1997*, 421-431. La Grange Park, Illinois: American Nuclear Society, Inc.; New York, New York: American Society of Civil Engineers. 237262.

Wasywich, K.M.; Frost, C.R.; and Freire-Canosa, J. 1986. "Storage of Irradiated CANDU Fuel in Dry and Moist Air." *Proceedings of the Second International Conference on Radioactive Waste Management, Winnipeg, Manitoba, Canada, September 7-11, 1986*, 616-624. Toronto, Ontario, Canada: Canadian Nuclear Society. 237147.

Whipple, C.; Budnitz, R.; Ewing, R.; Moeller, D.; Payer, J.; and Witherspoon, P. 1997. *Peer Review of the Total System Performance Assessment-Viability Assessment, First Interim Report*. June, 1997. Las Vegas, Nevada: TRW Environmental Safety Systems. MOL.19970731.0823.

Wicks, G.G. 1985. "2 Nuclear Waste Glasses." *Treatise on Materials Science and Technology, Volume 26, Glass IV*, 57-118. Tomozawa, M. and Doremus, R.H., eds., Orlando, Florida: Academic Press, Inc. 238484.

Wilkinson, W.D. 1962. *Uranium Metallurgy. Volume II: Uranium Corrosion and Alloys*. New York, New York: Interscience Publishers, A Division of John Wiley and Sons. 240740.

Wilson, C.N. 1985. *Results from NNWSI Series 1 Spent Fuel Leach Tests*. HEDL-TME-84-30. Richland, Washington: Hanford Engineering Development Laboratory. 210347.

Wilson, C.N. 1987. *Results from Cycles 1 and 2 of NNWSI Series 2 Spent Fuel Dissolution Tests*. HEDL-TME-85-22, DE87011598. Richland, Washington: Westinghouse Hanford Company. 202294.

Wilson, C.N. 1990a. *Results From NNWSI Series 2 Bare Fuel Dissolution Tests*. PNL-7169. Richland, Washington: Pacific Northwest Laboratory. NNA.19900814.0048.

Wilson, C.N. 1990b. *Results from NNWSI Series 3 Spent Fuel Dissolution Tests*. PNL-7170. Richland, Washington: Pacific Northwest Laboratory. NNA.19900329.0142.

- Wilson, C.N. and Bruton, C.J. 1990. "Studies on Spent Fuel Dissolution Behavior Under Yucca Mountain Repository Conditions." *Nuclear Waste Management III, Proceedings of the Fourth International Symposium on Ceramics in Nuclear Waste Management, American Ceramic Society Annual Meeting, Indianapolis, Indiana, April 24-26, 1989, Ceramic Transactions 9*, 423-442. Mellinger, G.B., eds., Westerville, Ohio: The American Ceramic Society, Inc. 235673.
- Wilson, M.L.; Gauthier, J.H.; Barnard, R.W.; Barr, G.E.; Dockery H.A.; Dunn, E.; Eaton, R.R.; Guerin, D.C.; Lu, N.; Martinez, M.J.; Nilson, R.; Rautman, C.A.; Robey, T.H.; Ross, B.; Ryder, E.E.; Schenker, A.R.; Shannon, S.A.; Skinner, L.H.; Halsey, W.G.; Gansemer, J.D.; Lewis, L.C.; Lamont, A.D.; Triay, I.R.; Meijer, A.; and Morris, D.E. 1994. *Total System Performance Assessment for Yucca Mountain - SNL Second Iteration (TSPA-1993)*. SAND93-2675. Albuquerque, New Mexico: Sandia National Laboratories. 211047.
- Witte, M.C.; Chun, R.C.; and Schwartz, M.W. 1989. "Dynamic Impact Effects on Spent Fuel Assemblies." *9<sup>th</sup> International Symposium on the Packaging and Transportation of Radioactive Materials Proceedings, Washington, D.C., June 11-16, 1989, 1*, 186-194. Oak Ridge, Tennessee: Oak Ridge National Laboratory. 102955.
- Wolery, T.J. 1992. *EQ3/6, A Software Package for Geochemical Modeling of Aqueous Systems: Package Overview and Installation Guide (Version 7.0)*. UCRL-MA-110662 PT I. *EQ3NR, A Computer Program for Geochemical Aqueous Speciation-Solubility Calculations: Theoretical Manual, User's Guide, and Related Documentation (Version 7.0)*. UCRL-MA-110662 PT III. Livermore, California: Lawrence Livermore National Laboratory. NNA.19921023.0028.
- Wolery, T.J.; Palmer, C.E.; and Knauss, K. 1995. *The Neptunium Solubility Problem in Repository Performance Assessment: A White Paper*. Livermore, California: Lawrence Livermore National Laboratories. MOL.19981012.0280.
- Wronkiewicz, D.J.; Bates, J.K.; Gerding, T.J.; Veleckis, E.; and Tani, B.S. 1992. "Uranium Release and Secondary Phase Formation During Unsaturated Testing of UO<sub>2</sub> at 90°C." *Journal of Nuclear Materials*, 190, 107-127. Amsterdam, The Netherlands: North-Holland Publishing Company. 236558.
- Wronkiewicz, D.J.; Bates, J.K.; Wolf, S.F.; and Buck, E.C. 1996. "Ten-Year Results from Unsaturated Drip Tests with UO<sub>2</sub> at 90°C: Implications for the Corrosion of Spent Nuclear Fuel." *Journal of Nuclear Materials*, 238 (1), 78-95. Amsterdam, The Netherlands: North-Holland Publishing Company. 233339.
- Wronkiewicz, D.J.; Buck, E.C.; and Bates, J.K. 1997. "Grain Boundary Corrosion and Alteration Phase Formation During the Oxidative Dissolution of UO<sub>2</sub> Pellets." *Scientific Basis For Nuclear Waste Management XX, Materials Research Society Symposium Proceedings, Boston, Massachusetts, December 2-6, 1996*, 465, 519-526. Gray, W.J. and Triay, I.R., eds., Pittsburgh, Pennsylvania: Materials Research Society. 23855.
- Yang, R.L. 1997. "Meeting the Challenge of Managing Nuclear Fuel in a Competitive Environment." *Proceedings of the 1997 International Topical Meeting on LWR Fuel Performance, Portland, Oregon, March 2-6, 1997*, 3-10. La Grange Park, Illinois: American Nuclear Society, Inc.; New York, New York: American Society of Civil Engineers. 237148.

1  
Yau, T. L., 1984, "Zirconium Versus Corrosive Species in Geothermal Fluids," Paper 140/1-140/8. Corrosion 84, April 2-6, 1984. Houston, Texas: National Association of Engineers. 238987.

Yau, T.L. and Webster, R.T. 1987. "Corrosion of Zirconium and Hafnium." *Metals Handbook. Ninth Edition. Volume 13 Corrosion.* 707-721. Metals Park, Ohio: American Society for Metals International. 237160.

INTENTIONALLY LEFT BLANK